Miles Morel Aron

Hertford College

Supervised by

Professor Eleanor Stride

Investigating the Role of Microbubble Composition in Ultrasound-Mediated Drug Delivery

A thesis submitted for the degree of

Doctor of Philosophy

Trinity 2018

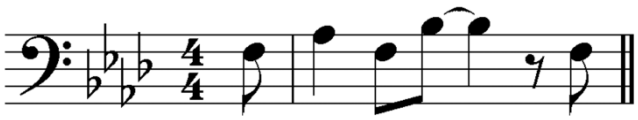

To my family.

-John Coltrane

Abstract

Ultrasound exposure of circulating cavitation agents (e.g. phospholipid-shelled microbubbles) and/or drug-carrying vehicles (e.g. liposomes) has been shown to enable the delivery of a therapeutic payload to target locations within the human body. The destruction of these agents also results in the localized deposition of the surfactant material used to encapsulate the payload. The impact of this deposition upon cell membrane properties, and/or its impact on therapeutic outcomes, has not been investigated previously. This thesis explores several of the current and potential roles of localized surfactant deposition in ultrasound-mediated drug delivery.

Initial observations demonstrate that transfer of phospholipids between microbubbles and cells can alter cell membrane hydration and lipid order. Further characterization of this phenomenon showed, critically, a microbubble formulation-dependence. The impact of lipid transfer from microbubbles to cell membranes on ultrasound and cavitation-mediated pore formation, known as sonoporation, was then systematically investigated with different formulations. Both short chain saturated cylindrical lipids and long chain saturated conical lipids were found to influence lipid order and cell membrane permeability. Microbubbles incorporating conical lipids (lysophosphatidylcholine, Lyso-PC) were ultimately developed. The ultrasound-mediated triggered release of Lyso-PC from microbubbles was found to significantly increase sonoporation as measured by the uptake of a fluorescent model drug. Lyso-PC-incorporating microbubbles are also an interesting candidate for ultrasound-mediated blood-brain barrier opening, as evidenced by the reversible disruption of tight junctions by Lyso-PC exposure.

This thesis thus demonstrates for the first time that lipid transfer initiated by ultrasound and cavitation agent exposure can modify biological barriers, which may potentiate the enhancement of therapeutic outcomes.

Statement of originality

I hereby declare that this submission is my own work and, to the best of my knowledge, it contains no materials previously published or written by another person, or substantial proportions of material which have been accepted for the award of any other degree or diploma at the University of Oxford or any other educational institution, except where due acknowledgement is made in the thesis.

Any contribution made to the research by others, with whom I have worked at the University of Oxford or elsewhere, is explicitly acknowledged in the thesis.

I also declare that the intellectual content of this thesis is the product of my own work, except to the extent that assistance from others in the project's design and conception or in style, presentation and linguistic expression is acknowledged.

Miles Aron

Trinity 2018

Acknowledgements

First and foremost, I would like to express my gratitude to my supervisor, Professor Eleanor Stride. Over five years ago, I was inspired to study ultrasound-mediated drug delivery by one of Professor Stride's online lectures. Her skilful leadership and scientific prowess continue to inspire and her generous support throughout my DPhil was exceptional. I am forever indebted.

I would also like to express gratitude to the other professors of BUBBL. Professor Robin Cleveland, Professor Constantin Coussios, and Professor Robert Carlisle. Their generosity and vision has had a material impact on the way I think, for which I am truly grateful.

I would also like to thank all those who contributed to the work that became this thesis. Especially, Professor Dario Carugo, Dr. Lester Barnsley, Dr. Christophoros Mannaris, Oliver Vince, Dr. Michael Gray, Professor James Kwan, Valerio Pereno, Dr. Shamit Shrivastava, Dr. Richard Browning, Estelle Beguin, Dr. Anjali Seth, Anna Smith, Roberto Duca, James Fisk, David Salisbury, Professor Christian Eggeling, Dr. Jorge Bernardino de la Serna, and Dr. Erdinc Sezgin from the University of Oxford.

I would also like to extend my gratitude to those collaborators that I had the opportunity to work with from the University of Twente: Dr. Guillaume Lajoinie, Professor Michel Versluis, and Dr. Marinke van der Helm.

I am also grateful to Professor Vartan Kurtcuoglu and all those at the Interface Group at the University of Zurich for introducing me to biomedical science and for graciously hosting me during my Fulbright.

To my mentors, those who challenged me and took a chance on me: Will Schramm and Doug Wilson at PVI Systems, Dr. Richard Pardridge at the U.S. Department of Energy, Dr. Ben Sim, Dr. Bill Warmbrodt, and Shirley Burek at NASA, Dr. Aslihan Demirkaya and Dr. Bob Celmer at the University of Hartford, Steve Davis, and Nat Reeves at the Jackie McLean Institute, Dr. James Rourke and Mr. Jay Driscoll at The Norwich Free Academy, Maggie Schumacher at the piano, and Rich Goldstein at the guitar: Your combined influence on my life is immeasurable and I thank you whole-heartedly. I would also like to extend my gratitude to my funding sources: the Martin Trust, the EPSRC, and OxCD3.

A huge thank you also goes out to Brandon Moffitt, Chazwick Cleckley, Mike Dick, Jeff Hullfish, Taylor Paisie, Abby Larkin, Eleonora Berra, Tayo Sanders, Claudia Hill, Megan Grundy and the whole Tyndale Rd. crew for your unwavering friendship and support.

I am so incredibly grateful for the love, support, friendship, and patience of my girlfriend, Irini Skaripa-Koukelli, through these past two years.

To my family, past and present, I would not be here without your love and support, and without your example.

Mom and Dad, Bryon and Alex, words cannot express the depth of my gratitude. Thank you.

Dissemination

Peer-reviewed journal publications

Aron, M., Vince, O., Gray, M., Stride, E. Investigating the role of lipid transfer in sonoporation. *In preparation.*

Aron, M., Veerle, B., Stride, E. Lysophosphatidylcholine transiently opens the blood-brain barrier *in vitro*. *In preparation.*

Browning, R., Booth, A., **Aron, M.**, Shrivastava, S., Cleveland, R., Carugo, D., Stride, E. The lipid packing in ultrasound contrast-agent microbubbles from production to destruction. *In preparation.*

Pereno, V., **Aron, M.**, Vince, O., Mannaris, C., Seth, A., de Saint Victor, M., Lajoinie, G., Versluis, M., Coussios, C., Carugo, D., Stride, E. Layered acoustofluidic resonators for the simultaneous optical and acoustic characterisation of cavitation dynamics, microstreaming, and biological effects. *Biomicrofluidics* **12(3)**, 034109 (2018).

Aron, M., Browning, R., Carugo, D., Sezgin, E., Bernardino de la Serna, J., Eggeling, C., Stride, E. Spectral imaging toolbox: segmentation, hyperstack reconstruction, and batch processing of spectral images for the determination of cell and model membrane lipid order. *BMC Bioinformatics* **18**, 254-262 (2018).

Barnsley, L.C., Carugo, D., **Aron, M.**, Stride, E. Understanding the dynamics of superparamagnetic particles under the influence of high field gradient arrays. *Physics in Medicine and Biology* **62(6)**, 2333-2360 (2017).

Carugo, D., **Aron, M.**, Sezgin, E., Bernardino de la Serna, J., Kuimova, M.K., Eggeling, C., Stride, E. Modulation of the molecular arrangement in artificial and biological membranes by phospholipid-shelled microbubbles. *Biomaterials* **113**, 105-117 (2016).

Conference presentations

Aron, M., Barnsley, L., Shrivastava, S., van der Helm, M., Segerink, L., Stride, E. Ultrasound-mediated blood-brain barrier disruption: correlation with acoustic emissions, Acoustic ’17 Boston, The Journal of the Acoustical Society of America 141, 3460 (2017).

Aron, M., Barnsley, L., Shrivastava, S., van der Helm, M., Segerink, L., Stride, E. Ultrasound-mediated blood-brain barrier disruption and recovery kinetics *in vitro*, The 7th UK & Ireland Early Career BBB Symposium (2017).

Aron, M., Carugo, D., Vince, O., Pereno, V., Shrivastava, S., Owen, J., Sezgin, E., Bernardino de la Serna, J., Kuimova, M., Eggeling, C., Stride, E. Sonoporation-sensitization by microbubble constituents?, The 23rd European symposium on ultrasound contrast imaging (2016).

Carugo, D., **Aron, M.**, Sezgin, E., Bernardino de la Serna, J., Kuimova, M., Eggeling, C., Stride, E. Modulation of cell membrane properties by lipid transfer from microbubbles - a potential mechanism for sonoporation?, The 22nd European symposium on ultrasound contrast imaging (2016).

Contents

I.

Introduction

1.1. Ultrasound-mediated drug delivery

The delivery of therapeutic agents has been improved in recent years by developments in technology including: encapsulation in nanoparticles that can provide longer circulation times, triggered release based on endogenous stimuli, passive targeting by enhanced permeability and retention in tumours, and active targeting by attaching ligands that bind proteins that are over-expressed on target cells[1,2].

In parallel, there have been significant developments in reducing off-target effects through the use of tissue specific therapeutics. This has, however, unfortunately led to the use of larger therapeutic agents such as liposomes, antibodies, gene vectors, and viruses[3–5]. These larger agents are more difficult to deliver on account of the physical barriers to drug delivery, namely, the endothelium, the cell membrane, and those barriers specific to the tumour microenvironment[6–9] (see Figure 1). Ultrasound-mediated drug delivery provides a non-invasive, non-ionizing, and localized means of

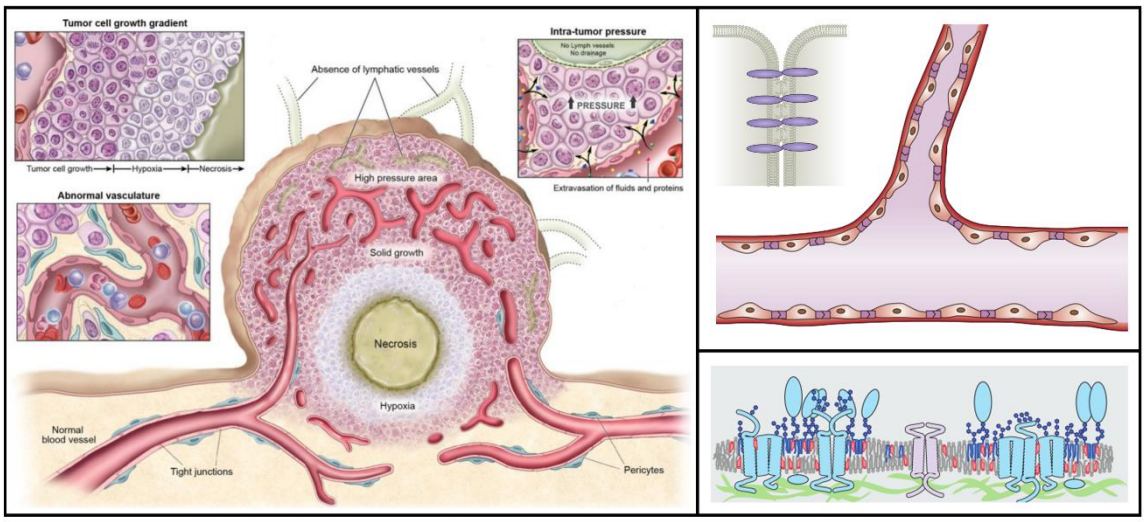

Figure 1: Generalized illustrations of various barriers to drug delivery. Left: The abnormalities of the tumour microenvironment include high interstitial pressure, a stiff extracellular matrix, a hypoxic region, and a tortuous, leaky vasculature, all of which contribute to difficulties in drug delivery. Adapted from Kobayashi et al.[6]. Right, top: Extravasation of drugs across the blood-brain barrier endothelium is severely restricted by the mesh of proteins and lipids that form tight junctions (inset). Adapted from Dejana[7] and Zihni et al.[8]. Right-bottom: The cell membrane, comprised of a dynamic and heterogeneous mixture of lipids, proteins, and carbohydrates supported by the cytoskeleton, serves as a transport barrier between extracellular drugs and the intracellular milieu. Adapted from Lingwood and Simons[9].

overcoming both off-target effects and physical barriers to drug delivery, and is compatible with modern therapeutic agents.

In this thesis, the ultrasound-mediated drug delivery techniques discussed include the temporary permeabilization of cell membranes (sonoporation)[10] and the blood-brain barrier[11], as well as mild hyperthermia for triggered-release[12]. These techniques are discussed without regard to a specific clinical indication, although it is emphasized that improving cancer treatment is a top priority in the field. In the case of ultrasound-mediated blood-brain barrier disruption, previously immedicable diseases and disorders including Alzheimer's disease, Huntington's disease, Lou Gehrig's disease, stroke, and autism, are also clinical indications of interest. In this chapter the phenomena associated with ultrasound and its interactions with engineered cavitation agents in the context of drug delivery are introduced. The cell membrane, a critical barrier[i] to drug delivery, is also described in detail.

1.2. Ultrasound terminology

In this section, the terminology associated with ultrasound-mediated drug delivery as used in the remainder of the thesis is introduced.

1.2.1. Sound

Sound waves are mechanical vibrations that arise from perturbations in pressure (p). Herein, sound is discussed with regard to the propagation of longitudinal waves, whereby molecules in the medium undergo compression and rarefaction in the direction of propagation. The speed at which sound waves propagate in fluids, under the condition that sound is described by an adiabatic and reversible (isentropic) process with sound pressure, p, small compared with the equilibrium pressure, is given by the

[i] the blood-brain barrier is introduced in detail in Chapter 5

Newton-Laplace equation, $c = \sqrt{\frac{K}{\rho}}$, where the isentropic bulk modulus, K, is given by $K = -V\frac{dp}{dV} = \rho\frac{dp}{d\rho} = \frac{1}{\beta}$, and V is volume and β is compressibility, such that $c = \sqrt{\frac{dp}{d\rho}}$. Repeated perturbations of the medium are associated with a frequency (f, in Hz = s^{-1}) defined as the reciprocal of the time elapsed between perturbations (the period, $T = \frac{1}{f}$). The physical distance between successive regions of compression or rarefaction in a sound wave is the wavelength ($\lambda = \frac{c}{f}$).

1.2.2. Ultrasound

Ultrasound is defined as sound that occurs at frequencies beyond the range of human hearing ($f >$ 20 kHz). In ultrasound-mediated drug delivery, ultrasound (with f ~ 0.2 to 2 MHz) is typically generated by piezoelectric transducers, which produce an oscillatory mechanical strain in response to the application of an alternating current. In ultrasound-mediated drug delivery, ultrasound is often pulsed, i.e. the ultrasound is repeatedly turned on and off at a rate described by the pulse repetition frequency (PRF in Hz). The period of time that the ultrasound is on in each pulse is referred to throughout the thesis as the burst length (in s). The duty cycle (DC), or percentage of time the ultrasound is on, is defined as the ratio of the burst length to the inverse of the PRF. The total time of ultrasound exposure is referred to as the duration (in s).

1.2.3. Acoustic impedance

The ratio of the acoustic pressure to the particle velocity ($\tilde{Z} = \frac{\tilde{p}}{\tilde{v}}$), known as the complex acoustic impedance, describes the relative magnitude and phase of vibration with respect to space. For harmonic plane waves, where the pressure is in phase with the

particle velocity, the impedance $\tilde{Z} = r = \rho_0 c$ where r is the characteristic impedance describing the response of a material to dynamic stimulus.

1.2.4. Reflection, transmission and scattering

When a sound wave propagates from one medium to another with a different acoustic impedance, the wave is not completely transmitted. If the boundary is acoustically hard ($r_1 \ll r_2$), the wave is reflected in-phase and if the boundary is acoustically soft ($r_1 \gg r_2$), the wave reflected is out-of-phase. When the impedances are otherwise mismatched, the wave is neither completely reflected nor transmitted. The superposition of incident and reflected waves can give rise to standing waves, whereby the wave amplitude varies as a function of space. "Specular" reflection occurs when the boundaries extend for distances much larger than λ. Objects in the path of the wave of contrasting impedance that are of the order of λ produce diffractive scattering; whilst objects much smaller than λ produce diffusive or Rayleigh scattering.

1.2.5. Refraction

When a sound wave travels through a medium in which density changes as a function of space, or through an acoustic boundary at an oblique angle of incidence, the wave travels at different speeds along the wave front such that the propagation direction can change. This phenomenon, known as refraction, is described by Snell's Law for plane waves ($\frac{\sin\theta_i}{c_1} = \frac{\sin\theta_t}{c_2}$, where θ_i and θ_t denote the angle of incidence and transmission respectively, and c_1 and c_2 indicate the speeds of sound on either side of the interface).

1.2.6. Absorption and attenuation

As a sound wave travels through a viscous medium, energy is dissipated as a result of various molecular processes leading to the production of heat. If the medium contains layers with different acoustic impedances or scattering objects, the intensity of the sound wave as measured on the axis of propagation is further decreased. The cumulative loss of sound intensity with distance is known as attenuation, the frequency-dependence of which is well-described for some tissues by the empirical power law, $\alpha(\omega) = \alpha_0 f^b$, where b typically ranges from 0 to 2. Heating by ultrasound propagation through tissue can be significant, especially when the local ultrasound intensity and/or duty cycle is high. Ultrasound-mediated heating has been implemented for the triggered release of drugs from thermosensitive liposomes[12], and for tissue ablation[13].

1.2.7. Primary radiation force and acoustic streaming

A propagating wave imparts momentum to particles of contrasting impedance. This primary radiation force, or acoustic radiation force, is proportional to the gradient of the acoustic potential, the particle size, compressibility, and density[14]. The gradient in momentum transfer from the ultrasound wave to the medium also gives rise to a net fluid flow known as acoustic streaming.

1.3. Cavitation nucleation and cavitation agents

A liquid at constant temperature subject to a pressure below its saturated vapor pressure, is said to be under tension. When the tension in the liquid exceeds the tensile strength of the liquid, it ruptures and vaporizes in a process known as cavitation. Cavitation requires the presence of nucleation sites, precursors to the macroscopic voids or bubbles formed in the liquid. In the classical description of cavitation, nucleation sites are molecule-sized

voids created by the thermal fluctuations of liquid molecules[15]. In practice, however, gas-trapping impurities in the liquid and inhomogeneities in the surrounding surfaces serve as far more effective cavitation nuclei, lowering the threshold tension for cavitation[15].

Owing to there being relatively low concentrations of cavitation nuclei in mammalian tissue, large negative pressures are required to induce cavitation in the human body. Clinical high intensity focused ultrasound transducers and shockwave sources are therefore used e.g. in lithotripsy[16] or cavitation-mediated histotripsy[17]. Owing to the stochastic nature of cavitation, however, these do pose a risk of unwanted damage to healthy tissue[18]. In ultrasound-mediated imaging and therapy, particles that serve as cavitation nuclei, referred to hereafter as cavitation agents, are used to achieve cavitation at pressures below those associated with excessive tissue damage. In this section, the development of these cavitation nuclei is introduced. Throughout this thesis the term cavitation is used to refer to the interaction of these engineered cavitation nuclei with an ultrasound field and not the formation of bubbles from "native" nuclei.

In the 1960s, Dr. Charles Joyner observed transient enhancements in US signal while injecting a patient with indocyanine green[19]. This phenomenon was further explored by Gramiak and Shah in 1968 and ultimately led to the development of coated gas-filled microbubbles as ultrasound contrast agents, for improving cardiovascular visualization with ultrasound[20].

Two decades later, Feinstein led a series of clinical trials for the contrast-agent Albunex®, microbubbles of air coated with a heat-denatured human albumin shell, which, despite lasting only seconds *in vivo*, became the first clinically available microbubble ultrasound contrast agent[21,22]. By replacing the air in Albunex® with a

higher molecular weight gas, perflutren (F-propane), Optison®, still with an albumin-derived shell, was introduced in 1998[21], becoming the first clinically available ultrasound contrast agent small enough and lasting long enough to circulate meaningfully in the microvasculature. Soon after, Definity® was released clinically in 2001, a perflutren-filled microbubble with a phospholipid shell, followed by SonoVue®, also with a phospholipid shell and sulphur hexafluoride as the core[21].

Microbubble shells can be loaded with therapeutic compounds including DNA, chemotherapeutics, antibodies, and liposomes, and can be decorated with targeting ligands for biological targeting[23]. Microbubbles also typically incorporate polyethylene glycol covalently bonded to either phospholipids or fatty acids to enhance stability and reduce immunogenicity[24,25]. Microbubbles have further been loaded with therapeutic gases such as oxygen and nitric oxide[26]; and the incorporation of iron-oxide nanoparticles into microbubble shells enables magnetic resonance imaging and magnetically-targeted drug-delivery[27,28]. Today, microbubbles are used clinically to enhance ultrasound imaging in echocardiography, to measure blood flow using Doppler ultrasonography, and are in clinical development for therapeutic applications in focused ultrasound surgery, sonothrombolysis, and drug and gene delivery[20,29–31].

In addition to microbubbles, sub-micrometre phase-shift droplets have been developed that incorporate a liquid perfluorochemical with a boiling point close to physiological temperature (37°C) that vaporizes to form microbubbles upon exposure to ultrasound[32]. Solid cavitation nuclei such as sub-micron gas-trapping polymeric cups[33], gold nanocones[34], mesoporous silica nanoparticles[35], or nanoparticles that produce pH-triggered CO_2 microbubbles[36] have also been developed. These novel cavitation agents offer advantages over microbubbles for ultrasound-mediated drug delivery in certain

indications in which longer circulation times, smaller particle sizes, different chemical characteristics, and/or different cavitation behaviour is required.

1.4. Cavitation phenomena

The following section discusses the cavitation phenomena relevant to ultrasound-mediated drug delivery and this thesis.

1.4.1. Non-linear oscillations

Microbubble oscillations impart high-frequency oscillatory stresses to the surrounding environment with steep spatial and temporal gradients[37]. Although microbubbles can oscillate linearly at very low ultrasound pressures, the ultrasound pressures employed in ultrasound imaging and therapy induce non-linear oscillations owing to asymmetry in the expansion and compression of the bubble in the ultrasound field[38]. This nonlinearity gives rise to the leakage of energy into discrete frequencies other than the driving frequency of the ultrasound (e.g. harmonics and ultraharmonics)[39,40]. Owing to their low density and high compressibility, microbubbles re-radiate harmonics at much greater amplitudes than that attributed to tissue in the propagation path. Acoustic emissions associated with the non-linear oscillation of microbubbles exposed to ultrasound are thus critical for ultrasound-contrast imaging and cavitation detection[41].

The behaviour of a microbubble under ultrasound duress depends on the microbubble size, the ultrasound frequency, and the ultrasound pressure amplitude among other factors. The resonant frequency of a spherical microbubble in an infinite domain of water excited by an oscillatory pressure small compared with the equilibrium pressure was given by Minnaert as $f = \frac{1}{2\pi R_0}\left(\frac{3\kappa p_0}{\rho}\right)^{\frac{1}{2}}$, where R_0 is the radius of the microbubble, κ is the polytropic coefficient, p_0 is the ambient pressure, and ρ is the density of the

liquid. The microbubble size is clearly a major factor in determining the resonant frequency. Using common values for κ (1.1), ρ (1000 kg/m3), and p_0 (100 kPa), the microbubble resonant size for a 1 MHz driving frequency (employed throughout this thesis) is ~3 µm[42].

The behaviour of an oscillating microbubble depends on its size relative to the ultrasound frequency. The greatest radial oscillations occur when the microbubble is excited at the frequency of maximum response amplitude, which may shift slightly from the resonant frequency with damping. Excitation below or above resonance results in lesser radial oscillations. As the pressure amplitude increases, nonlinear effects become more pronounced and the resonant frequency progressively shifts, further affecting microbubble behaviour[15]. Microbubbles produced for ultrasound-mediated drug delivery are typically 1-10 um such that they can flow through small vessels. Ultrasound excitation at 1 MHz will thus excite a sub-population of microbubbles near resonance which can enhance the cavitation-mediated effects associated with successful drug delivery (e.g. fluid mixing, shear stress, drug release etc.)[42]. The microbubbles employed in ultrasound-mediated drug delivery are consequently much smaller than the acoustic wavelength.

If a microbubble expands to the extent that the pressure inside cannot resist the inertia of the surrounding fluid, it violently collapses in what is termed inertial cavitation. Inertial cavitation has been shown to result in the generation of shockwaves, heat, light (known as sonoluminescence), and reactive chemical species[15,38]. As the gas is violently compressed by the incoming fluid during inertial cavitation, temperatures can approach 3000°C at the gas water interface, persisting for only a fraction of a microsecond[15]. Asymmetrical inertial collapse can also result in jetting, imparting high magnitude, transient, and spatially localized fluid stresses[15]. Unlike the discrete harmonic

components emitted during non-inertial cavitation, inertial collapse has been associated with broadband acoustic emissions[41]. The ultrasound pressures employed in this thesis yield primarily non-inertial cavitation, although owing to the stochastic nature of cavitation phenomena, inertial cavitation cannot be excluded entirely.

1.4.2. Cavitation microstreaming

Microbubbles undergoing continuous oscillation transfer momentum to the surrounding fluid. This can give rise to vorticity and high shear stresses in a thin, viscous layer surrounding the microbubble that generate larger vortices and steady net fluid flows in the bulk fluid. These are referred to as "cavitation microstreaming," as distinct from acoustic streaming generated by the ultrasound field, and have been both experimentally observed and theoretically described[43,44]. The high fluid shear stress from cavitation microstreaming falls off rapidly with distance from the microbubble (within micrometres[45]) yet can still influence particle transport and mixing of fluid constituents at a considerable distance (on the order of mm from the microbubble[46]). In addition to the spatial gradients associated with streaming, steep temporal gradients in shear stress are associated with the start and end of each ultrasound pulse.

1.4.3. Secondary radiation forces

The re-radiated sound from oscillating microbubbles can also influence the motion of microbubbles in solution. If the cosine of the phase difference between the volumetric oscillation of a microbubble and the incident ultrasound wave is non-zero, a steady force acts on the microbubble such that above resonant size, the force is in the direction of decreasing pressure, and below resonant size, the force is in the direction of increasing pressure[47]. Microbubble translation can be oscillatory or unidirectional and can also contribute considerable stresses to the surrounding environment (e.g. cells or vessel walls)[48]. When microbubbles attract one another they can also cluster or coalesce to form larger microbubbles[49].

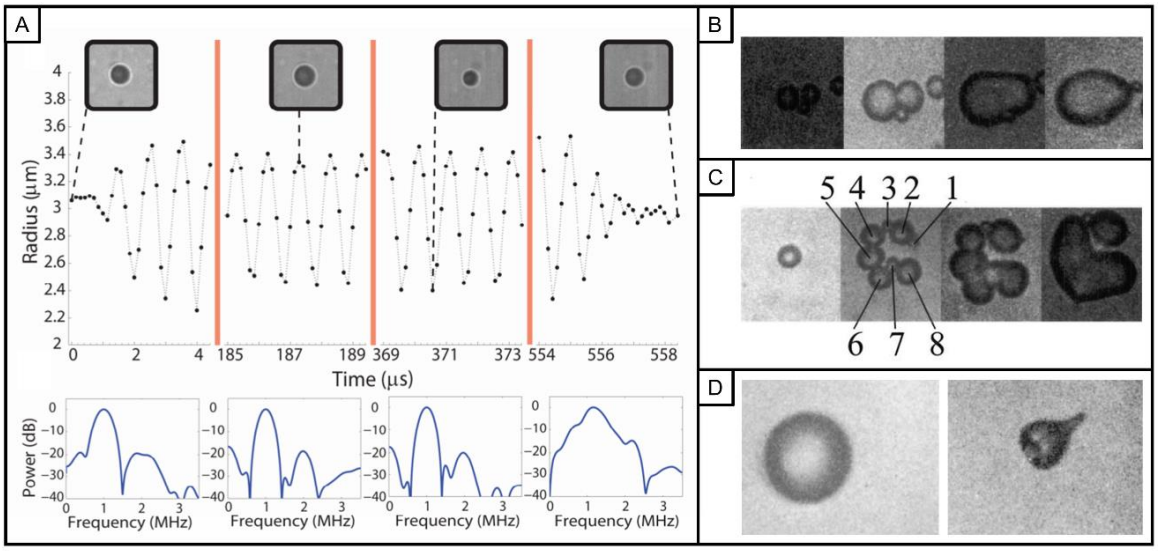

Figure 2: Microbubble cavitation phenomena captured by high-speed microscopy. A) The volumetric oscillations of a microbubble exposed to 1 MHz 100 kPa PNP ultrasound (top) and associated power spectra (bottom). Adapted from Khokuis et al[39]. B) Microbubble coalescence. C) Microbubble fragmentation and coalescence. D) Jetting from a microbubble asymmetrically collapsing. 0.85 MPa PNP ultrasound exposure at 1.7 MHz was employed. B-D) are adapted from Postema et al.[49].

1.4.4. Fragmentation, deflation, and shedding

Oscillating microbubbles are known to fragment or deflate at relatively low acoustic pressures[49]. This can contribute to additional mechanical stresses on the surrounding environment and alteration of the cavitation behaviour and acoustic emissions. In addition, microbubble destruction releases gas into the surrounding environment[50,51], which can generate additional chemical stresses when employing nitric oxide or oxygen carrier gasses, for instance[26,52]. The shedding of lipids from oscillating microbubbles additionally chemically modifies the surrounding environment[53], a phenomenon that is explored in detail later in the thesis.

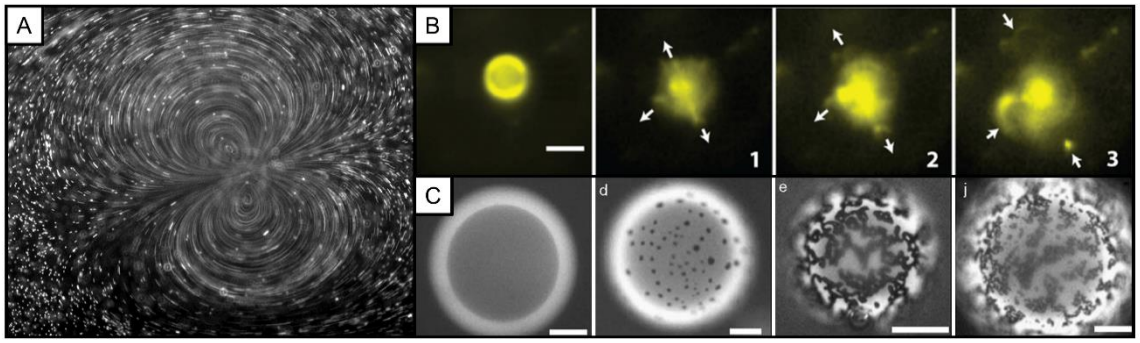

Figure 3: Microbubble cavitation phenomena and shell characteristics. A) Cavitation microstreaming pattern from a SonoVue microbubble exposed to 511 kHz ultrasound at ~0.05 MPa PNP at by streak velocimetry with fluorescent tracer beads. B) Lipid shedding from a microbubble with a fluorescently-labelled shell exposed to 250 kPa PNP ultrasound at 1 MHz. Adapted from Luan et al.[53] C) Fluorescently-tagged emulsifier showing domain formation in microbubble shells dependent on microbubble composition. Adapted from Borden et al.[47]. Microbubble formulations from left to right are 12:0 PC-PEG40S, 16:0 PC-PEG40S, 18:0 PC-PEG40S, and 22:0 PC-PEG40S all prepared in a 9:1 molar ratio. The lipid organization in the microbubble shell can affect microbubble stability and gas dissolution[48]. These formulations are discussed in detail throughout the thesis.

1.5. Cell response to cavitation phenomena

In this section, cellular responses to cavitation phenomena in ultrasound-mediated drug delivery, specifically sonoporation, are discussed.

For some cavitation-mediated phenomena, direct observation of the effects on cells is feasible. For instance, the propulsion of microbubbles under acoustic radiation forces

towards and through cell membranes has been directly observed[54–56]. Direct observations of jetting from single cycle high-pressure ultrasound exposures have also been shown to coincide with sonoporation (1 MHz, 1.1 MPa, 3µs duration ultrasound)[57]. Experiments with ROS scavengers under the same ultrasound exposure conditions further demonstrated that sonoporation was not significantly altered by the presence or absence of ROS generated by inertial cavitation[58].

Using a state-of-the-art high-speed camera ($25*10^6$ fps for 6x128 frames), van Wamel et al. demonstrated that the oscillatory deformations (~1 µm) of a cell membrane near an oscillating microbubble under ultrasound exposure (1 MHz, 0.4 MPa, 10µs bursts, 50 Hz PRF, 5s) correlate with sonoporation[37,59]. De Cock et al. also observed membrane deformation coincided with sonoporation (1 MHz, 100-500 kPa, 2 ms bursts, 125 Hz PRF, 5 s)[55]. By using microbubbles targeted to cell membranes, sonoporation, coinciding again with oscillatory membrane deformation, was achieved at low acoustic pressures (1 MHz, 80 kPa, 10 µs bursts, 12.5 Hz PRF, 0.5 s)[60], not expected to produce sonoporation with non-targeted microbubbles[61]. In addition to the direct observations of oscillatory membrane strain, these studies, and others[62,63], demonstrate that microbubble proximity is correlated with cell membrane permeabilization, which, based on the aforementioned spatial dependence of cavitation effects, is to be expected.

Interestingly, cavitation microstreaming has not been directly observed to correlate with sonoporation, yet is often cited as a primary mechanism of sonoporation (this is discussed in more detail in Chapter 2). Other microbubble phenomena such as fragmentation, coalescence, clustering, and lipid shedding have similarly not been characterized in the literature with regard to sonoporation, to the best of the author's knowledge.

In sonoporation, the cellular uptake of extracellular compounds has been observed by several distinct mechanisms. Non-specific pore formation in the cell membrane, whereby inner and outer membrane leaflets are fused, forming an aqueous channel that connects extracellular and intracellular spaces, has been demonstrated by transmembrane current monitoring, electron microscopy, and confocal microscopy[64–67]. Specific ion channel inhibitors have also been employed to show that changes in the ionic permeability of the cell membrane, resulting in hyperpolarization, also involve ion channels[68]. Whether ion channels are opened as a consequence of cavitation phenomena directly or by secondary mechanisms is not known. Cavitation has also been shown to increase membrane trafficking of extracellular molecules into the cell by caveolin- and clathrin-dependent endocytosis as well as macropinocytosis[55,56,69].

In addition to drug uptake pathways, there is mounting evidence that biological effects induced by cavitation phenomena act as secondary mechanisms for permeabilization. One such example is the observation that an increase in intracellular reactive oxygen species (ROS) following ultrasound and microbubble exposure is correlated with ultrasound pressure and calcium influx (e.g. ionic permeabilization)[70–72]. When ROS were scavenged by the addition of catalase to the extracellular medium, the influx of Ca^{2+} was inhibited or reduced in a manner inversely proportional to the ultrasound pressure. Intracellular ROS production and the associated oxidative stress, not to be confused with extracellular ROS production by cavitation, is thus a candidate secondary mechanism in sonoporation[10,71]. Indeed, Kooiman et al. demonstrated that addition of either a calcium chelating agent or an antioxidant prior to sonication significantly decreased endothelial barrier ionic permeability recovery time from ultrasound and microbubble exposure[70]. The transient rearrangement of the actin and tubulin cytoskeleton[73,74], however, has also been shown to coincide with sonoporation under

similar exposure conditions[72]. Furthermore, the shear stress-sensing signalling cascade has been implicated in the downstream effects of cavitation[75]. These studies highlight the complexity in determining the secondary mechanisms associated with ultrasound-mediated drug delivery and point to the likelihood that a combination of biological effects or secondary mechanisms, each with varying kinetics and effect sizes, play a role in ultrasound-mediated drug delivery.

1.6. Lipids in drug delivery

Much of this thesis focuses on the molecular arrangement of lipids in cell membranes and intracellular vesicles and their role in ultrasound-mediated drug delivery. The aim of this section is to provide an introduction to the characteristics of lipids in biological barriers (e.g. cell membranes and cell-cell junctions) and in drug delivery vehicles (e.g. liposomes and phospholipid-shelled cavitation agents). The role of lipids in cell-cell junctions specifically is discussed at length in Chapter 5. Lipid and cholesterol exchange between extracellular lipidic particles and the cell membrane, which is hypothesized to impact ultrasound-mediated drug delivery, is also discussed.

1.6.1. Introduction to lipids in biology

Lipids are molecules that are soluble in non-polar solvents and insoluble or virtually insoluble in water. At the time of writing, there are over 42684 lipid structures identified in the largest open-source lipid database, LipidMAPS[76], divided into eight

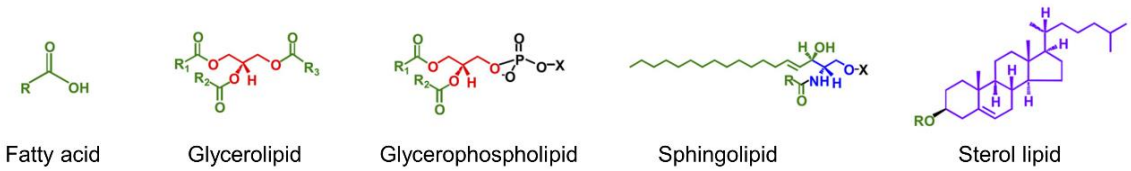

Figure 4: Selected classes of biological lipids including fatty acids, glycerolipids, glycerophospholipids, sphingolipids, and sterol lipids. Colour-coding shows lipid substituents derived from fatty acyl (green), glycerol (red), serine (blue), and isoprene (purple). Figure modified from McDonald et al.[112].

lipid classes, of which, fatty acids, glycerolipids, glycerophospholipids, sphingolipids, and sterols are introduced here[76,77].

Fatty acids are characterized by repeating methylene groups (e.g. aliphatic hydrocarbon chains) terminating with carboxylic acid and serve important roles in cell lipid metabolism and in cell membranes. Glycerolipids, consisting of glycerol that is esterified at each hydroxyl group, typically with fatty acids or sugars, comprise a principle source of energy in the body in the form of triglycerides. When one position on the glycerol backbone of a glycerolipid is occupied by a phosphate-containing polar group, the lipid is classified as a glycerophospholipids, or phospholipid. The polar group can be connected to the glycerol by an ester linkage (phosphatidates) or ether linkage (plasmologens), the latter of which is more resistant to chemical degradation.

Biological phospholipids consist of a glycerol backbone with two fatty acid esters and one phosphate group ester terminating in choline, ethanolamine, serine, or inositol, referred to as phosphatidylcholine (PC), phosphatidylethanolamine (PE), phosphatidylserine (PS), and phosphatidylinositol (PI) respectively. The polar phosphate-containing ester is referred to as the phospholipid head group. The positively charged nitrogen in choline and ethanolamine, in combination with the phosphate anion, render PC and PE zwitterionic. PC and PE are the core constituents of cell membranes and play important roles in many biological functions. The deprotonated carboxyl group and positively charged nitrogen in serine render PS anionic. PS contributes to the negative charge of cell membranes and plays an important role in apoptosis (programmed cell death). PI, which is also anionic owing to the neutral charge of inositol, plays an important role in cell signalling and membrane trafficking. In combination with fatty acids, PC and PE are also commonly employed in drug-carrying liposome and cavitation-agent formulations.

Sphingolipids are lipids that contain a sphingoid backbone consisting of a long hydrocarbon chain (usually 18C) with two functional groups. The sphingoid backbone typically contains fatty acid residues, charged headgroups, or sugars. Sphingolipids with sugar residues (glycosphingolipids) are a core constituent of lipid rafts which are responsible for the compartmentalization of cell membrane proteins, essential to membrane function.

Sterol lipids consist of a non-polar four carbon ring structure with a polar hydroxyl group. In eukaryotic cells, cholesterol, a sterol with an additional hydrocarbon chain extending from the non-polar carbon rings, is an essential cell membrane constituent. Cholesterol is required for the formation of lipid rafts and is involved in cell signalling, membrane trafficking, and establishing the mechanical properties of the cell membrane along with the phospholipids and sphingolipids. Other biologically important sterol lipids, of which cholesterol is a precursor, include hormones and fat-soluble vitamins.

1.6.2. Characteristics of lipids in biology

The lipids comprising biological membranes are amphipathic, meaning they have distinct polar (hydrophilic) and non-polar (hydrophobic) regions. When dispersed in aqueous solutions, the polar parts of lipids align with polar molecules (e.g. water or polar parts of other lipids) and the non-polar parts minimize their contact with polar molecules (e.g. by aligning with the non-polar parts of other lipids). This results in the self-assembly of amphipathic lipids into organized structures. Lipids exhibit polymorphism, meaning that the same lipids can self-assemble into different organized structures depending on their physical state. Lipid organizations include micelles, bilayers, and inverse micelles corresponding with hexagonal I (H_I), lamellar (L), and hexagonal II (H_{II}) lipid phases (see Table 1). These lipid organizations typically assume

approximately spherical, cylindrical, or layered forms depending on what is thermodynamically favourable. Spherical bilayers containing aqueous solution are known as liposomes and constitute the most widely used nanoparticles for clinical drug delivery, as well as intracellular and extracellular vesicles. The cell membrane is locally planar and thus referred to as a lamellar bilayer. The roles of non-lamellar lipid phases in biology, e.g. in membrane fusion intermediates and cell-cell junctions, have yet to be fully understood[78,79].

Self-assembled lipid polymorphs depend on both lipid phase and molecular geometry, the latter of which is characterized by the critical packing parameter, $p = \frac{v}{al}$, where v is the volume of the molecule, a is the headgroup area, and l is the length of the hydrocarbon chains. Lipids with $p < 1$ are conical, $p = 1$ are cylindrical, and $p > 1$ are inverse conical. The critical packing parameter can be used to predict lipid self-assembly in water such that $p < \frac{1}{3}$ favours micelles, $\frac{1}{3} < p < \frac{1}{2}$ favours cylindrical (prolate) micelles, $\frac{1}{2} < p < 1$ favours bilayers, and $p > 1$ favours inverted micelles. Table 1 shows the lipid packing, organization, and phase of common biological lipids under physiological conditions.

For lipid bilayers, the hydrophobic core is dominated by Van der Waal's forces and steric repulsion whereas the hydrophilic regions experience steric forces, electrostatic forces involving bound and unbound ions, and hydrogen bonding with highly ordered water molecules (responsible for a diffusion barrier known as the "unstirred water layer"), among other forces[80]. The hydrophobic core is typically characterized by the average motion or flexibility of the lipid hydrocarbon chains, known as the lipid order. The term "lipid order" comes from the order parameter in NMR studies which provides the average angle between a C-deuterium bond and a magnetic field, providing a characterization of hydrocarbon rotational (anti/gauche bonds) and geometrical (cis/trans bonds) isomerism. The lipid order of a phospholipid in a bilayer is highest near the lipid headgroups and decreases toward the core of the bilayer.

In addition to lipid order, lipids are often characterized by their lateral diffusion (membrane fluidity, the ability of lipids to flow in the plane of the bilayer) and

Lipid	Molecular shape	Organization	Phase
Lysophospholipids Detergents Soaps	 Cone	 Micelles	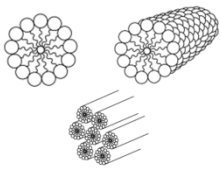 Hexagonal I
Phosphatidylcholine Phosphatidylserine Phosphatidylinositol Sphingomyelin	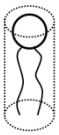 Cylinder	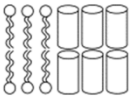 Bilayers	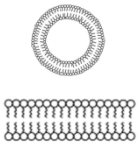 Lamellar
Phosphatidylethanolamine Cardiolipin Phosphatidic acid	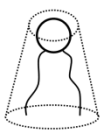 Inverted cone	 Inverted micelles	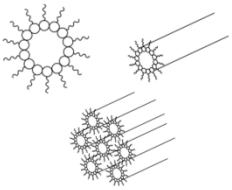 Hexagonal II

Table 1: Lipid shape and self-assembly in water. Modified from Cullis et al.[113] and Lasic[114].

transverse diffusion ("flip-flop", the ability of lipids to translocate from one bilayer leaflet to the other), the latter of which is far less energetically favourable. Membrane fluidity is generally inversely proportional to lipid order and bilayer thickness, and proportional to the membrane permeability to water (e.g. membrane hydration), ions, and small molecules[81–83].

Lipid phase transitions are characterized by a step change in the lipid order and membrane fluidity with a small change in a state variable such as temperature, pressure, and chemical species concentration (e.g. protons, lipids, or cholesterol). Lipid phase transitions are most often referred to by their transition temperatures (T_m), which are influenced by hydrocarbon chain length, hydrocarbon unsaturation, head group size, head group ionization, and hydration among other factors. Cell membranes and liposomes are in lamellar (L) phase under physiological conditions. The L phase can be further divided into distinct lamellar phases. These include, in order of decreasing temperature: fluid lamellar or liquid-disordered (L_α or L_d), gel or solid-ordered (L_β), and liquid-crystalline or liquid-ordered (L_c or L_o) phases. The gel phase can exhibit further polymorphism into the interdigitated gel phase ($L_{\beta I}$), tilted gel phase ($L_{\beta'}$), and rippled

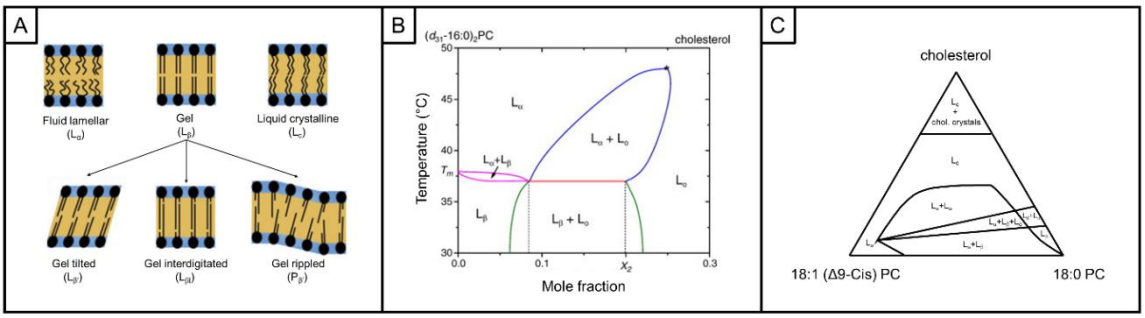

Figure 5: Lamellar phases and phase diagrams. Lamellar phases are shown in panel (A) in order of decreasing temperature from left to right, along with gel phase polymorphs (below). A binary phase diagram for dipalmitoylphosphatidylcholine (16:0 PC) and cholesterol is shown in (B). A ternary phase diagram for distearoylphosphatidylcholine 18:0 PC, cholesterol, and dioleoylphosphatidylcholine (18:1 (Δ9-Cis) PC) is shown in (C). (A) is modified from Kulkarni[115], (B) is modified from Marsh[116], and (C) is modified from Feigenson[117].

gel phase ($P_{\beta'}$). Illustration of these phases and typical binary and ternary lipid phase diagrams are illustrated in Figure 2.

1.6.3. Lipid phase transition in biology

The cell membrane, composed of ~40% lipids by mass (mostly phospholipids, cholesterol, and sphingolipids with a lipid-to-protein molar ratio ~ O (10^2)), forms the selectively permeable barrier between the inner and outer realms of a cell. Given the maintenance of remarkably stable thermal conditions by many organisms, it might be expected that phase transition is a comparatively negligible process in living matter. The membranous structures essential to living matter, however, are sensitive to phase transition by non-thermal environmental changes. Indeed, environmental factors such as the interactions of lipids with metal ions, pH, proteins, and other polymers can induce isothermal phase transition[81].

Lipid phase transitions within cell membranes can alter their physical properties such as elasticity and compressibility, as well as the insertion, sequestration, and diffusion characteristics of membrane proteins[81]. The lipid phase state has also been shown to play an important role in, for instance, enzymatic activity, nerve excitation, regulation of cell-cell contacts, and fusion with extracellular vesicles[81,84]. It follows that cells have evolved mechanisms for maintaining membrane fluidity and phase state in response to environmental stress by restructuring acyl chains, phospholipid headgroups, and acyl chain unsaturation, and by adjusting cholesterol levels[85].

In the absence of proteins, cell membrane permeability is governed by the lipid phase state of the bilayer, however, permeability is greatly increased with the inclusion of membrane proteins[83]. There are 6000+ known human membrane proteins which comprise 20-30% of the entire human proteome, contributing to ~60% of cell

membrane mass[86]. These proteins are primarily enzymes that catalyse chemical reactions, transporters that that move molecules across the bilayer, receptors that mediate cell response upon binding of a ligand, ligands that bind to receptors, and proteins that establish structure and adhesion between cells and the extracellular environment[86]. Unsurprisingly, the organization and function of many proteins responsible for regulating permeability are dependent on the phase behaviour of the surrounding lipids.

It is well known that lipids of differing phase transition temperatures can organize into liquid-ordered and liquid-disordered domains, a phenomenon known as phase separation. Owing to the presence of a plethora of molecular species, the cell membrane comprises a dynamic and responsive system of multiple lipid phases. In the liquid-disordered cell membrane, protein-containing cholesterol-rich liquid-ordered domains, called lipid rafts, appear and disappear in rapid response to local environmental conditions[87]. The dynamic compartmentalization of proteins by lipid rafts is an accepted phenomena of cell membranes while the precise role of lipid rafts in protein behaviour remains a burgeoning field of study. One example that highlights the relevance of lipid rafts to membrane permeability is that of clathrin-independent endocytosis, associated with caveolin-1 protein, which depends on the stabilization and accumulation of lipid rafts and can be inhibited by reducing membrane cholesterol[87,88]. Another example is the permeability of the blood-brain barrier which depends on the cholesterol-rich membrane domains that anchor tight junctional scaffolding proteins[89,90] (as discussed further in Chapter 5).

The thermal behaviour of lipids is thus critical for maintaining low permeability through the cell membrane and cell-cell junctions by both restricting passive diffusion

and by compartmentalizing membrane proteins in the local environments necessary to their function.

1.6.4. Lipid transfer and cholesterol depletion

Throughout this thesis the effects of liposomes and microbubbles used in ultrasound-mediated drug delivery on cell lipids are investigated. When alteration of cell lipid order is observed, the mechanism often involves lipid transfer between cells and lipidic particles and/or depletion of cell membrane cholesterol. These mechanisms are described in this section in order to provide a basis for understanding the experimental results that follow.

The cellular plasma membrane contains 60-70% of the free cholesterol in a cell where it plays a critical role in membrane form and function[91]. While cells have mechanisms for the de novo synthesis of cholesterol and means of intracellular cholesterol storage, cells require exogenous cholesterol for survival, which either adsorbs to the plasma membrane or is endocytosed from circulating lipoproteins[91].

Cholesterol and phospholipids have been shown to require neither cellular metabolic energy nor specific proteins to exchange between cells and serum[81]. Several hypothetical mechanical and/or thermodynamic mechanisms of lipid and cholesterol transfer have been described in the literature. First, cells and lipid particles could undergo membrane hemi-fusion upon collision such that transferring lipid or cholesterol could flow across the hemi-fused lipid membranes. Second, lipid or cholesterol could flip-flop into the acceptor particle when the acceptor and donor particles are close together but not necessarily fused. Finally, lipid or cholesterol could desorb from donor particle membranes and diffuse as monomers through the aqueous phase, entering acceptor particles upon collision. The first two mechanisms result in models for

cholesterol or lipid transfer known as collision models, whereas the third mechanism results in purely kinetic or aqueous diffusion models[91].

In a pure collision model, the rate of cholesterol or lipid transfer is proportional to the concentration of both acceptor and donor particles[91]. Experimental results, however, demonstrate that transfer rates are not solely dependent on acceptor concentration when acceptor particles are in excess[91]. In addition, experiments have shown that fusion (by

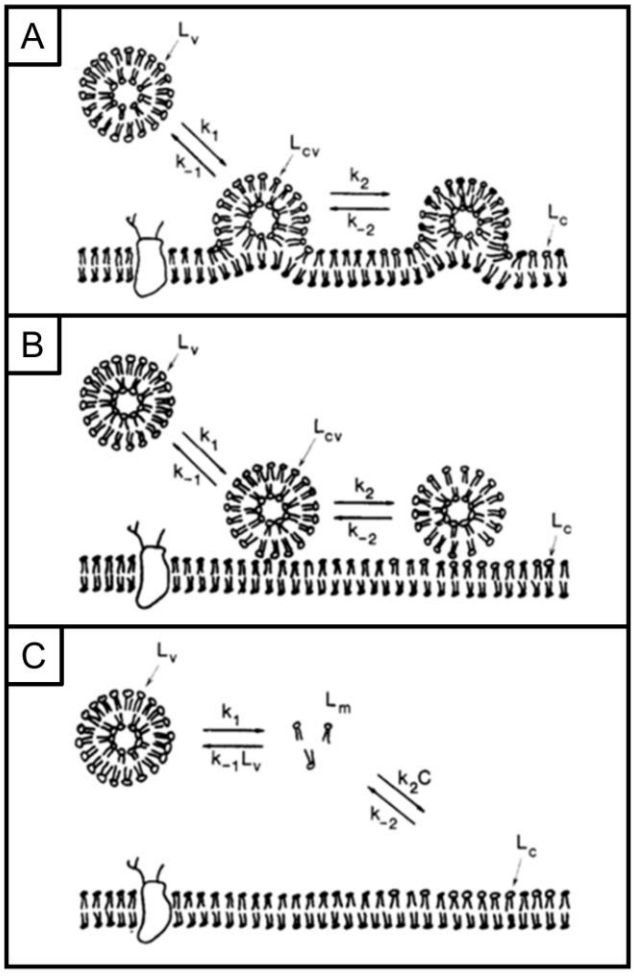

Figure 6: Schematic of vesicle-to-cell lipid transfer models. A) Collision model where a vesicle-cell intermediate is formed such that lipids can flow between fused vesicle and the cell membrane along their respective lipid bilayers. B) Collision model where lipid transfer occurs via transverse diffusion (bilayer flip-flop) between vesicles and cells that are close together. C) Aqueous diffusion model where lipid monomer desorbs from vesicles or cell membranes and transfers via diffusion through the aqueous bulk. L_v, L_c, L_m, and L_{cv} indicate lipids in vesicles, cell membranes, monomer form in solution, and in cell-vesicle complexes respectively. C is the surface area of cell membranes. The lipid transfer rate constants are represented by k with arrows indicating adsorption and desorption. Adapted from Ferrel et al.[91].

NMR) and direct contact (by separating acceptors and donors with a membrane) are not necessary for transfer[91]. From these results, the collision model on its own is clearly inadequate, and the kinetic model should be considered.

In a pure kinetic model, the rate of cholesterol or lipid transfer depends on their concentration in donors and is independent of acceptor concentration when the acceptors are in excess[91]. The rate of transfer is then considered independent of dilution factor so long as the ratio of acceptors to donors remains unchanged. Experimental results, however, show that the absolute concentrations of donors and acceptors do indeed matter[92]. Furthermore, a pure kinetic model does not consider the shape, size, composition, or state of the acceptor, whereas experimental results show that transfer rates from cells to liposomes, from cells to cells, and from cells to lipoproteins differ greatly[92]. Finally, in a pure kinetic model, addition of plasma would compete for adsorption of free molecules diffusing between donors and acceptors, however a small amount of plasma was found to increase transfer by 3-fold, suggesting a more complex mechanism[92]. Indeed, the rate of desorption of lipid or cholesterol from donors is often the rate-limiting factor for transfer in biological circumstances[91,92].

The energy barrier for desorption depends on the state and properties of the transferring molecule and its microenvironment in the donor membrane. If the transferring molecule can overcome the activation energy barrier required for desorption, it is available for transfer. For instance, in a model membrane system, the interfacial flux of cholesterol was measured at more than 5-fold that of 16:0 PC. This supports an aqueous diffusion or kinetic model whereby cholesterol is more than 100-fold more soluble in water[91]. Conversely, phospholipids have a much greater energy barrier to overcome such that the activation energy for desorption increases with the chain length of their hydrophobic hydrocarbon tails[91]. Indeed, removal of two methylene groups from the phospholipid

hydrocarbon tails results in roughly a 10-fold increase in the rate of desorption[91]. Correspondingly, the rate of phosphatidylcholine lipid transfer from vesicles to cells has been shown to increase exponentially as the phospholipid chain length is reduced[93].

The surrounding lipids in the donor particle also have an effect on lipid and cholesterol transfer. If the surrounding lipid order decreases, the Van der Waals interactions of cholesterol with the surrounding phospholipids is reduced, and desorption is facilitated, and vice-versa for an increase in lipid order[91].

Thus, it is a complex combination of the aforementioned mechanisms, particle collisions leading to hemi-fusion or molecular flip-flop, aqueous diffusion of lipids and cholesterol between acceptor and donor particles, and the local thermodynamic properties of lipids and cholesterol in donor particles that define their desorption-rates, that provide a basis for understanding lipid and cholesterol transfer as it occurs in this thesis.

1.6.5. Lipids in ultrasound-mediated drug delivery

Having established the importance of cell lipid ordering in regulating the permeability of cell membranes and cell-cell junctions, the central role of lipids in ultrasound-mediated drug delivery is now considered.

The physical properties of lipids have been exploited both directly and indirectly in in ultrasound-mediated drug delivery. Cavitation nuclei, such as microbubbles and phase-shift emulsions, are often coated with lipids, which, by their amphipathic nature are excellent at trapping gas. These cavitation nuclei can be loaded with drugs by incorporating drugs into the coating or an encapsulated oil layer beneath it (e.g. in the case of a lipid-soluble drug), or by conjugating a drug to the shell using electrostatic binding or a biochemical linking moiety[23]. Drug payload can also be increased by

loading the drug into liquid-filled lipid-shelled nanoparticles (e.g. liposomes), that can then be co-injected with the cavitation agent or biochemically linked to the cavitation agent shell[94–96]. Loading cavitation agents with drugs by the aforementioned methods is motivated by the potential to increase local drug concentration at a target site while reducing off-target side-effects.

Recent studies have demonstrated the shedding of lipids from phospholipid-shelled microbubbles[53], the deposition of liposomal lipids onto cell membranes[97], and the transfer of lipids from phospholipid-shelled microbubbles to synthetic membranes[98] during ultrasound excitation. While few studies evaluate the bio-distribution of lipids following ultrasound-mediated drug delivery, cavitation-assisted deposition of lipids in the rat kidney has been demonstrated *in vivo* using microPET and ^{18}F-labelled lipid, suggesting a propensity of unmeasured lipid deposition in many ultrasound studies[99]. Lipids and lipid thermal behaviour-modifying substances (e.g. poly-ethylene glycol), such as those employed in FDA-approved cavitation agents, are easily metabolized by cells, generally recognized as safe, and are consequently not expected to present regulatory hurdles. Ultrasound thus provides a unique and powerful modality for delivering lipids to target locations at arbitrary depth within the human body.

In addition to providing a means of localized lipid delivery, cavitation phenomena have been associated with modification of cell membrane behaviour. Ultrasound and microbubble-mediated pore-formation[64,65] and increased rates of endocytosis[55,69,100], for instance, demonstrate that cavitation alters the behaviour of cell lipids. In addition, there is an abundance of evidence demonstrating penetration of microbubbles through cell membranes[55,56], and the distension of cell membranes in proximity to an oscillating microbubble[37,101].

The mechanical and chemical effects associated with cavitation have also been shown in isolation to modify lipid thermal behaviour in artificial models and cell membranes[102,103]. The cavitation microstreaming induced by microbubbles[43], for instance, gives rise to shear stresses, often with steep temporal and spatial gradients, which have independently been shown to alter cell membrane lipid order[103–105]. Cavitation microstreaming is thus expected to affect membrane lipid behaviour in the few cells closest to the centre of the microstreaming pattern (see Chapter 2). The reactive oxygen species generated by collapsing microbubbles may also contribute to cavitation-induced alteration of cell lipid order[106]. Other cavitation-mediated bio-effects including degradation of the actin cytoskeleton, opening of ion channels, formation of non-specific pores, blebbing, and rapid hyperpolarization of the cell membrane would also be expected to alter cell lipid order[69,70,73,107–111]. It is not known whether alteration of lipid order may conversely play a role in these observed bio-effects.

By optimizing a drug delivery vehicle or cavitation agent to modulate the lipid phase behaviour of cell membranes or cell-cell junctions, it is conceivable that successful drug delivery could be achieved with less ultrasound energy, reducing the likelihood of off-target effects and/or damage from cavitation. Continued research into the role of lipids in ultrasound-mediated drug delivery is thus warranted and constitutes one of the aims of the work described in this thesis. Specifically, saturated phosphatidylcholine and their derivatives (lysophosphatdylcholine and fatty acids) were investigated owing to 1. their compatibility with microbubble and liposome formulation, 2. their widespread use in the clinic in both nano-medicine and ultrasound imaging with microbubbles, and 3. their biocompatibility as demonstrated by their ubiquity within the body and the existence of endogenous biological systems for their regulation. Certain lipids that may induce the desired biological effects but were not amenable to microbubble formulation

(e.g. unsaturated lipids) were decidedly out of the scope of the present work. Several lipid classes that have interesting properties for ultrasound-mediated drug delivery but also fall outside of the scope of this thesis are commented on in Chapter 4.

1.7. Thesis overview

In this chapter, ultrasound in combination with either surfactant-containing cavitation agents or thermosensitive drug-carrying lipid vesicles was introduced as a non-invasive and localized means of delivering both lipids and therapeutic agents at arbitrary depth within the human body. While great progress has been made in ultrasound-mediated drug delivery with regard to developing cavitation agents well-suited to drug delivery, characterizing cavitation phenomena, and investigating the biological responses to cavitation, little focus has been spent in understanding the influence and the potential of lipid delivery. As the barriers to drug delivery such as the cell membrane and cell-cell junctions are highly sensitive to the thermal behaviour of the lipids of which they are composed, it follows that ultrasound-mediated lipid delivery may offer hitherto unexplored opportunities for enhancing drug uptake to target regions with ultrasound. This thesis thus focuses on the influence of lipids in existing ultrasound-mediated drug delivery techniques, in addition to investigating the potential for developing of phospholipid-based agents to alter cell membranes and cell-cell junctions for the enhancement of drug delivery.

1.8. Research questions

This thesis endeavours to address the following research questions concerning the current and potential roles of lipids in ultrasound-mediated drug delivery[ii]:

[ii] stated with respect to microbubbles but equally applicable to liposomes and phase-shift droplets

1. Do lipids exchange between microbubbles and cell membranes, and if so, how does this impact cell membrane physicochemical properties? (Chapter 2)
2. What aspects of microbubble composition impact cell membrane physicochemical properties via lipid exchange mechanisms? (Chapters 3-4)
3. How does cavitation influence cell membrane physicochemical properties and lipid exchange in ultrasound-mediated drug delivery? (Chapter 2 and 4)
4. How can lipid exchange-mediated permeabilization mechanisms be leveraged in ultrasound-mediated drug delivery? (Chapters 4-5)

1.9. References

1. Peer, D. *et al.* Nanocarriers as an emerging platform for cancer therapy. *Nat. Nanotechnol.* **2,** 751–760 (2007).
2. Mura, S., Nicolas, J. & Couvreur, P. Stimuli-responsive nanocarriers for drug delivery. *Nat. Mater.* **12,** 991–1003 (2013).
3. Russell, S. J., Peng, K.-W. & Bell, J. C. Oncolytic virotherapy. *Nat. Biotechnol.* **30,** 658–670 (2012).
4. Verma, I. M. & Somia, N. Gene therapy - promises, problems and prospects. *Nature* **389,** 239–242 (1997).
5. Jain, R. K. Physiological barriers to delivery of monoclonal antibodies and other macromolecules in tumors. *Cancer Res.* **50,** 814s–819s (1990).
6. Kobayashi, H., Watanabe, R. & Choyke, P. L. Improving Conventional Enhanced Permeability and Retention (EPR) Effects; What Is the Appropriate Target? *Theranostics* **4,** 81–89 (2014).
7. Dejana, E. Endothelial cell-cell junctions: happy together. *Nat. Rev. Mol. Cell Biol.* **5,** 261–270 (2004).
8. Zihni, C., Mills, C., Matter, K. & Balda, M. S. Tight junctions: from simple barriers to multifunctional molecular gates. *Nat. Publ. Gr.* **17,** (2016).
9. Lingwood, D. & Simons, K. Lipid rafts as a membrane-organizing principle. *Science* **327,** 46–50 (2010).
10. Lentacker, I., De Cock, I., Deckers, R., De Smedt, S. C. & Moonen, C. T. W. Understanding ultrasound induced sonoporation: Definitions and underlying mechanisms. *Adv. Drug Deliv. Rev.* **72,** 49–64 (2014).
11. Aryal, M., Arvanitis, C. D., Alexander, P. M. & McDannold, N. Ultrasound-mediated blood-brain barrier disruption for targeted drug delivery in the central nervous system. *Adv. Drug Deliv. Rev.* **72,** 94–109 (2014).
12. Lyon, P. C. *et al.* Clinical trial protocol for TARDOX: a phase I study to investigate the feasibility of targeted release of lyso-thermosensitive liposomal doxorubicin (ThermoDox®) using focused ultrasound in patients with liver tumours. *J. Ther. Ultrasound* **5,** (2017).
13. Elias, W. J. *et al.* A Pilot Study of Focused Ultrasound Thalamotomy for Essential Tremor. *N. Engl. J. Med.* **369,** 640–648 (2013).
14. Bruus, H. Acoustofluidics 7: The acoustic radiation force on small particles. *Lab Chip* **12,** 1014 (2012).
15. Brennen, C. E. (Christopher E. *Cavitation and bubble dynamics*.
16. Bailey, M. R. *et al.* CAVITATION DETECTION DURING SHOCK-WAVE LITHOTRIPSY. doi:10.1016/j.ultrasmedbio.2005.02.017
17. Parsons, J. E., Cain, C. A., Abrams, G. D. & Fowlkes, J. B. Pulsed cavitational ultrasound therapy for controlled tissue homogenization. *Ultrasound Med. Biol.*

32, 115–129 (2006).

18. Coussios, C. C., Farny, C. H., Ter Haar, G. & Roy, R. A. Role of acoustic cavitation in the delivery and monitoring of cancer treatment by high-intensity focused ultrasound (HIFU). *Int. J. Hyperth.* **23,** 105–120 (2007).

19. Calliada, F., Campani, R., Bottinelli, O., Bozzini, a & Sommaruga, M. G. Ultrasound contrast agents: basic principles. *Eur. J. Radiol.* **27 Suppl 2,** S157–S160 (1998).

20. Stride, E. Physical principles of microbubbles for ultrasound imaging and therapy. *Cerebrovasc. Dis.* **27,** 1–13 (2009).

21. Schutt, E. G., Klein, D. H., Mattrey, R. M. & Riess, J. G. Injectable microbubbles as contrast agents for diagnostic ultrasound imaging: The key role of perfluorochemicals. *Angew. Chemie - Int. Ed.* **42,** 3218–3235 (2003).

22. Feinstein, S. B. *et al.* Safety and efficacy of a new transpulmonary ultrasound contrast agent: initial multicenter clinical results. *J. Am. Coll. Cardiol.* **16,** 316–324 (1990).

23. Lentacker, I., De Smedt, S. C. & Sanders, N. N. Drug loaded microbubble design for ultrasound triggered delivery. *Soft Matter* **5,** 2161 (2009).

24. Abou-Saleh, R. H., Swain, M., Evans, S. D. & Thomson, N. H. Poly(ethylene glycol) lipid-shelled microbubbles: Abundance, stability, and mechanical properties. *Langmuir* **30,** (2014).

25. van Rooij, T., Daeichin, V., Skachkov, I., de Jong, N. & Kooiman, K. Targeted ultrasound contrast agents for ultrasound molecular imaging and therapy. *Int. J. Hyperth.* **31,** 90–106 (2015).

26. Fix, S. M., Borden, M. a. & Dayton, P. a. Therapeutic gas delivery via microbubbles and liposomes. *J. Control. Release* **209,** 139–149 (2015).

27. Owen, J. *et al.* Understanding the structure and mechanism of formation of a new magnetic microbubble formulation. *Theranostics* **2,** 1127–39 (2012).

28. Owen, J., Pankhurst, Q. & Stride, E. Magnetic targeting and ultrasound mediated drug delivery: Benefits, limitations and combination. *Int. J. Hyperth.* **28,** 362–373 (2012).

29. Unger, E. C. *et al.* Therapeutic applications of lipid-coated microbubbles. *Adv. Drug Deliv. Rev.* **56,** 1291–1314 (2004).

30. Frenkel, P. a., Chen, S., Thai, T., Shohet, R. V. & Grayburn, P. a. DNA-loaded albumin microbubbles enhance ultrasound-mediated transfection in vitro. *Ultrasound Med. Biol.* **28,** 817–822 (2002).

31. Lentacker, I. *et al.* Ultrasound-responsive polymer-coated microbubbles that bind and protect DNA. *Langmuir* **22,** 7273–8 (2006).

32. Sheeran, P. S., Luois, S. H., Mullin, L. B., Matsunaga, T. O. & Dayton, P. A. Design of ultrasonically-activatable nanoparticles using low boiling point perfluorocarbons. *Biomaterials* **33,** 3262–3269 (2012).

33. Kwan, J. J. *et al.* Ultrasound-Propelled Nanocups for Drug Delivery. *Small* n/a-

n/a (2015). doi:10.1002/smll.201501322

34. Mannaris, C. *et al.* Gas-Stabilizing Gold Nanocones for Acoustically Mediated Drug Delivery. *Adv. Healthc. Mater.* 1800184 (2018). doi:10.1002/adhm.201800184

35. Paris, J. L., Cabañas, M. V., Manzano, M. & Vallet-Regí, M. Polymer-Grafted Mesoporous Silica Nanoparticles as Ultrasound-Responsive Drug Carriers. *ACS Nano* **9,** 11023–11033 (2015).

36. Feng, Q. *et al.* pH/Ultrasound Dual-Responsive Gas Generator for Ultrasound Imaging-Guided Therapeutic Inertial Cavitation and Sonodynamic Therapy. *Adv. Healthc. Mater.* **7,** 1700957 (2018).

37. van Wamel, A. *et al.* Vibrating microbubbles poking individual cells: Drug transfer into cells via sonoporation. *J. Control. Release* **112,** 149–155 (2006).

38. Stride, E. P. & Coussios, C. C. Cavitation and contrast: the use of bubbles in ultrasound imaging and therapy. *Proc. Inst. Mech. Eng. Part H J. Eng. Med.* **224,** 171–191 (2010).

39. Kokhuis, T. J. A. *et al.* Segmented high speed imaging of vibrating microbubbles during long ultrasound pulses. in *2012 IEEE International Ultrasonics Symposium* 1343–1346 (IEEE, 2012). doi:10.1109/ULTSYM.2012.0335

40. Pereno, V. *et al.* Layered acoustofluidic resonators for the simultaneous optical and acoustic characterisation of cavitation dynamics, microstreaming, and biological effects. *Biomicrofluidics* **12,** 034109 (2018).

41. Arvanitis, C. D., Bazan-Peregrino, M., Rifai, B., Seymour, L. W. & Coussios, C. C. Cavitation-Enhanced Extravasation for Drug Delivery. *Ultrasound Med. Biol.* **37,** 1838–1852 (2011).

42. Kooiman, K., Vos, H. J., Versluis, M. & De Jong, N. Acoustic behavior of microbubbles and implications for drug delivery. *Adv. Drug Deliv. Rev.* **72,** 28–48 (2014).

43. Elder, S. A. Cavitation Microstreaming. *J. Acoust. Soc. Am.* **31,** 54 (1959).

44. Longuet-Higgins, M. S. Viscous streaming from an oscillating spherical bubble. *Proc. R. Soc. A Math. Phys. Eng. Sci.* **454,** 725–742 (1998).

45. Doinikov, A. a & Bouakaz, A. Theoretical investigation of shear stress generated by a contrast microbubble on the cell membrane as a mechanism for sonoporation. *J. Acoust. Soc. Am.* **128,** 11–9 (2010).

46. Manasseh, R., Tho, P., Ooi, A., Petkovic-Duran, K. & Zhu, Y. Cavitation microstreaming and material transport around microbubbles. *Phys. Procedia* **3,** 427–432 (2010).

47. Kolb, J. & Nyborg, W. L. Small-Scale Acoustic Streaming in Liquids. *J. Acoust. Soc. Am.* **28,** 1237 (1956).

48. Ooi, A., Tho, P. & Manasseh, R. *Cavitation microstreaming patterns in single and multiple bubble systems*. *The Journal of the Acoustical Society of America* **122,** (2007).

49. Postema, M., Wamel, A., Lancée, C. T. & De Jong, N. ULTRASOUND-INDUCED ENCAPSULATED MICROBUBBLE PHENOMENA. doi:10.1016/j.ultrasmedbio.2004.02.010

50. Borden, M. a. & Longo, M. L. Dissolution behavior of lipid monolayer-coated, air-filled microbubbles: Effect of lipid hydrophobic chain length. *Langmuir* **18,** 9225–9233 (2002).

51. Borden, M. a., Pu, G., Runner, G. J. & Longo, M. L. Surface phase behavior and microstructure of lipid/PEG-emulsifier monolayer-coated microbubbles. *Colloids Surfaces B Biointerfaces* **35,** 209–223 (2004).

52. McEwan, C. *et al.* Oxygen Carrying Microbubbles for Enhanced Sonodynamic Therapy of Hypoxic Tumours. *J. Control. Release* **203,** 51–56 (2015).

53. Luan, Y. *et al.* Lipid shedding from single oscillating microbubbles. *Ultrasound Med. Biol.* **40,** 1834–1846 (2014).

54. Delalande, A., Kotopoulis, S., Rovers, T., Pichon, C. & Postema, M. Sonoporation at a low mechanical index. *Bubble Sci. Eng. Technol.* **3,** 3–12 (2011).

55. De Cock, I. *et al.* Ultrasound and microbubble mediated drug delivery: Acoustic pressure as determinant for uptake via membrane pores or endocytosis. *J. Control. Release* **197,** 20–28 (2015).

56. Delalande, A., Leduc, C., Midoux, P., Postema, M. & Pichon, C. Efficient Gene Delivery by Sonoporation Is Associated with Microbubble Entry into Cells and the Clathrin-Dependent Endocytosis Pathway. *Ultrasound Med. Biol.* **41,** 1913–1926 (2015).

57. Kudo, N., Okada, K. & Yamamoto, K. Sonoporation by single-shot pulsed ultrasound with microbubbles adjacent to cells. *Biophys. J.* **96,** 4866–4876 (2009).

58. Okada, K., Kudo, N., Kondo, T. & Yamamoto, K. Contributions of mechanical and sonochemical effects to cell membrane damage induced by single-shot pulsed ultrasound with adjacent microbubbles. *J Med Ultrason.* **35,** 169–176 (2008).

59. Dijkmans, P. a. *et al.* Microbubbles and ultrasound: From diagnosis to therapy. *Eur. J. Echocardiogr.* **5,** 245–256 (2004).

60. Kooiman, K., Foppen-Harteveld, M., Der Steen, A. F. W. Van & De Jong, N. Sonoporation of endothelial cells by vibrating targeted microbubbles. *J. Control. Release* **154,** 35–41 (2011).

61. Karshafian, R., Bevan, P. D., Williams, R., Samac, S. & Burns, P. N. Sonoporation by Ultrasound-Activated Microbubble Contrast Agents: Effect of Acoustic Exposure Parameters on Cell Membrane Permeability and Cell Viability. *Ultrasound Med. Biol.* **35,** 847–860 (2009).

62. Wang, M. *et al.* Sonoporation-induced cell membrane permeabilization and cytoskeleton disassembly at varied acoustic and microbubble-cell parameters. *Sci. Rep.* **8,** 3885 (2018).

63. Kudo, N., Okada, K. & Yamamoto, K. Sonoporation by Single-Shot Pulsed Ultrasound with Microbubbles Adjacent to Cells. *Biophys. J.* **96,** 4866–4876 (2009).

64. Zhou, Y., Kumon, R. E., Cui, J. & Deng, C. X. The Size of Sonoporation Pores on the Cell Membrane. *Ultrasound Med. Biol.* **35,** 1756–1760 (2009).

65. Hu, Y., Wan, J. M. F. & Yu, A. C. H. Membrane Perforation and Recovery Dynamics in Microbubble-Mediated Sonoporation. *Ultrasound Med. Biol.* **39,** 2393–2405 (2013).

66. Deng, C. X., Sieling, F., Pan, H. & Cui, J. Ultrasound-induced cell membrane porosity. *Ultrasound Med. Biol.* **30,** 519–526 (2004).

67. Zeghimi, A., Uzbekov, R., Arbeille, B., Escoffre, J. M. & Bouakaz, A. Ultrastructural modifications of cell membranes and organelles induced by sonoporation. *IEEE Int. Ultrason. Symp. IUS* 2045–2048 (2012). doi:10.1109/ULTSYM.2012.0511

68. Juffermans, L. J. M., Kamp, O., Dijkmans, P. A., Visser, C. A. & Musters, R. J. P. LOW-INTENSITY ULTRASOUND-EXPOSED MICROBUBBLES PROVOKE LOCAL HYPERPOLARIZATION OF THE CELL MEMBRANE VIA ACTIVATION OF BK Ca CHANNELS. doi:10.1016/j.ultrasmedbio.2007.09.010

69. Meijering, B. D. M. *et al.* Ultrasound and microbubble-targeted delivery of macromolecules is regulated by induction of endocytosis and pore formation. *Circ. Res.* **104,** 679–687 (2009).

70. Kooiman, K., Van Der Steen, A. F. W. & De Jong, N. Role of intracellular calcium and reactive oxygen species in microbubble-mediated alterations of endothelial layer permeability. *IEEE Trans. Ultrason. Ferroelectr. Freq. Control* **60,** 1811–1815 (2013).

71. Juffermans, L. J. M., Dijkmans, P. a, Musters, R. J. P., Visser, C. a & Kamp, O. Transient permeabilization of cell membranes by ultrasound-exposed microbubbles is related to formation of hydrogen peroxide. *Am. J. Physiol. Heart Circ. Physiol.* **291,** H1595–H1601 (2006).

72. Juffermans, L. J. M. *et al.* Ultrasound and Microbubble-Induced Intra- and Intercellular Bioeffects in Primary Endothelial Cells. *Ultrasound Med. Biol.* **35,** 1917–1927 (2009).

73. Chen, X., Leow, R. S., Hu, Y., Wan, J. M. F. & Yu, A. C. H. Single-site sonoporation disrupts actin cytoskeleton organization. *J. R. Soc. Interface* **11,** 20140071 (2014).

74. Zeghimi, A. & Bouakaz, A. Involvement of cytoskeleton in sonoporation and drug delivery. 850–853 (2014).

75. Jalali, S., Huang, Y., Dumont, D. J. & Hynynen, K. Focused ultrasound-mediated bbb disruption is associated with an increase in activation of AKT: experimental study in rats. *BMC Neurol.* **10,** 114 (2010).

76. Sud, M. *et al.* LMSD: LIPID MAPS structure database. *Nucleic Acids Res.* **35,** D527-32 (2007).

77. Christie, W. The Lipid Web - an Alternative Lipid Library. Available at: http://www.lipidhome.co.uk/index.html. (Accessed: 3rd May 2018)

78. Jouhet, J. Importance of the hexagonal lipid phase in biological membrane organization. *Front. Plant Sci.* **4,** 494 (2013).

79. Hein, M. *et al.* Implications of a non-lamellar lipid phase for the tight junction stability PartII: Reversible modulation of transepithelial resistance in high and low resistance MDCK-cells by basic amino acids, Ca 2+, protamine and protons. *Chem. Phys. Lipids* **63,** 223–233 (1992).

80. Israelachvili, J. N., Mitchell, D. J. & Ninham, B. W. Theory of self-assembly of hydrocarbon amphiphiles into micelles and bilayers. *J. Chem. Soc. Faraday Trans. 2 Mol. Chem. Phys.* **72,** 1525–1568 (1976).

81. Chapman, D. Phase transitions and fluidity characteristics of lipids and cell membranes. *Q. Rev. Biophys.* **8,** 185–235 (2017).

82. Bittman, R. & Blau, L. KINETICS OF WATER PERMEABILITY IN LIPOSOMES The Phospholipid-Cholesterol Interaction. Kinetics of Water Permeability in Liposomest.

83. Carruthers, A. & Melchior, D. L. Studies of the Relationship between Bilayer Water Permeability and Bilayer Physical State1. *Biochemistry* **22,** 5797–5807 (1983).

84. Lee, D. B. N., Jamgotchian, N., Allen, S. G., Abeles, M. B. & Ward, H. J. A lipid-protein hybrid model for tight junction. doi:doi:10.1152/ajprenal.00097.2008

85. R.Hazel, J. & Williams, E. E. The role of alterations in membrane lipid composition in enabling physiological adaptation of organisms to their physical environment. *Prog. Lipid Res.* **29,** 167–227 (1990).

86. Almén, M., Nordström, K. J., Fredriksson, R. & Schiöth, H. B. Mapping the human membrane proteome: a majority of the human membrane proteins can be classified according to function and evolutionary origin. *BMC Biol.* **7,** 50 (2009).

87. Simons, K. & Vaz, W. L. C. Model Systems, Lipid Rafts, and Cell Membranes. *Annu. Rev. Biophys. Biomol. Struct* **33,** 269–95 (2004).

88. Nabi, I. R. & Le, P. U. Caveolae/raft-dependent endocytosis. *J. Cell Biol.* **161,** 673–7 (2003).

89. Calderón, V. *et al.* Tight Junctions and the Experimental Modifications of Lipid Content. *J. Membr. Biol.* **164,** 59–69 (1998).

90. Feltkamp, C. A. & Van Der Waerden, A. W. M. JUNCTION FORMATION BETWEEN CULTURED NORMAL RAT HEPATOCYTES AN ULTRASTRUCTURAL STUDY ON THE PRESENCE OF CHOLESTEROL AND THE STRUCTURE OF DEVELOPING TIGHT- JUNCTION STRANDS. *J. Cell Sci* **63,** 271–286 (1983).

91. Phillips, M. C., Johnson, W. J. & Rothblat, G. H. Mechanisms and consequences of cellular cholesterol exchange and transfer. *Biochim. Biophys. Acta* **906,** 223–276 (1987).

92. Steck, T. L., Kezdy, F. J. & Lange, Y. THE JOURNAL OF BIOLOGICAL CHEMISTRY An Activation-Collision Mechanism for Cholesterol Transfer between Membranes*. **263,** 13023–13031 (1988).

93. Ferrell, J. E., Lee, K.-J. & Huestis, W. H. Lipid Transfer between Phosphatidylcholine Vesicles and Human Erythrocytes: Exponential Decrease in Rate with Increasing Acyl Chain Lengthy. *Biochem. Proc. Natl. Acad. Sci. U.S.A. Biochem. Biophys. Res. White, J. G. Am. J. Pathol. Clin. Hematol. J. Lab. Clin. Med. Febiger* **24,** 2857–2864 (1985).

94. Treat, L. H., McDannold, N., Zhang, Y., Vykhodtseva, N. & Hynynen, K. Improved Anti-Tumor Effect of Liposomal Doxorubicin After Targeted Blood-Brain Barrier Disruption by MRI-Guided Focused Ultrasound in Rat Glioma. *Ultrasound Med. Biol.* **38,** 1716–1725 (2012).

95. Kheirolomoom, A. *et al.* Acoustically-active microbubbles conjugated to liposomes: Characterization of a proposed drug delivery vehicle. *J. Control. Release* **118,** 275–284 (2007).

96. Escoffre, J. M. *et al.* Doxorubicin liposome-loaded microbubbles for contrast imaging and ultrasound-triggered drug delivery. *IEEE Trans. Ultrason. Ferroelectr. Freq. Control* **60,** 78–87 (2013).

97. De Cock, I., Lajoinie, G., Versluis, M., De Smedt, S. C. & Lentacker, I. Sonoprinting and the importance of microbubble loading for the ultrasound mediated cellular delivery of nanoparticles. *Biomaterials* **83,** 294–307 (2016).

98. Der Loughian, C. *et al.* Jumping acoustic bubbles on lipid bilayers. *Soft Matter* 3460–3469 (2015). doi:10.1039/c5sm00427f

99. Tartis, M. S. *et al.* Dynamic microPET imaging of ultrasound contrast agents and lipid delivery. *J. Control. Release* **131,** 160–166 (2008).

100. Jin, L. F. *et al.* Ultrasound targeted microbubble destruction stimulates cellular endocytosis in facilitation of adeno-associated virus delivery. *Int. J. Mol. Sci.* **14,** 9737–9750 (2013).

101. Van Wamel, A., Bouakaz, A., Versluis, M. & De Jong, N. Micromanipulation of endothelial cells: Ultrasound-microbubble-cell interaction. *Ultrasound Med. Biol.* **30,** 1255–1258 (2004).

102. Yamamoto, K. & Ando, J. Endothelial cell and model membranes respond to shear stress by rapidly decreasing the order of their lipid phases. *J. Cell Sci.* **126,** (2013).

103. Haidekker, M. a, L'Heureux, N. & Frangos, J. a. Fluid shear stress increases membrane fluidity in endothelial cells: a study with DCVJ fluorescence. *Am. J. Physiol. - Hear. Circ. Physiol.* **278,** H1401–H1406 (2000).

104. Butler, P. J., Norwich, G., Weinbaum, S. & Chien, S. Shear stress induces a time- and position-dependent increase in endothelial cell membrane fluidity. *Am. J. Physiol. Cell Physiol.* **280,** C962–C969 (2001).

105. Li, Y.-S. J., Haga, J. H. & Chien, S. Molecular basis of the effects of shear stress on vascular endothelial cells. *J. Biomech.* **38,** 1949–1971 (2005).

106. Watanabe, H. *et al.* Alterations of human erythrocyte membrane fluidity by oxygen-derived free radicals and calcium. *Free Radic. Biol. Med.* **8,** 507–514 (1990).

107. Fan, Z., Liu, H., Mayer, M. & Deng, C. C. X. Spatiotemporally controlled single cell sonoporation. *Proc. Natl. Acad. Sci. U. S. A.* **109,** 16486–16491 (2012).

108. Leow, R. S., Wan, J. M. F. & Yu, A. C. H. Membrane blebbing as a recovery manoeuvre in site-specific sonoporation mediated by targeted microbubbles. (2015).

109. Tran, T. A., Le Guennec, J. Y., Bougnoux, P., Tranquart, F. & Bouakaz, A. Characterization of cell membrane response to ultrasound activated microbubbles. *IEEE Trans. Ultrason. Ferroelectr. Freq. Control* **55,** 44–49 (2008).

110. Kumon, R. E. *et al.* Spatiotemporal Effects of Sonoporation Measured by Real-Time Calcium Imaging. *Ultrasound Med. Biol.* **35,** 494–506 (2009).

111. Carugo, D. *et al.* Modulation of the molecular arrangement in artificial and biological membranes by phospholipid-shelled microbubbles. *Biomaterials* (2016). doi:10.1016/j.biomaterials.2016.10.034

112. McDonald, J. G. *et al.* Lipidomics reveals a remarkable diversity of lipids in human plasma. *J. Lipid Res.* **51,** (2010).

113. Hafez, I. M. & Cullis, P. R. Roles of lipid polymorphism in intracellular delivery. *Adv. Drug Deliv. Rev.* **47,** 139–148 (2001).

114. Lasic, D. D. Novel applications of liposomes. *Trends Biotechnol.* **16,** 307–21 (1998).

115. Kulkarni, C. V. Lipid crystallization: from self-assembly to hierarchical and biological ordering. *Nanoscale* **4,** 5779 (2012).

116. Marsh, D. Liquid-ordered phases induced by cholesterol: A compendium of binary phase diagrams. *Biochim. Biophys. Acta - Biomembr.* **1798,** 688–699 (2010).

117. Feigenson, G. W. Phase behavior of lipid mixtures. *Nat. Chem. Biol.* **2,** 560–3 (2006).

II.

The role of cell membrane modification by microbubbles in sonoporation

2.1. Abstract

In this chapter, the role of cell membrane modification by microbubble (MB) exposure in sonoporation is investigated[1]. In the first part of the work, cancer cells were exposed to microbubbles and ultrasound *in vitro* within a microfluidic layered acoustic resonator device. Transfer of MB constituents to cell membranes and the effect upon membrane physicochemical properties were examined using quantitative fluorescence microscopy techniques. Of the MB formulations tested, 18:0 PC-PEG40S MBs were found to be the only formulation that produced repeatable and significant cell membrane lipid disordering. Washing MBs by centrifugation was found to inhibit this effect but had no significant effect upon acoustic emissions. Further investigation was therefore made to determine whether there was a difference in sonoporation produced by washed and unwashed 18:0 PC-PEG40S MBs.

2.2. Introduction

Sonoporation is a phenomenon whereby the interactions between MBs and ultrasound in the vicinity of cells permeabilize cell membranes[1]. Although the underlying mechanisms have not been clearly identified, it has been postulated that the mechanical action of ultrasound-activated MBs causes the formation of temporary pores within nearby cell membranes[2], which can be exploited to deliver compounds into the intracellular milieu. Pore formation has been observed and characterized *in vitro* using confocal microscopy[1], membrane potential measurements[3] and scanning and transmission electron microscopy[4]. In some cases, however, pores do not reseal spontaneously, and this can lead to cell death[1,5–7].

[1] Portions of this work have been published previously[29,41,89].

The mechanical perturbation of the cellular microenvironment during ultrasound exposure in the presence of MBs has been attributed to distinct physical phenomena, including the oscillatory strain imparted on the cell membrane by a volumetrically oscillating MB[8,9], acoustic radiation forces causing MB translation against or across the cell membrane[10,11], fluid shear stress fields generated by acoustic microstreaming[12], and/or shock waves and fluid jets produced by MB collapse[1,13]. Alternative mechanisms have also been suggested to govern or enhance ultrasound-mediated intracellular delivery, including activation of clathrin-mediated endocytic pathways[10,14,15], alteration of reactive oxygen species (ROS) homeostasis[16] potentially due to increased intracellular H_2O_2 levels[17], influx of calcium ions (Ca^{2+})[17], and exchange or fusion of MB shells with the cell membrane[18–20].

In recent years, significant efforts have been made to characterize the behaviour of cell membranes exposed to ultrasound-activated MBs and to identify the underlying interaction phenomena[21], particularly regarding membrane permeabilization and recovery dynamics[1,22]. In the first part of the work reported in this chapter, a cell culture-compatible microfluidic layered acoustic resonator (µLAR) was employed in combination with quantitative fluorescence microscopy techniques to measure changes in the lipid order of cell membranes exposed to MBs and ultrasound. Lipid order is important in a variety of biophysical and biological processes (see Chapter 2), including mobility, function and organization of membrane proteins[23,24], formation and dynamics of membrane domains[25], membrane mechanical properties[26], ion permeability[27], and membrane hydration, which is coupled with the probability of pore formation, and thus, hypothetically, with sonoporation. After identifying MBs that alter cell membrane lipid order, the potential of these MBs to enhance sonoporation was investigated.

2.3. Methods

2.3.1. Methods overview

In the initial study, the transfer of lipid-like probe, DiI, from microbubble shells to cell membranes under ultrasound exposure was assessed in the µLAR (described below), which enables simultaneous microscopy and ultrasound exposure with living cells (see Figure 1A). Following the observation of material transfer from MBs to cells, the effects of ultrasound and MBs on cell membrane lipid order were evaluated using

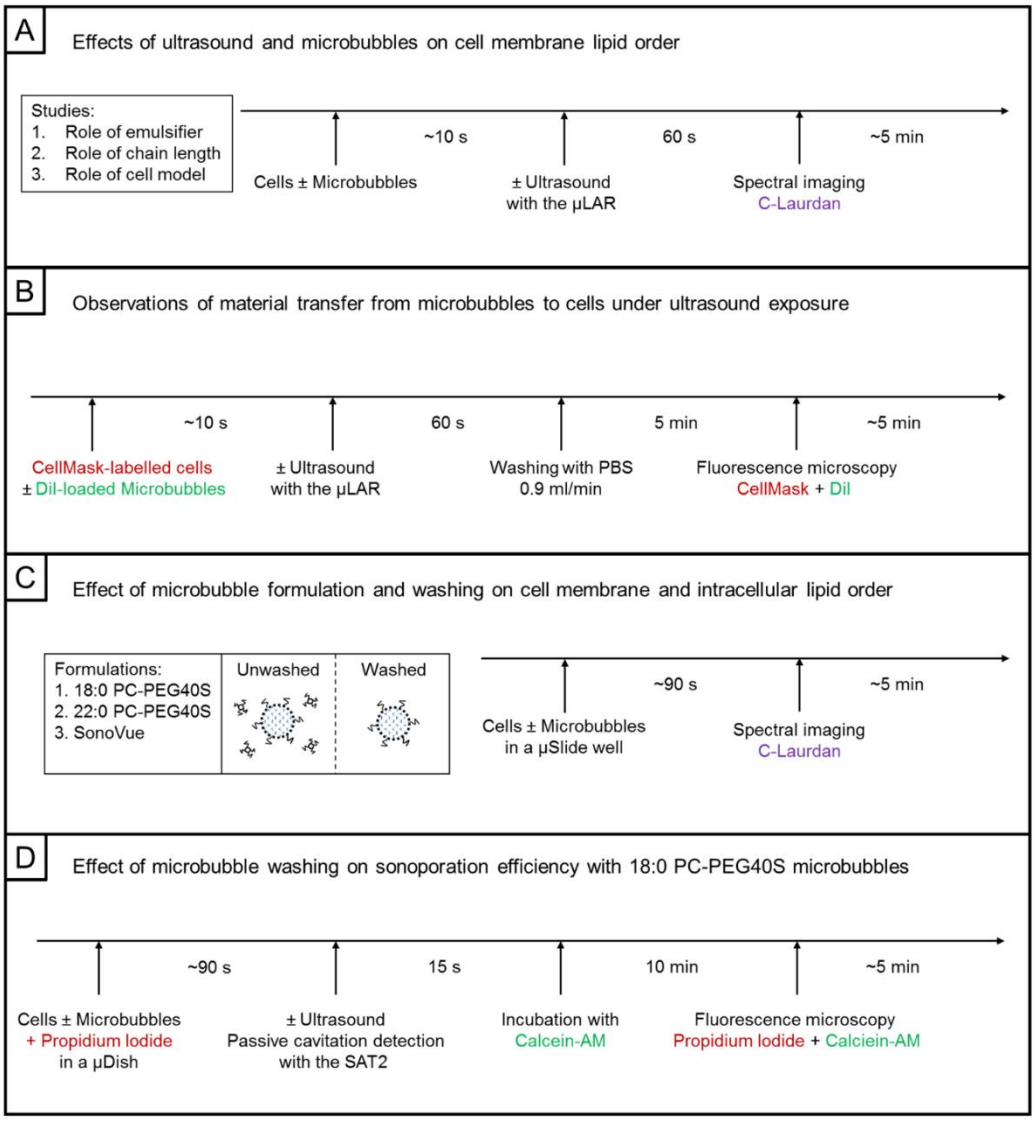

Figure 1: Experimental timelines for the experiments of the present chapter.

spectral imaging with C-Laurdan, again in the µLAR (see Figure 1B). It was found that MB exposure alters cell membrane lipid order, even in the absence of ultrasound exposure.

A second study was subsequently performed to assess the impact of MB-mediated cell membrane lipid disordering on sonoporation. To this end, spectral imaging with C-Laurdan was performed with additional MB formulations, including the clinical formulation SonoVue®, at the concentrations used for sonoporation experiments (see Figure 1C). The impact of washing MBs was also assessed, owing to the significant effect of free lipid and emulsifier upon membrane lipid order identified in the first study. Similarly, the impact of temperature on the effect of MBs on cell membrane lipid order was measured. In these experiments, the primary interest was the sensitizing effect of the MBs. They were therefore performed in the absence of ultrasound exposure. This enabled use of multi-welled microscopy slides (µSlides) instead of the µLAR previously employed.

18:0 PC-PEG40S MBs were found to induce repeatable and significant disordering of cell membrane lipids, an effect that was inhibited by washing the MBs of free lipid and emulsifier. It was thus hypothesized that the unwashed 18:0 PC-PEG40S MBs would be more likely to induce sonoporation than their washed counterparts, provided that the MB size distributions, concentrations, and acoustic emissions were indistinguishable. To test this hypothesis, a water tank setup was employed that enabled better characterization of the ultrasound field and acoustic emissions than in experiments with the µLAR, in combination with fluorescence microscopy for the assessment of sonoporation (see Figure 1D).

2.3.2. Microbubble methods

2.3.2.1. MB formulations

In this chapter, MB formulations commonly employed in ultrasound-mediated drug delivery research and in the clinic (18:0 PC-PEG40S, 22:0 PC-PEG40S, and

Microbubble	Lipids and emulsifiers	Gas	Molar Ratio	Lipid preparation	Resuspension	Formation
DSPC-PEG40S	DSPC, PEG40S	SF_6	9:1	Film from chloroform evaporation	PBS	Sonication
DBPC-PEG40S	DBPC, PEG40S	SF_6	9:1	Film from chloroform evaporation	PBS	Sonication
SonoVue	DSPC, PEG4000, DPPG, Palmitic acid	SF_6	71:9806:75:46	Lyophilized powder	0.9% saline	Manual shaking

Table 2: Microbubble formulations. Microbubble constituents, molar ratios, lipid preparation methods, resuspension media, and microbubble formation techniques are detailed for 18:0 PC-PEG40S, 22:0 PC-PEG40S, and SonoVue® microbubbles respectively. Phosphate-buffered saline (PBS) is 137 mM NaCl, 2.7 mM KCl, 10 mM Na_2HPO_4, and 1.8 mM KH_2PO_4 in H_2O and 0.9% saline is ~154 mM NaCl in H_2O. SonoVue® was purchased in lyophilized form from Bracco. Chloroform evaporation was performed at 60°C for at least 12 hours.

Short name	22:0 PC (DBPC)	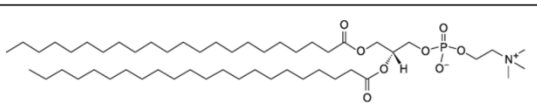
Chemical name	1,2-dibehenoyl-sn-glycero-3-phosphocholine	
Molecular weight	902.358	
T_m (°C)	75	
Short name	18:0 PC (DSPC)	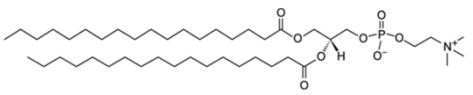
Chemical name	1,2-distearoyl-*sn*-glycero-3-phosphocholine	
Molecular weight	790.145	
T_m (°C)	55	
Short name	PEG40S	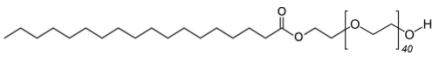
Chemical name	Polyethylene glycol (40) stearate	
Molecular weight	2064.5	
Short name	16:0 PG (DPPG)	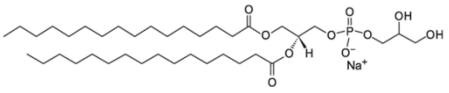
Chemical name	1,2-dipalmitoyl-sn-glycero-3-phospho-(1'-rac-glycerol) (sodium salt)	
Molecular weight	744.952	
T_m (°C)	41	
Short name	PEG4000	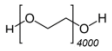
Chemical name	Polyethylene glycol (4000)	
Molecular weight	744.952	
Chemical name	Palmitic acid	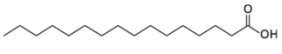
Molecular weight	256.43	
T_m (°C)	63.1	
Short name	SF6	
Chemical name	Sulfur hexafluoride (gas)	
Molecular weight	146.06	
Density (kg/m³)	6.17	

Table 1: Microbubble constituents. The chemical constituents of the microbubbles employed in the present study are described with molecular weights, transition temperatures (where applicable), and molecular line drawings. The density at STP of SF_6 gas used in the microbubbles is also provided. This highlights its high density compared to dry air (~6.17 kg/m^3 vs ~1.2 kg/m^3). From the line drawings it should be noted that 18:0 PC and 22:0 PC are zwitterionic, palmitic acid, PEG and PEG40S are non-ionic, and DPPG is negatively charged in aqueous solution.

SonoVue®) were tested for their ability to modulate A-549 cell membrane lipid order using spectral imaging with the environmentally-sensitive probe, C-Laurdan. The MB formulations with molar ratios, resuspension media, lipid preparation methods, and MB formation techniques employed are shown in Table 1. The chemical constituents employed in each of these MB formulations are shown in Table 2 complete with molecular weights, transition temperatures (where applicable), and molecular line drawings.

The effect of washing MB solutions by centrifugation was evaluated for each of these main formulations. Representative microscopy images and measured size distributions of the unwashed and washed MBs for each formulation employed can be seen in Figure 1.

2.3.2.2. MB preparation

A batch sonication protocol previously reported was used to prepare MBs[10]. The protocol is as follows: 1,2-distearoyl-sn-glycero-3-phosphocholine or 1,2-dibehenoyl-sn-glycero-3-phosphocholine (18:0 PC or 22:0 PC, Avanti Polar Lipids) and polyoxyethylene (40) stearate (PEG40S, Sigma Aldrich, UK) were dissolved in chloroform (Sigma Aldrich, UK) and mixed in a glass vial at a molar ratio of 9:1 (total volume = 1.1 mL). The mixture was subsequently heated on a hotplate set to 50ºC for 12 h, to allow for the solvent to evaporate. The obtained dry lipid film was suspended in 5 mL of filtered phosphate buffered saline (PBS, pH 7.4) solution (Thermo Fisher Scientific Inc.) for 1 h on a hotplate set at 100ºC. Lipids were then homogeneously dispersed for 90 s using a sonicator (XL 2000, probe diameter 3 mm, 20 W, 22.5 kHz, Misonix) with the tip completely immersed in the lipid solution (power setting 4). MBs were subsequently formed by placing the sonicator tip at the air-water interface under

constant sulphur hexafluoride flow (The BOC Group plc, UK) and sonicating for 30 s (power setting 14). Immediately after production, the vial containing the MB suspension was capped and placed in ice for approximately 5 min.

2.3.2.3. MB size and concentration

For quantification of MB size and concentration, 10 µL of the microbubble suspension were transferred onto a Neubauer improved cell counting chamber (Hausser Scientific Company) under a 24 mm × 24 mm glass coverslip (VWR International). At least 10 images of MBs were acquired at 40x magnification using a Leica DM500 microscope (Leica Microsystems GmbH, Germany) coupled with a CCD camera (MicroPublisher 3.3 RTV, Imaging, Canada). MB sizing and counting was performed using a purpose-

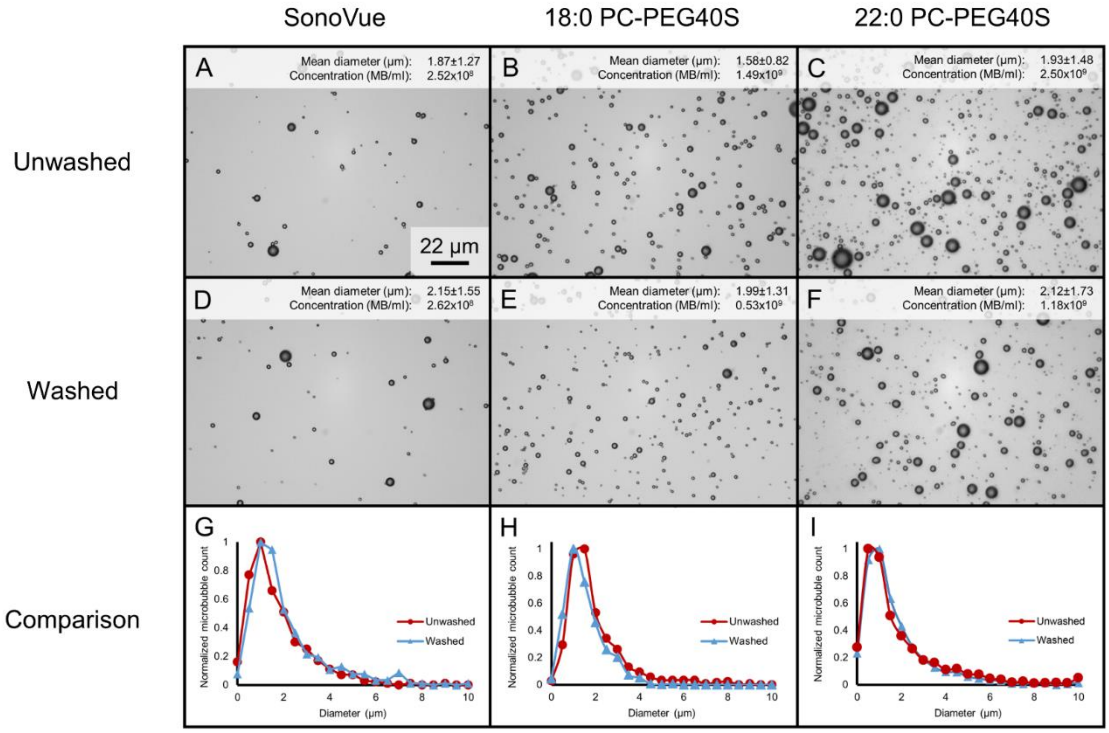

Figure 2: Effect of washing various MB formulations. Unwashed MBs are shown in panels A-C. Washed MB are shown in panels D-F. A comparison of the normalized size distributions of washed and unwashed MBs are shown in panels G-I. The columns from left to right contain SonoVue® MB,18:0 PC-PEG40S MB, and 22:0 PC-PEG40S MB respectively. Images were taken with 40X magnification following a 10X dilution. The scale bar in (A) applies for all panels.

written code in MATLAB® (The MathWorks Inc.)[11].

MB mean diameters and concentrations used in µ-LAR experiments are presented in Table 3. Concentrations were approximately equivalent except for 18:0 PC MBs formed without emulsifier which were less numerous by ~4-fold. To test the role of the emulsifier, PEG40S, 18:0 PC-PEG40S MBs were also made with 10-fold less PEG40S (90:1 lipid to emulsifier molar ratio) and 18:0 PC and 22:0 PC MBs were made without PEG40S by the same methods described previously.

MB formulation	Diameter (µm)	Concentration (MB/ml)
18:0 PC-PEG 9:1	1.59 ± 1.24	$6.15x10^7$
18:0 PC-PEG 90:1	2.05 ± 1.59	$6.14x10^7$
18:0 PC	1.69 ± 0.99	$1.48x10^7$
22:0 PC	2.04 ± 1.59	$5.93x10^7$
Washed 18:0 PC-PEG40S 9:1	2.18 ± 1.08	Matched

Table 3: Table of MB size and concentrations used in µLAR experiments. Washed MBs were concentration matched to their unwashed counterparts.

2.3.2.4. MB washing

Washed MBs were prepared by the centrifugation method without size isolation[28]. Briefly, MBs were loaded into a 10 ml syringe and centrifuged for 5 minutes at 200g. Following centrifugation, the subnatent was discarded and the MBs were resuspended in phosphate buffered saline (PBS). It was found that roughly half of the MBs were lost to centrifugation upon washing. This could be prevented in part by waiting longer for the smallest MBs to float to the top of the syringe before removing the subnatent during the washing process[28]. Indeed, the mean MB diameter shifted from 1.80 ± 0.31 to 2.24 ± 0.27 µm upon washing (see Figure 3A-C).

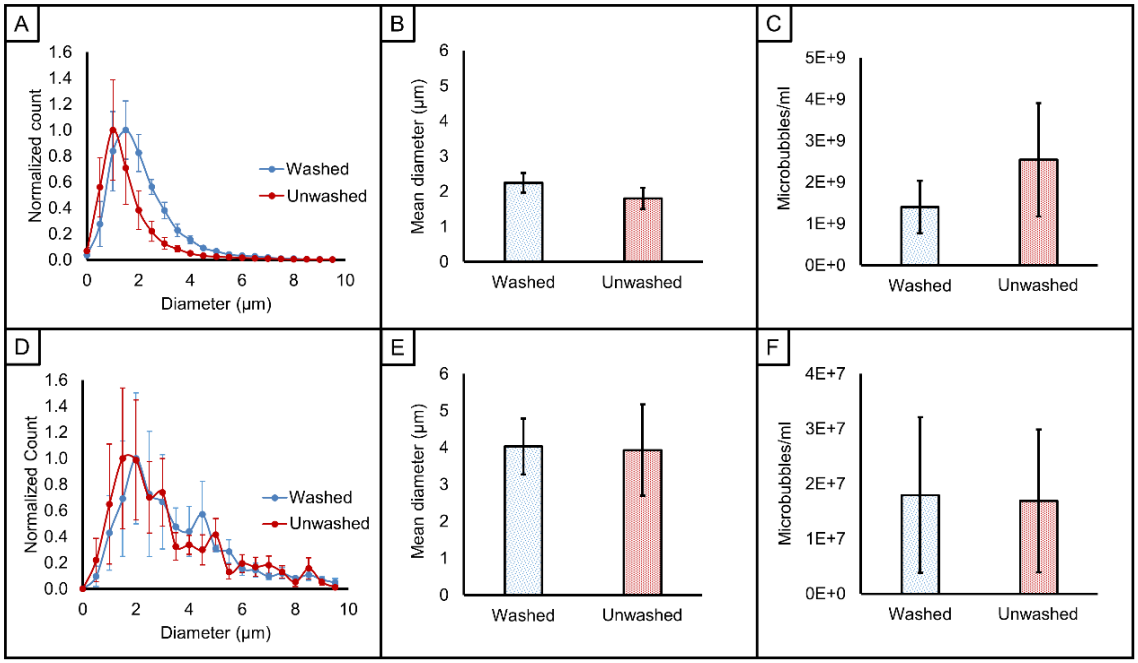

Figure 3: Effect of washing and temperature on 18:0 PC-PEG40S MB size and concentration. (A) and (D) show the size distributions of n = 3 standard and washed 18:0 PC-PEG40S MB preparations at 22°C and 37°C respectively. (B) and (E) show the mean MB diameter of the same samples respectively. (C) and (F) show the concentrations for the same samples respectively. Note that in (F) the concentrations were matched to 5.5 E7 MB/ml prior to incubation at 37°C and sizing and counting by brightfield microscopy.

2.3.2.5. MBs in sonoporation and spectral imaging experiments

Unwashed and washed MBs employed in sonoporation experiments with µDishes and spectral imaging experiments with µSlides were concentration matched to 5.5 x 10^7 MB/ml (see Figure 2 for initial concentrations and size distributions). To evaluate the effect of heating on these MB suspensions, samples of MBs were introduced to a 37°C PBS solution for 60 s, and then counted and sized again (see Figure 3D-F). It was found that the 37°C exposure increased the mean MB diameter by a factor of two and lowered the concentration by a factor of three for both standard and washed MBs. Once heated to 37°C, no significant differences in MB size distributions or concentrations between unwashed and washed MB populations were evident. The final diameters and concentrations used in sonoporation experiments at 37°C were estimated to be 3.93 ±

1.24 µm at 1.69 ± 1.30 x 10^7 MB/ml, and 4.03 ± 0.76 µm at 1.79 ± 1.42 x 10^7 MB/ml for standard and washed MBs respectively.

2.3.2.6. Fluorescent labelling of MBs

For those experiments involving fluorescent labelling of MBs, a stock solution of the lipophilic dye 1,1'-dioctadecyl-3,3,3',3'-tetramethylindocarbocyanine perchlorate (DiI, Thermo Fisher Scientific Inc.) at a concentration of 2.5 mg/mL in dimethyl sulfoxide (DMSO, Sigma Aldrich, UK) was prepared. 7 µL of the stock solution were added to the lipid solution, and the protocols outlined previously were followed for MB production. In order to remove excess DiI from the formed MB suspension, the MB sample was centrifuged twice at 1000g for 10 min (400R Heraeus Labofuge, Thermo Fisher Scientific Inc.), and MBs were re-suspended in PBS after each centrifugation cycle. In order to assess the success of MB shell labelling, fluorescent images were acquired at 63x magnification using a confocal microscope (LSM 780, Carl Zeiss AG, Germany). For this purpose, a MB sample was placed between a 75 mm × 25 mm × 0.17 mm glass coverslip (Logitech Ltd., Scotland) and a 24 mm × 24 mm glass coverslip (VWR International). A representative fluorescent image of DiI-labelled MBs

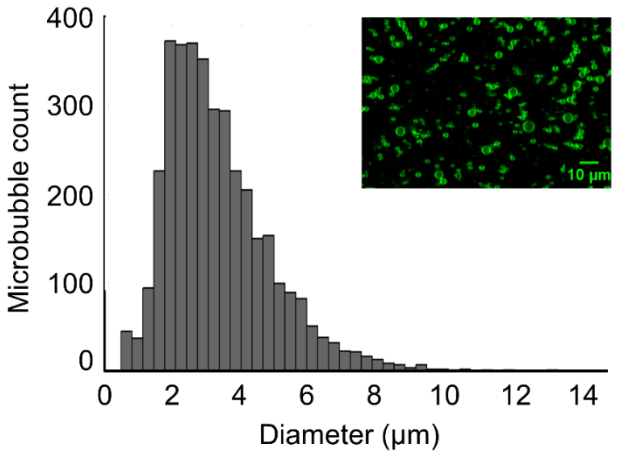

Figure 4: DiI-labelled MB size histogram and representative fluorescence microscopy image (inset).

and the corresponding size distribution is presented in Figure 4.

2.3.3. Cell culture

Immortalized human alveolar adenocarcinomic cells (A-549s), were grown in Dulbecco's Modified Eagle Medium (DMEM) with 10% fetal bovine serum (FBS) and 1% penicillin/streptomycin (P/S). A-549s were chosen as a representative model for a human cancer phenotype and were also employed for the sake of comparison with existing work that Carugo and colleagues had performed with A-549s. While the lung is not considered a viable target organ for ultrasound-mediated drug delivery owing to the presence of gas which lowers the threshold for cavitation damage to healthy tissue, A-549 cells in culture do not have this property.

Immortalized Chinese hamster ovarian cells (CHO-K1s), were grown in Ham's F-12 medium with 10% FBS. Dr. Serdic Sezgin, a co-author on the Biomaterials paper, had already gathered substantial experience with C-Laurdan spectral imaging with CHO-K1s and recommended them for their morphology which is well-suited to this method. CHO-K1s were thus chosen as a non-cancerous cell line for comparison with A-549s.

Cells were grown in a temperature- and CO_2-controlled incubator at 37°C and 5% CO_2. Cells were removed from T-75 culture flasks at ~80% confluence by ~2 min exposure to 0.25% trypsin/EDTA. Cells were then suspended in 10 ml culture medium (DMEM with 10% FBS) to deactivate the trypsin and centrifuged for 5 min at ~200g to form a pellet. Cells were then re-suspended in 10 ml culture medium. Cell concentration and viability was measured using trypan blue and a Countess® Automated Cell Counter (Invitrogen).

For experiments with the µLAR (described below), ~1×10^6 cells were seeded in 80 mm diameter petri dishes containing a single 75 mm × 25 mm × 0.17 mm glass coverslip

(Logitech Ltd., Scotland) in 10 mL growth medium. Coverslips were sterilized in 70% ethanol for 30 minutes followed by washing with phosphate buffered saline (PBS) and 30 min UV exposure prior to seeding. Cells grown to ~40% confluence on glass coverslips, were carefully transported to the µLAR using sterile tweezers and washed twice with PBS.

Cells were plated at ~40% seeding density in 35 mm Ibidi µ-Dishes for sonoporation experiments and 8-well Ibidi µ-Slides for spectral imaging experiments and were used in experiments ~16 h after plating. Sub-confluent cells were employed to improve the reliability of image segmentation and to reduce uncertainty introduced by the varying tightness of cell-cell contacts at confluence. All cell culture materials were purchased from ThermoFisher Scientific (UK) unless stated otherwise.

2.3.4. Experimental methods for exposure of cells to ultrasound and MBs

2.3.4.1. A microfluidic layered acoustic resonator (µLAR)

A microfluidic layered acoustic resonator (µLAR) designed by Dr. Dario Carugo was implemented for exposing living cells within a confined microfluidic environment to ultrasound and microbubbles, compatible with high-magnification microscopy[29] (see Figure 5). The µLAR layers comprise a piezoelectric ultrasound source, a machinable ceramic (Macor®) carrier layer coupling the acoustic energy into the other layers of the device and isolating the transducer from the fluid layer, a fluid layer, and a thin-

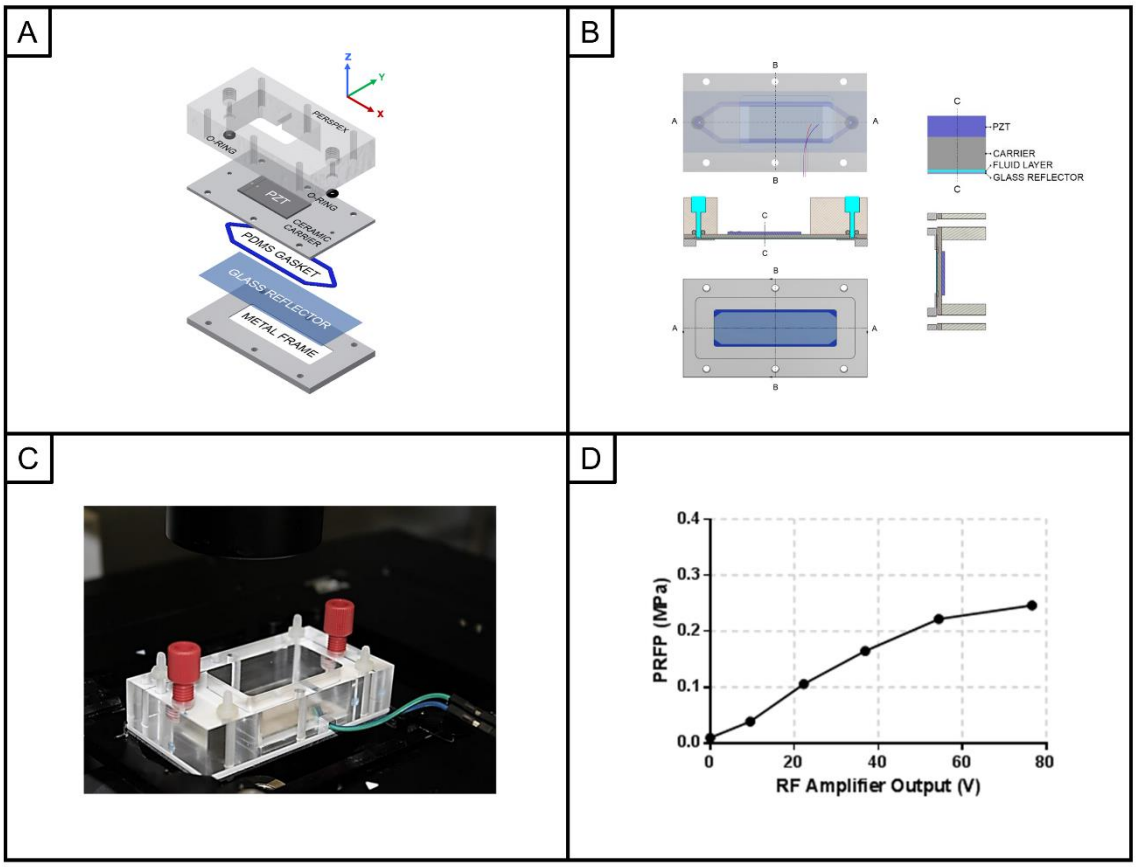

Figure 5: Design of a µLAR device. (A) Expanded view of the layered acoustic resonator including, top to bottom: Perspex manifold, o-rings, piezoceramic element coupled to the MACOR carrier layer, PDMS gasket that forms the channel geometry, glass coverslip, and aluminium frame. (B) Schematic drawing of the assembled acoustofluidic device, showing relative layer thicknesses and cut-view in C-C and A-A planes. (C) photograph of the assembled µLAR device at the confocal microscope. (D) Peak rarefactional pressure (PRFP) as a function of transducer driving voltage as determined with a fibre-optic hydrophone. Adapted from Pereno et al.[29].

reflector layer (glass coverslip) to reduce acoustic reflections at the fluid-glass boundary. Cells are grown on the glass coverslip and a Perspex® manifold provides inlets and outlets for the exchanging fluid in the fluid layer or running experiments under flow. A polydimethylsiloxane (PDMS) gasket is used to provide a water-tight seal around the fluid layer. Detailed methods concerning the design, characterization, and use of the μLAR have been published elsewhere[29]. The acoustic pressure in the layered acoustic resonator was measured using a calibrated fibre optic hydrophone (Precision Acoustics, UK) in a 0.5 mm diameter hole drilled through the reflector layer.

2.3.4.2. Exposure of cells to MBs and ultrasound with the μLAR

The μLAR with a cell-coated reflector was assembled and placed onto the microscope stage at 37ºC for cell imaging. Prior to imaging, 1-2 mL of at 37ºC PBS was slowly injected into the μLAR using a 5 mL plastic syringe (BD, Becton, Dickinson and Company) to remove any remaining free fluorophore from the solution. 37ºC PBS with or without ~5×10^7 MBs/mL (freshly added from a stock solution kept at room temperature) was then slowly injected into the μLAR for two device volumes.

Cells were exposed to 60 sec continuous wave ultrasound at ~0.97 MHz with peak rarefactional pressure of ~0.21 MPa. The μLAR was actuated by a radio frequency (RF) power amplifier (55 dB, Electronics & Innovation, Ltd.) driven by a sinusoidal signal from a function generator (33220A, Agilent Technologies Inc.). An oscilloscope (HM2005, Hameg Instruments GmbH, Germany) was used to monitor the applied voltage and operating frequency.

Between samples the μLAR was disassembled and washed thoroughly with acetone, ethanol, and filtered, distilled, and deionized water, and re-assembled with a new cell-coated glass coverslip thin-reflector layer.

2.3.4.3. Ultrasound for sonoporation experiments (SAT2)

Ultrasound exposure for the sonoporation experiments was conducted in a water tank system (~1 L) consisting of a 1 MHz unfocused ultrasound transducer (Imasonic 8233 A101, 40 mm diameter, 120 mm radius of curvature), a purpose-built sample holder, acoustic absorber, and passive cavitation detector (7.5 MHz centre frequency, V320 Panametrics, Olympus) designed by Dr. Michael Gray (see Figure 6). The acoustic absorber was placed opposite the transducer to attenuate reflections. The sample holder was designed to hold cell culture dishes (µ-Dishes, Ibidi) with plastic substrates much

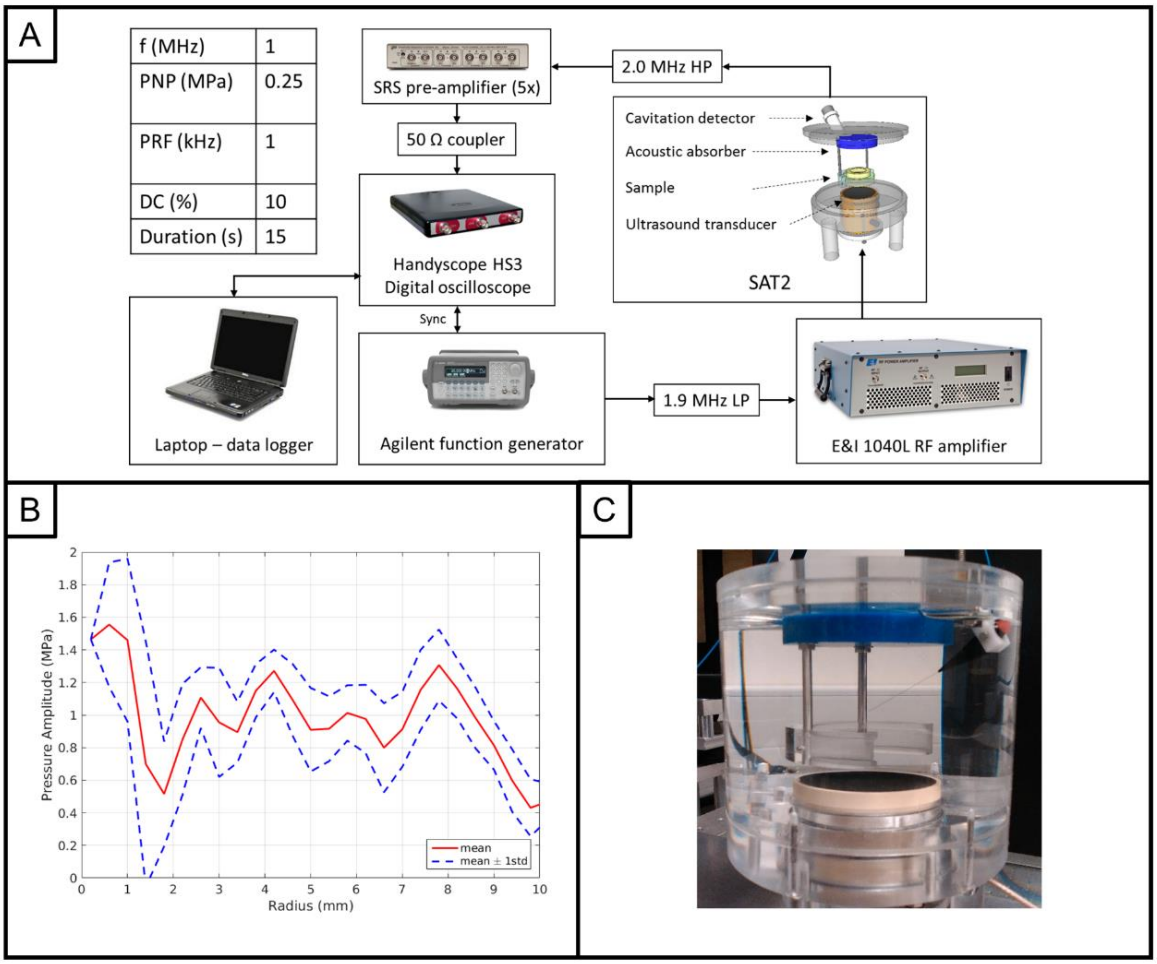

Figure 6: The SAT2 system. (A) The signal chain and ultrasound parameters used in sonoporation experiments. (B) The circumferentially averaged radial pattern of the ultrasound pressure field in the SAT2 measured ~32 mm above the transducer. (C) Photograph of the SAT2 with the fibre-optic hydrophone used to measure the ultrasound pressure field. The pressure measurements and photograph in (B) and (C) are courtesy of Post-Doc Michael Gray.

thinner (~100 µm) than the acoustic wavelength in water enclosed with a custom polydimethylsiloxane (PDMS) lid (~1.2 mm thick). Characterization of the acoustical properties of the PDMS lid has been described in detail by Carugo et al.[30]. The ultrasound transducer was driven by a 1 MHz sinusoidal signal from a function generator passed through a 1.9 MHz low-pass filter and amplified 55 dB by a radiofrequency amplifier (E&I 1040L).

2.3.4.4. Acoustic emissions monitoring with the SAT2

Acoustic emissions monitoring during sonoporation was achieved using a passive cavitation detector (PCD) (V320 Panametrics, Olympus), which allowed for characterization of inter-sample variability and any differences in washed and unwashed 18:0 PC-PEG40S MBs with regard to cavitation dynamics. The digital oscilloscope (Handyscope HS3), and hence the PCD, was triggered with the function generator. The PCD was passed through a 2.0 MHz high-pass filter, pre-amplified 5x (Stanford Research Systems), and sent through a 50 Ω coupler. For each recorded voltage trace from the PCD, a fast Fourier transform (FFT) was computed using the number of points recorded rounded to the next power of two. Prior to FFT calculation, the voltage sample was truncated in the time domain to include only the portion with cavitation noise and a Hanning window was applied to the voltage trace to reduce edge effects. The power spectral density was computed by dividing the FFT by the number of points, truncating to include half the number of points, and multiplying by the complex conjugate of the result. The power average was determined by averaging the power spectral densities for each recorded pulse. The harmonic and ultraharmonic powers were determined by integrating the power spectral density with respect to frequency over 30 kHz bands at each harmonic and ultraharmonic from 3 to 8 MHz. The broadband power was determined by integrating the power spectral density with

respect to frequency over the remaining frequencies from 3 to 8 MHz. The energy of acoustic emissions was calculated by integrating the power with respect to time.

2.3.4.5. Exposure of cells to MBs and ultrasound with the SAT2

For the sonoporation experiments, an Ibidi µ-Dish with adherent cells was enclosed by a thin PDMS lid designed for ultrasound exposure as described by Carugo et al.[30]. A 10 ml solution of unwashed or washed MBs (5.5 x 10^7 MB/ml final concentration) and propidium iodide (40 µL at 10 mg/ml) prepared at 37°C was then injected through the acoustically-compatible PDMS lid, ensuring that there were no bubbles were trapped in the µ-Dish. The inlet and outlet of the PDMS lid were subsequently plugged using 1.4 mm diameter plastic rods. The µ-Dish was then inverted to increase microbubble-cell proximity, transferred into the water tank setup filled with filtered, distilled, deionised, and degassed water at 37°C, and exposed to 15 s of ultrasound at 1MHz, 0.125 MPa PNP with a 10% duty cycle and 1 kHz PRF, during which acoustic emissions monitoring was performed. Upon removal from the water tank, the acoustically-compatible lid was removed from the µ-Dish, the cells were washed twice times with PBS and incubated at 37°C with calcein-AM (5 µM) for five minutes prior to imaging. Propidium iodide and calcein staining were evaluated using fluorescence microscopy with multipoint scanning to account for area effects, e.g. from inhomogeneity of the ultrasound field or cavitation microstreaming events. The experimental timeline is illustrated in Figure 1D.

The ultrasound driving frequency was chosen as 1 MHz in the present study for several reasons. As described in Chapter 1, 1 MHz is close to the resonant frequency of a sub-population of the microbubbles employed in the present study, which were observed to increase in size at 37°C (see Figure 3) and upon ultrasound exposure (e.g. from coalescence[29]). When microbubbles are excited close to their resonant frequency, those effects which have been hypothesized to drive ultrasound-mediated drug delivery are enhanced (e.g. shear stress, fluid mixing, lipid shedding etc.). This is especially relevant

considering that the pressure amplitudes employed in the present study fall within the lower range of those successfully employed in the ultrasound-mediated drug delivery canon, and exciting further from resonance would result in lower amplitudes of oscillation and correspondingly less biological effects. Indeed, 1 MHz is the most commonly employed sonoporation frequency in the literature with pressure amplitudes typically ranging from ~0.10-1.00 MPa PNP, burst length from several microseconds to many milliseconds, PRFs from ~1-1000 Hz, and exposure durations from microseconds (e.g. single pulse) to minutes[21,31,32]. Higher frequencies such as 2 and 5 MHz have also been employed in sonoporation experiments[33], although these frequencies are more susceptible to attenuation if employed *in vivo* with a deep target region. Lower frequencies, such as 0.5 MHz[33], have been investigated as well, although more commonly for blood-brain barrier opening to facilitate the generation of the requisite ultrasound field through the intact skull[34].

2.3.5. Observing material transfer between cells and MBs

Material transfer between the MB shell and cell membrane was qualitatively assessed by confocal fluorescence microscopy. For this purpose, MBs were labelled with the lipophilic dye, DiI, whilst cells were labelled using CellMask Deep Red (Life Technologies) diluted 1:100 in PBS and incubated for 10 min in the µLAR. The medium was gently replaced with fresh PBS prior to imaging, and cells were kept at 37°C using the temperature-controlled chamber of the confocal microscope for the duration of the experiments.

Experiments were conducted using 18:0 PC-PEG40S 9:1, 18:0 PC, and 22:0 PC MBs, with and without ultrasound exposure. Prior to adding MBs, the excitation laser power (<1.5%) and gain (750) were set such that minimal fluorescence signal from the DiI

channel was observed. The medium was then replaced by the MB suspension. For experiments involving acoustic stimulation, ultrasound was applied immediately after adding the MBs. Following the incubation period, residual suspended MBs and shell fragments were washed away with PBS at a flow rate of 0.9 mL/min for 5 min. After washing, final fluorescent images were acquired. The experiment was repeated three times for each condition and additionally, images were taken with free DiI added to the medium with labelled cells. Colocalization of DiI and CellMask was confirmed by the Costes method using the Coloc2 plugin in ImageJ[36]. Three-dimensional colocalization maps were obtained using MATLAB. While DiI has been shown to orient in a lamellar phase parallel with phospholipids and to have a diffusion rate similar to that of 16:0 PC (a phospholipid of great abundance in cell membranes)[37], and as such has been employed for assessing lipid fluidity in cell membranes[49], DiI is not a phospholipid and was thus regarded as a tracer for material transfer, rather than for lipid-transfer specifically. Evidence for the transfer of lipids was supported by complementing observations of DiI-transfer with spectral imaging data, as described in the following sections.

2.3.6. Measuring cell membrane lipid order using spectral imaging

2.3.6.1. Introduction to spectral imaging for measuring lipid order

Changes in the lateral order of the lipids (revealing how densely the lipids are packed) due to exposure to ultrasound and/or MBs were quantified using C-Laurdan, an environmentally-sensitive fluorescent probe with similar spectral characteristics to Laurdan, but with greater photostability. The emission spectrum of Laurdan shifts as a function of the dipolar water relaxation, and thus the level of hydration within its surrounding microenvironment, which in turn is indicative of relative lipid packing[38].

C-Laurdan fluorescence emission spectra were measured for each pixel at 63X magnification by spectral imaging on a confocal microscope equipped with a 32-channel GaAsP detector array (Zeiss LSM 780, Carl Zeiss AG, Germany), following a method previously reported[39]. C-Laurdan was excited at 405 nm and the lambda detection range was set between 415 nm and 691 nm.

Generalized polarization (GP, ranging from −1 to 1) was employed as a relative measure of lipid order[40], and was calculated as follows:

$$GP = \frac{I_{440} - I_{490}}{I_{440} + I_{490}} \quad (1)$$

Where I_{440} and I_{490} correspond to the fluorescence intensity at 440 nm and 490 nm emission wavelengths, respectively. Notably, 440 nm corresponds to a blue emission in the wavelength spectrum and is associated with lower hydration and polarity, resulting in GP = +1 when only this wavelength is emitted. This indicates higher lipid order and means that lipids are in the gel-phase (ordered). Conversely, 490 nm corresponds to a red emission and is associated with greater hydration and polarity, resulting in GP = −1.

This indicates lower lipid order and prevalence of a liquid-crystalline phase (disordered, or less ordered).

The mechanism by which the C-Laurdan spectral shift occurs can be described as follows. When C-Laurdan molecules absorb excitation photons they gain energy, entering an excited state. The excited state dipole of C-Laurdan interacts with the surrounding solvent dipole (e.g. water in biological systems). The energy associated with this interaction results in a red-shift in the fluorescence emission spectrum that depends on the C-Laurdan dipole moment and the dielectric constant of the solvent, and is also time, temperature, and viscosity dependent. The relaxation time of C-Laurdan is slow in the gel phase (~7 ns) and fast in the liquid phase (~4 ns) of a lipid bilayer resulting in state-dependent mechanisms for the dye[40]. In the gel phase, there is time for the solvent molecules to reorganize following C-Laurdan excitation and the emission depends primarily on the dielectric property of the solvent[40]. In the liquid phase C-Laurdan emission spectrum shift depends more on the dissipation of energy into the surrounding solvent molecules rather than the reorientation of solvent dipoles[40]. For both mechanisms, the spectral shift of polarity-sensitive C-Laurdan embedded in biological membranes results from surrounding water molecules, providing a measure of local hydration. Owing to the strong lipid phase dependence of the C-Laurdan emission spectrum, the C-Laurdan generalised polarization (GP, a quantification of spectral shift) has been described as an indirect measure of lipid order. Furthermore, because an increase in water molecules around C-Laurdan in a biological context is commensurate with an increase in the area occupied per lipid, the C-Laurdan GP is also an indirect measure of lipid packing.

Having introduced the mechanism by which C-Laurdan is employed for measuring lipid order in cell membranes, several limitations of this probe are now discussed. C-Laurdan

is known to align parallel to the hydrophobic tails of phospholipids in biological membranes resulting in an orientation-dependent intensity shift called the photoselection effect. The excitation efficiency of C-Laurdan depends on the angle between the polarization plane of the exciting light and the electric transition moment of the molecule such that its efficiency is maximized when the transition moment is parallel to the polarization plane[40]. C-Laurdan thus exhibits fluorescence anisotropy such that the liquid phase may exhibit higher intensity than the gel phase owing to the ability of the probe to align with the polarization plane during excitation. The mid-plane of the nucleus was taken as the imaging plane for the adherent cells imaged throughout this thesis to minimize the influence of the photoselection effect on the experimental results. Additionally, by averaging 1000s of pixels from each cell membrane imaged such that an average GP value was taken which was effectively weighted by the distribution of the orientations of C-Laurdan within the membrane under study, this source of uncertainty was further minimized. As the influence of the photoselection effect is not expected to vary meaningfully across all conditions studied, relative changes in C-Laurdan GP across conditions are interpreted as changes in cell lipid order. It also bears mentioning that the presence of C-Laurdan can alter the measured GP if the concentration is too high. A range of concentrations were tested prior to experimentation and a concentration that resulted in no measured effect on the GP values of control cell membranes (400 nM) was employed throughout (data not shown).

2.3.6.2. Labelling cells with C-Laurdan for spectral imaging

For experiments, cells were washed with phosphate-buffered saline (PBS) twice and then exposed to MBs in PBS for ~90 s (see Figure 3A). The MB solution was then removed, cells were washed again with PBS, and labelled with 400 nM C-Laurdan in

PBS for ~1 min before imaging. Temperature control was achieved using the incubation chamber of the confocal microscope and verified using a thermocouple.

2.3.6.3. Spectral image processing

A custom image processing routine was developed in MATLAB for batch processing of spectral images with cell and cell membrane segmentation and outputs of pseudo-coloured GP maps, GP histograms, and sample statistics. This software, "The Spectral

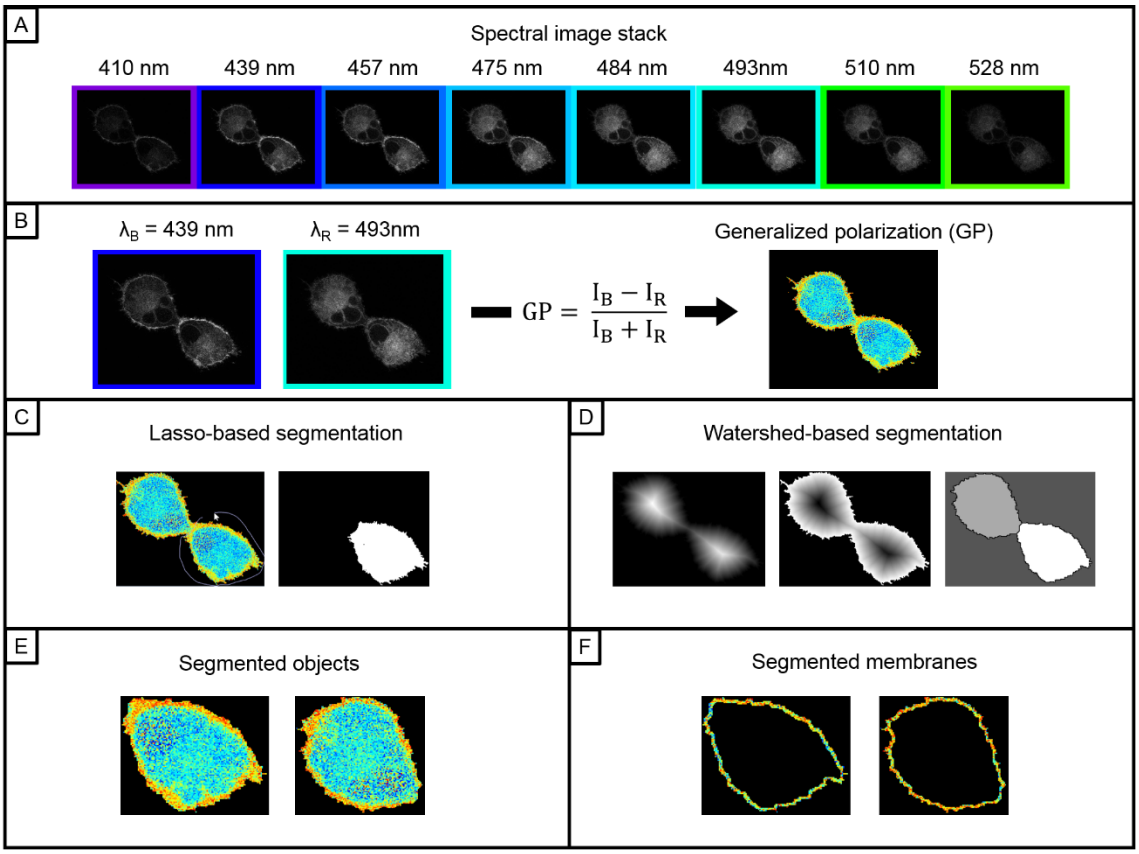

Figure 7: The Spectral Imaging Toolbox. A) An auto-thresholded spectral image stack containing images of C-Laurdan fluorescence emis-sion from labelled A-549 cells collected at wavelengths ranging from 410-528 nm. B) Generalized polarization (GP) is then calculated at each pixel using the intensities (IB and IR) from the images collected at λ_B and λ_R (left) using the equation (center). Pseudocolored GP maps can then be generated (right, color bar same as Figure 2). C) Segmentation can then performed on the GP maps using lasso-based segmentation, where the user draws a region-of-interest (ROI) (left) used to generate a segmentation mask (right). D) Segmentation can alternately be performed using a watershed-based approach. From left to right in, the distance transform, the negated distance transform, and the labelled components following the watershed transform. E) Either segmentation routine will result in the segmented objects. F) From the segmented objects, a given number of border pixels are taken as the segmented membranes.

Imaging Toolbox", was published in *BMC Bioinformatics* in 2017 and open-sourced (see graphical methods in Figure 7)[41].

For initial experiments employing the μLAR, a ΔGP value was determined for cells in experiments by imaging the same cells before and after exposure. Before and after spectral images were acquired to account for cell-to-cell variation in the sample. In later experiments with the Ibidi μ-Slides, an average GP value was taken for samples only after treatment which enabled greater experimental throughput with less experimental complexity, although potentially more sensitive to intercellular variation.

2.3.7. Sonoporation assessment

To evaluate the impact of MB-mediated membrane modulation on sonoporation, the sonoporation efficiency of a membrane-modulating MB (e.g. with PEG40S emulsifier) versus an acoustically-equivalent, non-membrane-modulating MB (e.g. washed of lipid and emulsifier not associated with MBs) was measured (see Figure 1D).

Propidium iodide and calcein-AM were used to label permeabilized and non-permeabilized cells as an end-point in sonoporation experiments. Propidium iodide, which fluoresces brightly upon binding DNA, cannot permeate the intact cell membrane, and thus was employed to label permeabilized cells. While propidium iodide is conventionally used to indicate cell death, this is not accurate in sonoporation experiments where cells can be permeabilized such that they take up propidium iodide without actually dying. Calcein-AM is non-fluorescent and cell permeant. Inside a living cell, calcein-AM is converted to fluorescent calcein by intracellular esterases. In permeabilized cells, calcein-AM can be converted to calcein by remaining intracellular esterases but will diffuse out of the cell through the compromised cell membrane resulting in a punctate rather than a diffuse staining. In addition, it is not clear when a

cell killed by sonoporation would cease to be labelled with calcein (e.g. when intracellular esterases cease to be produced and are sufficiently absent in the cytosol). Calcein-AM was thus employed in the present study specifically to measure cell count for the calculation of permeabilization. In summary, calcein-AM and propidium iodide were employed to determine the percentage of cells permeabilized only, and provide no information regarding cell viability in the present study.

The leakage of calcein from permeabilized cells may contribute an imaging artifact since less pixels are counted and thus the cell count may be lower, increasing the percentage of permeabilized cells detected. Similarly, in severely damaged cells, the nuclear material stained by propidium iodide may leak out of the cells, reducing fluorescence intensity, potentially below the limit of detection. The narrow range of cell densities measured across all experimental conditions however suggests that such sources of uncertainty were inconsequential. In addition, the negligible permeabilization observed in control cells demonstrates that the fluorescent probes were not a factor in cell permeabilization.

2.3.8. Comparison of experimental conditions

In the current study, separate devices were employed for microscopy and ultrasound experiments (µ-LARs, Ibidi µ-Slides and Ibidi µ-Dishes, see Table 4). While the MB-to-cell ratio (~6 MB/cell) was maintained for ultrasound experiments, the MB-to-cell ratio was much higher (>100 MB/cell) for the microscopy study employing 8-well µ-Slides. This difference arises from the differences in cell growth area and medium volume whereby equivalent MB volume concentrations were employed rather than MB-to-cell ratios. The heights of the µ-LAR, µ-Dish, and µ-Slide (0.25 mm, 12 mm, and 0.3 mm respectively) and cell orientations (see Table 4) may also impact the local MB-to-

cell ratio whereby MBs float toward cells in the µ-Dish and away from cells in the µ-LAR and µ-Slide.

Experimental device	Investigation	Volume (~µL)	Growth area (~mm²)	Height (~mm)	Cell orientation	MB/ml	MB/cell
µ-LAR 	Effect of ultrasound and microbubbles on cell lipid order (*Biomaterials* paper)	200	960	0.25	bottom	$3.1x10^7$	6
µ-Dish (Ibidi) + SonoLid 	Role of microbubble-mediated cell lipid disordering in sonoporation	10000	780	12	top	$5.5x10^7$	6
8-well µ-Slide (Ibidi) 	Role of temperature and washing on the effects of laboratory and clinical microbubbles on cell lipid order	250	100	0.3	bottom	$5.5x10^7$	110

Table 4: Comparison of experimental devices for cell lipid order studies with regard to confinement and microbubble-to-cell ratios. In rows from top to bottom the µ-LAR, µ-Dish (Ibidi) with the acoustically-compatible lid (SonoLid), and 8-well µ-Slide (Ibidi) are described respectively. Properties detailed include from left to right, a cartoon or image of the experimental device (µ-Dish and µ-Slide images are from Ibidi), the investigation the device was employed in, the volume of fluid, cell growth area, height of fluid, cell orientation, microbubble concentration, and microbubble-to-cell ratio respectively.

2.3.9. Statistical analysis

For statistical analysis of the experiments with CHO-K1 cells, one-way analysis of variance (ANOVA) was employed. For the experiments with A-549 cells conducted in the µLAR, a three-way ANOVA was employed with PEG40S concentration, lipid chain length, and ultrasound exposure as factors. A three-way ANOVA was also performed for experiments with A-549 cells conducted in the µ-Slides using MB formulation, temperature, and washing as factors. A two-way ANOVA with MB formulation and ultrasound exposure as factors was employed for analysis of the sonoporation results. All ANOVAs with alpha values below 0.05 were followed with multiple comparisons using Tukey-Kramer tests (significant for $p < 0.01$).

2.4. Results

2.4.1. Molecular transfer from MBs to cell membranes

Material transfer from 18:0 PC-PEG40S, 18:0 PC, and 22:0 PC MBs to A-549 cells with and without ultrasound exposure was investigated using confocal fluorescence microscopy. A green fluorescent membrane probe (DiI) was employed to stain the MBs and to indicate material transfer from the MBs, and a red fluorescent membrane stain (CellMask) was employed to mark the cellular plasma membrane (Figure 8). The fluorescence images highlight that following ultrasound exposure, DiI was transferred to the cellular membranes for all three MB formulations, with a diffuse pattern for 18:0 PC-PEG40S (suggesting integration within the membrane) (Figure 8D) and a punctate pattern for 18:0 PC and 22:0 PC (indicative of the formation of vesicles or aggregates that appear to associate with the membrane) (Figure 8E-F). Without ultrasound exposure, significant DiI transfer was observed for 18:0 PC MBs (in form of vesicles), but not for 18:0 PC-PEG40S and 22:0 PC MBs. Three-dimensional Costes' method colocalization of DiI and CellMask from a confocal z-stack, demonstrates that DiI was extensively colocalized with cell membranes for the case of 18:0 PC-PEG40S MB and

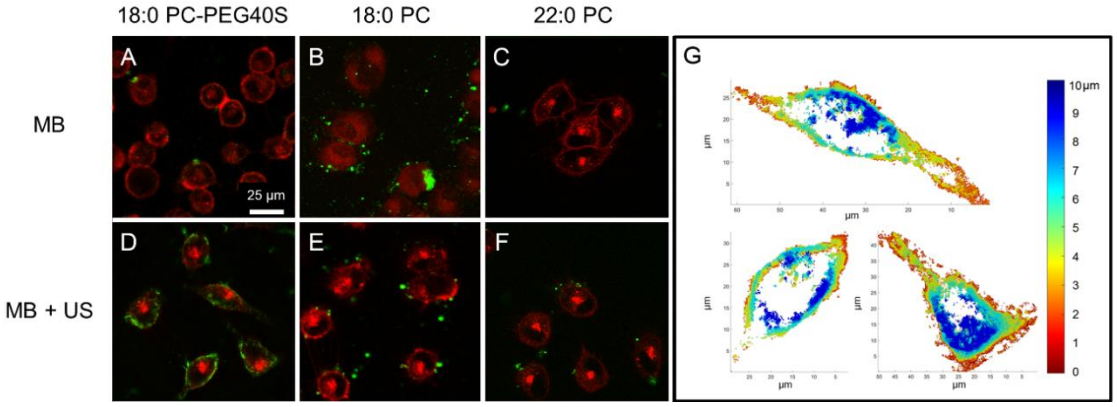

Figure 8: Observations of the transfer of DiI from microbubbles to cells by fluorescence microscopy. (A)-(F): Representative composite images of transfer from DiI-loaded 18:0 PC-PEG40S, 18:0 PC, and 22:0 PC MBs (DiI, green) to A-549 cells (CellMask, red), with and without ultrasound (ultrasound). Panels A, B, D, and E were acquired with a 20x microscope objective and panels C and F were acquired with a 63x objective. The scale bar applies for all images. (G): Three-dimensional map of Costes' colocalization of DiI and CellMask from a confocal z-stack (1 µm slice thickness) of the same cells in (D). The color bar indicates distance from the substrate in microns.

ultrasound exposure (Figure 8G).

2.4.2. Effects of ultrasound and MB exposure on cell membrane lipid order measured by spectral imaging in the μLAR

2.4.2.1. The role of PEG40S

To evaluate the effect of the molar ratio of 18:0 PC to PEG40S in the MB formulation on lipid order in A-549 cells, the cells were exposed to MB of molar ratio 9:1, 90:1 and 1:0 (18:0 PC only MBs) with and without ultrasound exposure respectively, and to sonicated PEG40S (no MBs). The presence of PEG40S in all cases significantly decreased lipid order ($\Delta GP = -0.035 \pm 0.050$, $\Delta GP = -0.035 \pm 0.075$, and $\Delta GP = -0.157 \pm 0.076$ for cells exposed to MB with a 9:1 or 90:1 molar ratio or to sonicated

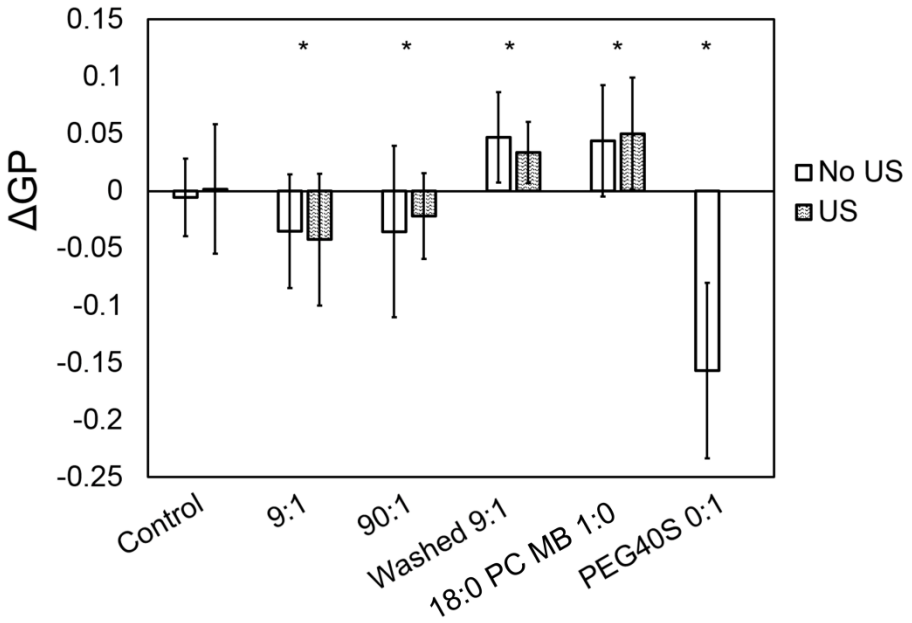

Figure 9: Effects of DSPC-PEG40S molar ratio on C-Laurdan generalized polarization (ΔGP) in A-549 cell membranes. A-549 cells were exposed to a PBS sham (control), and MB with DSPC-PEG40S molar ratios of 9:1 (with and without washing by centrifugation), 90:1, and 1:0 (DSPC only), with and without ultrasound. Cells were also exposed to sonicated PEG40S (0:1 molar ratio). ΔGP < 0 or ΔGP > 0 signify a decrease or increase in membrane lipid order, respectively. Over the course of 3 independent experiments per condition, 373 cell membranes were analyzed before and after exposure. Statistical significance indicated by * for $p < 0.01$ as compared to the control.

PEG40S respectively, $p < 0.01$) (see Figures 9). Conversely, 18:0 PC MB without PEG40S (1:0 molar ratio) were found to significantly increase lipid order in A-549 cell membranes ($\Delta GP = 0.050 \pm 0.049$ and $\Delta GP = 0.044 \pm 0.049$ with and without ultrasound exposure respectively, $p < 0.01$). Representative GP maps of cell membranes for these experiments are presented in Figure 10.

Since lowering PEG40S concentration by an order of magnitude had no significant effect on the induced membrane disordering in A-549 cells, the effect of washing 18:0 PC-PEG40S 9:1 MB by centrifugation (in an attempt to reduce levels of PEG40S in solution) was investigated. It was found that in contrast to the unwashed case, washed MB increased lipid order in A-549 cell membranes ($\Delta GP = 0.034 \pm 0.027$ and $\Delta GP = 0.047 \pm 0.039$ with and without ultrasound respectively, compared with $\Delta GP = -0.042 \pm 0.057$ and $\Delta GP = -0.035 \pm 0.050$ for the unwashed case, $p < 0.01$).

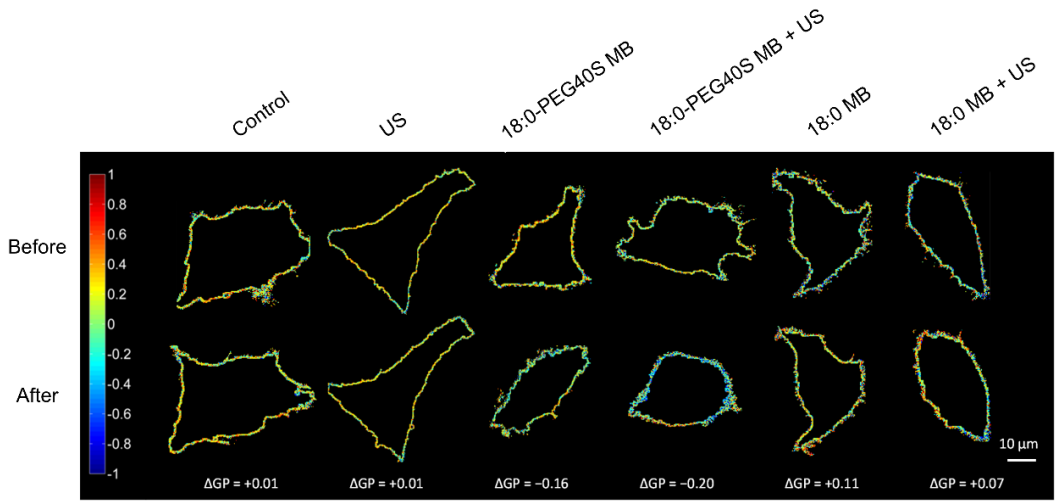

Figure 10: Representative pseudo-coloured membrane generalized polarization (GP) maps of A-549 cell membranes before (top) and after (bottom) exposure to a PBS sham (control), ultrasound (ultrasound), and 18:0 PC or 18:0 PC-PEG40S MBs with and without ultrasound respectively. The change in GP ($\Delta GP = GP_{after} - GP_{before}$) for each representative specimen is reported below its corresponding membrane GP map.

2.4.2.2. The influence of hydrocarbon chain length

Membrane lipid order depends on, among other factors, the hydrocarbon chain length of the lipids from which it is comprised. Therefore the effect of lipid chain length in the MB formulation upon the resultant changes in lipid order of A-549 cell membranes was investigated. Since, as above, PEG40S had a strong effect on membrane lipid order even at low concentrations, the use of PEG40S was avoided in these experiments. It was found, however, that lipids with chain lengths lower than 18:0 would not readily form stable microbubbles in the absence of PEG40S. Thus, only MBs composed of 18:0 PC and 22:0 PC were investigated, with and without ultrasound exposure. It was found that while exposure to 18:0 PC MBs significantly increased lipid order, exposure to 22:0 PC MBs did not have a significant effect ($\Delta GP = -0.023 \pm 0.050$ and $\Delta GP = -0.005 \pm 0.044$ for 22:0 PC MBs with or without ultrasound exposure respectively, $p >$

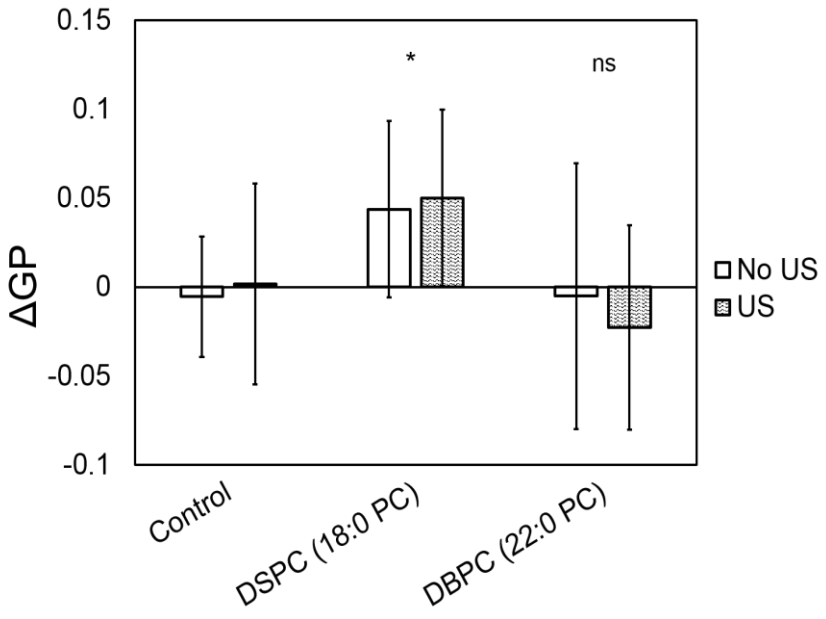

Figure 11: Effects of MB of different lipid chain lengths on C-Laurdan generalized polarization (ΔGP) in A-549 cell membranes. A-549 cells were exposed to a PBS sham (control), 18:0 PC MB, and 22:0 PC MB with and without ultrasound (ultrasound). Over the course of 3 independent experiments per condition, 258 cell membranes were analyzed before and after exposure. Bars and error bars indicate mean ± standard deviation ΔGP. Statistical significance (*) is indicated for $p < 0.01$ compared to the control.

0.01) (see Figure 11).

2.4.2.3. Observations in different cell lines

To determine whether the aforementioned effects are specific to A-549 cells only, repeated measurements of changes in lipid order after lipid transfer from MBs in ovarian hamster (CHO-K1) cells were carried out. Again, a significant decrease in cell membrane lipid order was found following exposure to 18:0 PC-PEG40S 9:1 MBs with and without ultrasound ($\Delta GP = -0.035 \pm 0.048$ and $\Delta GP = -0.010 \pm 0.050$ respectively, $p < 0.01$) (see Figure 12), which is in agreement with observations for the same experimental conditions in A-549 cells.

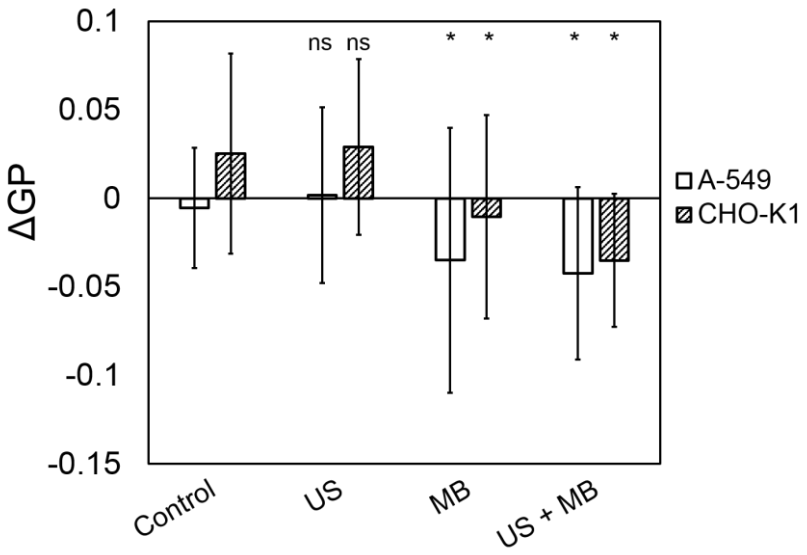

Figure 12: Effects of DSPC-PEG40S 9:1 MB on C-Laurdan generalized polarization (ΔGP) in A-549 and CHO-K1 cell membranes. A-549 and CHO-K1 cells were exposed to a PBS sham (control), ultrasound, MB, and MB with ultrasound. Over the course of 3 independent experiments per condition, 156 A-549 cell membranes and 225 CHO-K1 cell membranes were analyzed before and after exposure. Bars and error bars indicate mean ± standard deviation ΔGP. Statistical significance (*) indicated for $p < 0.01$ as compared to the respective controls for each cell line.

2.4.2.4. The role of MB formulation in MB-mediated alteration of cell membrane lipid order

The effects of 18:0 PC-PEG40S, 22:0 PC-PEG40S, and SonoVue® MB on cell lipid order were evaluated using spectral imaging with C-Laurdan. In preparation for sonoporation experiments, the roles of temperature (22°C and 37°C) and MB washing (e.g. removal of free lipid and emulsifier) as factors in cell lipid order modulation, were also investigated. These experiments, which did not require ultrasound exposure, were conducted using 8-well chamber slides (µSlides, Ibidi), enabling greater experimental throughput. Furthermore, only the post-treatment lipid order was measured unlike in previous experiments where before and after spectral images were collected for each cell. In addition to assessing cell membrane lipid order, the whole cell was processed to

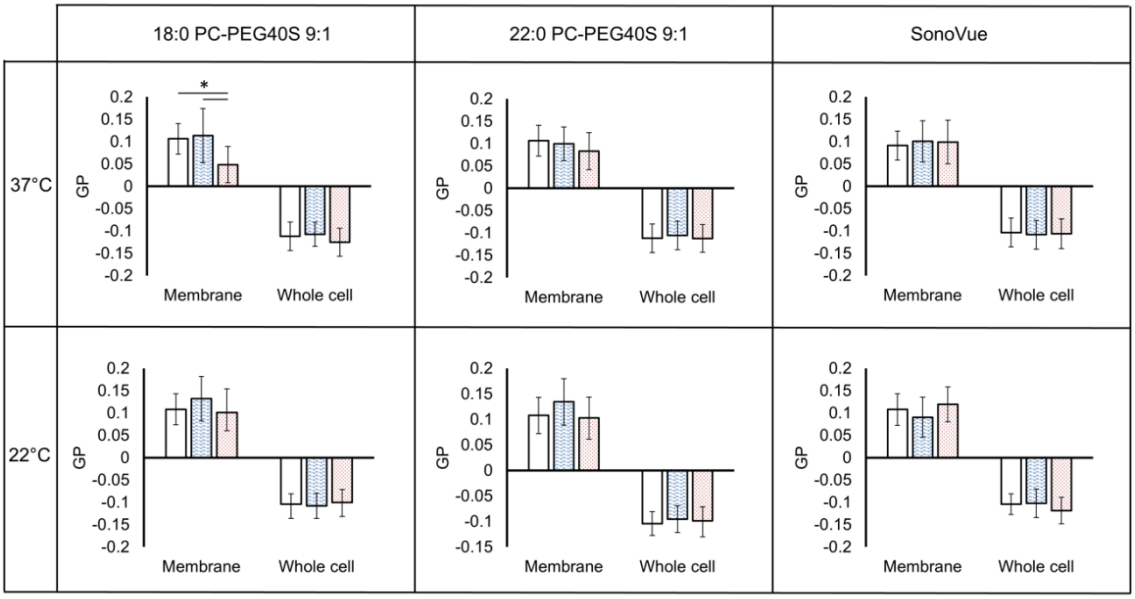

Figure 13: Effect of microbubbles on A-549 cell membrane and intracellular lipid order (GP). Microbubbles tested include (A) 18:0 PC-PEG40S, (B) 22:0 PC-PEG40S, and (C) SonoVue® with and without washing by centrifugation at RT and 37°C respectively. The only statistically significant result ($p < 0.01$, $n = 6$) is from standard 18:0 PC-PEG40S MB at 37°C which reduced cell membrane lipid order. A three-way ANOVA was performed using microbubble formulation, temperature, and washing as factors with an alpha value of 0.05, followed by a Bonferroni post-hoc multiple comparisons test.

determine if intracellular lipid order was also modulated by MB exposure.

In agreement with preliminary results in the µLAR, 18:0 PC-PEG40S MB were found to lower the lipid order of cell membranes (see Figure 13). This effect was observed to be temperature dependent, occurring at 37°C but not at 22°C. As previously found in the µLAR, the cell lipid disordering effect was inhibited by the removal of free lipid and emulsifier from the MB solution by washing. Contrary to previous experimental results with the µLAR, however, cell membrane lipid order was not observed to increase following exposure to washed 18:0 PC-PEG40S MB. This can be attributed either to differences in local MB-to-cell ratios between experiments (see Methods) or to differences in the sensitivities of the methods employed (e.g. pre- and post-treatment images collected in the µLAR experiments may enable greater sensitivity). Interestingly, neither SonoVue® nor 22:0 PC-PEG40S MBs had a significant effect on cell membrane lipid order at either 22°C or 37°C, with or without washing.

In summation, only one formulation, 18:0 PC-PEG40S, was found to have a significant effect on cell lipid order in the absence of externally applied stimuli, at concentrations relevant for *in vitro* drug delivery experiments. Consequently, the impact of cell membrane hydration and lipid disordering by 18:0 PC-PEG40S MBs on sonoporation efficiency was subsequently evaluated.

2.4.2.5. The effect of washing MBs on acoustic emissions

Because both washed and unwashed formulations were prepared with PEG40S, and the MBs were concentration matched and had equivalent size distributions at 37°C (see Figure 3D-F), the washed and unwashed MBs were expected to exhibit similar acoustic behaviour. This expectation was supported by evidence from Longo and colleagues demonstrating that PEG40S is largely squeezed out of the MB shell for 18:0 PC-

PEG40S MB[42,43]. Differences in acoustic properties arising from differences in MB stability, e.g. owing to the presence of PEG40S which provide steric hindrance and acts as an emulsifier, however, could not be excluded. Thus, the acoustic emissions for both washed and unwashed MBs were recorded from each sonoporated sample.

The power spectra of the acoustic emissions from both washed and unwashed MBs revealed significant harmonic and ultra-harmonic emissions with no evidence of broadband noise (see Figures 14C-D). It can be seen that negligible PCD signal is detected in the absence of microbubbles (see Figure 14C). By the design of the SAT2, the ultrasound transducer is opposite an acoustic absorber, and the PCD is set at an oblique angle, such that the PCD receives very little ultrasound energy from the transducer compared to that re-radiated by cavitating microbubbles. This suggests a primarily non-inertial cavitation regime which is desirable for achieving sonoporation

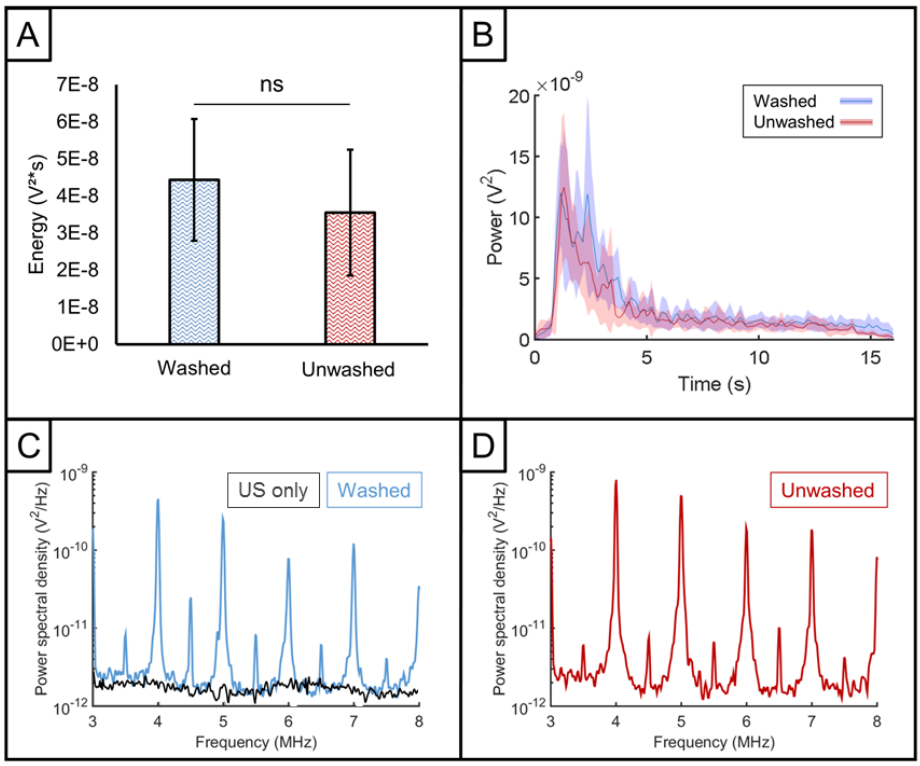

Figure 14: Acoustic emissions from sonoporation experiments. The harmonic energy (A), power vs time (shown with mean and 95% CI) (B), the power spectral density of ultrasound only (C), washed MB (C) and standard MB (D). No statistically significant differences are evident in (A) or (B) (n = 7).

without causing excessive cell death[33].

The mean energies of harmonic acoustic emissions from washed and standard MBs were not statistically different ($P > 0.05$) (see Figure 14A). The mean powers of harmonic acoustic emissions from washed and standard MBs were also not statistically different at any time point (averaged for each pulse) throughout the ultrasound exposure (see Figure 14B).

2.4.3. Sonoporation at 37°C

Sonoporation with unwashed and washed MBs resulted in 6.15 ± 3.48% and 6.62 ± 3.50% cell permeabilization respectively (see Figure 15). No correlations between cell density or acoustic emissions and cell permeabilization from sonoporation were found, indicating that any differences in the results should not be attributed to these factors. Thus, the cell membrane lipid disordering achieved by 18:0 PC-PEG40S MBs did not

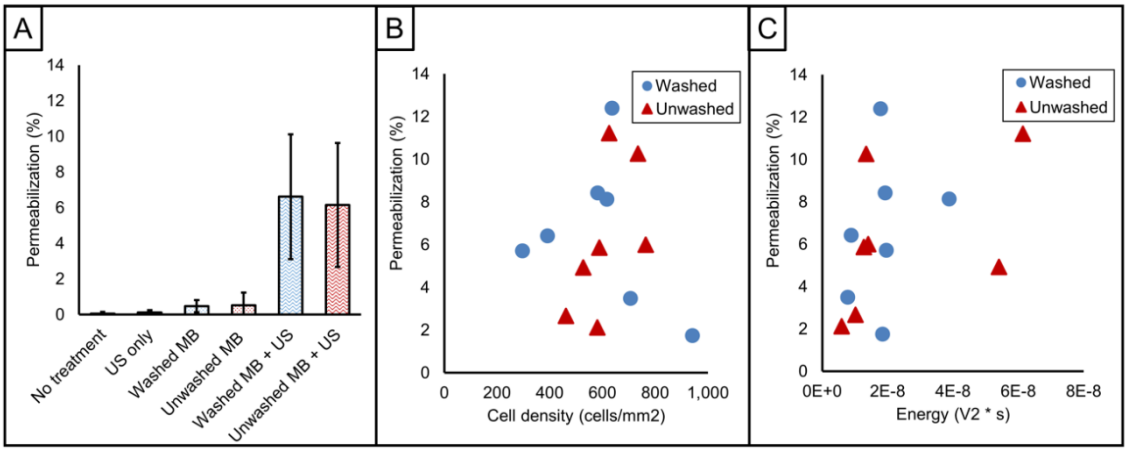

Figure 15: Effect of washing on 18:0 PC-PEG40S permeabilization efficiency. Permeabilization (defined as the percentage of cells imaged that show Propidium Iodide uptake) for controls (no treatment, ultrasound (ultrasound) only, and washed or unwashed MBs only) as well as treatment conditions (washed or unwashed MBs exposed to ultrasound) are shown in (A). (B) and (C) demonstrate no correlation between either the cell density or the harmonic acoustic emissions and the resultant permeabilization. In (B) and (C) each point is an independent sample. Blue circles represent samples sonoporated with washed MBs and red triangles represent samples sonoporated with unwashed MBs. Controls are n = 3. MB + ultrasound conditions are n = 7.

appear to play a significant role in sonoporation in these experiments.

The morphology of permeabilized and non-permeabilized cells, as demonstrated in Figure 16, did not qualitatively differ between samples exposed to washed or unwashed MBs. Non-permeabilized cells appeared healthy, fluoresced brightly with calcein, and appeared stretched out on the underlying substrate in the same manner as observed for cells in control samples. The permeabilized cells, however, appeared more rounded, which may suggest irreversible sonoporation.

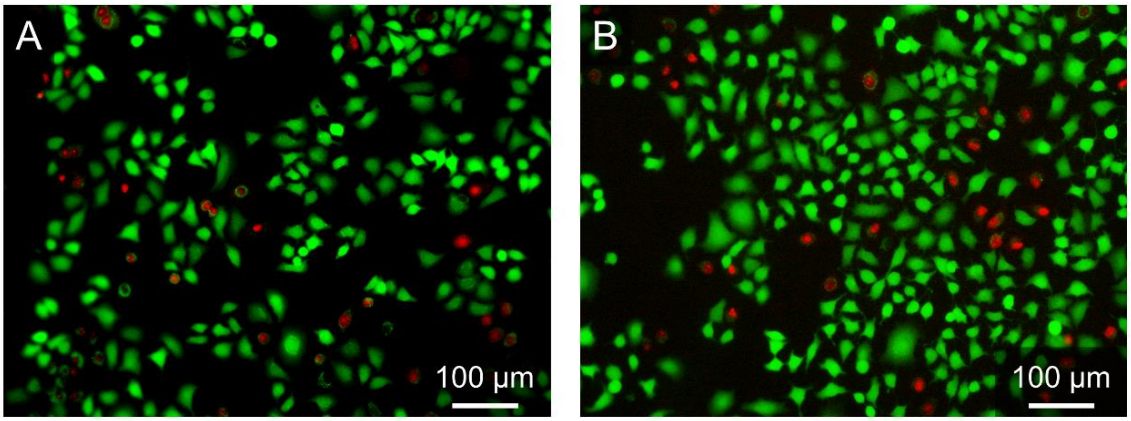

Figure 16: Representative fluorescence microscopy images of cells exposed to ultrasound and MBs. The cells in (A) were exposed to unwashed 18:0 PC-PEG40S MBs. The cells in (B) were exposed to 18:0 PC-PEG40S MBs washed by centrifugation. Propidium Iodide (red) indicates permeabilization. Those cells that are not stained with Propidium Iodide that also exhibit Calcein fluorescence (green) from calcein-AM staining, were not permeabilized. No differences were apparent in the permeabilization or morphology of the cells across the two conditions of interest.

2.5. Discussion

In the discussion that follows, insights from the present study are presented with support from parallel studies conducted at the University of Oxford BUBBL group and evidence from the literature. Strong evidence for the transfer of material from MBs to cell membranes is presented. It is shown that aspects of MB formulation (e.g. hydrocarbon chain length of the carrier lipid, emulsifier concentration, and chemical

species) influence the resultant effect on cell membrane physicochemical properties and material transfer, which has direct consequences for ultrasound-mediated drug delivery.

By considering the mechanisms governing the effects of MBs and ultrasound on cell membrane lipids, it was hypothesized that MB-mediated cell membrane lipid disordering enhances sonoporation. MB-mediated effects on cell membrane lipids with the MBs tested, however, were either negligible (22:0 PC-PEG40S MB and SonoVue) or were, surprisingly, not a significant factor in sonoporation (18:0 PC-PEG40S MB). The properties of MB-compatible lipids that may have a more significant impact on sonoporation are discussed with regard to the results of the present study and the chapters that follow.

2.5.1. Lipid transfer

2.5.1.1. Evidence for material transfer

Direct transfer of therapeutics from the MB shell to cellular membranes via MB-cell fusion, MB destruction, and/or lipid shedding, is a candidate mechanism for the enhancement of ultrasound-mediated drug delivery produced by phospholipid-coated MBs[15,18,19]. In this chapter, DiI, a lipophilic dye with molecular dynamics comparable to those of lipids[37], was used as a means of visualizing material transfer from MBs to cells. Exposure of cells to washed DiI-loaded MBs comprised of 18:0 PC-PEG40S and ultrasound resulted in a diffuse DiI staining of the cell membrane, confirmed by Costes' colocalization of DiI and a cell membrane label (CellMask). Interestingly, this diffuse staining of MB shell material in cell membranes was not observed for DiI-loaded 18:0 PC or 22:0 PC MBs (e.g. MBs prepared without the emulsifier PEG40S). Instead, these PEG40S-free formulations produced a punctate staining around cell membranes indicative of the association of liposomes or micelles with the cell membrane. The

observations of the present study are in agreement with the punctate staining observed by De Cock et al. from ultrasound-mediated deposition of cationic liposomes and polymer microspheres from MBs to cell membranes[44].

Furthermore, these results demonstrate that MB composition plays an important role in determining the transfer of molecules from MBs to cell membranes, which is also true of non-gas-filled vesicles[45]. Indeed MB material transfer may involve intermediary liposomal or micellar particles for material transfer. Such particles may come from lipid and emulsifier shed from the MB during ultrasound exposure[46], from lipid and

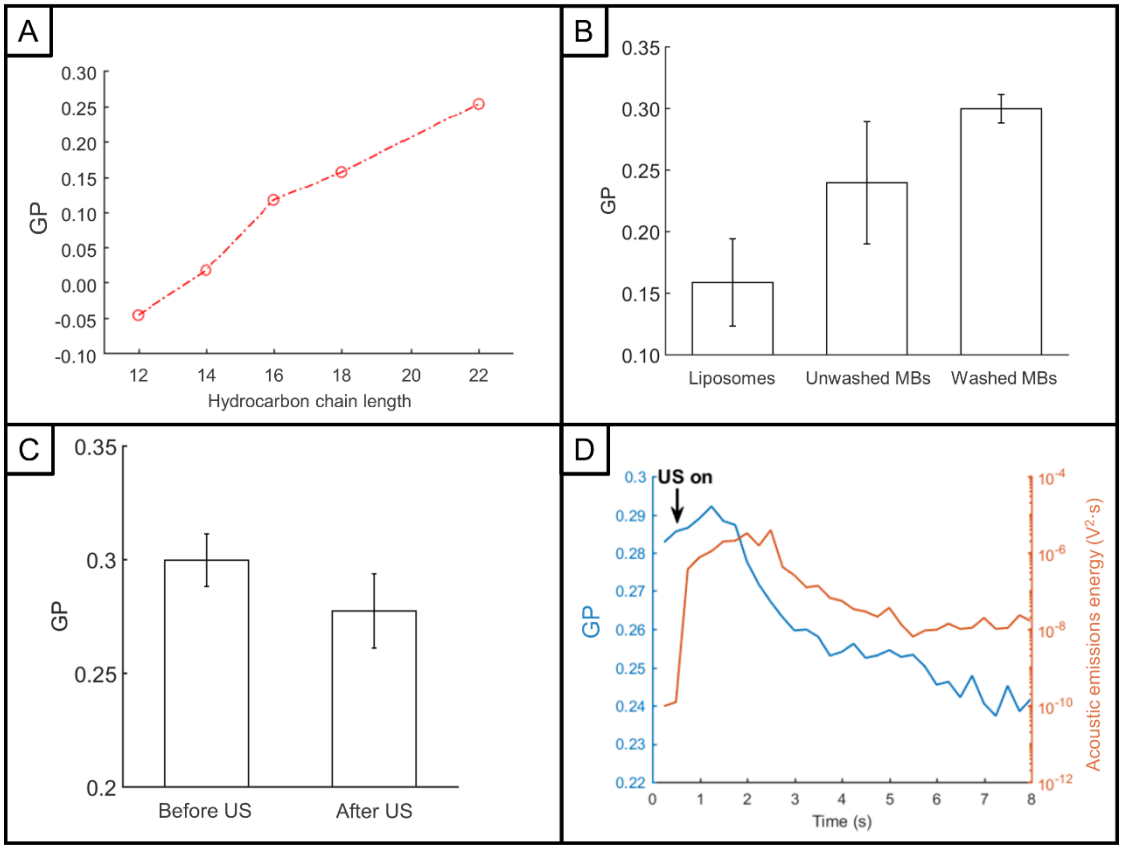

Figure 17: Effect of ultrasound exposure on MB suspensions. (A) Lipid order of lipid suspensions of varying hydrocarbon chain length as a system calibration. (B) The lipid order of MBs with and without washing compared to a lipid suspension of the same composition. (C) Ultrasound exposure resulted in significantly lower lipid order for washed MBs. (D) Dynamic GP measurement of the change in lipid order of the washed MBs as they were exposed to ultrasound. Data from the Master's Thesis of Anna Booth in preparation for publication.

emulsifier constructs in unwashed MB suspensions, or from lipoproteins in cell culture medium, for instance.

To this end, the temporally-resolved effect of ultrasound on the lipid order of MB suspensions was investigated in a parallel study employing photomultiplier tubes for high-speed fluorescence intensity measurements of C-Laurdan (see calibration in Figure 17A). These experiments were conducted by Ms. Anna Booth with direction from the author and Dr. Shamit Shrivastava. Full details of the setup and experiments can be found in Booth's Master's thesis. It was found that MBs have higher lipid order than non-gas-filled vesicles (e.g. micelles and liposomes) prepared with the same formulation (see Figure 17B), a finding that was confirmed for a multitude of phosopholipid-shelled MB formulations by Dr. Richard Browning (*paper in preparation*). Dynamic GP experiments revealed that when exposed to ultrasound, MBs are destroyed (indicated by the reduction in acoustic emissions, see Figure 17D), and the lipid order of the MB suspension is decreased (indicated by dynamic GP measurements, see Figure 17C-D), as they form a micellar and liposomal suspension (confirmed by live microscopy, data not shown). It follows that when MBs are destroyed, they re-assume the lipid thermal properties of their constituents which could be a critical factor in drug delivery, especially for drug-loaded MBs, and may play a role in the material transfer observed in the present study.

2.5.1.2. On the transfer of 18:0 PC from MBs to cells

In agreement with the direct visualization of material transfer from MBs to cells, significant changes in cell membrane lipid order following exposure to MBs were found. Exposures to 18:0 PC MBs or washed 18:0 PC-PEG40S MBs were found to increase cell membrane lipid order. While transfer of 18:0 PC from MBs to cell

membranes would explain these results[47], the measurable transfer of long-chain phosphatidylcholine (PC) lipids such as 18:0 PC, was not expected to occur so quickly[45]. Furthermore, washed 18:0 PC-PEG40S MBs increased lipid order in the µLAR but not in the µSlides, which could be attributed to differences in the sensitivity of the two experimental protocols (see Methods), but may point to more complex phenomena. Other molecules in the medium, for instance, may form intermediary constructs that facilitate the transfer of phospholipids from MBs to cells. The transfer of molecular species with sufficient solubility in the aqueous phase (e.g. cholesterol) from cells to MBs, in addition to residual lipoproteins in the medium after washing, may contribute to the increase in cell membrane lipid order. Nonetheless, this is the most compelling evidence for lipid transfer from MBs to cell membranes to the author's knowledge.

2.5.1.3. Lipid transfer depends on MB PC chain length

Exposure of cells to 22:0 PC MBs with longer hydrocarbon chains than 18:0 PC MBs, however, did not induce a significant change in lipid order in cell membranes. 22:0 PC MBs also resulted in punctate DiI fluorescence following ultrasound, and negligible fluorescence without ultrasound exposure. This suggests that it is energetically favourable for long-chained 22:0 PC lipids to stay in the MB shell or form liposomes, rather than integrating into cell membranes. This may be explained by the higher melting temperature of 22:0 PC (73.6 ± 2.1 °C) compared to 18:0 PC (54.5 ± 1.5 °C)[48], and the exponential relationship between lipid chain length and MB shell gas permeation resistance[40]. From a drug delivery perspective, these results suggest that 18:0 PC is better suited to transferring material to cell membranes than higher-ordered lipids.

2.5.2. MB-mediated modulation of cell membrane lipid order

2.5.2.1. Role of PEG40S

Including PEG40S in 18:0 PC MBs induced significant cell membrane lipid disordering within minutes of exposure. When the same formulation was loaded with DiI to observe material transfer from MBs to cells, negligible DiI was found associated with cell membranes in the absence of ultrasound exposure, unlike 18:0 PC MBs formed without PEG40S. It follows that 18:0 PC-PEG40S MBs do not appear to interact directly with cell membranes in the absence of ultrasound exposure, likely owing to steric hindrance provided by the PEG40S emulsifier. It follows that the presence of PEG40S in the 18:0 PC-PEG40S MB suspension plays a critical role in MB-mediated cell membrane lipid disordering, commensurate with enhanced DiI transfer to cell membranes under ultrasound exposure. The role of PEG40S is further supported by observations that washing 18:0 PC-PEG40S MBs, effectively removing free PEG40S and lipid constructs, inhibited the lipid disordering effect. Exposure of cells to PEG40S without MBs also significantly decreased lipid order, additionally supporting an important role for PEG40S. Mechanisms for the PEG40S-induced reduction in cell membrane lipid order may include membrane phospholipid hydration, conformational changes in membrane proteins, incorporation into the cell membrane, binding with membrane carbohydrates and proteins, facilitated transfer of lipids, or depletion of other chemical species from the cell membrane.

2.5.2.2. Cell lipid disordering by PEG40S depends on MB PC hydrocarbon chain length

22:0 PC-PEG40S MBs, which contains the same concentration of PEG40S as 18:0 PC-PEG40S MBs, but a longer PC chain length, did not significantly alter the lipid order of

A-549 cell membranes. This suggests that the interaction between PEG40S and 18:0 PC is responsible for the disordering of cell membrane lipids by 18:0 PC-PEG40S MB, rather than PEG40S alone.

Langmuir trough data kindly provided by Ms. Estelle Beguin, fellow DPhil student in the BUBBL group at the University of Oxford, reveals that PEG40S more readily forms stable constructs with 22:0 PC as opposed to 18:0 PC, which may explain this result (see Figure 18). This is indicated by the plateau in the Π-A isotherm near the collapse pressure for 22:0 PC-PEG40S when compared to 18:0 PC-PEG40S (see Figure 18A) and by the change in fluorescence in 22:0 PC-PEG40S with NBD-PEG (1%) from points A to B, C to D, and E to F in Figure 18B respectively. These data support that of Borden et al. which suggests that PEG40S is squeezed out of 18:0 PC-PEG40S MBs but not out of 22:0 PC-PEG40S MBs upon formation[42].

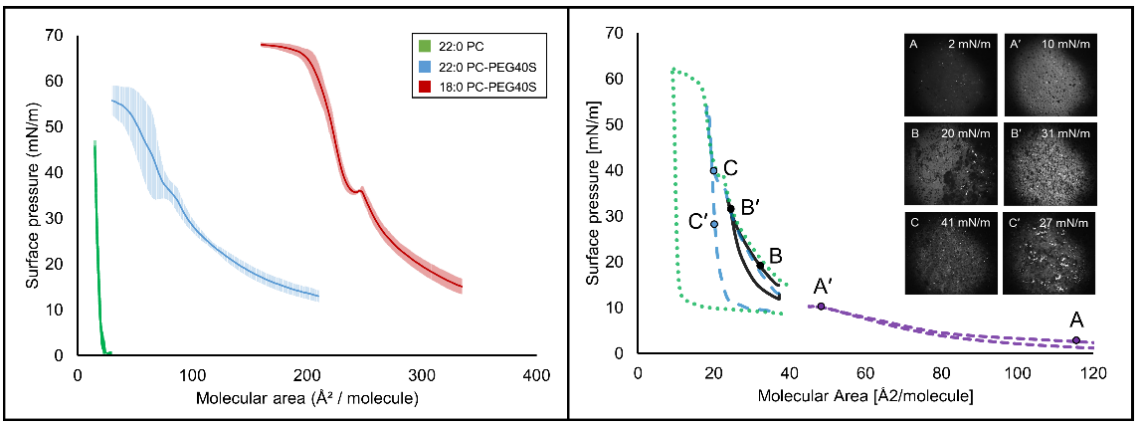

Figure 18: Π-A isotherms for the lipid-PEG40S microbubble formulations used in the present study (data courtesy of Estelle Beguin, Oxford University). Left: Π-A isotherms for 22:0 PC lipid only (green), 22:0 PC-PEG40S (blue), and 18:0 PC-PEG40S (red). Plot shows Π-A isotherms for compressions only with mean and standard deviation of 3 samples. The molecular area was not adjusted for concentration and is thus relative for each lipid but not across lipids. Right: Π-A isotherms for 22:0 PC-PEG40S + NBD-PE (1%). Each isotherm indicated by a different colour and dash-style represents a fresh sample that was compressed and expanded on the Langmuir trough. Right inset: fluorescence images of the 22:0 PC-PEG40S + NBD-PE (1%) monolayer at the points indicated by the labelled points on the Π-A isotherms.

2.5.2.3. PEG plus fatty acid vs. PEG-conjugated fatty acid in MBs

The complexity of the mechanism by which 18:0 PC-PEG40S MBs alters cell membrane lipid order is highlighted by the absence of such an effect from SonoVue®. SonoVue®, which has an excess of PEG-4000 (27.8 mM PEG), is prepared at ~31.5 µM palmitic acid compared to the laboratory formulations which employ ~400 µM PEG40S (e.g only ~344 µM PEG and ~56 µM stearic acid). The results of the present study suggest that PEG-conjugated fatty acid, PEG40S, may be more effective than free PEG (PEG4000) and free fatty acid (palmitic acid) at promoting microbubble-mediated alteration of cell membrane lipid order.

2.5.2.4. Role of temperature in the observed effects

It was found that the effect of 18:0 PC-PEG40S MB on cell membrane lipid order was statistically significant at 37°C but not at 22°C. The change in the phase behaviour of lipid-PEG mixtures between 22°C and 37°C is hypothesized to be the primary source of this difference. Transfer of lipid and emulsifier to cells is expected to increase at higher temperatures owing to the increase in the area per molecule in lipid-emulsifier constructs and in the desorption rate[42,49]. The temperature-dependant phase behaviour of lipid domains in the cell membranes is also expected to play a role in the observed effect.

2.5.3. The role of ultrasound in MB-mediated modulation of cell membrane lipid order

Upon ultrasound exposure, MBs can induce mechanical, chemical and thermal effects that were hypothesized to modulate cell membrane lipid order. Ultrasound and MB-mediated degradation of the actin cytoskeleton, opening of ion channels, formation of non-specific pores, generation of reactive oxygen species, and shear stress from

cavitation microstreaming, for instance, could conceivably contribute to such an effect[3,15,16,22,50–56]. Interestingly, despite our observations of clear effects of ultrasound and MBs in our setup (i.e., cavitation microstreaming, microbubble destruction, more diffuse DiI staining of cell membranes from DiI-loaded MBs), ultrasound was not a statistically significant factor in changing lipid order across all cases studied. It should be emphasized however that only a narrow set of ultrasound parameters were investigated. It is feasible that the role of ultrasound in MB-mediated modulation of cell membrane lipid order depends on factors not investigated such as the ultrasound frequency, pressure, and/or temporal parameters. In this section, supplementary data that help explain this result are presented.

2.5.3.1. Role of reactive oxygen species

Reactive oxygen species (ROS) that can affect phospholipid headgroups and damage cell membrane molecules have been reported to alter the lipid order of cell membranes[57]. It is also known that MBs exposed to ultrasound can generate ROS upon collapse. It follows that ROS from cavitation could alter cell membrane lipids. PhD student Estelle Beguin of the BUBBL group at the University of Oxford kindly shared a quantification of the ROS produced by 22:0 PC-PEG40S MBs under ultrasound exposure. 22:0 PC-PEG40S MBs, in this case produced with oxygen gas and decorated with a sonosensitizer (Rose Bengal) to amplify the ROS generated, were exposed to ultrasound at various pressures in degassed PBS. The resulting ROS was quantified using a fluorescent ROS sensor (SOSG, ThermoFisher). It was found that negligible ROS were generated, even with Rose Bengal present, at the pressures employed in the present study and throughout the thesis (data not shown). ROS can thus be excluded as a potential cavitation-mediated mechanism for cell lipid order modulation in the present

study. Beguin's results demonstrate that at higher pressures, ROS generation is non-negligible.

2.5.3.2. Role of shear stress from cavitation microstreaming

Cavitation microstreaming has often been cited as a primary mechanism of ultrasound and microbubble-mediated sonoporation[21,31,58–63]. The widely held hypothesis that cavitation microstreaming is responsible for sonoporation is attributed to the following: 1. the fluid shear stress and spatial gradients thereof from cavitation microstreaming theoretically reach values that form cell membranes pores[64–66], 2. observation of the permeabilization of non-adherent cells or vesicles in microstreaming flows has been observed[12,61], 3. fluid shear stress and temporal and spatial gradients thereof have been associated with the opening of ion channels and triggering of stress-sensing signalling cascades which can increase cell permeability[50,67], and have also been observed following ultrasound and MB exposure. It is proposed here, however, that the role of cavitation microstreaming in sonoporation could be minute in comparison with other cavitation-mediated phenomena, at least in *in vitro* experiments with adherent cells.

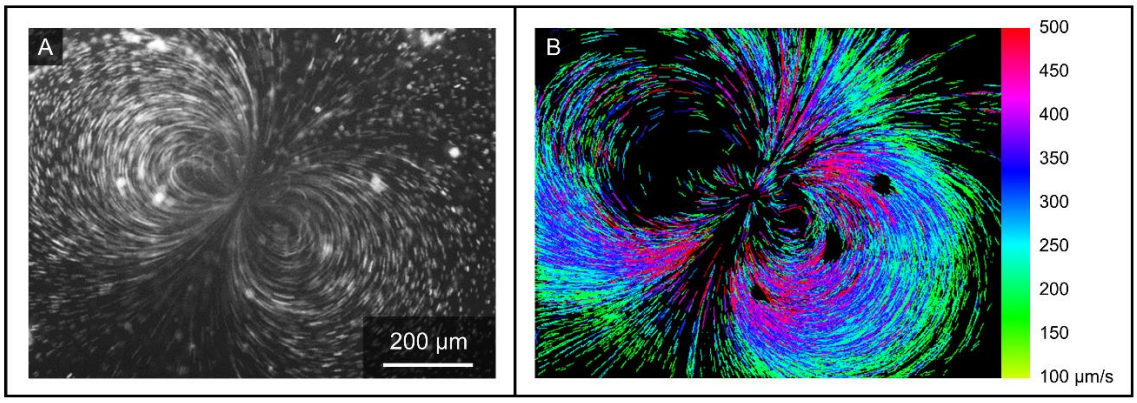

Figure 19: Streak velocimetry performed on videos of fluorescent tracer beads moving in cavitation microstreaming flows induced by SonoVue microbubbles under ultrasound exposure inside the µLAR (511 kHz and 145 kPa PNP). A) Still from the video analysed. B) Pseudo-coloured composite of the headless velocity vectors for each streak analysed in the video (112 frames). Colour bars are in µm/s.

Non-specific pore formation, i.e. the fusion of outer and inner membrane bilayers rather than the opening of integral membrane protein channels, is considered. Computational simulations of bilayer molecular dynamics reveal that as stress is applied above critical levels, the area per lipid increases rapidly allowing water to permeate the bilayer and eventually to form a cylindrical pore[68]. Estimates of the shear stress generated by oscillating MBs have also been shown to be capable of exceeding the theoretical thresholds for pore formation[61,69,70]. Indeed, sonoporation studies have demonstrated that one route for delivery of macromolecules into cells is through non-specific pores formed under cavitation duress[1,71–73]. These pores have been reported to range in size from tens of nanometres to micrometres in diameter and have been demonstrated to allow propidium iodide, the permeability tracer used in the present study, to flow into the intracellular space[3].

Haidekker et al. and Butler et al. have demonstrated a correlation between fluid shear stress (0.06 to 2.6 Pa) and endothelial cell membrane fluidity with onset and recovery times of ~5-10 s[54,56]. Furthermore, the effects were found to require a steep temporal gradient in fluid shear stress, as is expected with cavitation microstreaming[55]. Yamamoto and Ando, using Laurdan GP with confocal microscopy also employed in the present study, similarly found that the lipid order of cell membranes decreased in response to 1 Pa fluid shear stress with recovery times on the order of seconds[74]. Comparison of these studies with the shear stress fields generated by cavitation microstreaming *in vitro* should elucidate the role of cavitation microstreaming in non-specific pore formation.

Cavitation microstreaming from exposing MBs to ultrasound in the µLAR was measured in a parallel study[29]. It was found that cavitation microstreaming patterns occupied several mm^2 in the µLAR and were associated with average fluid shear

stresses below 10 mPa. A typical streaming pattern from SonoVue MBs, shown in Figure 19, was estimated to produce an average fluid shear stress of ~3.0 ± 0.1 mPa (~8.2 mPa maximum). This is in agreement with the ~1.0 ± 0.65 mPa (~2.8 mPa maximum) measurement for cavitation microstreaming dipole from Collis et al.[75]. The enormous shear stress values in theoretical studies (on the order of 10 to 10000 Pa) can be reconciled with the low shear stress values in experimental work (on the order of 0.001 to 0.01 Pa) by considering the steep drop in shear stress with distance from the MB resulting in the high shear stresses dissipating within several microns[64,76]. Marmottant and colleagues measured ~1 mm/s with 10-100 µm vesicles[61], and 8 mm/s from a dust particle, in the vicinity of a MB, although this latter example was not confirmed as cavitation microstreaming (and drifted only ~300 nm or several pixels)[77]. Such measurements are challenging due to the higher velocities and three-dimensional flow near the MB.

The aforementioned theoretical studies that propose that cavitation microstreaming alone can describe sonoporation assume that it is feasible to have at least one MB per cell without considering the interaction between MBs (e.g. by secondary radiation forces), and that each MB thus produces an independent streaming pattern, at the centre of which the high shear stresses produced exceed the threshold for permeabilizing the cell membrane. Based on the experimental observations of the present study and in the literature, however, these assumptions, while potentially valid for cells in suspension with very few MBs, do not hold for the typical *in vitro* sonoporation study employing at least 1 x 10^5 MB/ml and adherent cells.

Indeed, high-speed camera experiments with the µLAR demonstrated that radiation forces influence the spatial distribution of MBs that produce microstreaming events, and that the flow of tracer beads in microstreaming flows was associated with larger

MBs formed by coalescence (e.g. supplementary video in Pereno et al.[29]). Cavitation microstreaming patterns in practice often occupied several mm^2. These length scales were observed in not only in μLAR devices at 0.5 and 1.0 MHz, but also in a 1 mm square glass capillary setup in both water and whole blood and in an agarose tissue mimicking phantom (data not shown).

Thus, if the shear stress at the centre of a cavitation microstreaming pattern is responsible for sonoporating the cell closest to the oscillating MB, and there are less than 10 microstreaming events/mm^2 (consistent with both microstreaming and high-speed camera studies), and conservatively, greater than 1000 cells/mm^2, cavitation microstreaming would account for less than 1% permeabilization of the sample. It follows that to demonstrate that cavitation microstreaming contributes to the sonoporation of adherent cells in a substantive manner, measurement of the spatial distribution of microstreaming patterns at the cell membrane-medium interface, and the movement of microstreaming patterns as a function of acoustic parameters must be compared with measured sonoporation efficiencies. The same argument applies to the impact of cavitation microstreaming on stress-gated ion channels and the stress-sensing signalling cascade in cells. Finally, it is important to note that the contribution to sonoporation from other MB-proximity-dependent cavitation-mediated phenomena, such as oscillatory membrane strain, for instance, have not been distinguished from that of cavitation microstreaming.

The observation that non-adherent cells or artificial cell membranes, e.g. consisting of lipid vesicles without proteins or a cytoskeleton, can be permeabilized in cavitation microstreaming flows[61,70], thus bears limited relevance to *in vitro* experiments concerning adherent cells, especially with regard to cavitation microstreaming where the spatial distribution of cells is critical. Yamamato and Ando exposed both adherent

cells and artificial membranes to ~1 Pa fluid shear stress and found that cell membrane lipid order recovered in seconds whereas artificial membranes required at least 30 min[74], further demonstrating the importance of the cytoskeleton and membrane proteins in biomechanical and flow-dependent phenomena.

Taken together, the literature suggests that a change in cell membrane lipid order in the present study would not be expected from fluid shear stress from cavitation microstreaming for the following reasons: 1. the average fluid shear stress was too low, 2. the recovery times are too fast, 3. high levels of shear stress and the spatial gradients thereof may only affect a vanishing proportion of cells under investigation. This result provides support for the hypothesis that cavitation microstreaming does not significantly contribute to the permeabilization of adherent cells in sonoporation studies *in vitro*, at least not as it is currently described in the literature.

2.5.4. Cell membrane modulation by MBs as a sonoporation mechanism

2.5.4.1. Background for hypothesis

Following the observations of the previous sections, it was hypothesized that cell membrane lipid disordering by 18:0 PC-PEG40S MBs contribute to sonoporation by lowering the energy barrier to pore formation. In this section a theoretical relationship between lipid order and pore formation and its relevance to the experiments of the present study are discussed.

The net energy associated with the formation of a single cylindrical pore of radius R, is

$$\Delta E = 2\pi R\gamma - \pi R^2 \Gamma, \tag{2}$$

given by,

where γ is the line tension (in Nm/m) and Γ is the interfacial tension (in Nm/m^2)[78]. It can be seen that pore formation results in a reduction of the surface area in the bilayer and an edge energy associated with the pore. Pores with a radius above a critical value,

$$R_c = \frac{\gamma}{\Gamma}, \tag{3}$$

will grow to rupture the membrane. Substituting (2) into (1), it can be seen that the

$$\Delta E_c = \pi \frac{\gamma^2}{\Gamma}. \tag{4}$$

critical energy for pore formation is given by,

While many studies determine the line tension by treating the pore as a deformation in an elastic solid, the assumption of small deformations is violated under this approach. An alternative method for defining γ is to consider the attractive and repulsive forces

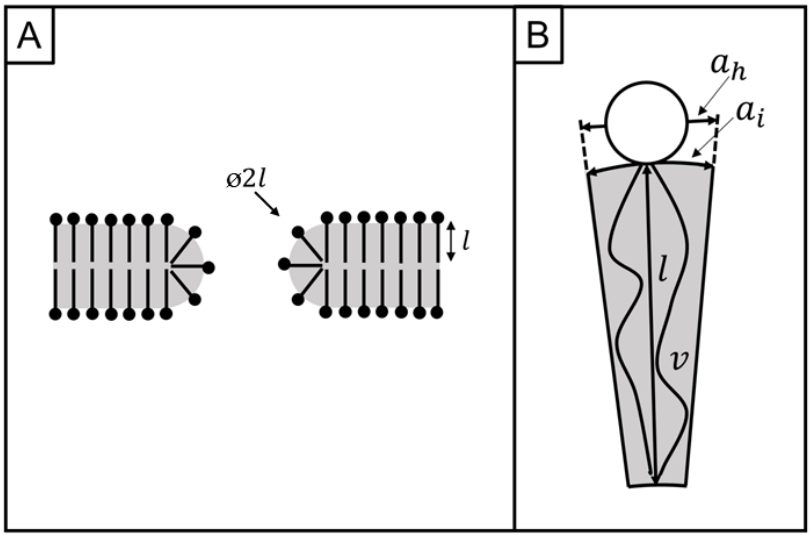

Figure 20: Diagrams showing the molecular arrangement and dimensions used to determine the line tension around a pore (modified from May[80]). In (A) lipid headgroups are dots and lipid chains are simplified to a single line per lipid. It can be seen that the pore size used to determine line tension is equal to the bilayer thickness. In (B) the variables used in determining the line tension are labelled on a diagram of a single lipid. The shaded area represents the chain volume. It is important to note that a_h and a_i are not always equal depending on the geometry of the lipid. a_h is taken as a projection of the area at the interface to the height at the midpoint of the lipid headgroup.

acting on the lipids in the bilayer as described by Israelachvili et al.[79] and May[80]. This model assumes that the boundary of the pore is micellar with diameter equal to the bilayer thickness (defined as twice the average lipid chain length), and includes only contributions to line tension from the uniform packing of lipids. The molecular free energy of the lipids can be described by,

$$f = \Gamma a_i + \frac{B}{a_h}, \tag{5}$$

where B is a lipid head group repulsion strength, and a_i is the molecular cross-sectional area at the hydrocarbon-water interface (e.g. interfacial area), and a_h is the head group area. It can be seen that at equilibrium, the molecular areas in the bilayer are given by,

$$a_{h,eq} = a_{i,eq} = \sqrt{\frac{B}{\Gamma}}. \tag{6}$$

Under the assumption that lipid hydrophobic chains are incompressible, the chain volume, v, is given by $v = l a_{h,eq}$, where l is the average chain length. As the lipid head groups spread out to accommodate the micellar geometry of the pore, the interfacial area along the pore diameter is increased such that $a_{i,pore} \sim 2a_{h,eq}$. This can be visualized as the transformation of a cylinder-shaped lipid in the bilayer into a cone-shaped lipid along the pore with chain volume conserved. It follows that the line tension (e.g. the excess free energy per unit length of the edge of the pore) is given by,

$$\gamma = \left[f\left(2a_{h,eq}\right) - f\left(a_{h,eq}\right)\right]N, \tag{7}$$

where $N = \frac{\pi l^2}{2v}$ is the number of lipids in the pore per unit length (e.g. by dividing the micellar area by the chain volume). This results in a useful expression for the line tension,

$$\gamma = \frac{\pi}{4}\Gamma l. \tag{8}$$

The critical energy required for pore formation is thus,

$$\Delta E_c = \frac{\pi^3}{16}\Gamma l^2 \tag{9}$$

From (5), the interfacial tension can be expressed as $\Gamma = \frac{B}{a_{h,eq}^2}$ such that,

$$\Delta E_c = \frac{\pi^3}{16} B \left(\frac{l}{a_{h,eq}}\right)^2. \tag{10}$$

The head group repulsion strength, B, primarily arising from electrostatic contributions, can be further defined under various assumptions as desired[81]. Equation (9) has some very important consequences for the experiments throughout this thesis.

With regard to lipid packing, it can be seen that as a lipid becomes more conical, either a_h is increased, l is decreased, or both, with chain volume conserved. Consequently, conical lipids stabilize pores (this concept is revisited in Chapters 4-5). Conversely, as the lipid packing decreases and lipids become more cylindrical (or even inverted conical in shape), pores in a lipid bilayer are destabilized.

The $\frac{l}{a_{h,eq}}$ term in Equation (9) can also be considered as an analogue to the lipid order, which describes the flexibility of the lipid chains, conventionally by the average angle of the CH bonds with respect to the bilayer normal. For disordered lipids, the chains occupy a larger area and a_h increases while l decreases, resulting in a decrease in the energy required for pore formation. The opposite is true for ordered lipids. It should be noted that near phase transition ΔE_c is expected to behave non-monotonically as a function of pH, temperature, pressure, and lipid order (e.g. volumetric fluctuations). A small change in lipid order near phase transition results in a large change in density

such that compressibility is non-negligible. Far from transition, a small change in lipid order results in a comparatively negligible change in density such that compressibility can be ignored and ΔE_c appears monotonic. Compressibility is also non-negligible at phase boundaries for the same reason.

Critically, the spectral shift of polarity-sensitive C-Laurdan (GP), as measured in this thesis, is a measure of membrane hydration. Membrane hydration in biological systems is inversely proportional to lipid packing and lipid order. It follows, therefore, that GP is also proportional to the energy required for pore formation ($\Delta E_c \propto$ GP), although the precise nature of this relationship is complex.

Assuming the cell membrane bilayer thickness is ~4 nm, the critical radius according to the above calculations is $R_c \sim$ 1.6 nm. The pore radius required to deliver propidium iodide, the permeabilization marker employed in the present study, is ~0.75 nm[82]. Thus, the critical energy required for pore formation in this section is also directly relevant to the permeabilization and sonoporation experiments described in Chapters 3-4.

2.5.4.2. MB-mediated cell membrane lipid disordering did not enhance sonoporation

In the previous section, theoretical arguments demonstrated that as cell membrane lipid order decreases, the energy required for pore formation also decreases. Indeed, the permeability of pure lipid bilayers to water molecules, ions, and other small molecules is inversely correlated with lipid order[83,84]. It follows that exposure to unwashed 18:0 PC-PEG40S MBs, which lower cell lipid order, was expected to decrease the energy required for pore formation, enhancing ultrasound-mediated permeabilization in comparison with non-membrane modulating MBs. It was thus surprising that no increase in permeabilization efficiency was observed.

One possible explanation for this result is that the cell membrane has mechanisms for destabilizing pores that form in the presence of increased water defects in the plasma membrane. The reduction of membrane interfacial tension by the cytoskeleton, a protein scaffolding that interfaces with the intracellular side of the cell membrane, for instance, would increase the critical radius and critical energy required for pore formation according to equations (2) and (3). With a stochastic model of pore growth and stability, Sung and Park demonstrated that the cytoskeleton would indeed be expected to greatly decrease the probability of pore formation[85]. Interestingly, sonoporation can also damage the cytoskeleton, which could further enhance pore formation (and the effects of lipid disordering thereof) by locally increasing membrane surface tension.

In summary, 18:0 PC-PEG40S MBs modulate membrane order but not sufficiently to enhance sonoporation under the conditions tested. In Chapter 3, the possibility that changes in cell lipid order greater than that achieved by 18:0 PC-PEG40S MBs could enhance sonoporation is investigated.

2.5.5. Limitations

Regarding the relevance and magnitude of the observed effects, comparable changes in GP have been associated with large changes in the cholesterol content (e.g. by ~10% in DPPC vesicles[86]), the pH (e.g. from 4.1 to 7.4 in DPPS:DPPC vesicles[40]), the temperature (e.g. in DMPC GUVs at 37°C vs 34°C[38]), or the phospholipid composition (e.g. DLPC vs DPPC, at 20°C[40]) in model membranes. Dilution in blood and the presence of lipoproteins and blood cells, however, would have to be evaluated to assess the relevance of these findings to *in vivo* drug delivery. Nonetheless, local concentrations of MB-associated lipid or emulsifier could be considerable *in vivo* when

the collision frequency of MB shell-fragments with vessel walls is enhanced under ultrasound exposure, and local extravasation of such fragments is facilitated[44,87].

It is also important to note that the lipid order assessment employed in the present study, spectral imaging with C-Laurdan, is agnostic to the mechanisms by which lipid order is changing. In future work, C-Laurdan spectral imaging which provides temporal and spatial resolution of membrane hydration and lipid order could be complemented with high-performance liquid chromatography and mass spectrometry or evaporative light scattering detection (HPLC-MS or HPLC-ELSD), for instance, to identify and quantify the exchange of molecular species between cells and microbubbles.

Additionally, counter-staining with hoescht, which only stains cell nuclei, may be an improvement over calcein-AM for cell count with regard to image processing. The present study is limited to the determination of the percentage of permeabilized cells but does not quantify the percentage of viable cells. It is therefore not possible to comment from the data presented herein on whether the observed permeabilization was reparable or not. To this end, MTS assays, or similar metabolic assays could be performed. Since the present study concerns the formation of pores in cell membranes rather than membrane repair, pore closure, or viability, such experiments are left as future work.

2.6. Conclusion

This investigation sought to test whether cell membrane lipid disordering by MBs could potentiate sonoporation. While sonoporation enhancement was not observed, several valuable insights were gained from this study. Namely:

(1) The ultrasound-mediated transfer of material from MBs to cell membranes depends on MB formulation.

(2) 18:0 PC-PEG40S MBs decrease lipid order and increase membrane hydration in cancer cell membranes.

(3) This effect is temperature dependent, occurring at 37°C but not at 22°C.

(4) This effect appears to be limited to the cell plasma membrane.

(5) This effect can be inhibited by removing free liposomes and free PEG40S from the 18:0 PC-PEG40S MB solution.

(6) This effect is dependent on the carrier-lipid chain length. Increasing the carrier PC chain length from 18 to 22 (e.g. 18:0 PC to 22:0 PC) inhibited the effect, possibly by forming 22:0 PC-PEG40S constructs that interact less with cells.

(7) This effect did not occur with SonoVue® which has both fatty acid and PEG but not PEG-conjugated fatty acid, e.g. PEG40S, which is used in 18:0 PC-PEG40S MB.

(8) The fact that no enhancement of sonoporation was observed suggests that either a more complex pore formation mechanism is responsible for sonoporation, or a greater increase in cell membrane hydration is required to enhance sonoporation.

In the following chapter, a systematic approach is taken to further test the hypothesis that a change in membrane physicochemical state acts as a perturbation for enhanced sonoporation.

2.7. Author contributions

When I arrived at the University of Oxford, Professor Stride, my supervisor, and Professor Dario Carugo of the University of Southampton, then a Post-Doc, were in collaboration with Professor Eggeling and Dr. Jorge Bernardino de la Serna and Dr.

Erdinc Sezgin. They had already collected promising data on artificial membranes demonstrating a change in lipid order and lipid mobility following exposure to ultrasound and microbubbles (data not shown). Carugo and I then carried out the remainder of the work on live cells published in *Biomaterials* under the continued guidance of Professor Stride and presented here (e.g. the experiments with the µLAR). Professor Kuimova is also an author on the paper for her contributions to the experimental methods, as published in a previous paper with Professors Carugo and Stride[88]. In this project I took a critical role in the generation of hypotheses, development of methods, execution of experiments, processing and analysis of data, and writing of the manuscript.

Sonoporation experiments and spectral imaging experiments with µSlides were conducted in collaboration with PhD student Oliver Vince who helped with ultrasound exposure of cell samples, microbubble formation and characterization, and image processing. The SAT2 system used for sonoporation experiments was developed and characterized by Dr. Michael Gray. Cavitation microstreaming data was collected in collaboration with Professor Carugo and Professor James Kwan, then a Post-Doc. The dynamic GP experiments were a collaborative effort lead by PhD student Anna Booth, then a Master's student supervised by Professor Stride, Dr. Shamit Shrivastava supervised by Professor Robin Cleveland, and myself, which is in preparation for publication with additional data from Dr. Richard Browning. Further acknowledgement is owed to PhD student Estelle Beguin who provided data on reactive oxygen species generation by MBs and Langmuir trough data on MB formulations, the latter of which was collected with Dr. Shamit Shrivastava. Acknowledgement is further extended to James Fisk and David Salisbury for machining of the µLAR parts, the SAT2 system, and the dynamic GP measurement system sample holder.

2.8. References

1. Hu, Y., Wan, J. M. F. & Yu, A. C. H. Membrane Perforation and Recovery Dynamics in Microbubble-Mediated Sonoporation. *Ultrasound Med. Biol.* **39,** 2393–2405 (2013).
2. Lentacker, I., De Smedt, S. C. & Sanders, N. N. Drug loaded microbubble design for ultrasound triggered delivery. *Soft Matter* **5,** 2161 (2009).
3. Fan, Z., Liu, H., Mayer, M. & Deng, C. C. X. Spatiotemporally controlled single cell sonoporation. *Proc. Natl. Acad. Sci. U. S. A.* **109,** 16486–16491 (2012).
4. Kudo, N., Okada, K. & Yamamoto, K. Sonoporation by single-shot pulsed ultrasound with microbubbles adjacent to cells. *Biophys. J.* **96,** 4866–4876 (2009).
5. Honda, H., Kondo, T., Zhao, Q.-L., Feril, L. B. & Kitagawa, H. Role of intracellular calcium ions and reactive oxygen species in apoptosis induced by ultrasound. *Ultrasound Med. Biol.* **30,** 683–692 (2004).
6. van Rooij, T. *et al.* Viability of endothelial cells after ultrasound-mediated sonoporation: Influence of targeting, oscillation, and displacement of microbubbles. *J. Control. Release* **238,** 197–211 (2016).
7. Zhong, W., Sit, W. H., Wan, J. M. F. & Yu, A. C. H. Sonoporation Induces Apoptosis and Cell Cycle Arrest in Human Promyelocytic Leukemia Cells. *Ultrasound Med. Biol.* **37,** 2149–2159 (2011).
8. van Wamel, A. *et al.* Vibrating microbubbles poking individual cells: Drug transfer into cells via sonoporation. *J. Control. Release* **112,** 149–155 (2006).
9. Van Wamel, A., Bouakaz, A., Versluis, M. & De Jong, N. Micromanipulation of endothelial cells: Ultrasound-microbubble-cell interaction. *Ultrasound Med. Biol.* **30,** 1255–1258 (2004).
10. De Cock, I. *et al.* Ultrasound and microbubble mediated drug delivery: Acoustic pressure as determinant for uptake via membrane pores or endocytosis. *J. Control. Release* **197,** 20–28 (2015).
11. Delalande, A., Leduc, C., Midoux, P., Postema, M. & Pichon, C. Efficient Gene Delivery by Sonoporation Is Associated with Microbubble Entry into Cells and the Clathrin-Dependent Endocytosis Pathway. *Ultrasound Med. Biol.* **41,** 1913–1926 (2015).
12. Wu, J., Ross, J. P. & Chiu, J.-F. Reparable sonoporation generated by microstreaming. *J. Acoust. Soc. Am.* **111,** 1460–4 (2002).
13. Zhou, Y., Yang, K., Cui, J., Ye, J. Y. & Deng, C. X. Controlled permeation of cell membrane by single bubble acoustic cavitation. *J. Control. Release* **157,** 103–111 (2012).
14. Unger, E. C. *et al.* Therapeutic applications of lipid-coated microbubbles. *Adv. Drug Deliv. Rev.* **56,** 1291–1314 (2004).
15. Meijering, B. D. M. *et al.* Ultrasound and microbubble-targeted delivery of macromolecules is regulated by induction of endocytosis and pore formation. *Circ. Res.* **104,** 679–687 (2009).

16. Kooiman, K., Van Der Steen, A. F. W. & De Jong, N. Role of intracellular calcium and reactive oxygen species in microbubble-mediated alterations of endothelial layer permeability. *IEEE Trans. Ultrason. Ferroelectr. Freq. Control* **60,** 1811–1815 (2013).

17. Juffermans, L. J. M. *et al.* Ultrasound and Microbubble-Induced Intra- and Intercellular Bioeffects in Primary Endothelial Cells. *Ultrasound Med. Biol.* **35,** 1917–1927 (2009).

18. Dijkmans, P. a. *et al.* Microbubbles and ultrasound: From diagnosis to therapy. *Eur. J. Echocardiogr.* **5,** 245–256 (2004).

19. Der Loughian, C. *et al.* Jumping acoustic bubbles on lipid bilayers. *Soft Matter* 3460–3469 (2015). doi:10.1039/c5sm00427f

20. Kheirolomoom, A. *et al.* Acoustically-active microbubbles conjugated to liposomes: Characterization of a proposed drug delivery vehicle. *J. Control. Release* **118,** 275–284 (2007).

21. Lentacker, I., De Cock, I., Deckers, R., De Smedt, S. C. & Moonen, C. T. W. Understanding ultrasound induced sonoporation: Definitions and underlying mechanisms. *Adv. Drug Deliv. Rev.* **72,** 49–64 (2014).

22. Leow, R. S., Wan, J. M. F. & Yu, A. C. H. Membrane blebbing as a recovery manoeuvre in site-specific sonoporation mediated by targeted microbubbles. (2015).

23. Owen, D. M., Rentero, C., Magenau, A., Abu-Siniyeh, A. & Gaus, K. Quantitative imaging of membrane lipid order in cells and organisms. *Nat. Protoc.* **7,** 24–35 (2012).

24. McIntosh, T. J. & Simon, S. A. ROLES OF BILAYER MATERIAL PROPERTIES IN FUNCTION AND DISTRIBUTION OF MEMBRANE PROTEINS. *Annu. Rev. Biophys. Biomol. Struct.* **35,** 177–198 (2006).

25. Schäfer, L. V *et al.* Lipid packing drives the segregation of transmembrane helices into disordered lipid domains in model membranes. *Proc. Natl. Acad. Sci. U. S. A.* **108,** 1343–8 (2011).

26. Olbrich, K., Rawicz, W., Needham, D. & Evans, E. Water Permeability and Mechanical Strength of Polyunsaturated Lipid Bilayers. *Biophys. J.* **79,** 321–327 (2000).

27. Xia, W. J. & Onyuksel, H. Mechanistic studies on surfactant-induced membrane permeability enhancement. *Pharm. Res.* **17,** 612–8 (2000).

28. Feshitan, J. A., Chen, C. C., Kwan, J. J. & Borden, M. A. Microbubble size isolation by differential centrifugation. *J. Colloid Interface Sci.* **329,** 316–324 (2009).

29. Pereno, V. *et al.* Layered acoustofluidic resonators for the simultaneous optical and acoustic characterisation of cavitation dynamics, microstreaming, and biological effects. *Biomicrofluidics* **12,** 034109 (2018).

30. Carugo, D., Owen, J., Crake, C., Lee, J. Y. & Stride, E. Biologically and Acoustically Compatible Chamber for Studying Ultrasound-Mediated Delivery of Therapeutic Compounds. *Ultrasound Med. Biol.* **41,** 1927–37 (2015).

31. Kooiman, K., Foppen-Harteveld, M., Der Steen, A. F. W. Van & De Jong, N.

Sonoporation of endothelial cells by vibrating targeted microbubbles. *J. Control. Release* **154,** 35–41 (2011).

32. Kudo, N., Okada, K. & Yamamoto, K. Sonoporation by Single-Shot Pulsed Ultrasound with Microbubbles Adjacent to Cells. *Biophys. J.* **96,** 4866–4876 (2009).

33. Karshafian, R., Bevan, P. D., Williams, R., Samac, S. & Burns, P. N. Sonoporation by Ultrasound-Activated Microbubble Contrast Agents: Effect of Acoustic Exposure Parameters on Cell Membrane Permeability and Cell Viability. *Ultrasound Med. Biol.* **35,** 847–860 (2009).

34. Vykhodtseva, N., McDannold, N. & Hynynen, K. Progress and problems in the application of focused ultrasound for blood-brain barrier disruption. *Ultrasonics* **48,** 279–296 (2008).

35. Chen, X., Wan, J. M. F. & Yu, A. C. H. SONOPORATION AS A CELLULAR STRESS: INDUCTION OF MORPHOLOGICAL REPRESSION AND DEVELOPMENTAL DELAYS. (2013). doi:10.1016/j.ultrasmedbio.2013.01.008

36. Bolte, S. & Cordelieres, F. P. A guided tour into subcellular colocalisation analysis in light microscopy. *J. Microsc.* **224,** 13–232 (2006).

37. Gullapalli, R., Demirel, M. & Butler, P. Molecular dynamics simulations of DiI-C18 bilayer (3) in a DPPC lipid. *Phys Chem* **10,** 3548–3560 (2012).

38. Sanchez, S. a., Tricerri, M. a. & Gratton, E. Laurdan generalized polarization fluctuations measures membrane packing micro-heterogeneity in vivo. *Proc. Natl. Acad. Sci.* **109,** 7314–7319 (2012).

39. Sezgin, E., Waithe, D., Bernardino De La Serna, J. & Eggeling, C. Spectral imaging to measure heterogeneity in membrane lipid packing. *ChemPhysChem* **16,** 1387–1394 (2015).

40. Parasassi, T., De Stasio, G., Ravagnan, G., Rusch, R. M. & Gratton, E. Quantitation of lipid phases in phospholipid vesicles by the generalized polarization of Laurdan fluorescence. *Biophys. J.* **60,** 179–189 (1991).

41. Aron, M. *et al.* Spectral imaging toolbox: Segmentation, hyperstack reconstruction, and batch processing of spectral images for the determination of cell and model membrane lipid order. *BMC Bioinformatics* **18,** (2017).

42. Borden, M. a., Pu, G., Runner, G. J. & Longo, M. L. Surface phase behavior and microstructure of lipid/PEG-emulsifier monolayer-coated microbubbles. *Colloids Surfaces B Biointerfaces* **35,** 209–223 (2004).

43. Shen, Y., Powell, R. L. & Longo, M. L. Interfacial and stability study of microbubbles coated with a monostearin/monopalmitin-rich food emulsifier and PEG40 stearate. *J. Colloid Interface Sci.* **321,** 186–194 (2008).

44. De Cock, I., Lajoinie, G., Versluis, M., De Smedt, S. C. & Lentacker, I. Sonoprinting and the importance of microbubble loading for the ultrasound mediated cellular delivery of nanoparticles. *Biomaterials* **83,** 294–307 (2016).

45. Ferrell, J. E., Lee, K.-J. & Huestis, W. H. Lipid Transfer between Phosphatidylcholine Vesicles and Human Erythrocytes: Exponential Decrease in Rate with Increasing Acyl Chain Lengthy. *Biochem. Proc. Natl. Acad. Sci. U.S.A. Biochem. Biophys. Res. White, J. G. Am. J. Pathol. Clin. Hematol. J. Lab.*

Clin. Med. Febiger **24,** 2857–2864 (1985).

46. Luan, Y. *et al.* Lipid shedding from single oscillating microbubbles. *Ultrasound Med. Biol.* **40,** 1834–1846 (2014).

47. Carugo, D. *et al.* Modulation of the molecular arrangement in artificial and biological membranes by phospholipid-shelled microbubbles. *Biomaterials* (2016). doi:10.1016/j.biomaterials.2016.10.034

48. Harris, F. M., Best, K. B. & Bell, J. D. Use of laurdan fluorescence intensity and polarization to distinguish between changes in membrane fluidity and phospholipid order. *Biochim. Biophys. Acta - Biomembr.* **1565,** 123–128 (2002).

49. McLean, L. R. & Phillips, M. C. Mechanism of cholesterol and phosphatidylcholine exchange or transfer between unilamellar vesicles. *Biochemistry* **20,** 2893–2900 (1981).

50. Li, Y.-S. J., Haga, J. H. & Chien, S. Molecular basis of the effects of shear stress on vascular endothelial cells. *J. Biomech.* **38,** 1949–1971 (2005).

51. Chen, X., Leow, R. S., Hu, Y., Wan, J. M. F. & Yu, A. C. H. Single-site sonoporation disrupts actin cytoskeleton organization. *J. R. Soc. Interface* **11,** 20140071 (2014).

52. Tran, T. A., Le Guennec, J. Y., Bougnoux, P., Tranquart, F. & Bouakaz, A. Characterization of cell membrane response to ultrasound activated microbubbles. *IEEE Trans. Ultrason. Ferroelectr. Freq. Control* **55,** 44–49 (2008).

53. Kumon, R. E. *et al.* Spatiotemporal Effects of Sonoporation Measured by Real-Time Calcium Imaging. *Ultrasound Med. Biol.* **35,** 494–506 (2009).

54. Butler, P. J., Norwich, G., Weinbaum, S. & Chien, S. Shear stress induces a time- and position-dependent increase in endothelial cell membrane fluidity. *Am. J. Physiol. Cell Physiol.* **280,** C962–C969 (2001).

55. Butler, P. J., Tsou, T. C., Li, J. Y. S., Usami, S. & Chien, S. Rate sensitivity of shear-induced changes in the lateral diffusion of endothelial cell membrane lipids: a role for membrane perturbation in shear-induced MAPK activation. *FASEB J.* **16,** 216–218 (2002).

56. Haidekker, M. a, L'Heureux, N. & Frangos, J. a. Fluid shear stress increases membrane fluidity in endothelial cells: a study with DCVJ fluorescence. *Am. J. Physiol. - Hear. Circ. Physiol.* **278,** H1401–H1406 (2000).

57. Watanabe, H. *et al.* Alterations of human erythrocyte membrane fluidity by oxygen-derived free radicals and calcium. *Free Radic. Biol. Med.* **8,** 507–514 (1990).

58. Fan, Z., Kumon, R. E., Park, J. & Deng, C. X. Intracellular delivery and calcium transients generated in sonoporation facilitated by microbubbles. *J. Control. Release* **142,** 31–39 (2010).

59. Forbes, M. M. & O'Brien, W. D. Development of a theoretical model describing sonoporation activity of cells exposed to ultrasound in the presence of contrast agents. *J. Acoust. Soc. Am.* **131,** 2723 (2012).

60. Moosavi Nejad, S., Hosseini, S. H. R., Akiyama, H. & Tachibana, K. Optical observation of cell sonoporation with low intensity ultrasound. *Biochem.*

Biophys. Res. Commun. **413,** 218–223 (2011).

61. Marmottant, P. & Hilgenfeldt, S. Controlled vesicle deformation and lysis by single oscillating bubbles. *Nature* **423,** 153–156 (2003).

62. Helfield, B., Chen, X., Watkins, S. C. & Villanueva, F. S. Biophysical insight into mechanisms of sonoporation. *Proc. Natl. Acad. Sci.* 201606915 (2016). doi:10.1073/pnas.1606915113

63. Delalande, A., Kotopoulis, S., Postema, M., Midoux, P. & Pichon, C. Sonoporation: Mechanistic insights and ongoing challenges for gene transfer. *Gene* **525,** 191–199 (2013).

64. Doinikov, A. a & Bouakaz, A. Theoretical investigation of shear stress generated by a contrast microbubble on the cell membrane as a mechanism for sonoporation. *J. Acoust. Soc. Am.* **128,** 11–9 (2010).

65. Wang, L., Tu, J., Guo, X.-S., Xu, D. & Zhang, D. Microstreaming velocity field and shear stress created by an oscillating encapsulated microbubble near a cell membrane. *Chinese Phys. B* **23,** 124302 (2014).

66. Wu, J. Theoretical study on shear stress generated by microstreaming surrounding contrast agents attached to living cells. *Ultrasound Med. Biol.* **28,** 125–129 (2002).

67. Ando, J. & Yamamoto, K. Effects of shear stress and stretch on endothelial function. *Antioxid. Redox Signal.* **15,** 1389–1403 (2011).

68. Tieleman, D. P., Leontiadou, H., Mark, A. E. & Marrink, S.-J. Simulation of Pore Formation in Lipid Bilayers by Mechanical Stress and Electric Fields. *J. Am. Chem. Soc.* **125,** 6382–6383 (2003).

69. Helfield, B., Chen, X., Watkins, S. C. & Villanueva, F. S. Biophysical insight into mechanisms of sonoporation. *Proc. Natl. Acad. Sci. U. S. A.* **113,** 9983–8 (2016).

70. Marmottant, P., Biben, T. & Hilgenfeldt, S. Deformation and rupture of lipid vesicles in the strong shear flow generated by ultrasound-driven microbubbles. *Proc. R. Soc. A Math. Phys. Eng. Sci.* **464,** 1781–1800 (2008).

71. Zhou, Y., Kumon, R. E., Cui, J. & Deng, C. X. The Size of Sonoporation Pores on the Cell Membrane. *Ultrasound Med. Biol.* **35,** 1756–1760 (2009).

72. Deng, C. X., Sieling, F., Pan, H. & Cui, J. Ultrasound-induced cell membrane porosity. *Ultrasound Med. Biol.* **30,** 519–526 (2004).

73. Zeghimi, A., Uzbekov, R., Arbeille, B., Escoffre, J. M. & Bouakaz, A. Ultrastructural modifications of cell membranes and organelles induced by sonoporation. *IEEE Int. Ultrason. Symp. IUS* 2045–2048 (2012). doi:10.1109/ULTSYM.2012.0511

74. Yamamoto, K. & Ando, J. Endothelial cell and model membranes respond to shear stress by rapidly decreasing the order of their lipid phases. *J. Cell Sci.* **126,** (2013).

75. Collis, J. *et al.* Cavitation microstreaming and stress fields created by microbubbles. *Ultrasonics* **50,** 273–279 (2010).

76. Lewin, P. A. Acoustically induced shear stresses in the vicinity of microbubbles

in tissue. *J. Acoust. Soc. Am.* **71,** 728 (1982).

77. Marmottant, P., Versluis, M., De Jong, N., Hilgenfeldt, S. & Lohse, D. High-speed imaging of an ultrasound-driven bubble in contact with a wall: ‘“Narcissus”’ effect and resolved acoustic streaming. (2005). doi:10.1007/s00348-005-0080-y

78. Litster, J. D. STABILITY OF LIPID BILAYERS AND RED BLOOD CELL MEMBRANES. (1975).

79. Israelachvili, J. N., Marcelja, S. & Horn, R. G. Physical principles of membrane organization. *Q. Rev. Biophys.* **13,** 121–200 (1980).

80. May, S. A molecular model for the line tension of lipid membranes. *Eur. Phys. J. E* **3,** 37–44 (2000).

81. Israelachvili, J. N., Mitchell, D. J. & Ninham, B. W. Theory of self-assembly of hydrocarbon amphiphiles into micelles and bilayers. *J. Chem. Soc. Faraday Trans. 2 Mol. Chem. Phys.* **72,** 1525–1568 (1976).

82. Bowman, A. M., Nesin, O. M., Pakhomova, O. N., Pakhomov, A. G. & Net, A. Analysis of Plasma Membrane Integrity by Fluorescent Detection of Tl + Uptake. doi:10.1007/s00232-010-9269-y

83. Bittman, R. & Blau, L. KINETICS OF WATER PERMEABILITY IN LIPOSOMES The Phospholipid-Cholesterol Interaction. Kinetics of Water Permeability in Liposomest.

84. Chapman, D. Phase transitions and fluidity characteristics of lipids and cell membranes. *Q. Rev. Biophys.* **8,** 185–235 (2017).

85. Sung, W. & Park, P. J. Dynamics of pore growth in membranes and membrane stability. *Biophys. J.* **73,** 1797–804 (1997).

86. Koynova, R. & Caffrey, M. Phases and phase transitions of glycoglycerolipids. *Chem. Phys. Lipids* **69,** 181–207 (1994).

87. Arvanitis, C. D., Bazan-Peregrino, M., Rifai, B., Seymour, L. W. & Coussios, C. C. Cavitation-Enhanced Extravasation for Drug Delivery. *Ultrasound Med. Biol.* **37,** 1838–1852 (2011).

88. Hosny, N. a *et al.* Mapping microbubble viscosity using fluorescence lifetime imaging of molecular rotors. *Proc. Natl. Acad. Sci. U. S. A.* **110,** 9225–30 (2013).

89. Carugo, D. *et al.* Modulation of the molecular arrangement in artificial and biological membranes by phospholipid-shelled microbubbles. *Biomaterials* **113,** (2017).

III.

Cell membrane modulation by saturated phosphatidylcholines for the enhancement of ultrasound-mediated drug delivery

3.1. Introduction

In preliminary experiments, it was found that microbubble (MB) composed of 18:0 phosphatidylcholine (18:0 PC) and polyethylene glycol 40 stearate (PEG40S) are capable of rapidly and significantly altering the lipid order of cell membranes, even in the absence of ultrasound exposure[1] (see Chapter 2). The decrease in cell membrane lipid order induced by 18:0 PC-PEG40S MBs was expected to lower the energy required for pore formation during exposure to ultrasound, and thus enhance sonoporation. As shown in Chapter 6, however, interestingly, no such enhancement was observed. One possible explanation is that in living cells the cytoskeleton acts to lower surface tension, increasing the energy barrier to pore formation. A decrease in cell lipid order greater than that induced by 18:0 PC-PEG40S MBs may thus be required to enhance sonoporation. In this chapter, the potential of more potent cell lipid order modulators that can be incorporated into cavitation agents and/or drug delivery vehicles for use in ultrasound-mediated drug delivery, were investigated. It was hypothesized that molecules that sufficiently decrease cell lipid order, increase sonoporation efficiency by lowering the energy barrier to pore formation, while other molecules that increase lipid order, inhibit or promote recovery from sonoporation by destabilizing pores.

While many molecules are capable of modulating cell lipid order, saturated phosphatidylcholine lipids (PCs) were investigated for the following reasons:

(1) At full saturation, PCs are more compatible with the viscous and lipid-ordered shells of phospholipid-coated MBs than, for instance, unsaturated lipids[2],

(2) The PC hydrocarbon chain-length provides a well-characterized independent variable for the proposed experiments that is theoretically correlated with the energy barrier to pore formation (see Chapter 2),

(3) PCs play a well-known role in establishing cell membrane lipid order,

(4) PCs are widely used in the design of liposomes and MBs,

(5) PCs are widely used in the clinic and present no new regulatory hurdles.

In the following sections, the effects of PCs in the form of liposomes on the lipid order of cell membranes and intracellular vesicles are investigated. The most safe and effective cell lipid order-modulating PC was then assessed for its potential to enhance sonoporation efficiency in combination with ultrasound and MBs.

3.2. Methods

3.2.1. Liposome preparation

Phosphatidylcholine (PC) lipids suspended in aqueous solution self-assemble to form multi-lamellar structures with polar heads oriented toward aqueous solution and hydrophobic tails oriented toward the hydrophobic tails of opposing lamellae. These structures are referred to throughout the text as liposomes. Liposomes are commonly employed as drug delivery vehicles because they are small enough to take advantage of the enhanced permeability and retention (EPR) effect in tumours, self-assemble from biological components (e.g. lipids), and can be designed with excellent characteristics for drug-loading, drug release, biomolecular targeting, and binding to cavitation agents, among other features.

Lipid films consisting of a single phosphatidylcholine (PC) species (purchased from Avanti Polar Lipids) were prepared by chloroform evaporation at 60°C for at least 12 h. PC lipid films were then suspended in phosphate-buffered saline (PBS) at ~85°C (above the longest chain length PC melting point) for at least 30 min with magnetic stirring. The PC solution (5 mM) was then dispersed by sonication at low power (power setting 4, ~8 V_{RMS}) for 90 s. Fully saturated PCs of varying chain length were investigated, including 10:0, 12:0, 14:0, 16:0, 18:0, and 22:0 PC. 10:0 PC was the PC with the shortest hydrocarbon chain length investigated because PCs with shorter hydrocarbon chains are effectively water soluble and would not be amenable to microbubble formulation.

Short name	22:0 PC (DBPC)	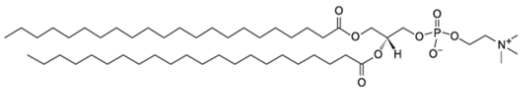
Chemical name	1,2-dibehenoyl-sn-glycero-3-phosphocholine	
Molecular weight	902.358	
T_m (°C)	75	
Short name	18:0 PC (DSPC)	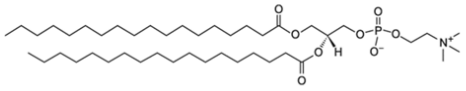
Chemical name	1,2-distearoyl-*sn*-glycero-3-phosphocholine	
Molecular weight	790.145	
T_m (°C)	55	
Short name	16:0 PC (DPPC)	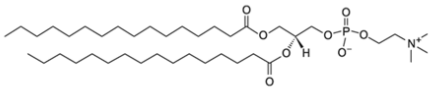
Chemical name	1,2-dipalmitoyl-sn-glycero-3-phosphocholine	
Molecular weight	734.039	
T_m (°C)	41	
CMC (nM)	0.46	
Short name	14:0 PC (DMPC)	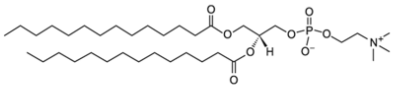
Chemical name	1,2-dimyristoyl-sn-glycero-3-phosphocholine	
Molecular weight	677.933	
T_m (°C)	24	
CMC (nM)	6	
Short name	12:0 PC (DLPC)	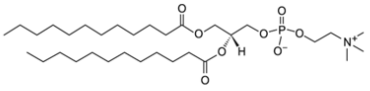
Chemical name	1,2-dilauroyl-sn-glycero-3-phosphocholine	
Molecular weight	677.933	
T_m (°C)	-2	
CMC (nM)	90	
Short name	10:0 PC (DDPC)	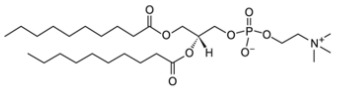
Chemical name	1,2-didecanoyl-sn-glycero-3-phosphocholine	
Molecular weight	565.720	
CMC (nM)	5000	

Table 1: Phosphatidylcholines (PCs) employed in the current study. The short names, chemical names, molecular weights, transition temperatures (where applicable), and critical micelle concentrations (CMC) (where applicable), and molecular line drawings (right) courtesy of Avanti Polar Lipids are provided for each of the fully saturated PCs employed in the current study in order of descending chain length from top to bottom.

3.2.2. MB preparation

22:0 PC-PEG40S MB were chosen for sonoporation experiments because they were shown not to significantly alter the lipid order of cell membranes (unlike 18:0 PC-PEG40S MBs) which is desirable for investigating the impact of PC liposome exposure on sonoporation (see Chapter 2). 22:0 PC-PEG40S MB were prepared according to the protocol detailed in Chapter 2. The average MB size distribution and sizing statistics can be seen in Figure 1A. A representative brightfield image of 22:0 PC-PEG40S MB used in the sonoporation experiments can be seen in Figure 1B. MBs had a mean diameter of 2.3 ± 0.3 µm and were produced at a concentration of 1.41 ± 0.66 x 10^9 (n=5).

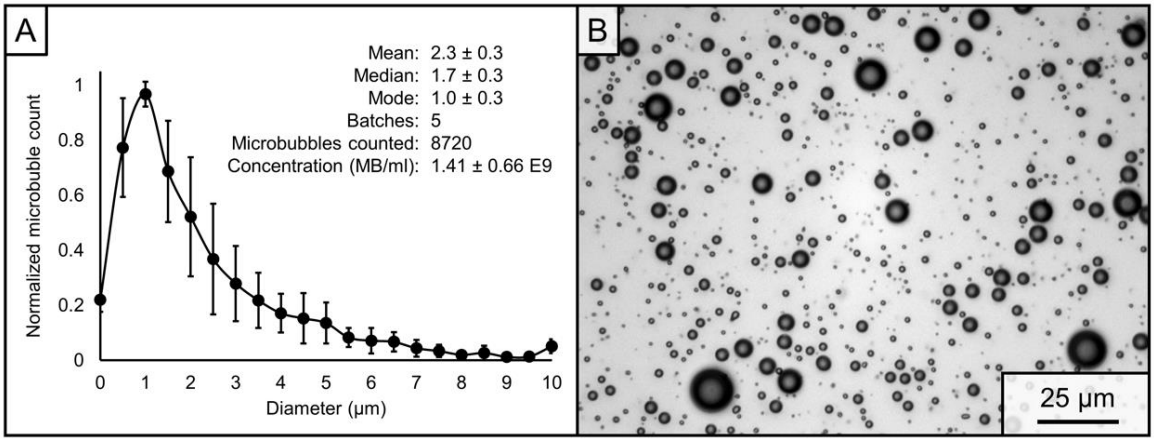

Figure 1: 22:0 PC-PEG40S microbubbles used for sonoporation experiments. Size distribution (A) and representative image (B).

3.2.3. Cell culture

Cells were grown on Ibidi µ-Dishes as described in Chapter 2.

3.2.4. Spectral imaging experiments

Cells were exposed to liposomes containing a single PC species for either ~90s or 10 min. Cells were then washed with PBS and labelled with C-Laurdan (400 nM) for ~1 min prior to spectral imaging (see Figure 2A). In experiments concerning the time-

dependence of cell lipid order on exposure to PCs, PCs were not removed from the sample and multiple spectral imaging acquistions of C-Laurdan emission spectra were performed (see Figure 2B). Detailed spectral imaging methods are presented in Chapter 2.

3.2.5. Viability assays

3.2.5.1. Propidium iodide and calcein-AM

Cells were treated with PCs for 10 min, washed with PBS, and co-labelled with propidium iodide (15 µM) to identify cells with compromised cell membranes, and calcein-AM (5 µM) to identify living cells (see Figure 2C). After a 5~ min incubation at 37°C, cell permeabilization and viability were assessed qualitatively by confocal microscopy. In sonoporation experiments, the propidium iodide and calcein-AM labelling methods detailed in Chapter 2 were employed.

3.2.5.2. MTS assay

In the presence of phenazine methosulfate (PMS), present in metabolically-active cells, MTS reagent (3-(4,5-dimethylthiazol-2-yl)-5-(3-carboxymethoxyphenyl)-2-(4-sulfophenyl)-2H-tetrazolium) produces a formazan product with an absorbance at 490 nm. MTS assays were performed to determine the cytotoxicity of PCs that induced large changes in cell lipid order and/or cell permeability (see Figure 2E). Cells grown for at least 24 h in 96-well plates were treated for 24 h, washed with PBS, and exposed to MTS reagent diluted 1:6 in PBS for ~15 min before absorbance spectra were then measured using a fluorescence plate reader. Samples were remeasured at 5 min intervals until the absorbance reached optimal levels (e.g. just below the level at which the relationship between absorbance and formazan concentration becomes non-linear). The baseline-corrected formazan product absorbance at 490 nm was then compared to

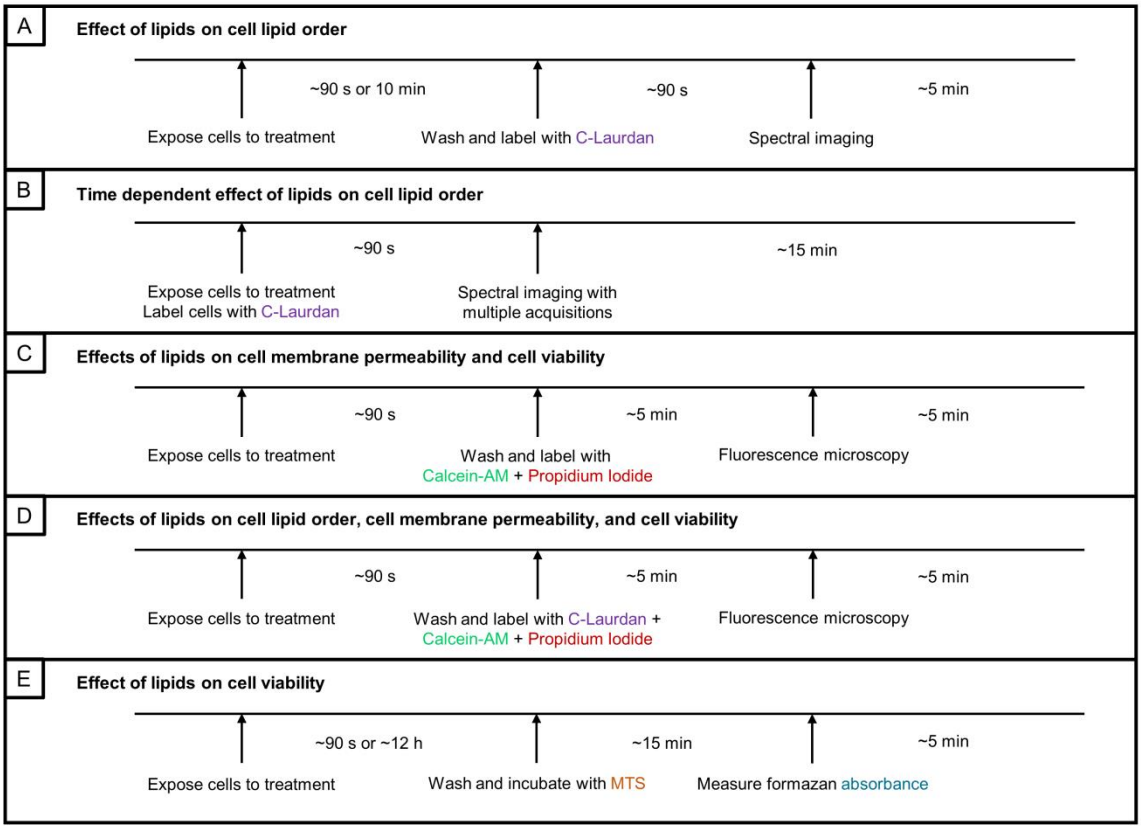

Figure 2: Timing for experiments investigating the effect of PCs on cell lipid order, membrane permeability, and viability.

control values to quantify cell viability.

3.2.6. Combined spectral imaging and viability assessment

In the case where exposure to PCs resulted in a change in cell membrane permeability, spectral imaging with C-Laurdan fluorescence, and fluorescence microscopy with propidium iodide and calcein-AM were performed on the same cell samples to determine whether the permeabilized cells also experienced a change in lipid order. This is described graphically in Figure 2D.

3.2.7. Sonoporation experimental methods

To investigate the effect of PC-induced cell lipid order modulation, cells were pre-treated with 12:0 PC for 0 (control), 5, or 10 min prior to sonoporation (see Figure 3). Following incubation with 12:0 PC, cells were washed with PBS and immediately exposed to ultrasound and 22:0 PC-PEG40S MBs (5.5 E7 MB/ml). The time between PC removal and ultrasound exposure was ~60 s. The sonoporation methods, including acoustic emissions monitoring and fluorescence microscopy of propidium iodide and calcein-AM, were otherwise identical to the methods described in Chapter 2.

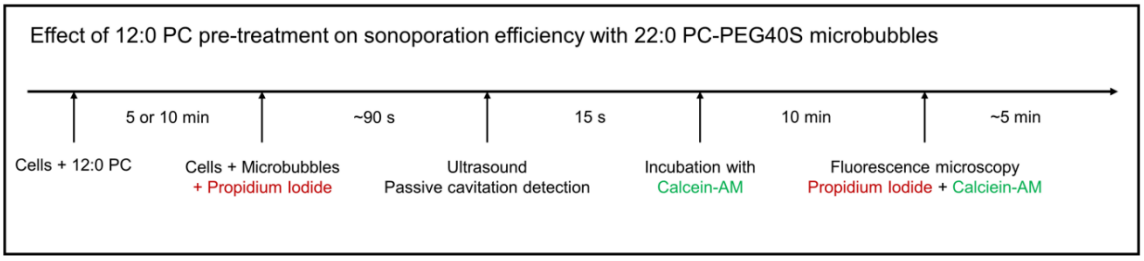

Figure 3: Sonoporation with 12:0 PC pre-treatment experimental timeline.

3.3. Results

3.3.1. Effect of hydrocarbon chain length

A-549 cells were treated with liposomes composed of saturated PCs of varying chain length for ~90 s at a concentration of 5 mM. This concentration and duration of treatment was chosen to represent that of a typical *in vitro* sonoporation experiment. Greater effect would be expected at higher concentrations and for longer exposure times[3]. Representative maps of C-Laurdan generalized polarization (GP), representative of cell lipid order, are presented in Figure 4. While the differences in the average GP of cells treated with 12:0 PC or 14:0 PC and control cells were not statistically significant,

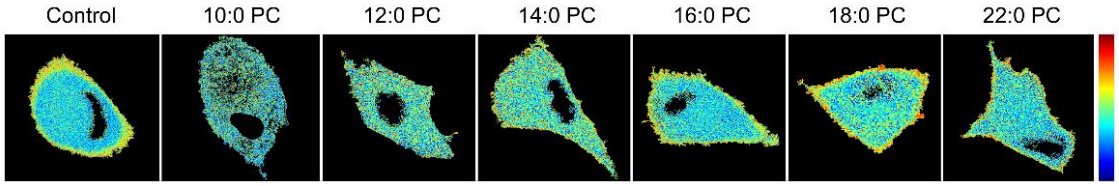

Figure 5: Representative GP maps of A-549s cells treated with 5 mM PCs of varying chain length for 90 s. The lower chain length PCs (10:0, 12:0, 14:0) appeared qualitatively different from control cells and those treated with longer PCs (16:0, 18:0, and 22:0).

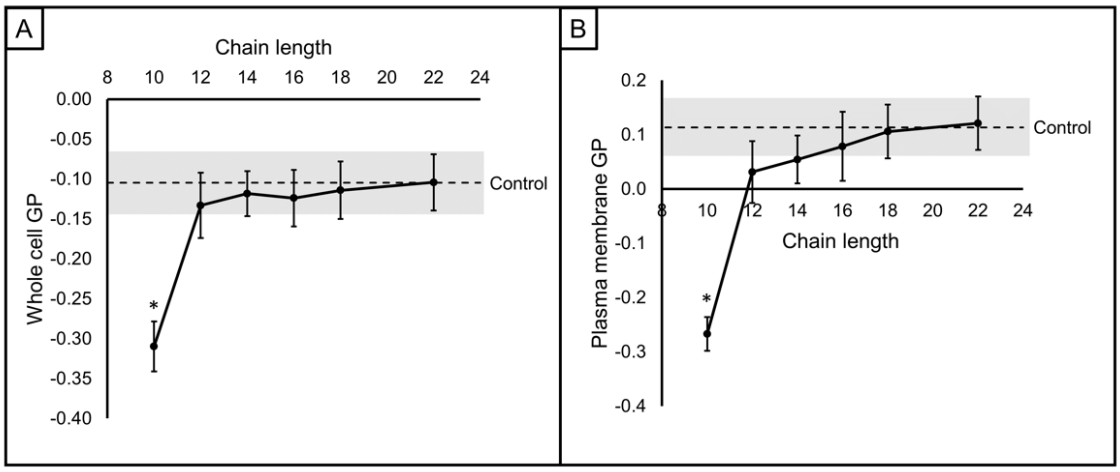

Figure 4: The effect of saturated phosphatidylcholine (PC) lipids of varying hydrocarbon chain length on A-549 cell lipid order. Cells were exposed to 5 mM PC at 37°C for ~90 s prior to spectral imaging with C-Laurdan (n = 5 each). Plots show the mean and standard deviation of generalized polarization (GP ∝ lipid order) for (A) whole cells and (B) segmented cell membranes. Statistical significance (*) is indicated for conditions with $p < 0.01$ from Tukey-Kramer post-hoc following 1-way ANOVA.

many of the treated cells appeared qualitatively altered (see Figure 5).

While PCs with a chain length below 16 were expected to effect the thermal behaviour of cell lipids[4,5], only 10:0 PC was found to induce a significant effect on cell membrane and intracellular lipid order. The effect of 10:0 PC was drastic, lowering cell membrane GP by nearly the entire physiological range[6] ($\Delta GP \sim -0.38$), especially compared to that achieved by 18:0 PC-PEG40S MBs described in Chapter 2 ($\Delta GP \sim -0.05$)[1]. Furthermore, the change in membrane GP induced by 18:0 PC-PEG40S MBs was limited to cell membranes whereas 10:0 PC was found to additionally disorder intracellular lipids.

Finally, it is worth observing the linearity between chain length and membrane GP from 12:0 to 18:0 PC. In the sections that follow it is shown that longer exposure times do indeed result in statistically significant changes in cell membrane lipid order for exposure to 12:0 and 14:0 PC in a chain length dependent manner. This observation is consistent with Ferrell et al. who demonstrated an exponential increase in PC monomer dissociation and transfer from vesicles to cells with decreasing phospholipid chain length[7].

3.3.2. 10:0 PC liposomes are lipid disordering, permeabilizing, and cytotoxic

In the previous section investigating the role of hydrocarbon chain length in the ability of PCs to modify cell lipid order, it was found that 10:0 PC severely reduced the lipid order of cells at both the whole cell and plasma membrane levels. This effect was not observed for the other hydrocarbon chain lengths and was thus investigated further.

Further investigation revealed that 10:0 PC disorders lipids in cell membranes and intracellular vesicles in a concentration-dependent manner as quantified by C-Laurdan GP (e.g. lipid order, see Chapter 2). The concentration threshold required to induce a

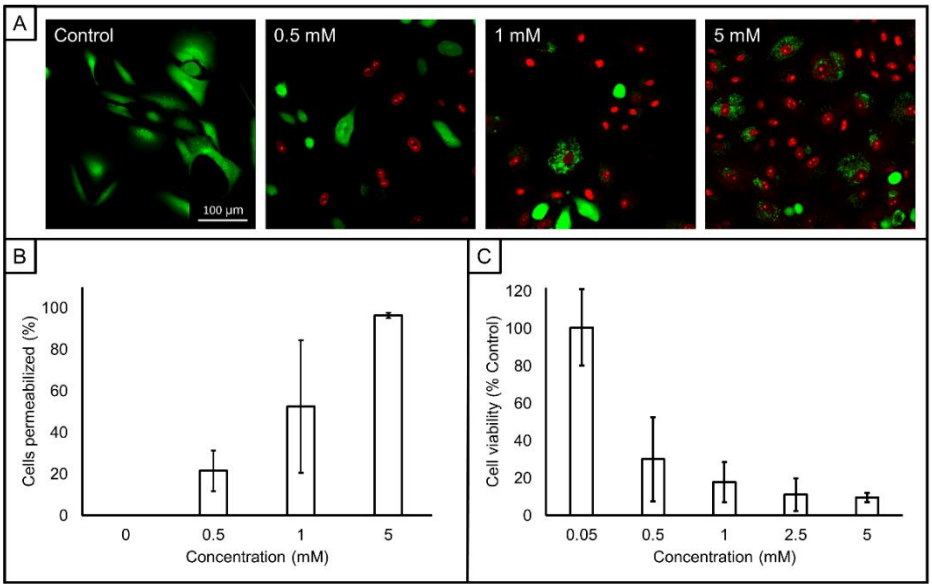

Figure 6: The effect of 10:0 PC on A-549 cell permeability and viability. (A) Representative fluorescence microscopy images of cells stained with Calcein AM (green) and Propidium Iodide (red) exposed to 10:0 PC at 0, 0.5, 1, and 2.5 mM concentrations from left-to-right respectively. The mean and standard deviation in % of cells permeabilized as indicated by Propidium Iodide uptake is quantified in (B) (n = 3, 5 images analysed per sample). Permeabilization alone does not indicate cell death. Panel (D) shows formazan product absorbance from an MTS assay. Cell viability can be estimated by the ratio of absorbance between 10:0 PC exposed cells and controls (e.g. 0 mM).

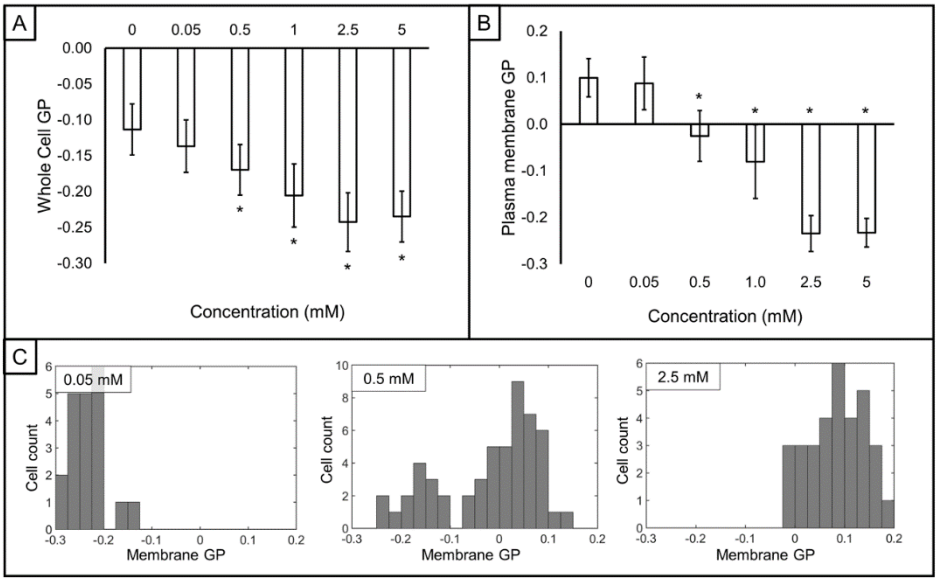

Figure 7: Effect of 10:0 PC concentration on A-549 cell lipid order. Cells were exposed to 10:0 PC at a range of concentrations (0, 0.05, 0.5, 1, 2.5, or 5 mM respectively) at 37°C for ~90 s prior to spectral imaging with C-Laurdan (n = 3 each). Panels (A) and (B) contain bar plots with the mean and standard deviation of generalized polarization (GP ∝ lipid order) vs. 10:0 PC concentration for (A) whole cells and (B) segmented cell membranes. Statistical significance (*) is indicated for conditions with $p < 0.01$ from Tukey-Kramer post-hoc following 1-way ANOVA. Panel (C) shows the same data represented in histograms of cell membrane GP for exposure to 10:0 PC at 0.05, 0.5, and 2.5 mM from left-to-right respectively. It can be observed from the histograms that the effect of 10:0 PC has a binary threshold between 0.05 and 1 mM for a ~90 s exposure.

significant response in cell lipid order was found to be between 50 µM and 500 µM (see Figure 6A-B). Lipid disordering by 10:0 PC was found to saturate at concentrations between 1 and 5 mM. The effect of 10:0 PC on individual cells was not dose-dependent, but rather acted in a step-like fashion such that cell lipid order was either completely unaffected or drastically reduced. This bimodal distribution in lipid order between cells was most evident at 500 µM 10:0 PC (see Figure 7C), which acted as a threshold above which 10:0 PC disordered the lipids of most cells exposed.

Following the measurement of intense lipid disordering from 10:0 PC exposure, the permeability of the cells were evaluated using a propidium iodide (PI) and calcein-AM assay performed by confocal fluorescence microscopy. Cell viability was also measured using a MTS assay. It was found that both permeabilization and cell death correlated with the lipid disordering induced by 10:0 PC, and exhibited the same concentration-dependence and threshold levels for effect onset and saturation (see Figure 7). A final

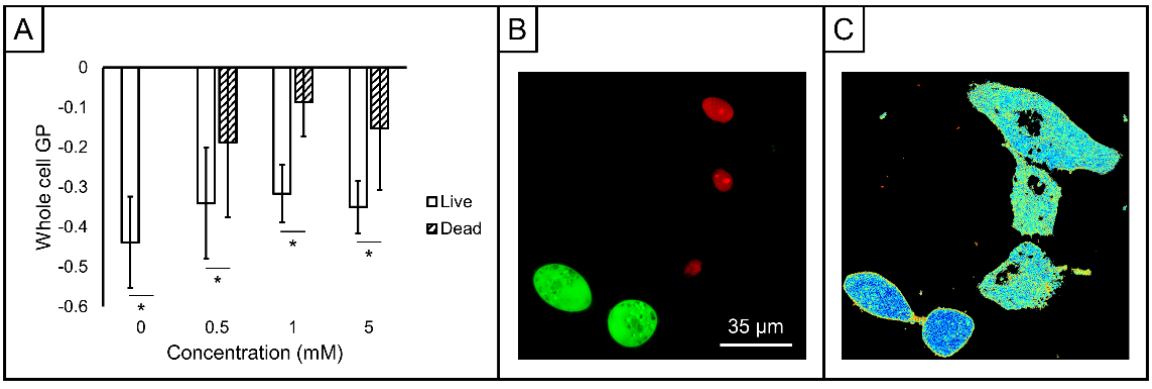

Figure 8: A-549 cells permeabilized by 10:0 PC also exhibit modulated lipid order. Cells were exposed to 10:0 PC at a range of concentrations (0, 0.5, 1, or 5 mM respectively) at 37°C for ~90 s prior to spectral imaging with C-Laurdan and fluorescence microscopy with Calcein-AM and Propidium Iodide (PI) (n = 3 each). Panel (A) shows the mean and standard deviation of whole cell C-Laurdan generalized polarization (GP ∝ lipid order) vs. 10:0 PC concentration for live (Calcein-AM staining only) and dead (PI staining) respectively. Statistical analysis by two-way ANOVA with 10:0 PC concentration and cell viability as factors followed by Bonferroni post-hoc tests revealed that viability was a significant factor for the change in lipid order. The same representative cells treated with 0.5 mM 10:0 PC as imaged by fluorescence microscopy with Calcein-AM (green) and PI (red), and spectral imaging with C-Laurdan are shown in panels (B) and (C) respectively.

experiment where cells were labelled with both C-Laurdan for spectral imaging of lipid order and PI and Calcein-AM for measuring permeabilization after 500 µM 10:0 PC exposure, revealed that only the cells that were lipid disordered were permeabilized (see Figure 8).

It is thus clear that at the concentrations in which 10:0 PC has an effect on cell lipid order, it is also permeabilizing and cytotoxic. Inhibition of ion flux by 10:0 PC could be responsible for the observed cell death[8]. 10:0 PC is thus not an ideal candidate for enhancing drug delivery in indications where preserving cell viability is desired.

3.3.3. 12:0 PC and 14:0 PC liposomes can disorder cell membrane lipids

Unlike longer chain PCs, short to medium chain length (e.g. 10:0 to 14:0) PCs are found only in scarce quantity in biological membranes. These shorter chain PCs are known to transfer more readily to cell membranes than their longer chain length

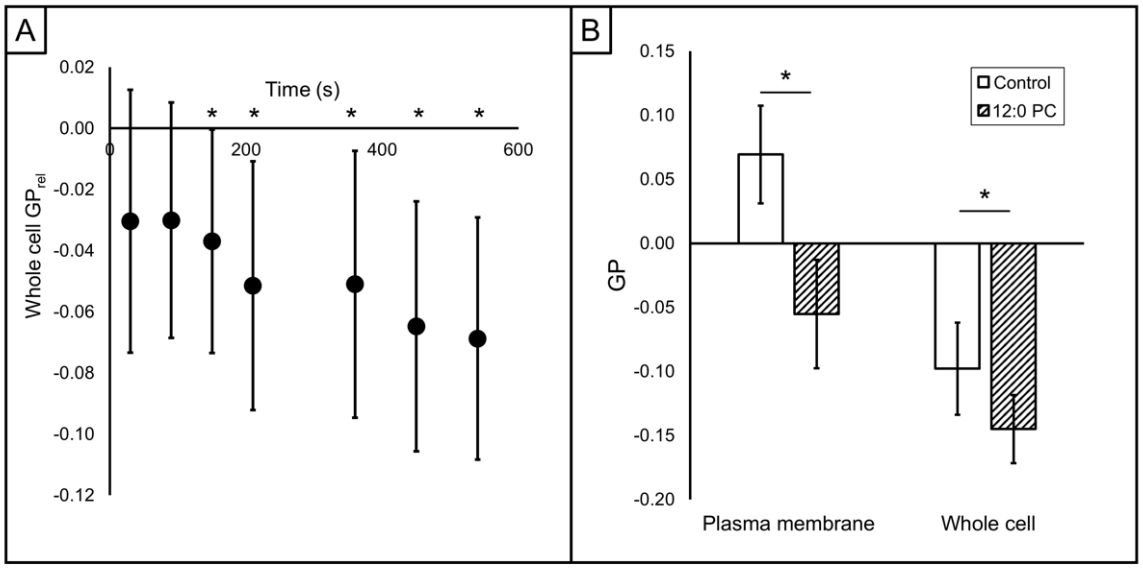

Figure 9: Effect of 12:0 PC on A-549 lipid order. A-549 cells were exposed to 5 mM 12:0 PC at 37°C for 10 minutes and either measured concurrently (A), or at the end of the treatment after washing (B), using C-Laurdan and spectral imaging. (A) Whole cell lipid order (as indicated by GP relative to controls) over time. Significant decrease of cell lipid order can be observed from 150 s exposure onwards. (B) At 10 min exposure with post-staining, both membrane and whole cell GP are significantly decreased. Both plots show means and standard deviations. Statistical significance is denoted by (*) for $p < 0.01$ using a one-way ANOVA and Bonferroni post-hoc in (A), and unpaired Student's t-tests in (B).

counterparts[7]. Having found severe effects induced by 10:0 PC in A-549 cells, and noting the decrease in lipid order with chain length in Figure 9 in which only a very brief exposure time was employed (~90 s), further investigation of the effects of 12:0 PC and 14:0 PC was undertaken with the hypothesis that these lipids would be similarly capable of disordering cell lipids given a higher concentration and/or longer exposure time. Owing to the greater similarity between 12:0 and 14:0 PC and endogenous lipids compared to 10:0 PC, it was posited that these lipids would be capable of altering cell lipid order with less severe consequences and ideally without inducing cell death at all.

It was found that 12:0 PC at 5 mM exhibited a time-dependent lipid disordering effect on A-549 cell membranes and intracellular lipids (see Figure 9) as determined by the experimental methods shown in Figure 1B. The GP relative to controls is plotted instead of absolute GP to account for drift from repeated exposures of the dye. By this

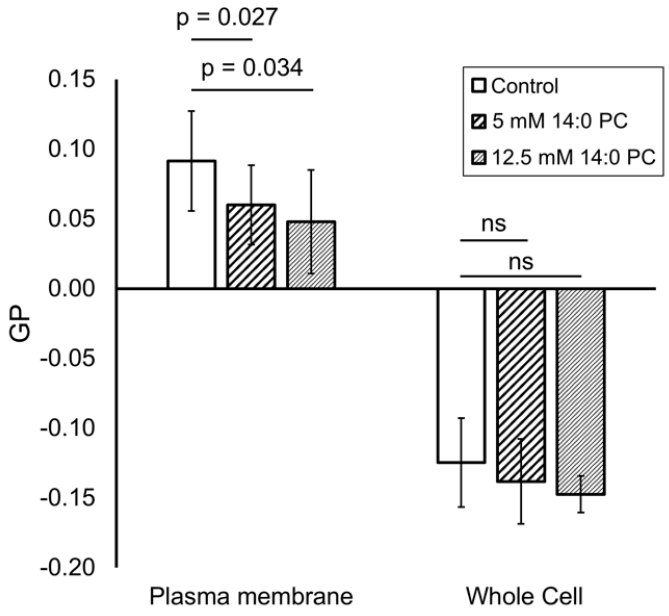

Figure 10: Effect of 14:0 PC on A-549 lipid order. A-549 cells were exposed to 14:0 PC at either 5 mM or 12.5 mM at 37°C for 10 minutes and measured using C-Laurdan and spectral imaging. (A) Whole cell lipid order (as indicated by GP relative to controls) over time. Statistical significance was tested using a two-way ANOVA with concentration and lipid exposure as factors followed by a Bonferroni post-hoc. P-values are displayed for changes in cell membrane lipid order for cells exposed to 5 mM and 12.5 mM 14:0 PC where $p < 0.05$. No conditions met a $p < 0.01$ significance level.

method it was found that at ~2 min exposure to 12:0 PC, a significant disordering of A-549 cell lipids became evident. This effect increased with exposure time until the end of the experiments (~10 min). This was confirmed by a more conventional GP measurement (see Figure 1A), performed on separate samples exposed to 12:0 PC for 10 min, then washed and labelled for spectral imaging. Exposure to 5 mM 12:0 PC for 10 min lowered cell membrane GP by 0.12 compared to control samples on average. This is more than double the change in GP induced by 18:0 PC-PEG40S MBs in Chapter 2 ($\Delta GP \sim -0.05$).

It was found that 14:0 PC reduced cell membrane lipid order at high concentrations (5 mM and 12.5 mM) following 10 min exposures (see Figure 10), but these changes were not statistically significant ($p > 0.01$) and were of a smaller magnitude than that of 18:0-PEG40S MBs (see Chapter 2). 14:0 PC exposure is thus not expected to enhance sonoporation under practical exposure conditions.

3.3.4. Acoustic emissions

Of the PCs investigated, 12:0 PC demonstrated the most potential for use in sonoporation experiments. 12:0 PC was found to disorder cell membrane lipids and intracellular lipids substantially ($\Delta GP \sim -0.12$) without the permeabilizing or cytotoxic effects of 10:0 PC. Thus, 12:0 PC was chosen for cell membrane modulation in sonoporation experiments.

Cells were pre-treated with 12:0 PC for either 5 or 10 min before sonoporation. Pre-treatment was used instead of co-injection with MBs to avoid the added complexity of 12:0 PC potentially altering the acoustic behaviour of the MBs. MBs, however, were observed to exhibit sufficient stability in the presence of 12:0 PC, which supports the

potential for co-injection of MBs and short to medium chain PC liposomes (data not shown).

No statistically significant differences observed for the total energy of harmonic acoustic emissions or for the harmonic acoustic emissions power over time between experiments with and without 12:0 PC pre-treatment were observed (see Figures 11-

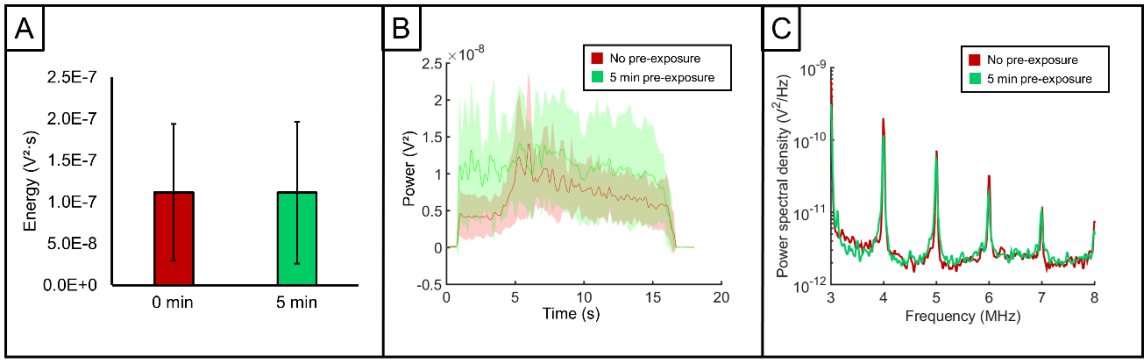

Figure 12: Acoustic emissions from 22:0 PC-PEG40S microbubbles used in sonoporation experiments at 37°C with and without pre-exposure of cells to 12:0 PC at 5 mM for 5 min. (A) Mean and standard deviation of the harmonic energy captured from acoustic emissions with and without 5 min pre-exposure to 14:0 PC. (B) The power in harmonic acoustic emissions vs time shown as mean (solid line) and 95% confidence interval (shaded area) with and without 5 min pre-exposure to 14:0 PC. (C) Representative power spectral density spectra for the acoustic emissions obtained during sonoporation experiments with and without 5 min pre-exposure to 14:0 PC. The data in (A), (B), and (C) are all from the same

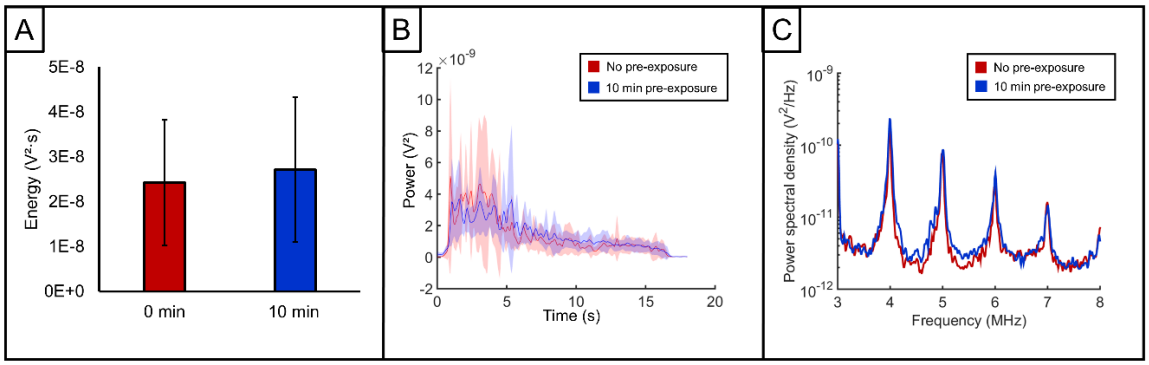

Figure 11: Acoustic emissions from 22:0 PC-PEG40S microbubbles used in sonoporation experiments at 37°C with and without pre-exposure of cells to 12:0 PC at 5 mM for 10 min. (A) Mean and standard deviation of the harmonic energy captured from acoustic emissions with and without 10 min pre-exposure to 14:0 PC. (B) The power in harmonic acoustic emissions vs time shown as mean (solid line) and 95% confidence interval (shaded area) with and without 10 min pre-exposure to 14:0 PC. (C) Representative power spectral density spectra for the acoustic emissions obtained during sonoporation experiments with and without 10 min pre-exposure to 14:0 PC. The data in (A), (B), and (C) are all from the same sonoporation experiments. The data in this figure was collected using a different filter than that of Figure 11 and so comparison of absolute energies and powers between these figures is to be avoided.

12). Any significant difference in sonoporation efficiency between samples exposed to 12:0 PC and control samples, therefore cannot easily be attributed to differences in cavitation dynamics between conditions.

3.3.5. Sonoporation with 12:0 PC pre-treatment

It was found that variations in cell density and acoustic emissions between samples and across conditions were not significant factors in determining the resultant sonoporation efficiency (see Figure 13 B-C). Furthermore, MB sizes were not statistically different and MB concentrations were matched across all experiments (as in Chapter 2). In addition, it can be seen that a narrow range of cavitation behaviours were induced, as intended by the experimental design, and also as in the sonoporation experiments in Chapter 2 (see Figure 13 C). With these factors excluded, any significant differences in the percentage of cells permeabilized in these experiments can be attributed to the effect of 12:0 PC exposure.

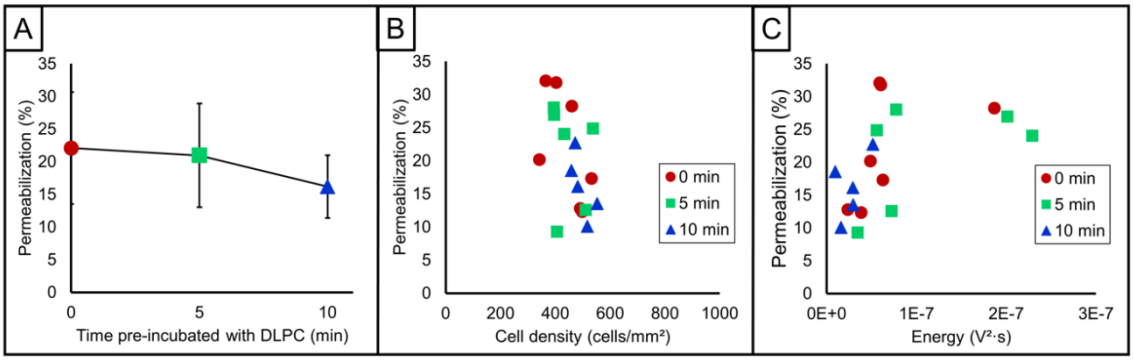

Figure 13: Effect of 14:0 PC pre-treatment on sonoporation efficiency. The percentage of permeabilized cells was measured immediately after sonoporation using a Calcein-AM and Propidium Iodide (PI) assay whereby any cell stained with PI was considered permeabilized. (A) Mean and standard deviation of permeabilization fraction as a function of 14:0 pre-treatment time (n = 6). While a decrease in permeabilization with pre-incubation time can be observed, no significant difference was found using a one-way ANOVA. (B) Scatter of the permeabilization data vs the observed cell density indicating no dependence between the two variables across the experiments. (C) Scatter of permeabilization data vs the measured harmonic energy in acoustic emissions indicating no dependence between the two variables across the experiments. In (B) and (C) each point represents an independent sonoporation experiment sample for pre-exposure times to 14:0 PC of 0 min (red circles, e.g. no pre-treatment), 5 min (green squares), and 10 min (blue triangles) respectively.

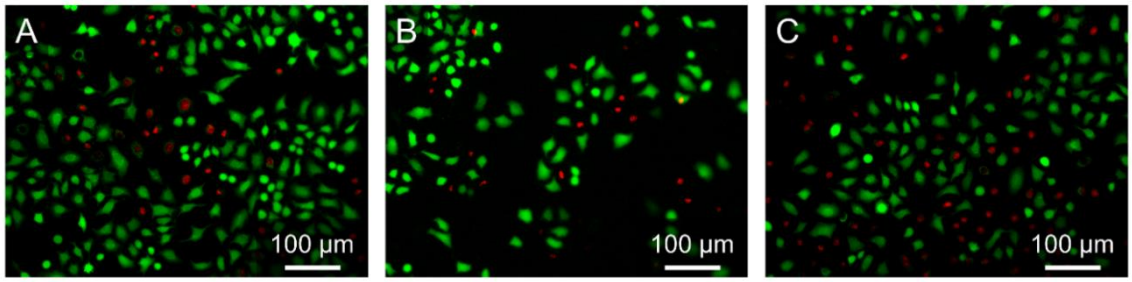

Figure 14: Representative microscopy images of cells following sonoporation with and without pre-treatment with 5 mM 12:0 PC. Cells were exposed to ultrasound and microbubbles in the presence of propidium iodide, a permeability tracer (red). Cells were then labelled with calcein-AM to mark non-permeabilized cells (green). Cells in (A) were not exposed to 12:0 PC. Cells in (B) and (C) were pre-treated with 12:0 PC for 5 min and 10 min respectively prior to sonoporation with ultrasound and microbubbles. No overall differences in cell morphology were evident across the three conditions.

Without pre-treatment with 12:0 PC, 22.09 ± 8.56% of cells were permeabilized by 22:0 PC-PEG40S MBs and ultrasound exposure. With 5 min exposure to 12:0 PC immediately prior to sonoporation, 20.96 ± 7.96% of cells were permeabilized. Extending pre-treatment 12:0 PC exposure times to 10 min resulted in 16.20 ± 4.81% cell permeabilization. Thus, despite the significant effect on cell lipid order which was expected to reduce the energy required for pore formation, it was found that pre-treatment with 12:0 PC had no significant effect on sonoporation (see Figure 13A). Furthermore, cell morphologies across the conditions tested were qualitatively indistinguishable (see Figure 14). The difference in cell permeabilization between 10 min 12:0 PC exposure and 0 and 5 min 12:0 PC exposure can be attributed to the three samples with slightly higher energies of harmonic acoustic emissions (see Figure 13C). Nonetheless, this difference was not statistically significant ($p > 0.05$, $n = 6$).

3.4. Discussion

3.4.1. On the effects of 10:0 PC on cells

Upon investigating the role of PC chain length in the effect of PC exposure on cell lipid order, it was found that 10:0 PC disorders cell membrane and intracellular lipids,

permeabilizes cells, and induces deleterious effects on cell metabolism and viability at concentrations commensurate with the observed changes in lipid order. In this section, these results are contextualized with regard to the literature and novel aspects of the present study are highlighted.

10:0 PC is known to enhance the transport of various polar compounds (e.g. human growth hormone or insulin) through the nasal epithelial barrier and the skin[9,10]. In the 1990s, pharmaceutical company Novo-Nordisk developed a liposomal formulation for insulin delivery that employed 10:0 PC-mediated absorption enhancement of the nasal airway epithelium. As a result of low bioavailability compared to subcutaneous injection, however, the formulation was not pursued further[10]. Absorption enhancement by 10:0 PC in the literature is consistent with the total sample permeabilization observed in the present study above threshold concentration of 500 µM.

In the literature, 10:0 PC has also been associated with the inhibition of sodium pumps[5,8]. Röpke and colleagues found that 10:0 PC rapidly and irreversibly inhibited intracellular ion flux and increased intercellular (e.g. junctional) ion flux in rabbit epithelium and in frog skin. Dwight and Hendry found that such effects were inhibited when 10:0 PC vesicles were prepared in a 3:4 molar ratio with cholesterol, suggesting a role for lipid transfer and/or cellular cholesterol depletion in the observed effects[5]. The results of the present study suggest that 10:0 PC-induced sodium pump inhibition may arise from the disordering of lipid rafts essential to sodium pump function[11].

Vermehren and Hansen also found that 10:0 PC had marked effects on cell viability (~50% haemolysis at ~200 µM for 30 min)[12]. This threshold is in total agreement with the present study in which the threshold for cell death was found to be between ~50 µM and ~500 µM for a 10 min exposure. Interestingly, Vermehren and Hansen found a

narrow window for modifying red blood cell membranes without inducing haemolysis at ~100 μM 10:0 PC for 30 min, while the threshold for cell death and for lipid disordering coincided in the present study. This may result from the differences between cell lines and between adherent and non-adherent cells.

10:0 PC exposure has also been associated with a concentration dependent increase in lipid transfer resulting in up to a 15% increase in total cellular acyl chain content following a 30 min exposure at 500 μM[5,13]. This is in agreement with the present study in which concentration-dependent lipid disordering was observed when observing sample-wise changes in lipid order. Wherein these studies observed sample-wise changes in cell lipid composition, the spectral imaging technique employed in the present study enables determination of changes in lipid thermal behaviour at the individual cell level. Consequently, the bimodal distribution of cells affected and unaffected by 10:0 PC exposure at the threshold concentration (~500 μM) has not been reported elsewhere. Furthermore, this is the first study to show that the 10:0 PC disorders both cell membrane and intracellular lipids. Lipid transfer, cholesterol depletion, and the inhibition of sodium pumps may contribute to the disordering of intracellular lipids. Transbilayer diffusion or so-called "flip-flop" of PCs may also play a role. It has been shown that PCs, for instance, have a lower activation energy for flip-flop than other phospholipid head groups[14]. Furthermore, the rate of flip-flop is doubled for every reduction of phospholipid chain length by two methylene groups, such that 10:0 PC has the highest flip-flop rate of the saturated phospholipids with low water solubility[14]. While the PC flip-flop half-life ranges from hours to days in model membranes, minutes or less have been reported in biological membranes, attributed to the presence of proteins. Thus disordering of intracellular lipids by the transfer of 10:0

PC to the cell membrane and subsequent flip-flop into the intracellular comportment cannot be neglected.

3.4.2. On the effects of 12:0 PC and 14:0 PC on cell membrane lipids

Exposure to 5 mM 12:0 PC was found to significantly disorder cell membranes within 2 min, an effect that intensified with increasing exposure time. 14:0 PC at 5 and 12 mM was found to lower cell membrane lipid order on average but was not statistically significant. This is in agreement with the findings of Stoll et al.[4] who showed that 12:0 PC and, to a lesser extent, 14:0 PC altered the phase behaviour of liposomes and red blood cell lipids. The present study demonstrated that exposure to 12:0 PC can disorder cell membranes two orders of magnitude faster than determined by Stoll et al.

As with 10:0 PC, 12:0 PC but not 14:0 PC, has been observed to inhibit sodium pumps[5]. Inhibition of sodium pumps may explain the results of the present study. It was found that 10:0 PC and 12:0 PC both induce lipid disordering in cell membranes and intracellular lipids, whereas 14:0 PC only affected lipid order at the cell membranes. If ion pumps are inhibited, the impairment of ion concentration regulation and the change in osmotic stress would be expected to alter the intracellular lipid order[15].

Lipid transfer from both 12:0 PC and 14:0 PC to the red blood cell membranes has also been confirmed by multiple studies[4,5]. In addition, Stoll et al. showed that the cholesterol-to-lipid ratio increased substantially in liposomes and decreased substantially in cells following treatment with 12:0 PC liposomes. Furthermore, an equimolar preparation of 12:0 PC and cholesterol did not alter cell lipid phase behaviour. Together this demonstrates that the mechanisms of 12:0 PC-induced cell lipid disordering include both lipid transfer from liposomes to cells and cell membrane cholesterol depletion.

In the present study it was found that shorter chain length PCs are capable of rapidly altering cell lipid order (within 90 s or 10 min depending on chain length). Cholesterol, owing to its increased solubility in water compared to PCs, can transfer from cells to liposomes much faster than PCs exchange between cells and liposomes[16], and thus may play a more critical role in the present study.

Finally, this study demonstrates that spectral imaging with polarity-sensitive probe C-Laurdan can provide insights that agree with results obtained by FITR, MALDI-TOF, colorimetric assays, and other analytical biochemistry techniques. While spectral imaging does not provide a direct quantification of lipid transfer or lipid/cholesterol ratio, it provides a mechanism-agnostic measurement of local lipid hydration or lipid order with superior temporal and spatial resolution, and is the only technique compatible with live confocal imaging. It is thus recommended that future studies on the interactions between lipid-shelled vessels and cells use a combination of spectral imaging with polarity-sensitive probes and analytical biochemistry techniques for interrogating the mechanisms underpinning the observed effects on lipid order.

3.4.3. Longer chain length MBs were more effective agents for sonoporation

In this study, 22.09 ± 8.56% of cells were permeabilized following exposure to 22:0 PC-PEG40S MBs and ultrasound exposure. Under the same ultrasound exposure conditions and MB concentrations, 22:0 PC-PEG40S MBs achieved significantly greater permeabilization than that achieved by the 18:0 PC-PEG40S MBs (6.15 ± 3.48%) employed in Chapter 2. Extending the chain length of the carrier lipid in the MB formulation from 18 to 22 hydrocarbons thus had a remarkable impact on sonoporation efficiency.

This result can be understood in terms of MB stability. As PC chain length is increased, the lipid packing and monolayer thickness is increased, lowering the diffusivity of gas through the lipids and increasing the diffusion distance, resulting in greater gas permeation resistances through the MB shells. Borden and Longo measured gas permeation resistances through PC-PEG40S MBs and found 86 ± 56 s/cm for 18:0 PC-PEG40S MBs and 315 ± 72 s/cm for 22:0 PC-PEG40S MBs[17]. The mechanical properties of PC-PEG40S MB shells have also been measured by visualizing the MB shells under manipulation by a micropipette[18]. Surface shear viscosity, defined as the ratio of tangential force per unit length of the surface to the rate of strain of the surface produced by the stress, and the surface yield shear, defined as the stress that a monolayer can sustain before undergoing two-dimensional shear flow, were both found to be significantly greater for 22:0 PC-PEG40S MBs as compared to 18:0 PC-PEG40S MBs. Furthermore, as shown in Chapter 2, 22:0 PC forms more stable complexes with PEG40S as opposed to 18:0 PC-PEG40S MBs which "squeeze out" most of the PEG40S from their MB shells[19,20]. The steric hindrance afforded by increased association of PEG40S with the 22:0 PC-containing MBs could further contribute to their enhanced stability. Taken together, 22:0 PC-PEG40S are expected to be more stable MBs.

While the mean energy and max power of the harmonic acoustic emissions from 22:0 PC-PEG40S MBs and 18:0 PC-PEG40S MBs were not significantly different, a difference in the stability of the emissions over time was observed. The time constants for an exponential decay of the form, $f(t) = Ae^{-\frac{1}{\tau}t}$, for the average power of harmonic acoustic emissions over time (calculated for a period > 30% of the exposure time) was $\tau \sim 15.6$ s ($R^2 = 0.84$) for 22:0 PC-PEG40S MB and $\tau \sim 2.4$ s ($R^2 = 0.88$) for 18:0 PC-PEG40S MB (see Chapter 2) as acquired with the same experimental hardware and

under the same ultrasound exposure conditions. The acoustic emissions data presented herein thus agree with the notion that MB stability is the primary mechanism by which greater sonoporation is achieved with PC-PEG40S MBs produced with longer chain lengths. Interestingly, more effective BBB opening with 22:0 PC-PEG40S MB compared to 18:0 PC-PEG40S MBs has also been observed *in vivo* and associated with MB stability[21], although to the author's knowledge this is the first time this effect has been directly observed for sonoporation. The dependence of this effect on ultrasound exposure parameters is left for future investigation.

3.4.4. On sonoporation with 12:0 PC pre-treatment

In Chapter 2, from the literature and the presented dimensional/theoretical arguments, it was shown that as the lipid order decreases in pure lipid bilayers, the energy required for pore formation would also decrease. It was found that exposure to unwashed 18:0 PC-PEG40S MBs lowered cell lipid order but did not enhance sonoporation compared to non-membrane modulating washed MBs.

In this chapter, a systematic study of the effects of fully-saturated PCs on cell membrane lipid order was conducted. It was found that 12:0 PC was the best candidate for disordering cell membranes without reducing cell viability. Exposure to 12:0 PCs resulted in a reduction in cell membrane C-Laurdan GP (e.g. lipid order) ($\Delta GP \sim -0.12$) that was more than 2-fold that induced by 18:0 PC-PEG40S MB exposure in Chapter 2 ($\Delta GP \sim 0.05$). It was thus hypothesized that exposure to 12:0 PC would further lower the energy barrier for pore formation, enhancing sonoporation. No such significant change in sonoporation efficiency, however, was observed.

Owing to the similarities in the mechanisms underpinning 10:0 PC and 12:0 PC disordering of cell membranes, a comparison of their relative effects may provide

further insight regarding this unintuitive result. For both of these PCs, PC transfer to cells and cellular depletion of cholesterol result in a disordering of membrane lipids which can disrupt membrane lipid rafts resulting in inhibition of sodium pumps and subsequent ionic osmotic stress that can induce further disordering of membrane lipids and intracellular lipids. In Chapter 2, a strong dependence on lipid chain length with regard to the energy barrier to pore formation was found. It is not unreasonable to assume that the average lipid chain length in cell membrane lipids is substantially reduced by incorporation of 15% 10:0 PC or 12:0 PC as has been demonstrated in similar experiments. Owing to its higher water solubility, 10:0 PC transfers more readily to cells than 12:0 PC and so it is not surprising that with higher transfer rates, and a shorter chain length, 10:0 PC further reduces cell lipid order and decreases the energy barrier to pore formation more than 12:0 PC.

It was found that 10:0 PC induces irreversible cell permeabilization commensurate with a reduction in cell membrane GP of $\Delta GP \sim -0.38$. Thus, a reduction in lipid order in this range appears to bring the critical energy for pore formation to within the thermal fluctuations of the bilayer such that pores can form and stabilize, resulting in cell permeabilization and death. 12:0 PC resulted in a $\Delta GP \sim -0.12$ which was found not to reduce the energy barrier to pore formation sufficiently to observe a difference in sonoporation efficiency. It follows that if cell lipid order could be modulated by saturated PCs in order to enhance sonoporation the change in lipid order would need to be in the range defined by the effects of these two species ($-0.38 < \Delta GP < -0.12$). It is clear from this work that to achieve such a change in GP without inducing cell death would require either PC concentrations that are too high, or exposure times to PCs that are too long, to be useful in drug delivery applications.

While it is conceivable that more efficient deposition of PCs into cell membranes could be achieved by PC co-injection with MBs rather than pre-treatment with PCs before sonoporation, e.g. by cavitation-induced fluid mixing and/or so-called "sonoprinting"[22,23], the concentrations employed are already high (5 mM), and the effect of co-injection of 12:0 PC on MB cavitation behaviour could render a direct comparison of sonoporation efficiencies difficult to interpret. Consequently, a co-injection study was not performed.

In summary, saturated PCs are not ideal candidates for enhancing sonoporation by cell lipid order modulation. It is hypothesized that an agent that achieves cell lipid disordering greater than that achieved by 12:0 PC but less than that achieved by 10:0 PC (e.g. $-0.38 < \Delta GP < -0.12$), such that cells are not irreversibly permeabilized by the agent alone, and the energy barrier to pore formation is lowered, could be employed to enhance sonoporation efficiency.

3.5. Concluding remarks

In this chapter, the ability of saturated phosphatidylcholine lipids (PCs) to modulate the lipid order of cell membranes and intracellular vesicles was investigated. The hydrocarbon chain length of PCs was varied from 10:0 PC to 22:0 PC and further experimentation was performed on those PCs (10:0, 12:0, and 14:0) which induced the most significant changes in cell membrane and intracellular lipid order. 12:0 PC was determined to have the most potential for use in ultrasound-mediated drug delivery without inducing cell death. Pre-treatment with 12:0 PC, however, was found not to have a significant effect on sonoporation efficiency for the experimental conditions tested. Nonetheless, several scientific contributions, not published elsewhere to the author's knowledge, were achieved throughout this investigation. Namely,

(1) 10:0 PC exposure rapidly (~90 s) alters the lipid order of cancer cell (A-549) plasma membranes and intracellular lipids, permeabilizes cells, and is cytotoxic with an on-off threshold between 50 μM and 500 μM exposure.

(2) 12:0 PC exposure at 5 mM rapidly (after ~150 s) disorders cancer cell plasma membranes and intracellular lipids without permeabilizing cells.

(3) 14:0 PC exposure for 10 min at 5 or 12.5 mM has a mild lipid disordering effect on cancer cell plasma membranes without inducing measurable changes in intracellular lipid order and without permeabilizing cells.

(4) Pre-treatment with 12:0 PC, which rapidly reduced the lipid order of cancer cell membranes, did not significantly alter sonoporation efficiency.

(5) Increasing the PC chain length from 18 to 22 in PC-PEG40S MBs resulted in MBs that produced more sustained acoustic emissions and a 3 fold increase in the percentage of cells sonoporated.

Cell membrane lipid disordering and hydration from the emulsifier PEG40S, employed in Chapter 2, and saturated 12:0 PCs, used in the present study, did not enhance sonoporation under the experimental conditions employed. Both of these results are counter-intuitive with regard to the dependence of pore formation on membrane hydration[24]. It is clear from the present study that saturated PCs at any reasonable concentration or exposure time would not be expected to enhance sonoporation. It is hypothesized that a lipid that rapidly disorders cell membrane lipids more than 12:0 PC but less than 10:0 PC (e.g. $-0.38 < \Delta GP < -0.12$), could be employed to enhance sonoporation. Having systematically evaluated the role of PC chain length on PC-mediated cell lipid disordering, it follows from the dimensional arguments in Chapter 2,

that the shape of the lipid could be further investigated for lowering the energy barrier to pore formation. Conical lipids, such as lysolipids, PCs with one hydrocarbon tail removed by hydrolysis, would be expected to further lower this energy barrier and should be compatible with phospholipid-shelled MBs owing to their positive spontaneous curvature. In the following chapter, the potential for drug delivery enhancement with lysolipids-containing thermosensitive liposomes exposed to mild hyperthermia is investigated.

3.6. References

1. Carugo, D. *et al.* Modulation of the molecular arrangement in artificial and biological membranes by phospholipid-shelled microbubbles. *Biomaterials* **113,** (2017).
2. Hosny, N. a *et al.* Mapping microbubble viscosity using fluorescence lifetime imaging of molecular rotors. *Proc. Natl. Acad. Sci. U. S. A.* **110,** 9225–30 (2013).
3. McLean, L. R. & Phillips, M. C. Mechanism of cholesterol and phosphatidylcholine exchange or transfer between unilamellar vesicles. *Biochemistry* **20,** 2893–2900 (1981).
4. Stoll, C. *et al.* Liposomes alter thermal phase behavior and composition of red blood cell membranes. *BBA - Biomembr.* **1808,** 474–481 (2011).
5. St Dwight, J. J. & Hendry, B. Effects of membrane incorporation of short-chain phospholipids on sodium pump function in human erythrocytes. *Clin. Chim. Acta* **243,** 73–85 (1995).
6. Parasassi, T., De Stasio, G., Ravagnan, G., Rusch, R. M. & Gratton, E. Quantitation of lipid phases in phospholipid vesicles by the generalized polarization of Laurdan fluorescence. *Biophys. J.* **60,** 179–189 (1991).
7. Ferrell, J. E., Lee, K.-J. & Huestis, W. H. Lipid Transfer between Phosphatidylcholine Vesicles and Human Erythrocytes: Exponential Decrease in Rate with Increasing Acyl Chain Lengthy. *Biochem. Proc. Natl. Acad. Sci. U.S.A. Biochem. Biophys. Res. White, J. G. Am. J. Pathol. Clin. Hematol. J. Lab. Clin. Med. Febiger* **24,** 2857–2864 (1985).
8. Röpke, M., Unmack, M. A., Willumsen, N. J. & Frederiksen, O. Comparative Aspects of Actions of a Short-Chain Phospholipid on Epithelial Na ♀ Channels and Tight Junction Conductance. *Biochem. Physiol* **118,** 211–214 (1997).
9. Vermehren, C., Hansen, H. S. & Thomsen, M. K. Time dependent effects of two absorption enhancers on the nasal absorption of growth hormone in rabbits. *Int. J. Pharm.* **128,** 239–250 (1996).
10. Hilsted, J. *et al.* Intranasal insulin therapy: the clinical realities. *Diabetologia* **38,** 680–684 (1995).
11. Simons, K. & Vaz, W. L. C. Model Systems, Lipid Rafts, and Cell Membranes. *Annu. Rev. Biophys. Biomol. Struct* **33,** 269–95 (2004).
12. Vermehren, C. & Hansen, H. S. Shape changes in the erythrocyte membrane induced by the absorption enhancer didecanoylphosphatidylcholine. *Int. J. Pharm.* **174,** 1–8 (1998).
13. Vermehren, C. & Hansen, H. S. Shape changes in the erythrocyte membrane induced by the absorption enhancer didecanoylphosphatidylcholine. *Int. J. Pharm.* **174,** 1–8 (1998).
14. Homan, R. & Pownall, H. J. Transbilayer diffusion of phospholipids: dependence on headgroup structure and acyl chain length. *Biochim. Biophys. Acta - Biomembr.* **938,** 155–166 (1988).
15. Arroyo, J., de Lopez, A. C. B., Bernik, D. L. & Disalvo, E. A. Surface Packing of

Lipid Bilayers in the Gel State Induced by Osmotic Stress As Measured by the Dimerization of Merocyanine 540. *J. Colloid Interface Sci.* **203,** 106–114 (1998).

16. Phillips, M. C., Johnson, W. J. & Rothblat, G. H. Mechanisms and consequences of cellular cholesterol exchange and transfer. *Biochim. Biophys. Acta* **906,** 223–276 (1987).

17. Borden, M. a. & Longo, M. L. Dissolution behavior of lipid monolayer-coated, air-filled microbubbles: Effect of lipid hydrophobic chain length. *Langmuir* **18,** 9225–9233 (2002).

18. Kim, D. H., Costello, M. J., Duncan, P. B. & Needham, D. Mechanical Properties and Microstructure of Polycrystalline Phospholipid Monolayer Shells: Novel Solid Microparticles. doi:10.1021/la034779c

19. Shen, Y., Powell, R. L. & Longo, M. L. Interfacial and stability study of microbubbles coated with a monostearin/monopalmitin-rich food emulsifier and PEG40 stearate. *J. Colloid Interface Sci.* **321,** 186–194 (2008).

20. Borden, M. a., Pu, G., Runner, G. J. & Longo, M. L. Surface phase behavior and microstructure of lipid/PEG-emulsifier monolayer-coated microbubbles. *Colloids Surfaces B Biointerfaces* **35,** 209–223 (2004).

21. Wu, S.-Y., Chen, C. C., Tung, Y.-S., Olumolade, O. O. & Konofagou, E. E. Effects of the microbubble shell physicochemical properties on ultrasound-mediated drug delivery to the brain. *J. Control. Release* **212,** 30–40 (2015).

22. De Cock, I., Lajoinie, G., Versluis, M., De Smedt, S. C. & Lentacker, I. Sonoprinting and the importance of microbubble loading for the ultrasound mediated cellular delivery of nanoparticles. *Biomaterials* **83,** 294–307 (2016).

23. Luan, Y. *et al.* Lipid shedding from single oscillating microbubbles. *Ultrasound Med. Biol.* **40,** 1834–1846 (2014).

24. Tieleman, D. P., Leontiadou, H., Mark, A. E. & Marrink, S.-J. Simulation of Pore Formation in Lipid Bilayers by Mechanical Stress and Electric Fields. *J. Am. Chem. Soc.* **125,** 6382–6383 (2003).

IV.

Cell membrane modulation by lysophosphatidylcholine for the enhancement of ultrasound-mediated drug delivery

4.1. Abstract

In Chapter 2, theoretical arguments and evidence from the literature indicated that the energy required for pore formation depends strongly on both the hydrocarbon chain length and lipid packing or shape. The results of Chapter 3 supported this premise, showing that the disordering of cell lipids from PC exposure is inversely correlated with hydrocarbon chain length (10:0 PC > 12:0 PC > 14:0 PC > 16:0 PC), with the shortest PC, 10:0 PC, inducing cell membrane permeabilization. It was hypothesized that treating cells with 12:0 PC prior to sonoporation would increase permeabilization compared to controls. When sonoporation enhancement was not observed, it was concluded that saturated PCs could not be used to enhance sonoporation by cell lipid order modulation, and that lipid disordering between that achieved with 10:0 PC and 12:0 PC may be required. The potential of PCs with a more conical shape, e.g. lysophosphatidylcholines (Lyso-PCs), to enhance ultrasound-mediated drug delivery is investigated in this chapter. Lyso-PCs are PCs partially hydrolysed such that one fatty acyl chain is removed.

Lyso-PC was hypothesized to promote pore formation during sonoporation for several reasons which are discussed at length in this chapter. Namely,

1) Lyso-PC is conical and its transfer to cell membranes should thus decrease the energy required for pore formation.
2) Lyso-PC has half the non-polar hydrocarbons of a non-hydrolysed PC of equivalent chain length, and thus exhibits higher rates of lipid transfer.
3) Lyso-PC has negligible rates of transverse diffusion across the bilayer owing to its reduced non-polar regions and conical shape, and thus induces curvature strain in the membrane via asymmetric changes in lipid packing between bilayer leaflets.

4) Lyso-PC has been shown to stabilize and promote pore formation in thermosensitive liposomes[1] (see Appendix I).
5) Lyso-PC is known to have effects on cell membrane lipids in red blood cells[2,3].

To this end, the effects of Lyso-PC on cell membrane lipid order and permeability were evaluated, and Lyso-PC-loaded MBs (Lyso-MBs) were developed for the ultrasound-mediated triggered release of Lyso-PC. Lyso-MBs were then assessed for their ability to potentiate sonoporation. It was found that ultrasound exposure of Lyso-MBs significantly increased the percentage of sonoporated cells compared to controls, a result which appears to arise from Lyso-PC-mediated effects on cell membranes.

4.2. Methods

4.2.1. Methods overview

The acute effects of Lyso-PCs on A-549 cancer cell membrane lipid order and permeability were evaluated by spectral imaging with C-Laurdan and fluorescence microscopy with propidium iodide by methods comparable to those employed in Chapter 3 (see Figure 1A-B). Lyso-MBs, MBs that incorporate Lyso-PC, were developed and compared with MBs loaded with non-hydrolysed PC lipids of equivalent

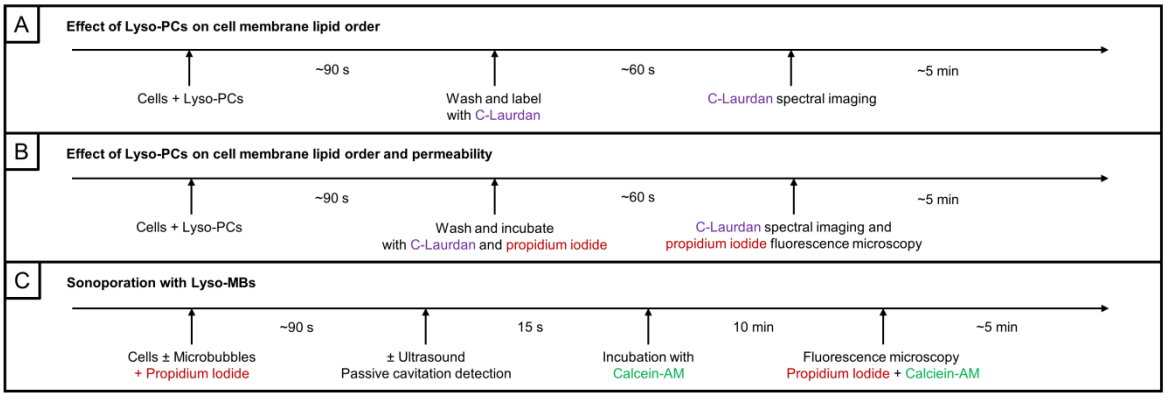

Figure 1: Experimental timelines for the experiments with cells in the present chapter.

hydrocarbon chain length for their sonoporation efficiency (see Figure 1C).

4.2.2. Lyso-PC preparation

In a parallel study, exposure of DLD-1 cancer cells to 1225 µM of either 16:0 Lyso-PC or 18:0 Lyso-PC, resulted in a substantial decrease in cell membrane lipid order (see Appendix I). The shorter chain length 16:0 Lyso-PC was found to have a significantly greater effect on cell membrane lipid order, which has also been reported elsewhere[3]. It follows that 16:0 Lyso-PC was employed in the present study for both its effects on cell membranes and its long hydrocarbon chain length well-suited to MB production.

Lyso-PC films were prepared by either evaporation of chloroform containing 16:0 Lyso-PCs (10 mg/ml) in glass vials on a 60°C hot plate for at least 12 h, or evaporation under vacuum and constant rotation in a water bath heated to 33°C for 30 min. Lyso-PC films were re-suspended in phosphate-buffered saline (PBS) under magnetic stirring at 85°C for 30 min. Re-suspended Lyso-PCs, which form mostly Lyso-PC micelles, were then dispersed by low power sonication for ~90 s. Lyso-PC films were always prepared within 24 h before experiments. Lyso-PCs were employed orders of magnitude above their critical micelle concentrations.

4.2.3. MB formulations, size, and concentration

MBs were formed by the sonication method described in Chapter 2. Formulations investigated include PC-PEG40S 9:1 molar ratio MBs as employed in Chapters 2 and 3, and the same formulation with the addition of either 16:0 Lyso-PC (referred to as Lyso-MBs) or 16:0 PC (referred to as PC-MBs). 22:0 PC-PEG40S 9:1 MBs are referred to as "Control-MBs" throughout this chapter rather than "22:0 PC MBs" as in Chapter 3, to avoid confusion whereby multiple MB formulations employed in this chapter contain 22:0 PC.

Microbubble	Lipids and emulsifiers	Gas	Molar Ratio	Experiments
Control-MB	22:0 PC, PEG40S	SF_6	9:1	Sonoporation Acoustic emissions characterization
Lyso-MB	22:0 PC, PEG40S, 16:0 Lyso-PC	SF_6	9:1:4	Sonoporation Acoustic emissions characterization
PC-MB	22:0 PC, PEG40S, 16:0 PC	SF_6	9:1:4	Sonoporation
Lyso-MB (16:0 PC carrier lipid, 9:1:1)	16:0 PC, PEG40S, 16:0 Lyso-PC	SF_6	9:1:1	MB formulations development
Lyso-MB (18:0 PC carrier lipid, 9:1:1)	18:0 PC, PEG40S, 16:0 Lyso-PC	SF_6	9:1:1	MB formulations development
Lyso-MB (22:0 PC carrier lipid, 9:1:1)	22:0 PC, PEG40S, 16:0 Lyso-PC	SF_6	9:1:1	MB formulations development

Table 1: MB formulations. Lipids, emulsifiers, and their molar ratios are provided for each MB formulation along with the experiments they are utilised in throughout the chapter. All MB formulations were filled with SF_6 gas.

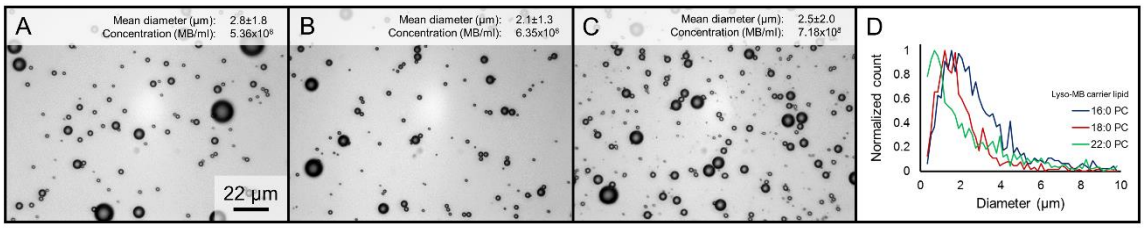

Figure 3: Lyso-MBs formed with carrier PC lipids of different hydrocarbon chain lengths. MB diameters and concentrations are shown with representative bright-field microscopy images in A-C for Lyso-MBs formed with 16:0 PC, 18:0 PC, and 22:0 PC carrier lipids respectively. Normalized histograms for MB size distributions are shown in panel D.

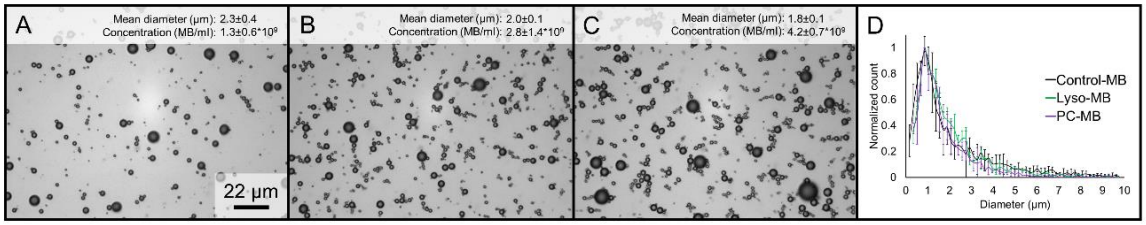

Figure 2: MB sizing and concentration used in sonoporation experiments. MB diameters and concentrations for three batches are shown with representative bright-field microscopy images in A-C for Control-MB, Lyso-MB, and PC-MB formulations respectively. Normalized histograms for MB size distributions are shown in panel D.

Initially, Lyso-MBs were formed by adding 16:0 Lyso-PC to PC-PEG40S 9:1 molar ratio MBs at a molar quantity equivalent to that of PEG40S (i.e. 9:1:1). It was found that Lyso-MBs could be produced with 16:0 PC, 18:0 PC, and 22:0 PC carrier lipids (see Figure 2). Lyso-MBs did not form in the absence of PEG40S in useable quantities. As the carrier lipid hydrocarbon chain length increased, so too did the concentration of Lyso-MBs.

Although Lyso-MBs were successfully produced with 16:0 PC and 18:0 PC carrier lipids, 22:0 PC was chosen as the carrier lipid for Lyso-MBs used in sonoporation experiments owing to its resulting in greater sonoporation than 18:0 PC-PEG40S MBs in previous experiments (see Chapters 2-3). Lyso-MBs were thus formed with 22:0 PC, PEG40S, and 16:0 Lyso-PC at a 9:1:4 molar ratio such that the Lyso-MB solution contained ~1.6 mM 16:0 Lyso-PC. After concentration matching to $5.5x10^7$ MB/ml with Control-MBs, Lyso-MBs had a final Lyso-PC concentration of either 25 or 80 µM for sonoporation experiments. Dilution for concentration matching was always performed immediately before sonoporation to limit the effects of dilution on MB size distribution, concentration, and stability.

PC-MBs were employed in sonoporation experiments as a control for the incorporation of a third constituent in Lyso-MBs. PC-MBs were formed with 22:0 PC, PEG40S, and 16:0 PC at a 9:1:4 molar ratio. Dilution for concentration matching yielded ~25 µM added constituent. To compare with the Lyso-MBs containing 80 µM Lyso-PC, however, PC-MBs were spiked with 16:0 PC liposomes immediately prior to sonoporation in order to achieve matching of both MB concentration and added constituent molarity.

4.2.4. Lyso-MB acoustic emissions and contrast imaging

The acoustic emissions and compatibility with ultrasound contrast imaging of Lyso-MBs and Control-MBs were characterized using a setup designed by Dr. Christophoros Mannaris[4i]. Briefly, MBs were flowed through a 1 mm diameter channel in a tissue mimicking flow phantom composed of degassed, low melting point, ultrapure agarose hydrogel (1.5% w/v). The flow phantom was submerged in a tank filled with filtered and degassed ddH_2O. Ultrasound was generated with a focused ultrasound transducer (H102, Sonic Concepts) driven with a sine-wave generated by a signal generator (Agilent) and amplified 55 dB with an RF amplifier (A300, E&I). Acoustic emissions were recorded with a coaxially and confocally-aligned passive cavitation detector (V320 Panametrics, Olympus), passed through a 5 MHz high-pass filter, and amplified 5x with a Stanford Research Systems pre-amplifier. The ultrasound transducer was calibrated at 1.0 MHz using a 0.4 mm diameter needle hydrophone (Onda 1121). Ultrasound contrast imaging was conducted using a linear array (L12-5) at low mechanical indices (MI) with an ultrasound imaging system (iU2Z, Philips). The ultrasound tranducer, PCD, and L12-5 were all confocally-aligned with the MB-containing channel.

MBs were exposed to 100 cycles of 1 MHz ultrasound as in sonoporation experiments. In a first experiment, the acoustic emissions from Control MB and Lyso-MB as recorded by the PCD were measured as a function of the ultrasound driving pressure which was increased step-wise until strong broadband noise was received. The pulse repetition frequency was set to 5 Hz to ensure that fresh MBs were available on each pulse in experiments conducted under flow. Thirty pulses were recorded at each driving

[i] Experiments conducted with Dr. Mannaris. Dr. Mannaris performed the B-mode imaging and wrote the LabVIEW control program used to acquire data and control the hardware in these experiments.

pressure and three independent samples were tested for each MB formulation. In a second experiment, ultrasound imaging was conducted for each MB formulation with the flow stopped such that the MB destruction could be observed.

Acoustic emissions data was processed and analysed by the methods described in Chapter 2. Ultrasound contrast imaging was processed using ImageJ[5].

4.2.5. Cell culture

A-549 cells were prepared for spectral imaging and sonoporation experiments as described in Chapter 3.

4.2.6. Spectral imaging

Cells were exposed to Lyso-PC for ~90s. Cells were then washed with PBS and labelled with C-Laurdan (400 nM) for ~1 min prior to spectral imaging (see Figure 1A). Detailed spectral imaging methods are presented in Chapter 2.

4.2.7. Sonoporation experiments

Sonoporation experiments and the associated processing and analysis of fluorescence microscopy images and acoustic emissions data were conducted as described in Chapter 2. A new PDMS lid was employed in the experiments of the present study owing to the material degradation of the PDMS lid employed in Chapters 2-3 over time. It was found that new lid resulted in a slight translation of the sample along the axis of ultrasound propagation (~1-2 mm). Following a three-dimensional scan of the ultrasound field in the SAT2 system performed with a needle hydrophone (Onda 1121, Onda Corporation), it was found that the spatially averaged PNP employed in the present study was lower than that employed in Chapter 2. The ultrasound parameters employed in the present study were thus 1 MHz, 0.10 MPa PNP, 1 kHz PRF, 10% DC, and 15 s exposure time.

4.2.8. Lyso-MB destruction without exposing cells to cavitation

To determine the effects of destroyed Lyso-MBs on cell membranes without the effects of cavitation, Lyso-MBs were repeatedly sonicated at low power for ~30 s and then set in a water bath maintained at ~85°C for ~60 s until the solution cleared indicating MB destruction.

4.2.9. Statistical analysis

For experiments with greater than two conditions, one-way analysis of variance (ANOVA, alpha = 0.05) was employed for statistical analysis followed by multiple comparisons using Tukey-Kramer tests. For experiments with two-conditions, two-sample t-tests were performed. In both cases, significance was indicated by $p < 0.01$.

4.3. Results

4.3.1. Effects of Lyso-PCs on cell membranes

16:0 Lyso-PC was found to have a significant disordering effect on cell membrane lipids with $\Delta GP = -0.058 \pm 0.038$ (see Figure 4A). To assess the membrane permeabilizing effects of Lyso-PC, a sample treated with 80 µM 16:0 Lyso-PC for ~90 s and spectrally imaged with C-Laurdan was counter-stained for fluorescence microscopy with propidium iodide. It was found that cells exhibiting propidium iodide uptake indicative of permeabilization, also exhibited, on average, more disordered membrane lipids (see Figure 4B). The distribution of GP values is notably different from that induced by 10:0 PC which produced a distinct bimodal distribution of GP values with more severe lipid disordering in permeabilized cells (see Chapter 3). Furthermore, the molarity of 16:0 Lyso-PC required for cell membrane permeabilization was found to be two orders of magnitude lower than that of 10:0 PC.

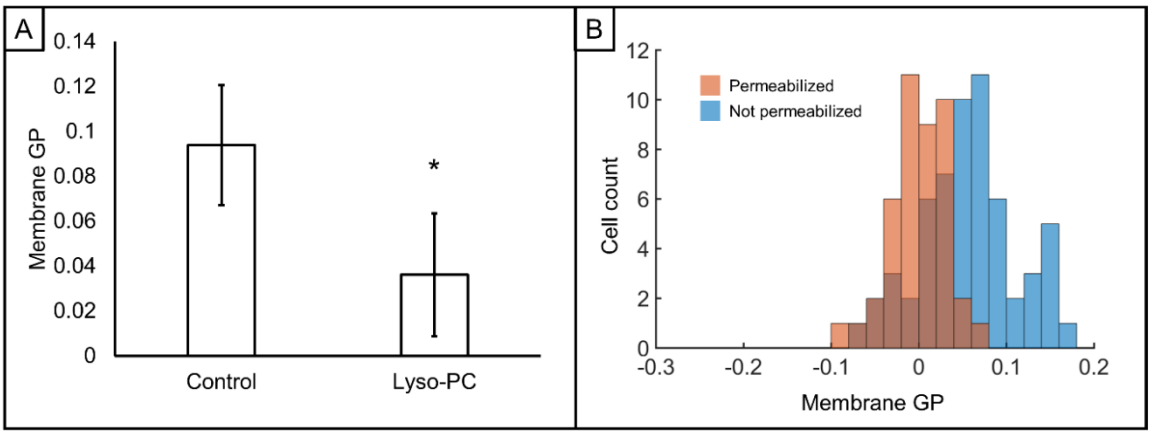

Figure 4: Effect of 16:0 Lyso-PC on A-549 cell lipid order and permeabilization. Cells were exposed to 80 µM Lsyo-PC at 37°C for ~90 s prior to spectral imaging with C-Laurdan (n = 3). The generalized polarization (GP) of segmented cell membranes is shown in (A) where GPcontrol = 0.094 ± 0.027 and GPLyso-PC = 0.036 ± 0.030 . Statistical significance (*) is indicated for $p < 0.01$ from a two-sample t-test. Panel (B) shows histograms for cell membrane GP from a sample counter-stained with propidium iodide for marking permeabilization after exposure to Lyso-PC and spectral imaging with C-Laurdan. Cells permeabilized by Lyso-PC exposure had lower GP on average (GPpermeabilized = 0.002 ± 0.034 and GPnot-permeabilized = 0.058 ± 0.055).

4.3.2. Lyso-MB characterization - acoustic emissions and contrast imaging

Acoustic emissions from Control-MB and Lyso-MB were recorded as a function of driving pressure. It was found that as the pressure was increased, both formulations produced harmonic emissions, followed by ultraharmonic emissions, followed by broadband emissions, a characteristic previously reported for clinically-used SonoVue®

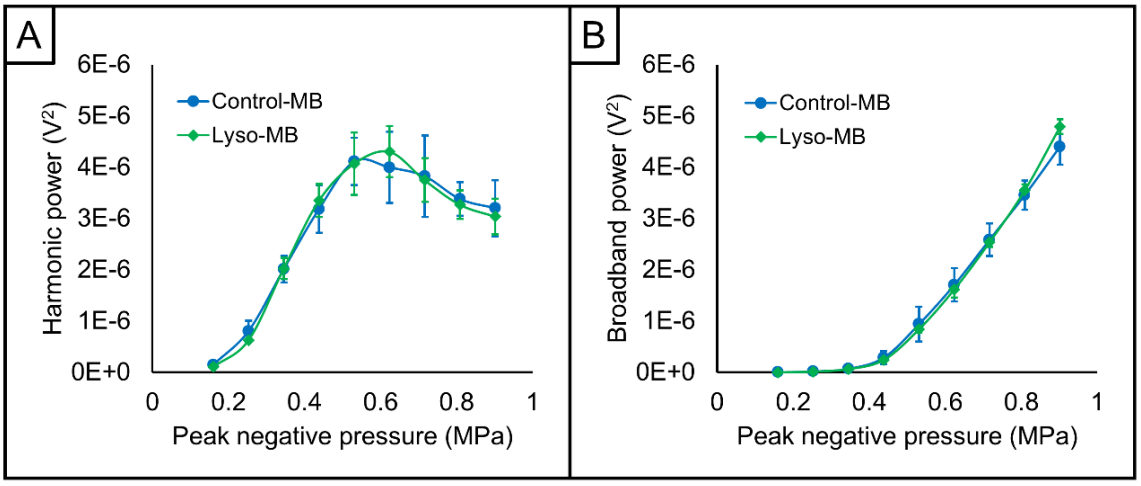

Figure 5: Acoustic emissions from Control-MB and Lyso-MB as a function of driving pressure. Lyso-MB acoustic emissions were indistinguishable from that of Control-MB with respect to the power in both harmonics and broadband frequency content.

MB[6]. Ultraharmonic emissions were detected at 0.35 MPa PNP and were most pronounced at 0.53 MPa PNP, after which broadband noise dominated the recorded emissions. Broadband acoustic emissions were detected at 0.44 MPa PNP and were clearly evident in power spectral density spectra at 0.53 MPa PNP and higher. The acoustic emissions produced by Lyso-MB were indistinguishable from that of Control-MB with respect to the power in both harmonics and broadband frequency content (see Figure 5). Representative power spectral density spectra are presented in Figure 6.

Ultrasound contrast images of Control-MBs and Lyso-MBs exposed to ultrasound under static conditions revealed that both MB formulations were capable of enhancing contrast for many pulses and cycles under ultrasound duress (see Figure 7).

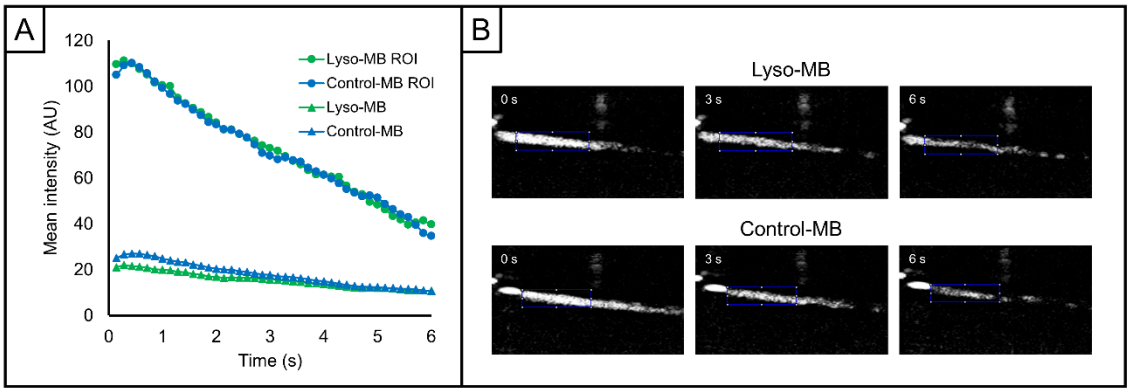

Figure 6: B-mode imaging of Control-MBs and Lyso-MBs. With the flow stopped in the MB characterization setup, B-mode ultrasound imaging was performed and the destruction of Lyso-MBs and Control-MBs observed. A) Mean intensity from B-mode images recorded at 7 frames per second for 6 s. The intensity for a region-of-interest (ROI) indicated by the blue rectangular region on the images in (B) are also plotted. B) Representative B-mode images from the videos of Lyso-MB and Control-MB. A slightly higher MI was employed for Lyso-MB, which explains the more extensive destruction of Lyso-MB in the first few frames. The contrast-enhancement was nonetheless similar between formulations.

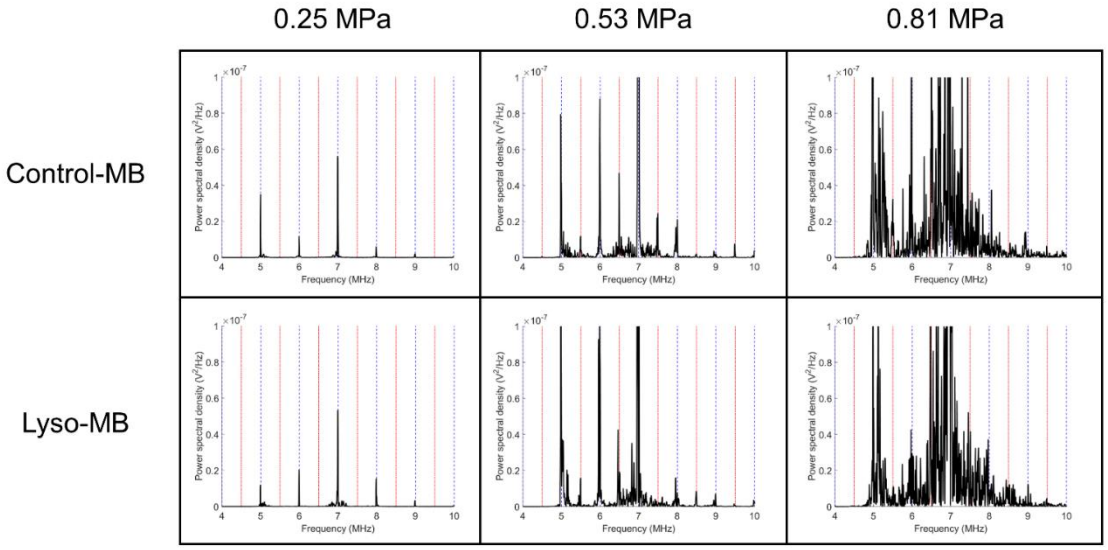

Figure 7: Representative power spectral density spectra from the acoustic emissions characterization of Control-MBs and Lyso-MBs. Harmonics were evident for both formulations at low peak negative pressures as shown in the left panels for exposure to 0.25 MPa PNP ultrasound. As the acoustic pressure was increased, ultraharmonic emissions were detected as shown in the centre panel for exposure to 0.53 MPa PNP ultrasound. Broadband acoustic emissions dominated the measured acoustic emissions at higher acoustic pressures as shown in the right panel for exposure to 0.81 MPa PNP ultrasound. Spectra for Control-MB and Lyso-MB were qualitatively similar with respect to driving pressure. The ultrasound frequency was 1 MHz.

4.3.3. Acoustic emissions in sonoporation experiments

The acoustic emissions from Control-MBs, Lyso-MBs (25 and 80 µM), and PC-MBs (25 and 80 µM) were measured in sonoporation experiments by passive cavitation detection (PCD) by the same methods employed in Chapters 2-3. Representative power

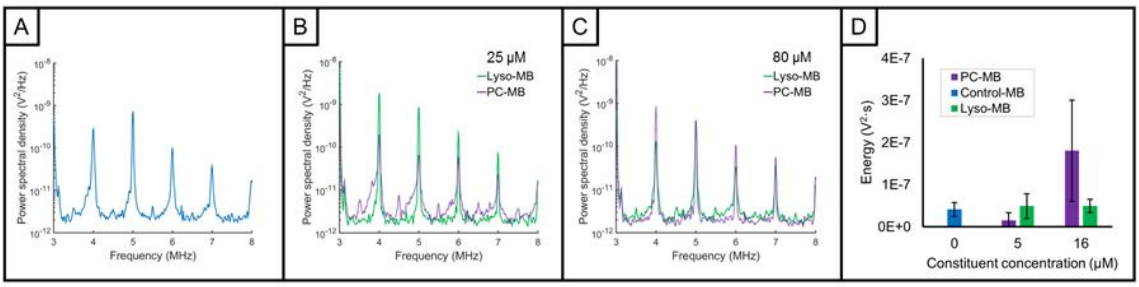

Figure 8: Acoustic emissions from sonoporation experiments with 1 MHz ultrasound at 0.1 MPa PNP. Representative power spectral density spectra from Control-MB (A), and Lyso-MB and PC-MB at 25 µM (B) and 80 µM (C) added lipid concentrations. The average harmonic energy for each condition across all samples tested is shown in (D). While PC-MB at 80 µM 16:0 PC produced greater acoustic emissions in two of three samples, the p values were greater than 0.01 compared to the other conditions. Specifically, $p = 0.031$, $p = 0.017$, $p = 0.044$, and $p = 0.064$ for comparison with Control-MB, PC-MB (25 µM), Lyso-MB (25 µM), and Lyso-MB (80 µM) respectively.

spectral density spectra for each formulation tested are presented in Figure 8A-C. Analysis of PCD data revealed the generation of harmonic acoustic emissions from all five MB formulations, without the generation of broadband acoustic emissions significantly above baseline. Ultraharmonic acoustic emissions and harmonic peak widening, however, were observed in a few samples (e.g. from Control-MB and 25 µM PC-MB, see Figure 8A-B). The energy in the harmonic acoustic emissions was indistinguishable for Control-MB and Lyso-MB at both concentrations of Lyso-PC employed. The energy in harmonic acoustic emissions from PC-MB was, however, more varied. Notably, two 80 µM PC-MB samples produced significantly more harmonic emissions than the other formulations tested, although 80 µM PC-MB overall was only mildly statistically different from the other conditions ($0.01 < p < 0.05$). It is conceivable that this difference arose from the method employed for 80 µM PC-MB preparation which involved spiking with 16:0 PC liposomes immediately prior to sonoporation (see methods).

Nonetheless, it is clear from these results that the increase in sonoporation efficiency between Lyso-MB containing 80 µM Lyso-PC and the other conditions tested cannot be attributed to MB size distributions, concentration, or acoustic emissions.

4.3.4. Sonoporation

Lyso-MBs with a final Lyso-PC concentration of 80 µM were found to significantly increase sonoporation efficiency ($p < 0.01$), achieving permeabilization of 35.1 ± 9.8 % of cells (n = 3) compared with 11.0 ± 5.5 % and 6.0 ± 5.2 % of cells permeabilized following exposure to ultrasound and Control-MBs (n = 4) and ultrasound and PC-MBs with 80 µM 16:0 PC (n = 3), respectively (see Figure 9A). Representative images of cells labelled with propidium iodide (indicating permeabilization) and calcein-AM for each of these conditions are presented in Figure 10. It was found that adding 16:0 PC lipids to MBs, i.e.: to form PC-MBs as a control for adding lipids and hydrolysis, did not have a significant impact on sonoporation compared to Control-MBs, despite the fact that some of the 80 µM PC-MB samples produced greater acoustic emissions (see Figure 9C). That PC-MBs did not achieve greater sonoporation provides evidence for

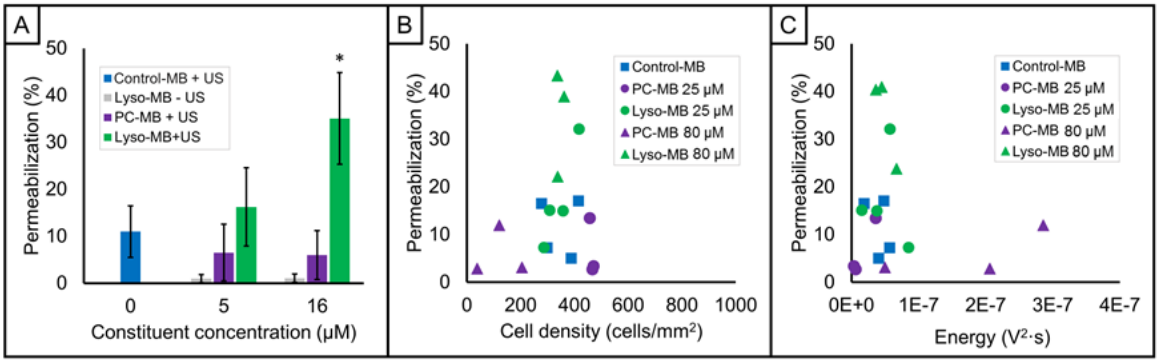

Figure 9: Effect of Lyso-PC on sonoporation efficiency. The percentage of permeabilized cells was measured immediately after sonoporation using a Calcein-AM and Propidium Iodide (PI) assay whereby any cell stained with PI was considered permeabilized. The mean and standard deviation of permeabilization for ultrasound exposure (+ US) of Control-MB, Lyso-MB with 25 and 80 µM 16:0 Lyso-PC, and PC-MB with 25 and 80 µM 16:0 PC, as well as controls for Lyso-MB with 25 and 80 µM 16:0 Lyso-PC with no ultrasound exposure (- US) are shown in (A). Exposure to Lyso-MB with 80 µM 16:0 Lyso-PC and ultrasound resulted in a statistically significant increase in cell permeabilization as determined by an ANOVA and Tukey-Kramer post-hoc test ($p < 0.01$). (B) Scatter of the permeabilization data vs the observed cell density. (C) Scatter of permeabilization data vs the measured harmonic energy in acoustic emissions. No dependence on these factors was evident. In (B) and (C) each point represents an independent sonoporation experiment sample where Control-MB are indicated by blue squares, PC-MB are in purple, and Lyso-MB are in green. Circles and triangles indicate 25 and 80 µM of the added lipid constituent respectively.

attributing the enhancement of sonoporation to the presence of 16:0 Lyso-PC in the Lyso-MB formulation. Additionally, no dependence of sonoporation on cell density was found (see Figure 9B).

Although the samples used for PC-MBs containing 80 µM 16:0 PC had a lower cell density on average, a decrease in cell density would be expected to increase the percentage of cells sonoporated, as has been observed in previous work (data not shown). The low degree of sonoporation achieved with PC-MBs, however, suggests that cell density was not a critical factor in these results.

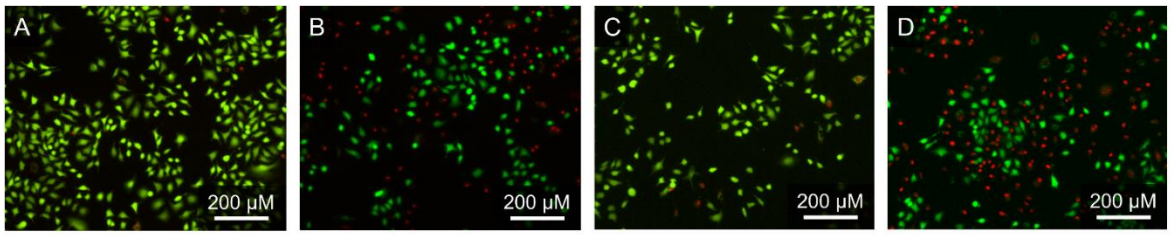

Figure 10: Representative fluorescence microscopy images of cells exposed to ultrasound and MBs. The cells in (A) were exposed to 25 µM PC-MBs. The cells in (B) were exposed to 25 µM Lyso-MBs. The cells in (C) were exposed to 80 µM PC-MBs. The cells in (D) were exposed to 80 µM Lyso-MBs. Propidium iodide (red) indicates permeabilization. Those cells that are not stained with propidium iodide that also exhibit calcein fluorescence (green) from calcein-AM staining, were not permeabilized. No differences were apparent in the permeabilization or morphology of the cells across all conditions.

4.3.5. The effect of Lyso-MBs on cell membrane permeabilization

To further investigate the effect of the Lyso-MBs on cell membrane permeabilization, cells were exposed to either Lyso-MBs, destroyed Lyso-MBs, or Control-MBs spiked with 25 µM Lyso-PC immediately prior to exposure for ~90 s at 37°C (see Figure 11). Interestingly, cells exposed to the destroyed Lyso-MBs exhibited negligible permeabilization, whereas cells exposed to Control-MBs spiked with Lyso-PC were significantly permeabilized (12.5 ± 7.8 %). Cells exposed to Lyso-MBs exhibited negligible permeabilization. This data suggests that Lyso-PC was successfully incorporated into Lyso-MB shells rather than forming Lyso-PC micelles exclusively. In addition, the Lyso-MB formulation itself does not appear to be toxic for the exposure conditions tested.

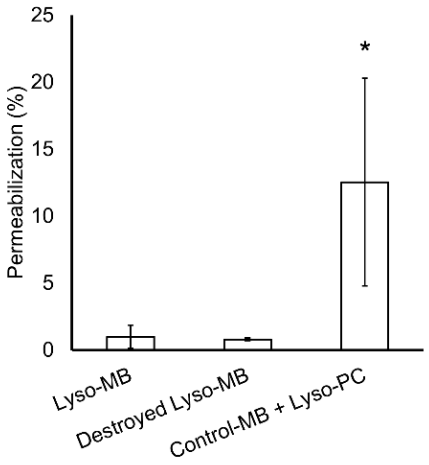

Figure 11: Cell membrane permeabilization by Lyso-PC and MBs. Exposure to Lyso-MBs (n = 3) or Lyso-MBs destroyed by repeated heating to 85°C and sonication (n = 4) caused negligible permeabilization. Exposure to Control-MBs spiked with 16:0 Lyso-PC, however, significantly permeabilized cells (n = 3, $p < 0.01$). 16:0 Lyso-PC concentration was 25 µM, incubation time was ~90 s, and cells were kept at 37°C for all conditions.

In comparing Figures 9 and 11, it is essential to highlight that the level of permeabilization induced by 25 µM Lyso-PC-containing Lyso-MBs exposed to ultrasound (Figure 9), is indistinguishable from that induced by exposure of cells to Control MBs spiked with 25 µM Lyso-PC in the absence of ultrasound (Figure 11).

Additionally, both of these conditions are not statistically different from the permeabilization induced by exposure to Control MBs and ultrasound without any Lyso-PCs (Figure 9). Interestingly, this data would suggest that while 5 uM Lyso-PC and Control-MB exposure results in lipid-mediated cell permeabilization, and Control MB with ultrasound results in cavitation-mediated cell permeabilization, Lyso-MBs with the same concentration of Lyso-PC did not result in significantly more permeabilization as might be expected. This may be reconciled by the availability of the Lyso-PC to interact with the cell membrane in these different experiments. When Control-MBs are spiked with Lyso-PC (Figure 11), it appears that Lyso-PC is available to interact with cell membranes, unlike Lyso-MBs which require ultrasound to have an effect. In the case of 80 µM Lyso-MBs, where ultrasound exposure resulted in significantly greater cell permeabilization when compared with either Control MBs with ultrasound, or Lyso-MBs without ultrasound, the additional permeabilization would appear to arise from Lyso-PC release from Lyso-MBs. Owing to omission of several controls which are on-going (detailed in the discussion that follows), these results are as of yet inconclusive.

4.4. Discussion

In this chapter, the effects of conical lipids, Lyso-PCs, on cell lipid order were investigated. It was found that Lyso-PCs, which form primarily micelles in aqueous solution, had strong lipid disordering and permeabilizing effects on cell membranes, the mechanisms of which are discussed. It was further found that Lyso-PCs could be incorporated into several of the laboratory MB formulations investigated in Chapters 2 and 3. Lyso-MBs were found to significantly increase the sonoporation efficiency compared with MBs absent of Lyso-PC.

4.4.1. On the mechanisms of Lyso-PC–induced cell membrane permeabilization

Exposure of A-549 cells to 80 µM 16:0 Lyso-PC resulted in significant disordering of membrane lipids ($\Delta GP = -0.058 \pm 0.038$) and cell membrane permeabilization. A similar membrane lipid disordering and membrane permeabilizing effect was also observed in DLD-1 cancer cells (see Appendix I). According to the literature, exposure to an excess of Lyso-PCs can simultaneously disorder and immobilize cell membrane lipids as a consequence of their rapid transfer to cell membranes and the depletion of cell membrane cholesterol[2,3,7]. In this section, findings from the literature are implemented to gather further insights regarding the effects of Lyso-PCs on cell membranes and cell permeability in the present study.

The equilibrium concentration of 16:0 Lyso-PC in cell membranes, C_m, can be estimated using the following equation,

$$C_m = \frac{C_i(V_b + V_m)K_p}{V_b + (V_m K_p)} \quad (1)$$

where C_i is the initial concentration of 16:0 Lyso-PC in the buffer (80 µM), V_b is the volume of the buffer (250 µL), V_m is the volume occupied by cell membranes, and K_p is the partition coefficient of 16:0 Lyso-PC in cell membranes (K_p = 7.25*10^4)[2]. Owing to the negligible rate of 16:0 Lyso-PC trans-bilayer diffusion relative to its transfer rate, V_m was taken as the product of the total area of the substrate occupied by cells and the outer leaflet thickness (~2 nm). It follows from equation (1) that observations in the literature where 16:0 Lyso PCs are in excess are relevant to the present study.

In understanding the effects of Lyso-PC on cell membranes it is valuable to consider the measurements of Golan et al. in terms of both Lyso-PC transfer and cholesterol depletion[3]. The study of Golan et al. is also in agreement with Chi and Wu who estimated the bilayer area expansion from 16:0 Lyso-PC exposure to be ~3%[7].

The total area occupied by lipids and cholesterol in the outer bilayer leaflet, A_{eq}, can be expressed as,

$$A_{eq} = N_{eq}\left(A_{chol} + A_{lip}\right), \tag{3}$$

where A_{chol} is the average area occupied by cholesterol (~70 Å^2), A_{lip} is the average area occupied by lipids (~70 Å^2), and N_{eq} is the number of lipid or cholesterol molecules from a 1:1 molar ratio at equilibrium[3]. At saturation, Golan et al. measured a ~25% increase in the total number of cell membrane lipids, such that the number of Lyso-PCs in the outer leaflet can be expressed as $N_{lyso} \sim \frac{1}{2} N_{eq}$. This is taking into consideration the fact that the trans-bilayer diffusion or "flip-flop" of Lyso-PC is extremely slow such that Lyso-PCs can be assumed to stay in the outer leaflet throughout experiments[3]. Golan et al. also observed a ~25% decrease in the cholesterol to lipid concentration ratio (excluding transferred Lyso-PCs)[3], such that $N_{chol} \sim \frac{3}{4} N_{eq}$.

Flip-flop of cholesterol is not rate-limiting for cholesterol depletion such that both bilayer leaflets can be considered as a single pool[8]. The outer bilayer leaflet area occupied by lipids and cholesterol, including cholesterol depletion and 16:0 Lyso-PC transfer, can thus be stated as,

$$A_{sat} \sim N_{eq}\left(\frac{3}{4}A_{chol} + A_{lip} + \frac{1}{2}A_{lyso}\right). \quad (4)$$

where A_{lyso} is the area expansion from transfer of a 16:0 Lyso-PC molecule (~50 Å^2)[7]. Any change in A_{lip} from cholesterol depletion or Lyso-PC deposition, for instance, is thus accounted for in the Lyso-PC term. Comparing the magnitudes of (3) and (4) suggests that the outer bilayer would expand to accommodate transferred Lyso-PCs. In addition, an expression for the area occupied by lipids in the inner bilayer following Lyso-PC exposure can be obtained by neglecting the Lyso-PC term in (4). Comparing this term with (3) suggests that the inner bilayer would contract as a result of cholesterol depletion. It follows that 16:0 Lyso PC in the present study induces an increase in the spontaneous curvature of the cell membrane which may be balanced by an increase in membrane surface tension or cell volume.

Cells tend to preserve membrane surface tension over volume such that an influx of water may occur to occupy membrane buds formed at sites of higher Lyso-PC concentration[9]. This is consistent with observations of actin fibre formation in endothelial cells following Lyso-PC exposure[10]. In either case, the probability of water defects forming in the bilayer is increased such that a decrease in the critical energy required for pore formation would be achieved. This could explain the observed uptake of propidium iodide and the decrease in C-Laurdan GP ($\Delta GP = -0.24 \pm 0.03$) from 16:0 Lyso-PC exposure in the present study.

4.4.2. Lyso-MBs – a novel cavitation agent

In this chapter, a novel cavitation agent, Lyso-MBs, which are MBs loaded with biologically-active 16:0 Lyso-PC, were produced. It was found that adding 16:0 Lyso-PC to PC-PEG40S MB formulations with 16:0, 18:0 22:0 PC carrier lipids yielded high MB concentrations using the sonication protocol from Chapter 2. Although diluted to 25 or 80 µM Lyso-PC for concentration matching with Control-MBs, Lyso-MBs were produced with ~1.6 mM Lyso-PC, and yielded over $2*10^9$ MB/ml, demonstrating that at least an order of magnitude higher Lyso-PC concentration is achievable.

The cavitation behaviour of Lyso-MBs and Control-MBs were indistinguishable as a function of driving pressure at 1 MHz. Lyso-MBs where found to produce harmonic, ultraharmonic, and broadband emissions with distinct pressure thresholds for the appearance of each acoustic emissions regime. Lyso-MBs also provided strong backscatter on B-mode imaging comparable with Control-MBs. It follows that Lyso-MBs have the size, concentration, and acoustic properties befitting a clinical-grade ultrasound imaging/therapy cavitation agent.

4.4.3. Lyso-MBs – evidence for Lyso-PC incorporation and shedding

While the Lyso-PC concentration in Lyso-MB shells was not directly measured using analytical chemistry techniques, compelling indirect evidence for its successful incorporation into Lyso-MB shells was presented. Specifically, when MB solutions were spiked with Lyso-PC, cells were permeabilized, but when cells were exposed to Lyso-MBs containing an equivalent concentration of Lyso-PC, minimal permeabilization was observed. If Lyso-PC was not incorporated into Lyso-MB shells, significant permeabilization would be expected without ultrasound exposure. Furthermore, following ultrasound exposure, Lyso-MBs permeabilized more cells than Control-MBs or PC-MBs. It thus appears that ultrasound exposure triggered the release

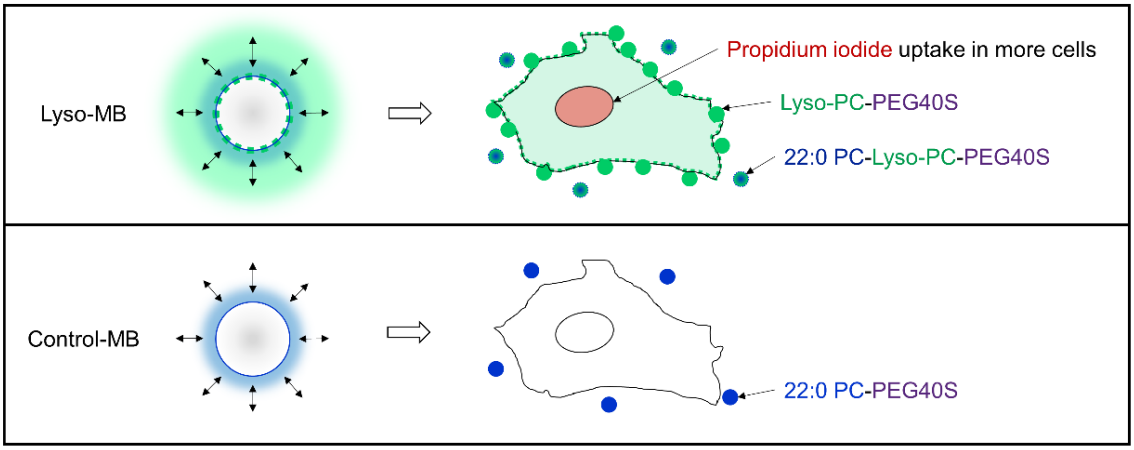

Figure 12: Illustration of the proposed mechanism of increased sonoporation with Lyso-MBs, simplified for clarity of communication. Under ultrasound duress, lipids are cast into the aqueous bulk from MB shells. Such lipid shedding should favour Lyso-PC (green) which has a higher desorption rate than long-chain 22:0 PC (blue, in both formulations) owing to its reduced hydrophobicity. 22:0 PC does not interact with cell membranes (pictured with nuclei, right) and rather forms stable vesicles. Similarly, 22:0 PC vesicles with Lyso-PC do not appear to induce cell membrane permeabilization. Lyso-PC micelles, however, can rapidly transfer to cell membranes, reducing the energy barrier to pore formation in cell membranes and increasing the uptake of propidium iodide (red). Pore formation with Lyso-MBs thus appears to be both cavitation-mediated and lipid transfer-mediated. PEG40S is also present in the MBs and aqueous bulk and may form compounds with the other lipids or transfer to cell membranes, although its role in these experiments is not known. Not shown are hypothesized changes in cell membrane cholesterol content and the effects of Lyso-PC on cell membranes.

of Lyso-PCs from Lyso-MBs resulting in additional cell membrane permeabilization.

From the acoustic emissions, which were sustained throughout ultrasound exposure, and by visual inspection of samples after ultrasound exposure, it was clear that Lyso-MBs were not completely destroyed in the sonoporation experiments. These experiments would thus benefit from evaluating the release of Lyso-PC from Lyso-MBs and the corresponding degree of Lyso-MB destruction and sonoporation as a function of ultrasound pressure, frequency, and temporal parameters. Further investigation in this regard may help clarify the mechanism of sonoporation with Lyso-MBs from which the current data can only provide the basis for hypothesis formation. Interestingly, exposure of cells to Lyso-MBs previously destroyed by heating and sonication did not result in the permeabilization expected from exposure to Lyso-PC micelles. One possible explanation is that Lyso-MB fragments after MB destruction may not transfer readily to cell membranes owing to the presence of 22:0 PC and/or PEG40S. This is consistent with the observations of material transfer from DiI-loaded MBs in Chapter 2, in which 22:0 PC-containing MBs were found to prevent incorporation of DiI into cell membrane. It is thus hypothesized that Lyso-PC, which is much more soluble in aqueous solution than 22:0 PC, is preferentially shed from Lyso-MBs during sonication, such that it can successfully transfer to cell membranes, thereby promoting pore formation. Lipid shedding from phospholipid-shelled MBs has been observed previously[11,12]. This proposed mechanism is illustrated in Figure 12.

4.4.4. Limitations

There are several important limitations of the present study which must be considered in the interpretation of the results. Namely, several controls are missing which must be completed to stand by the conclusions as made. These controls include an assessment of

Lyso-PC alone, and an assessment of both the effects of destroyed Lyso-MBs and Control MBs in the presence of Lyso-PCs at 16 uM Lyso-PC concentration. While Figure 9 does not show the no-treatment and ultrasound-only controls, these were presented in Chapter 2 and were found to result in negligible cell permeabilization (less than 1%). In the case of the Lyso-PC only controls, while it is acknowledged that it is standard to include such controls, as described in Chapter 1, lipid transfer depends on the surrounding lipid species to a great extent such that data concerning what Lyso-PC does to cell membranes on its own could not inform what Lyso-PC is doing to cells when loaded with microbubbles containing other lipid species and surrounded by liposomes and micelles of additional lipids and emulsifiers. It is nonetheless informative to characterize the potency of the effects of Lyso-PC on cell membranes in their isolated micellar form. Indeed, such Lyso-PC data would be more useful if a larger study of Lyso-PC-mediated cell membrane permeabilization were undertaken whereby Lyso-PC in the presence of other microbubble lipids and emulsifiers were investigated in the absence of ultrasound as a function of the concentrations of each species investigated.

Furthermore, the method of the present study does not distinguish between permeabilized cells that recover and permeabilized cells that ultimately die. This does not contribute error to the permeabilization percentages reported but rather must be interpreted strictly as just that: the percentage of cell permeabilized. While numerous studies employ calcein-AM and propidium iodide to report cell viability and permeabilization, referring to those cells which fluoresce with both probes as sonporated but recovered, this is often an incorrect use of the fluorescent probes. Calcein only reports those cells which have intracellular esterases present. It is not clear at which point after exposure to cavitation a dying cell stops producing these enzymes

and at which point there are too few remaining enzymes to result in measureable fluorescence. It follows that in the case of permeabilization experiments, calcein serves rather as a cell count indicator which enables the determination of the percentage of total cells that were permeabilized. For example, consider the results presented in Chapter 3 where it was found that while many cells permeabilized by 10:0 PC were also labelled with calcein, those cells were dying as indicated by the MTS assay. Indeed, one improvement to the experiments presented in Chapters 2-4 would be to conduct MTS assays or equivalent to determine the cell viabilities in response to the various treatments. The present study focuses formation of pores, which did not include an investigation of subsequent pore closure and cell survival.

Another aspect of the present study that requires comment is that regarding quantification of the Lyso-PC loading efficiency into Lyso-MB shells and quantification of the release of Lyso-PC from Lyso-MBs upon ultrasound exposure. Such data may lend support to the hypothetical mechanisms for the observed effects proposed in Sections 4.3.4 and 4.3.5. Indeed, there is an on-going effort to quantify the loading efficiency of Lyso-PC into Lyso-MB shells utilizing HPLC-ELSD-MS. If successful, quantification of the lipid transfer to cell membranes would be achievable by the same methods with an additional cellular membrane lipid isolation step.

4.4.5. On the oncolytic potential of Lyso-MBs

In this chapter, Lyso-MBs were found to increase sonoporation efficiency by ~3-fold compared to Control-MBs and ~6-fold compared to PC-MBs at equimolar concentration of added lipid. The ultrasound-mediated triggered release of Lyso-PC from Lyso-MBs appears to promote cell permeabilization by either directly

permeabilizing cells, or by reducing the energy barrier to pore formation such that cavitation-mediated permeabilization is more readily achieved.

It is interesting to note that PEG40S and Lyso-PC have in common the presence of a single fatty acid, and both were found to disorder cell membranes to a similar extent ($\Delta GP = -0.035 \pm 0.050$ and $\Delta GP = -0.058 \pm 0.038$ respectively, see also Chapter 2). Lyso-PCs were more readily incorporated into MB shells and had a significant impact on sonoporation, unlike PEG40S which is mostly squeezed out of MB shells and had no effect on sonoporation (see Chapter 2). It stands to reason that another conical lipid with a fatty acid bound to a different head-group may also have membrane disordering effects and may similarly affect sonoporation when incorporated into MB shells.

Additionally, the high lipid transfer rate of Lyso-PC and the presence of specific enzymes for its clearance *in vivo* (detailed in Chapter 5) are both beneficial and problematic for the clinical translation of Lyso-MBs. On the one hand, these factors may lead to the rapid onset of biological effects upon ultrasound-mediated triggered release followed by the enzymatic mutation of Lyso-PC into other innocuous chemical species. On the other hand, there is some risk of blood toxicity if Lyso-PC is not retained in MB shells *in vivo*, and transfers to blood cells or the endothelium prior to ultrasound exposure. While this must be evaluated experimentally, Lyso-PC desorption from Lyso-PC-containing thermosensitive liposomes has not prevented numerous clinical trials from taking place, one of which at BUBBL at the University of Oxford successfully set the precedent for ultrasound-mediated triggered release in the clinic[13] (see also related discussion in Appendix I). Additionally, no evidence of blood toxicity has been reported in humans from Lyso-PC-containing thermosensitive liposomes to the author's knowledge. Further to this point, it was shown in Chapter 2 that the

molecular packing of lipids in MBs is fundamentally different than that of liposomes whereby the lipid order is increased in MB shells, potentially hindering unwanted Lyso-PC desorption from MBs. While the acceptor-to-donor ratio is much higher in whole blood than in the present study, it is worth highlighting that exposure to Lyso-MBs without ultrasound exposure had no apparent toxic effects in the present study.

Interestingly, the Lyso-PC in Lyso-MBs can also likely be replaced by a number of structurally similar synthetic lysolipids (alkyl ether lipids) which may provide additional therapeutic benefit (see Figure 13). For example, Edelfosine, similar to Lyso-PC but with better metabolic stability *in vivo* provided by an ether bond, has been shown to inhibit tumour cell proliferation[14]. Edelfosine was also the first cancer drug to specifically target the cell membrane, with a mechanism involving the disruption of lipid rafts which ultimately induces apoptosis[15]. Similarly, Mitelfosine, which is Lyso-PC lacking the glycerol residue, has also been investigated to this end but its clinical translation, like Edelfosine, was hindered due to systemic toxicity[14]. Perifosine has

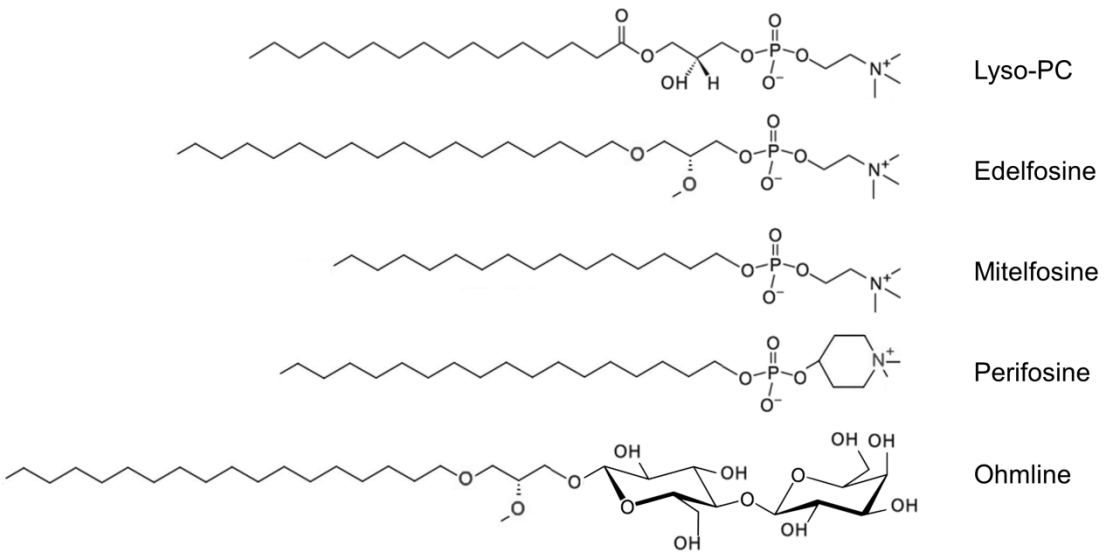

Figure 13: Molecular line drawings of Lyso-PC and its synthetic derivatives used in cancer therapy. Edelfosine, Mitelfosine, and Perifosine are known as alkylphospholipids and ohmline is a glycosidated ether lipids. All of these derivatives are known as alkyl ether lipids.

since been developed in which the choline head group on the Mitelfosine lipid is substituted for a moiety that improves the stability and half-life of the drug. Perifosine has had clinical success when orally administered in combination with other cancer therapies and exhibits selective cancer kill *in vitro*[14]. The clinical potential of alkyl ether lipids, either those mentioned or less haemolytic alkyl ether lipids under investigation, could be enhanced when incorporated into an ultrasound-mediated triggered-release delivery system. Indeed, a Lyso-MB which serves as drug, permeabilizing agent, delivery vehicle, and cavitation agent, would be an elegant approach to oncotherapy, provided off-target effects could be successfully reduced.

4.5. Concluding remarks

Lyso-PC, a fully-saturated conical lipid, both promotes pore formation in cell membranes and is well-suited to MB production. Accordingly, a novel cavitation agent, 16:0 Lyso-PC-incorporating MBs, or Lyso-MBs, were developed and tested for their ability to potentiate sonoporation. The present study demonstrated the following:

1) 16:0 Lyso-PC micelles (80 µM) were found to rapidly (within ~90s) disorder cell membrane lipids and permeabilize cell membranes to propidium iodide.

2) Cell membrane permeabilization by Lyso-PCs was hypothesized to be associated with asymmetric changes to bilayer leaflet surface areas which result in increased membrane surface tension and/or membrane hydration, the latter of which was confirmed by spectral imaging with C-Laurdan

3) Lyso-PC was successfully incorporated into Lyso-MBs which exhibit cavitation behaviour comparable to that of MBs without Lyso-PC (Control-MBs).

4) Lyso-MBs were found to increase sonoporation efficiency in cancer cells by ~3-fold compared to Control-MBs and ~6-fold compared to PC-MBs achieving 35.1 ± 9.8 % cell permeabilization at just 125 kPa PNP (1 MHz, 1 kHz PRF, 10% DC, 15 s).

5) The long hydrocarbon chains of the carrier PC lipid (22:0 PC) in Lyso-MBs was previously shown not to interact with cell membranes (see Chapter 2). It appears that destroyed Lyso-MBs form Lyso-PC constructs with 22:0 PC and/or PEG40S which do not permeabilize cells. This suggests that Lyso-MBs only produce cell permeabilization upon ultrasound-mediated triggered release of Lyso-PC, hypothesized to depend upon a lipid shedding mechanism.

6) The remarkable molecular similarity of Lyso-PC to antineoplastic agents such as Edelfosine and other alkyl ether lipids (synthetic lysolipids) suggests that these agents may also be utilized to form Lyso-MBs with enhanced oncolytic potential.

In the chapter that follows, Lyso-PCs are further investigated for their effects on cell-cell junctions for the potential application of Lyso-MBs to ultrasound-mediated blood-brain barrier opening.

4.6. References

1. Needham, D., Anyarambhatla, G., Kong, G. & Dewhirst, M. W. A New Temperature-sensitive Liposome for Use with Mild Hyperthermia: Characterization and Testing in a Human Tumor Xenograft Model 1. *CANCER Res.* **60,** 1197–1201 (2000).
2. Chi, L. M., Wu, W. G., Sung, K. L. & Chien, S. Biophysical correlates of lysophosphatidylcholine- and ethanol-mediated shape transformation and hemolysis of human erythrocytes. Membrane viscoelasticity and NMR measurement. *Biochim. Biophys. Acta* **1027,** 163–71 (1990).
3. Golan, D. E., Furlong, S. T., Brown, C. S. & Caulfield1 '#, J. P.

Monopalmitoylphosphatidylcholine Incorporation into Human Erythrocyte Ghost Membranes Causes Protein and Lipid Immobilization and Cholesterol Depletion^. *Biochemistry* **27,** 2661–2667 (1988).

4. Mannaris, C. *et al.* Gas-Stabilizing Gold Nanocones for Acoustically Mediated Drug Delivery. *Adv. Healthc. Mater.* 1800184 (2018). doi:10.1002/adhm.201800184

5. Schindelin, J., Rueden, C. T., Hiner, M. C. & Eliceiri, K. W. The ImageJ ecosystem: An open platform for biomedical image analysis. *Mol. Reprod. Dev.* **82,** 518–29 (2014).

6. Arvanitis, C. D., Bazan-Peregrino, M., Rifai, B., Seymour, L. W. & Coussios, C. C. Cavitation-Enhanced Extravasation for Drug Delivery. *Ultrasound Med. Biol.* **37,** 1838–1852 (2011).

7. Chi, L. M. & Wu, W. G. Effective bilayer expansion and erythrocyte shape change induced by monopalmitoyl phosphatidylcholine. Quantitative light microscopy and nuclear magnetic resonance spectroscopy measurements. *Biophys. J.* **57,** 1225–1232 (1990).

8. Phillips, M. C., McLean, L. R., Stoudt, G. W. & Rothblat, G. H. Mechanism of cholesterol efflux from cells. *Atherosclerosis* **36,** 409–422 (1980).

9. Devaux, P. F., Herrmann, A., Ohlwein, N. & Kozlov, M. M. How lipid flippases can modulate membrane structure. *Biochim. Biophys. Acta - Biomembr.* **1778,** 1591–1600 (2008).

10. Qiao, J. *et al.* Lysophosphatidylcholine impairs endothelial barrier function through the G protein-coupled receptor GPR4. at <https://www.physiology.org/doi/pdf/10.1152/ajplung.00508.2005>

11. Luan, Y. *et al.* Lipid shedding from single oscillating microbubbles. *Ultrasound Med. Biol.* **40,** 1834–1846 (2014).

12. Borden, M. A. *et al.* Influence of lipid shell physicochemical properties on ultrasound-induced microbubble destruction. *IEEE Trans. Ultrason. Ferroelectr. Freq. Control* **52,** 1992–2002 (2005).

13. Lyon, P. C. *et al.* Clinical trial protocol for TARDOX: a phase I study to investigate the feasibility of targeted release of lyso-thermosensitive liposomal doxorubicin (ThermoDox®) using focused ultrasound in patients with liver tumours. *J. Ther. Ultrasound* **5,** (2017).

14. Ríos-Marco, P., Marco, C., Gálvez, X., Jiménez-López, J. M. & Carrasco, M. P. Alkylphospholipids: An update on molecular mechanisms and clinical relevance. *Biochim. Biophys. Acta - Biomembr.* **1859,** 1657–1667 (2017).

15. Jaffrès, P.-A. *et al.* Alkyl ether lipids, ion channels and lipid raft reorganization in cancer therapy. *Pharmacol. Ther.* **165,** 114–131 (2016).

V.

Identification of lipids for blood-brain barrier disruption

5.1. Abstract

In most drug delivery applications, drugs must be transported not just through cell membranes as in sonoporation, but beyond the endothelium altogether. This chapter marks a shift in the focus of the thesis from the cell membrane to the endothelial barrier separating the central nervous system (CNS) from the circulation, known as the blood-brain barrier (BBB).

The BBB represents a formidable challenge for drug delivery, preventing virtually compounds from entering the brain. Developing safe and reversible methods for BBB penetration has been the subject of intense research over the past century. After more than six decades of research, successful ultrasound and microbubble-mediated BBB disruption (US-BBBD) was demonstrated in humans in 2016[1]. US-BBBD is thus a potentially revolutionary advancement in medicine, permitting the treatment of previously immedicable brain diseases and disorders.

As described in the previous chapters, the combination of ultrasound and microbubbles also provide a means of localized lipid delivery. Building on the previous findings of the thesis, attention is now paid to the interactions of lipids with tight-junctions, a key feature of the BBB, and how this might be employed to enhance US-BBBD. In this chapter, the effects of phosphatidylcholines (PCs) and lysophosphatidylcholines (Lyso-PCs) on the barrier integrity of cell monolayers with tight junctions are investigated. Lyso-PCs are found to be a promising candidate for lipid-enhanced US-BBBD.

Introduction

5.1.1. The blood-brain barrier

The blood-brain barrier (BBB), composed of brain microvascular endothelial cells and their tight junctions, is the largest interface of blood-CNS exchange[2]. The BBB was discovered at the turn of the twentieth century when it was found that certain compounds produced a significant effect when injected directly into the cerebrospinal fluid, but none when administered intravenously[3]. Administration of dyes into the CNS or circulation of animals shortly after, confirmed the existence of the BBB[4,5] (see Figure 1A). With advances in electron microscopy, the BBB was subsequently localized to the brain endothelium[6] (see Figure 1B-F).

The BBB is now understood to support an optimal environment for synaptic signalling by controlling the transport of molecules for brain nutrition, regulating the expression of neurotransmitters, and prohibiting entry of neurotoxins and damaging macromolecules[2] (see Figure 1G). The BBB regulates transport both through cells by ejecting prohibited molecules with specialized efflux transporters, and around cells by physical and electrical gates between neighbouring cells, known as tight junctions[6,7]. By these mechanisms, the BBB prevents successful delivery of virtually all large molecule drugs and ~98% of small molecule drugs to the brain[8].

To understand why certain lipids are hypothesized to permeabilize the BBB and thereby enhance drug delivery to the brain, the structure and function of tight junctions are introduced.

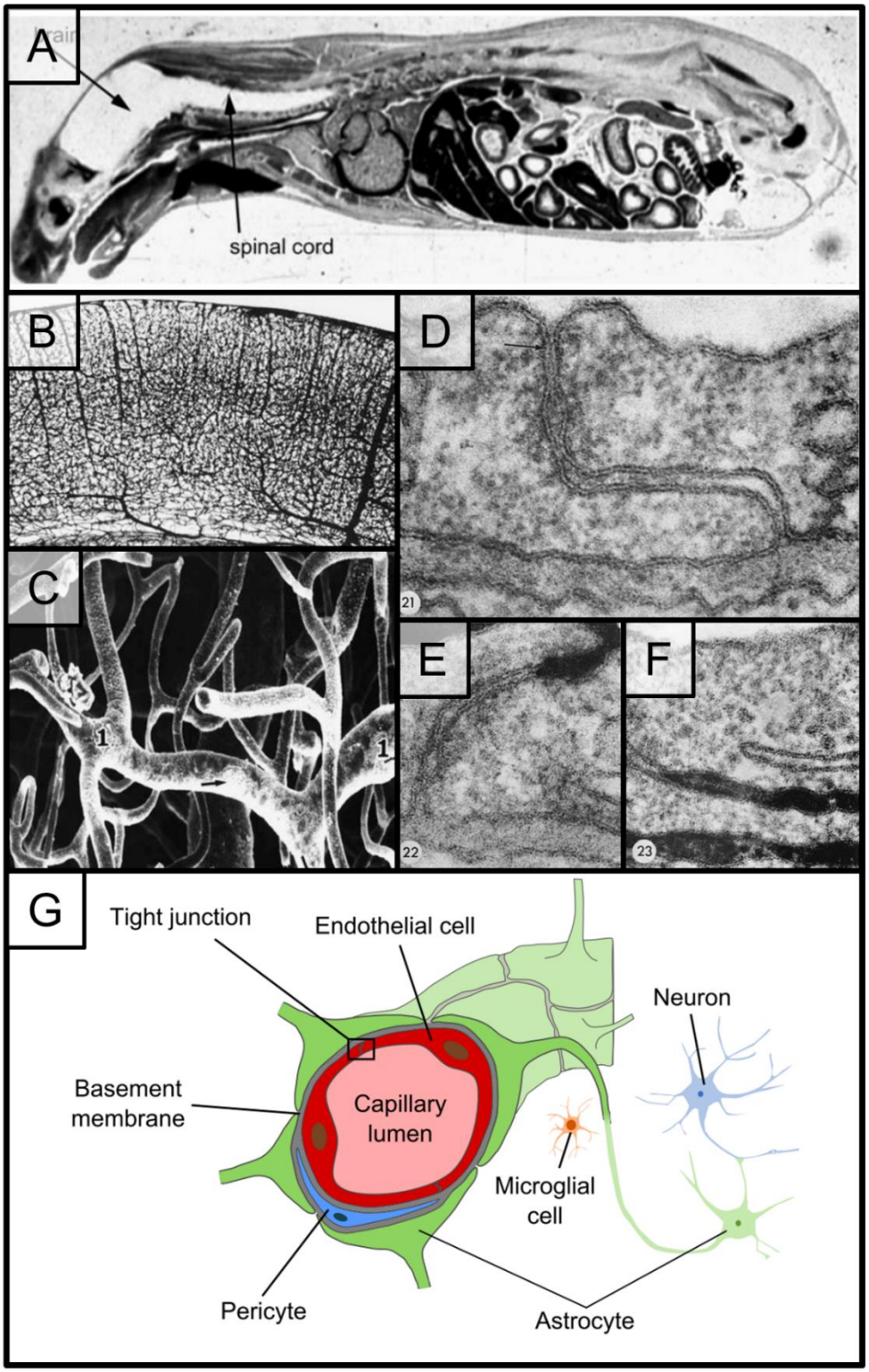

Figure 1: Introduction to the BBB. (A) Autoradiogram of an adult mouse demonstrating that radiolabelled histamine (gray) is excluded from the CNS when intravenously administered. (B) Hippocampal slice demonstrating the brain vasculature. (C) Brain microvasculature. (D) Endothelial cells with tight junctions. (E) and (F) demonstrate that substance cannot cross the tight junction from either side of the barrier. (G) The neurovascular unit demonstrating the anatomy of the BBB including astrocytes, pericytes, neurons, microglia, and endothelial cells. (A) is modified from Pardridge[5], (B) and (C) are modified from Pardridge[8], (D)-(F) are modified from Brightman and Reese[7], (G) is modified from Heye et al.[64].

5.1.2. A protein-centric conception of tight junctions

Tight junctions (TJs) between BBB endothelial cells severely limit paracellular diffusional pathways for ions and polar solutes, and effectively block the transport of macromolecules. TJs are typically described as a complex of integral membrane proteins that polymerize to form strands that connect to proteins from apposing cells, occluding the intracellular space.

The most significant components for barrier function in the BBB TJ protein complex include occludin, claudin-3, claudin-5, junctional adhesion molecules (JAMs), and VE-cadherin[9–14]. These proteins are linked to ZO-1, ZO-2, and ZO-3 (zonula occludins) scaffolding proteins[15], the expression of which are correlated with TJ integrity[2]. TJ scaffolding proteins are in turn linked to the cytoskeleton (see Figure 2A).

The complex interplay between TJ proteins is necessary for successful BBB formation and function. For instance, it has been shown that TJs will still form in an occludin knockout of embryonic stem cells[16], and in a claudin-5 deficient mouse model[17], but that both TJ proteins are required for optimal BBB function. More recently, by isolating tight junctional complexes and employing proteomics and bioinformatics techniques, Tang et al. associated 914 proteins with TJs, highlighting the immense complexity of the TJ protein complex and suggesting a role for TJs in cell-cell communication[18].

5.1.3. A protein-lipid hybrid conception of tight junctions

In early BBB studies, it was found that adjacent cell membranes come together at distinct focal regions along the intracellular cleft, described as membrane ‘kisses’. It was shown by electron microscopy of ultrathin sections that TJs can bring adjacent cells to near fusion distances of 70-90 Å (e.g. Figure 1D), giving rise to the hypothesis that these membrane ‘kisses’ form the basis for a lipidic TJ[19]. In the lipidic TJ hypothesis,

the exoplasmic leaflets of adjacent cells are fused (see Figure 2B). If this were the case, amphipathic molecules would be capable of diffusing from cell to cell along the fused exoplasmic leaflets. After some debate in the scientific community, it has since been shown that lipid probes can indeed diffuse from cell to cell with intact TJs[20,21]. Furthermore, TJs appear to prevent diffusion of molecules from apical to basolateral sides of the cell membrane, as evidenced by the correlation between the ability of a lipid probe to pass the TJ and its ability to 'flip-flop' to the cytoplasmic leaflet[22]. Further evidence for a lipidic TJ comes from Hein and colleagues who demonstrated parallels between the permeability and phase transitions of artificial lipid bilayers, and the electrical tightness of TJ-expressing cells[23,24].

For the lipidic model of TJs to hold true, the exoplasmic leaflets of adjacent cell membranes would need to overcome the thermodynamic energy barrier required to achieve hemifusion and to come to within the fusion distances seen in freeze-fracture studies[25]. This would require special membrane-bringing or membrane-fusion proteins which have yet to be confirmed in TJs[26,27]. A similar unanswered question persists for the protein-only model in that complete membrane-bridging TJ strands composed only of TJ proteins have not been experimentally verified. Direct evidence of the presence of both phospholipids and TJ proteins, occludin and claudin, in freeze-fractured TJ strands, however, has been described[12,28]. One hypothesis is that TJs contain cylindrical inverted micelles (H_{II} lipid phase) that act as bridging structures between TJ protein strands[19]. The hydrophobic tails of TJ cylindrical inverted micelles would be surrounded by the hydrophobic tails of the bilayer leaflets of adjacent cells exposed to the intracellular cleft by hemi-fusion (see Figure 2B).

Lipid rafts may also be essential components of TJs. Lipid rafts are membrane lipid domains rich in cholesterol and sphingolipids that partition specific proteins playing a

critical role in membrane protein signalling and organization. TJ proteins have been associated with detergent-insoluble lipid raft extractions[29,30]. Additionally, cholesterol has been found to accumulate in the cell membrane near TJs in ultrastructural studies[31]. Critically, reduction of cell membrane cholesterol, associated with lipid rafts, has also been associated with loss of TJ structure, protein distribution, and barrier function[29,30,32,33].

Given the wealth of compelling experimental evidence demonstrating a role for both lipids and proteins in TJs, a protein-lipid hybrid model for TJ formation, structure, and function should be considered in approaching drug delivery to the brain by TJ modification.

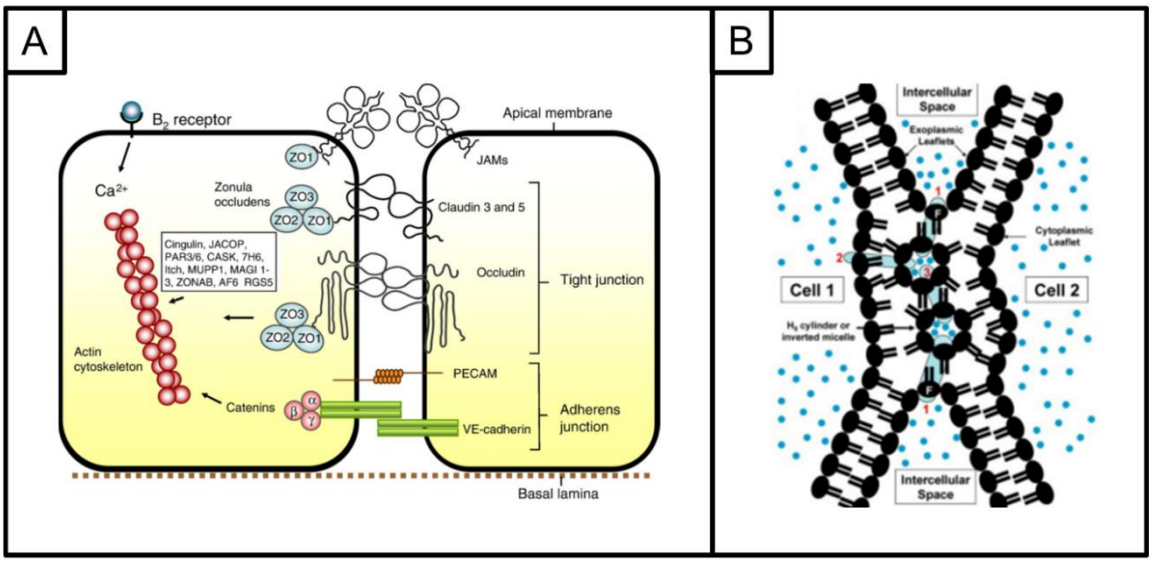

Figure 2: Protein-centric and a protein-lipid hybrid models of the TJ. In the protein-centric conception of TJs in the BBB in (A), TJ proteins claudin-3, claudin-5, and occludin anchor to the cytoskeleton via zonula occludins (ZO-1, ZO-2, ZO-3). In the protein-lipid hybrid TJ model in (B), TJ proteins anchor into inverted cylindrical micellar strands between cells and adjacent cell membranes are fused at their outer bilayer leaflets. (A) is modified from Abbott et al.[2] and (B) is modified from Lee et al.[25]

5.1.4. Study rationale

In this chapter, the effects of the PCs and Lyso-PCs (see Chapters 3-4) on TJ-expressing cells are investigated. The effects of PCs and Lyso-PCs on TJ tightness and

the permeability of the cells to drug-mimicking compounds were assessed. As described in previous chapters, PCs and Lyso-PCs were chosen for their potential to be implemented in the design of novel cavitation agents for the lipid-mediated enhancement of ultrasound-mediated drug delivery, in this case, to the brain.

It was hypothesized that the transfer of PCs or Lyso-PCs from drug-carrying agents or cavitation agents to the BBB could modulate BBB permeability by disrupting lipid rafts essential to the conformation of TJ scaffolding proteins, or by disrupting lipid structures that allow TJ proteins to span the intracellular cleft and lipid probes to diffuse across TJs. Owing to their conical shape and ability to rapidly transfer to cell membranes, Lyso-PCs are expected to locally alter cell membrane volume (e.g. budding) or membrane surface tension which was shown in Chapter 6 to increase membrane hydration in cancer cells, associated with the promotion and stabilization of membrane pores. The shorter chain PCs (10:0, 12:0, 14:0) were also found to rapidly hydrate cell membranes. The reduction of lipid order in cell membranes by either of these lipids is expected to disrupt membrane lipid rafts and may interfere with hemi-fusion at TJs. By these two mechanisms, it is conceivable that exposure to either long or short chain PCs could modulate BBB TJs, so the role of PC chain length was also investigated.

5.2. Methods

5.2.1. Lipid preparation

Suspensions of PCs and Lyso-PCs were prepared by chloroform evaporation, resuspension, and sonication, as described in Chapters 3-4.

5.2.2. Spectral imaging

To assess the effect of Lyso-PCs on MDCK cell lipid order, spectral imaging with C-Laurdan was performed with and without Lyso-PC treatment. MDCK cells were

washed with phosphate-buffered saline (PBS), treated for 10 min with either Lyso-PCs or a PBS sham control, washed twice more with PBS, and labelled with 400 nM C-Laurdan in PBS for 5 min prior to spectral imaging. Cells were maintained at 37±1°C throughout treatment and imaging. Detailed spectral imaging methods are described in Chapter 2.

5.2.3. MDCK cell culture

Madin-Darby canine kidney cells (MDCKs) were employed as a TJ-forming permeability model owing to their high trans-endothelial electrical resistance (TEER, inversely correlated with paracellular ionic permeability), rapid growth and differentiation in culture, and expression of TJ proteins. While MDCKs express certain proteins in the claudin and zonula occludins protein families differently than in the BBB, and under express certain BBB transporters such as p-glycoprotein[34], they have excellent properties for permeability studies and are a standard model for TJ research[35].

MDCKs (Public Health England, Salisbury, UK) were cultured in T-75 flasks and passaged at 80% confluence. MDCK growth medium consisted of DMEM with 10% fetal bovine serum, 2mM l-glutamine, 1% non-essential amino acids, and 1% penicillin-streptomycin.

5.2.4. Trans-endothelial electrical resistance (TEER)

Trans-endothelial electrical resistance (TEER) is inversely proportional to ionic paracellular permeability. TEER depends on the permeability of cell to cell junctions where the trans-endothelial ionic flux is greatest, whereas solute permeability is influenced by all transport pathways such that a nonlinear relationship between TEER and solute permeability exists[36]. Cell monolayers with TEER greater than 150 Ω-cm^2 have been repeatedly shown to be sufficient for permeability studies, owing to the

asymptotic decrease in solute permeability achieved at greater TEER, and the good correlation of solute permeabilities with *in vivo* data, despite the TEER of the *in vivo* human BBB residing at 1-2 kΩ-cm^2 [37–41].

TEER was evaluated using a commercial constant current source and ohm meter (End-Ohm-2, WPI) and two pairs of silver-silver chloride electrodes (EVOM-2 chopstick electrodes, WPI). For TEER measurements, cells were grown in 6.5 mm transwells in 24-well plates and measured daily. Prior to measurements, chopstick electrodes were sterilized in 70% ethanol for 20 minutes, then soaked in 0.22 μm filtered DI water under UV light for 20 minutes, and finally equilibrated in the same medium as the cells for five minutes before taking measurements. TEER (in Ω-cm^2) is calculated by multiplying the resistance across the monolayer by the surface area of the transwell chambers, and subtracting the no-cell control value.

5.2.5. Kinetics of the effects of PCs and Lyso-PCs on TEER

The effects of lipids on TEER as a function of time were measured by three experimental methods. For all three methods, baseline TEER measurements were performed before treatment, samples were incubated between measurements, and measurements were performed at 37 ± 1.5°C. For these experiments, treatment is exposure to a suspension of lipids (e.g. liposomes). Data are presented as the change in TEER relative to baseline (e.g. $\Delta TEER = \frac{TEER_{t=x} - TEER_{t=0}}{TEER_{t=0}}$).

In the first method, MDCKs were treated with PCs or Lyso-PCs for 10 min, the treatment was removed, and the medium replenished. TEER was measured immediately after medium replenishment, and after a 30 min incubation to assess recovery.

In the second method, MDCKs were treated with Lyso-PCs and TEER measurements were conducted at 15 min intervals for 60 min, at which point Lyso-PCs were removed,

and the medium was replenished. Cells were then incubated for 60 min before final TEER measurements were performed.

In the third method, cells were treated with Lyso-PCs and TEER was measured at 15-30 min intervals for 180 min. Lyso-PCs were not removed and the medium was not replenished throughout the experiment. It was found that this method was the most reliable and repeatable for TEER time course experiments.

Temperature control during TEER measurements was achieved by placing transwell plates in a plastic water bath (~ 1 cm filtered DI water) atop a laboratory hot plate. In between measurements, a magnetic stirrer was used to provide even heating. A needle thermocouple was employed to check the temperature in blank wells to guarantee that over-heating did not occur during measurement. The temperature was controlled to ~37 ± 1.5°C. For both experimental methods, samples were randomly assigned to wells such that systematic temperature-related errors could be avoided.

5.2.6. Apparent permeability

To evaluate trans-monolayer solute permeability, diffusion of a charge-neutral solute through both a transwell filter alone, and through cell monolayers grown on transwell filters, was measured and the permeability determined from the following equation[35],

$$P = \frac{\partial Q}{\partial t} * \frac{1}{C_0} * \frac{1}{A} \quad (1)$$

where $\frac{\partial Q}{\partial t}$ is the permeability rate (µg/s), C_0 is the initial concentration in the donor compartment (µg/cm^3), and A is the surface area of the filter (cm^2). The apparent permeability (P_{app}) of the cell monolayer was determined by assuming that the contributions of the cells and the filter (P_{filter}) behave like resistors in parallel[36],

$$\frac{1}{P_{app}} = \frac{1}{P} - \frac{1}{P_{filter}}. \quad (2)$$

For experiments, TRITC-dextrans (1 mg/ml) were added to the apical side of the transwells. After a 60 minute incubation period, three 100 µl samples were taken from the basal chamber (the receiver) of each transwell and measured with the fluorescent plate reader along with TRITC-dextran standards. The linear standard curve was used to determine the total amount of TRITC-dextrans that diffused from apical to basal chamber for each sample.

5.2.7. MTS assays

To assess the cytotoxicity of lipids of interest to MDCK cells, MTS assays were performed as described in Chapter 3.

5.3. Results

5.3.1. Effect of PCs on TEER

The role of hydrocarbon chain length in the effect of PCs on the ionic permeability of MDCK TJs was assessed by TEER measurements (see Figure 3). In these experiments the medium was replenished after treatment as described in the first TEER time-course methods detailed above. While 12:0, 14:0, and 18:0 PCs all reduced TEER, these changes were not statistically significant compared to controls. The TEER was also found to increase modestly following treatment with 12:0, 14:0, 16:0, and 18:0 PCs. The baseline TEER in these experiments was 576 ± 96 Ω-cm^2.

5.3.2. Role of concentration in the effect of 12:0 PC on TEER

The role of concentration in the effect of 12:0 PC on MDCK TEER was also assessed using the first TEER time-course method involving medium replenishment (see Figure 4). It was found that MDCK TEER was below baseline immediately after removing the

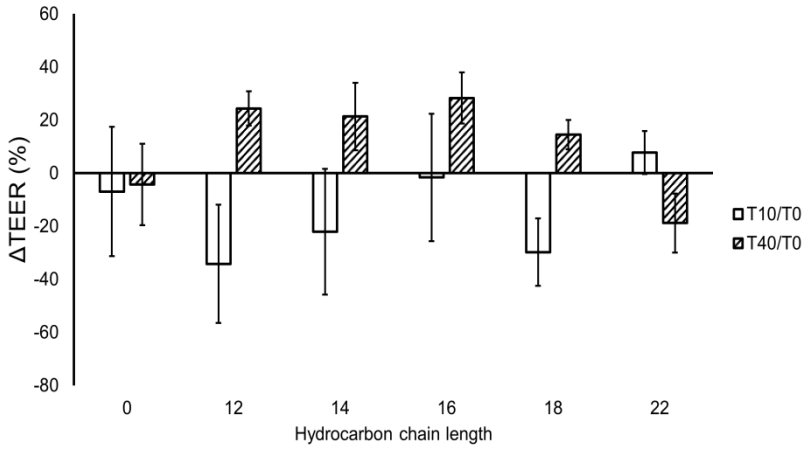

Figure 3: Effect of PCs on MDCK TEER. The change in TEER relative to baseline (ΔTEER) of MDCKs exposed to 12:0, 14:0, 16:0, 18:0, and 22:0 PCs at 500 µM for 10 min was measured immediately after treatment removal and medium replenishment (n = 3). Following a two-way ANOVA with time and chain length as factors, the interaction effect between time and chain length was found to be a statistically significant factor ($p < 0.05$). Bonferroni post-hoc tests, however, revealed that the reductions in TEER were not significant compared to controls.

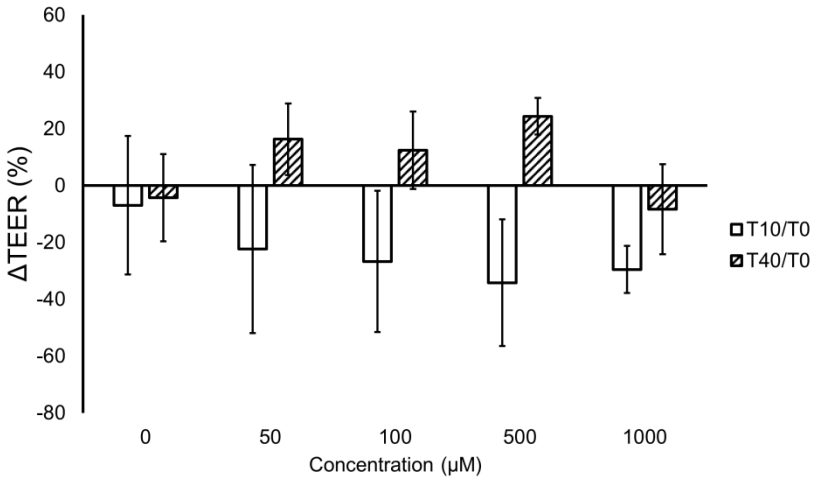

Figure 4: Effect of 12:0 PC on MDCK TEER. The role of lipid concentration in the effects of 12:0 PC exposure on the change in TEER relative to baseline (ΔTEER) of MDCKs with TEER 663 ± 134 Ω-cm^2 was measured. Following a two-way ANOVA with time and concentration as factors, time was found to be a statistically significant factor ($p < 0.05$) while 12:0 PC concentration was not. Bonferroni post-hoc tests ($a=0.01$) revealed statistical significance comparing T10/0 to T40/0 for 12:0 PC treated cells. This change, however, was not statistically significant compared to controls.

treatment, and above baseline after a 30 min incubation period. Exposure to 12:0 PC resulted in changes that were statistically significant over time but not compared with controls. The baseline TEER in these experiments was 663 ± 134 Ω-cm^2.

5.3.3. Cytotoxicity of short chain PCs to MDCKs

The cytotoxicity of 10:0 and 12:0 PCs to MDCKs grown for ~24 h was assessed by MTS assays (see Figure 5). MDCKs exhibited cytotoxicity to 10:0 PCs at concentrations above 100µM, and to 12:0 PCs at concentrations above 1000 µM.

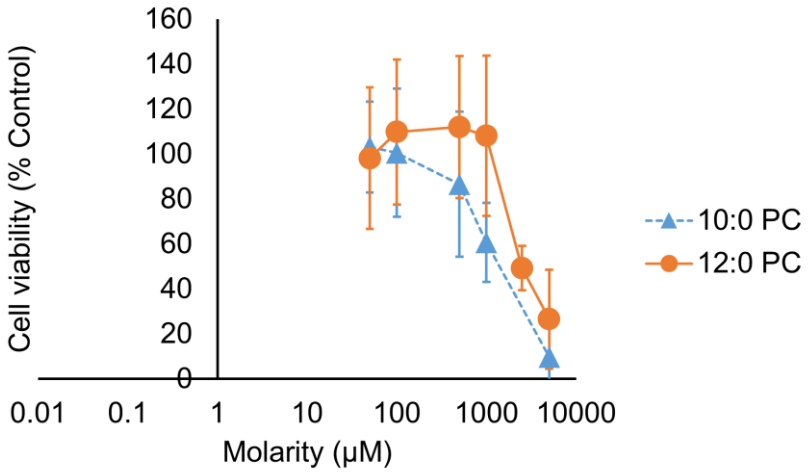

Figure 5: Effect of 10:0 and 12:0 PC concentration on MDCK cell viability. MDCKs were cultured for ~24 h prior to treatment and were treated for ~12 h.

5.3.4. Effect of Lyso-PCs on TEER

The effects of 16:0 and 18:0 Lyso-PCs on the TEER of TJ-expressing MDCKs were investigated (see Figure 6). It was found that Lyso-PC induced 77 ± 14 % and 67 ± 9 % decreases in MDCK TEER following a 10 min exposure to 16:0 and 18:0 Lyso-PCs respectively. The baseline TEER in these experiments was 547 ± 148 Ω-cm^2.

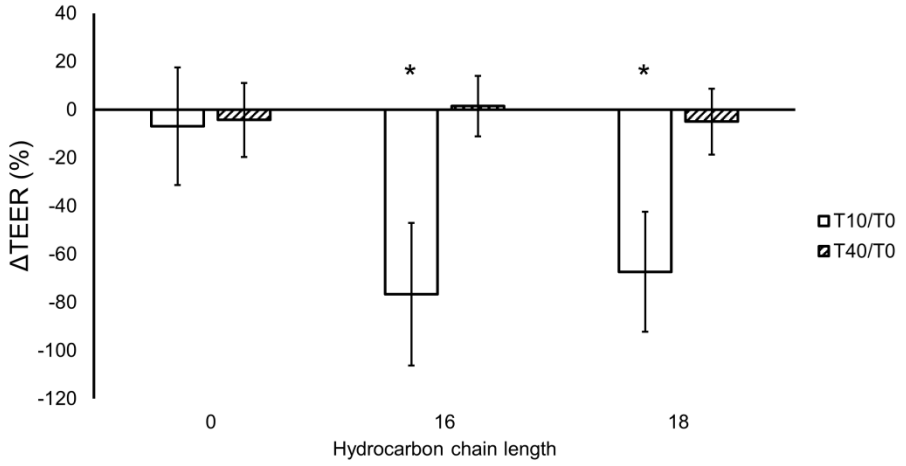

Figure 3: Effect of Lyso-PCs on MDCK TEER. The change in TEER relative to baseline (ΔTEER) of MDCKs with an initial TEER of 547 ± 148 Ω-cm^2 exposed to Lyso-PCs for 10 min, was measured after treatment removal and medium replenishment, and again after 30 min incubation. Two-way ANOVA with chain length and time as factors followed by Bonferroni post-hoc tests revealed that both 16:0 and 18:0 Lyso-PCs induced significant reductions in TEER compared to controls. Samples were found to completely recover within 30 min after removing the treatment. Significance indicated by * for $p < 0.01$.

5.3.5. Time-dependent effect of 16:0 Lyso-PCs on TEER

16:0 Lyso-PC between 10 and 100 µM was found capable of rapidly and severely reducing TEER in MDCKs with full recovery within minutes to hours. Specifically, 100

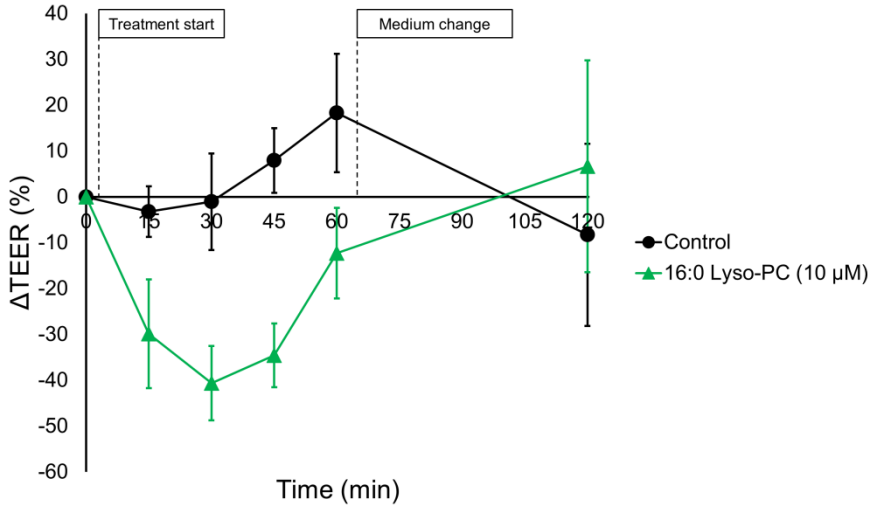

Figure 4: Effect of Lyso-PCs on MDCK TEER over time. MDCKs with an initial TEER of 906 ± 270 Ω-cm^2 were treated for 60 min with 10 µM 16:0 Lyso-PCs, washed, and measured after a 60 min incubation. The reduction in TEER at 30 min was 41 ± 8 % compared to baseline. Samples began to recover prior to removing Lyso-PCs and changing the media. Results were statistically significant relative to baseline and controls at 15, 30, 45, and 60 min as determined by two-sample t-tests (n=3, $p<0.01$).

µM induced a 89 ± 1 % reduction in <1 min in 1358 ± 70 Ω-cm^2 TEER cells (see Figure 8), and 10 µM induced a 41 ± 8 % reduction in <15 min in 906 ± 270 Ω-cm^2 TEER cells (see Figure 7). In cells with 1358 ± 70 Ω-cm^2 TEER, a significant reduction in TEER of 18 ± 6% was also achieved for 10 µM 16:0 Lyso-PC exposure but required a longer onset time (~90 min) (see Figure 8).

In the first experiment, the medium was replenished after 60 min treatment with 16:0 Lyso-PC, and cells were incubated for an additional 60 min (see Figure 7), as described in the second TEER time-course methods (see methods section). Owing to the observed recovery of MDCKs during treatment between 30 and 60 min, the experiment was repeated without removing the treatment or replenishing the medium (see Figure 8), as described in the third TEER time-course methods (see Methods). MDCKs began recovering within 15 min of exposure to 100 µM 16:0 Lyso PC and full recovery was observed within 1-3 h for all 16:0 Lyso-PC TEER time-course experiments performed.

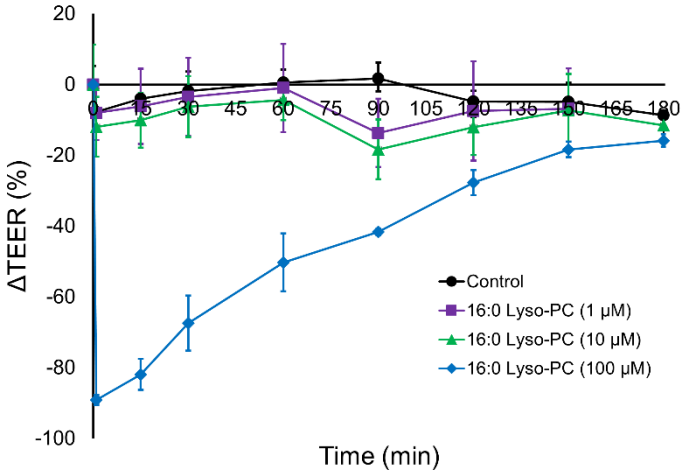

Figure 5: Effect of Lyso-PCs on MDCK TEER over time. MDCKs with an initial TEER of 1358 ± 70 Ω-cm2 were treated for 180 min with either 1, 10, or 100 µM 16:0 Lyso-PCs. The max reduction in TEER for 100 µM exposure was 89 ± 1 % at 1 min and was 42 ± 1 % at 90 min. The max reductions in TEER for 1 and 10 µM exposure at 90 min were 14 ± 10 % and 18 ± 6 %. Full recovery of TEER to control levels was observed for all conditions tested. With the TEER data at 90 min, 1-way ANOVA followed by Tukey-Kramer post-hoc tests were performed. Results were statistically significant relative to controls for 100 µM ($p < 0.01$) and were mildly significant for 10 µM ($p = 0.014$). For 1 µM exposure was $p = 0.052$. For all conditions tested, $n = 3$.

5.3.6. Effect of Lyso-PCs on permeability

The apparent permeability of MDCKs (TEER = 1448 ± 72 Ω-cm^2) to 4.4 kDa TRITC-dextrans during a 30 min exposure to 10 and 100 µM 16:0 Lyso PCs was determined by measuring the fluorescence intensity of TRITC that had crossed MDCK monolayers cultured in transwells (see Figure 9). The apparent permeabilities were $1.65*10^{-7}$ ± $1.37*10^{-7}$ cm-s^{-1} and $1.58*10^{-5}$ ± $0.10*10^{-5}$ cm-s^{-1} for samples exposed to 10 and 100 µM 16:0 Lyso PC respectively, up from $1.25*10^{-8}$ ± $2.28*10^{-8}$ cm-s^{-1} for controls (n = 4). The change in apparent permeability for samples exposed to 100 µM 16:0 Lyso PC was statistically significant ($p < 0.01$, n = 4) compared to controls.

5.3.7. Effect of Lyso-PCs on lipid order

Exposure of MDCK cells to 125 µM 16:0 Lyso-PC for 10 min resulted in significantly reduced cell lipid order and increased membrane hydration (ΔGP = −0.039 ± 0.027) as measured by spectral imaging with C-Laurdan (see Figure 10A). Inspection of C-Laurdan GP maps revealed fluidization or thinning of the highly ordered regions at cell boundaries (see Figure 10B-C).

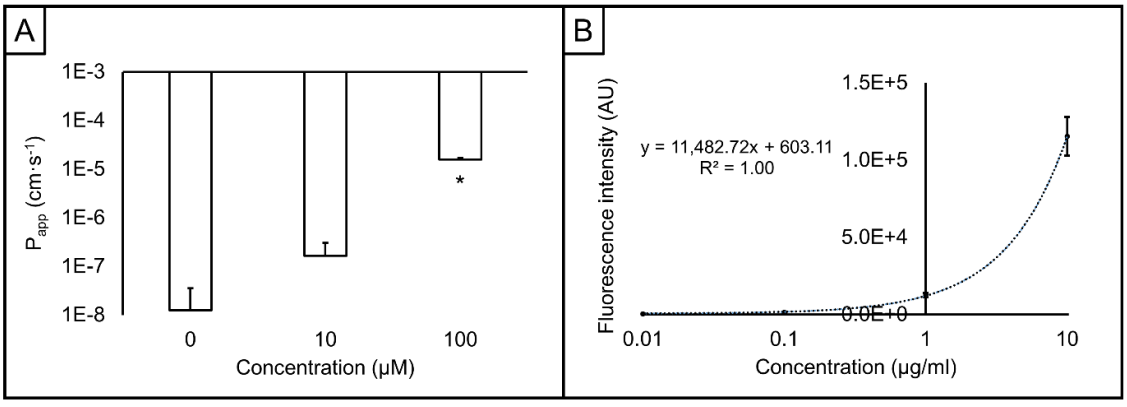

Figure 6: *Apparent permeability (P_{app}) to 4.4. kDa TRITC-Dextrans of MDCKs treated with 16:0 Lyso PCs. (A) P_{app} of MDCK controls (0 µM) and samples exposed to 10 and 100 µM 16:0 Lyso PCs for 30 min respectively. (B) 4.4 kDa TRITC-Dextran standards.*

5.3.8. Cytotoxicity of Lyso-PCs to MDCKs

The cytotoxicity of Lyso-PCs to MDCKs grown for ~24 h was assessed by MTS assays (see Figure 11). MDCKs exhibited some cytotoxicity to 16:0 Lyso-PCs between 10 and 100 µM, and to 18:0 Lyso-PCs between 100 and 1000 µM. Furthermore, the full recovery in the TEER assays suggests that if cells had been allowed to fully differentiate, they may have exhibited even less cytotoxicity to Lyso-PCs. Indeed, increased concentrations of certain proteins (e.g. PECAM and VE-cadherin) at fully-developed cell-cell junctions has been shown to protect cells from apoptosis[11].

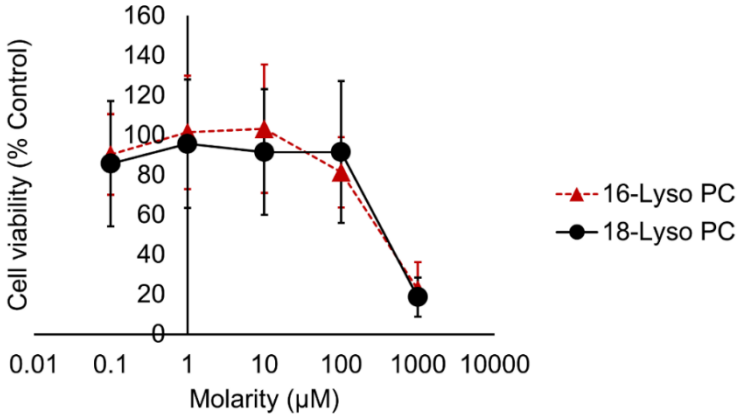

Figure 7: Effect of 16:0 and 18:0 Lyso-PC concentration on MDCK cell viability. MDCKs were cultured for ~24 h prior to treatment and were treated for ~12 h.

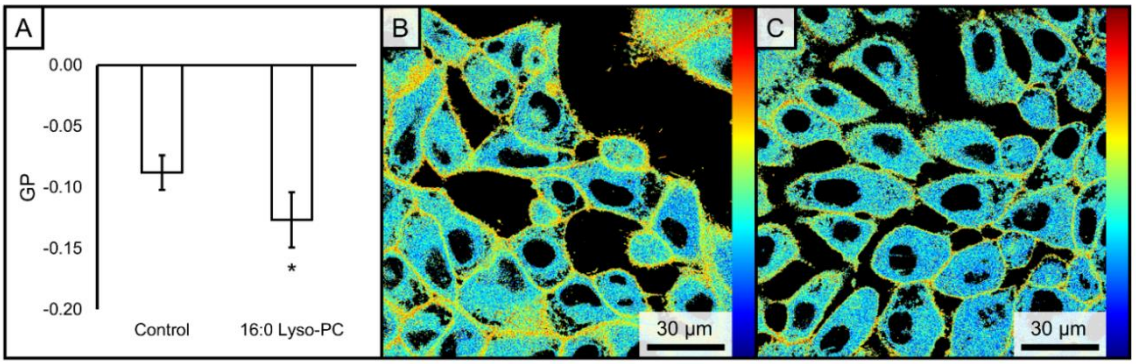

Figure 8: 16:0 Lyso-PC decreases lipid order in MDCK cells. MDCKs treated with 125 µM 16:0 Lyso-PC exhibited significantly reduced lipid order ($p < 0.01$) as shown by the C-Laurdan GP acquired by spectral imaging (without membrane segmentation, owing to the tight-packing of MDCK cells in many of the acquired images). Representative pseudo-coloured GP maps of MDCK controls (B) and treated cells (C) demonstrate thinning of cell membranes and visible lipid disordering. * indicates statistical significance from an unpaired two-tailed t-test ($p = 0.02$, $n = 4$).

Despite the use of background correction, a washing step before performing the MTS assay, and substantial sample numbers (n = 6), large standard deviations were found for the viabilities of MDCK cells exposed to PCs and Lyso-PCs relative control samples. This error may arise from the contribution to the measured absorbance from lipids remaining after washing. Thus, additional washing steps and a longer growth period are recommended for future MTS assays with lipid treatments.

5.4. Discussion

5.4.1. PCs are not ideal candidates for enhancing US-BBBD

The role of PC chain length, 12:0, 14:0, 16:0, 18:0, and 22:0 PC, on the TEER of MDCKs was investigated. It was found that while PCs appeared to lower TEER during treatment and increase TEER after removal of the treatment, these effects were not significant relative to controls. The role of concentration in the effect of 12:0 PC on MDCK TEER was also investigated, and a similar reduction in TEER followed by an increase in TEER after treatment removal was observed. It was found that replenishing the medium after treatment resulted in a large sample-to-sample variability, even in control samples, which may have prevented otherwise significant effects from being discovered. The TEER time course methodology was improved for the experiments concerning Lyso-PCs.

Few experiments investigating the effects of PCs on TEER were found in the literature. 12:0 fatty acid exposure at 750 µM, for example, has been shown to induce ~3-fold increases in permeability in 40 min, and ~11% decrease in TEER in 10 min, in tight-junction-expressing Caco-2 cells[42]. In addition, 10:0 PC has been shown to reversibly permeabilize TJs in frog skin and rabbit nasal epithelial *ex vivo*[43], although was not tested here (the 10:0 PC stock was depleted and the decision was made not to purchase

more, having demonstrated that 10:0 PC cytotoxicity was high in Chapter 3, and having determined that these short-chain PCs were not as well-suited to MB production as Lyso-PCs and longer-chain PCs).

Nonetheless, it is clear from these results that the effects of PCs on MDCK TEER, if any, would require high concentrations or excessively long incubation times. It can thus be concluded that PCs are not ideal candidates for enhancing US-BBBD.

5.4.2. Lyso-PCs reversibly disrupt TJs

The results of the present study demonstrate that exposure to 16:0 or 18:0 Lyso-PCs temporarily disrupts TJs in MDCK monolayers. Exposure of MDCKs with 1358 ± 70 Ω-cm^2 initial TEER to 100 µM 16:0 Lyso-PC achieved a 89 ± 1% reduction in TEER in less than 1 min, and a ~1260-fold increase in permeability to 4.4 kDa TRITC-dextran over 30 min, with a full recovery of TEER in 3 h. While TJ disruption and/or BBB opening by Lyso-PCs has not been previously demonstrated *in vitro* to the author's knowledge, Lyso-PC has been observed to permeabilize the BBB *in vivo* from the CNS-side of the BBB, following injection into the mouse spinal cord[44].

Few studies investigate the effects of lipids on cell monolayers with TJs. The work of Chen-Quay et al. investigating the effects of seven classes of lipids on tight junctions and cell viability using human tracheal/bronchial epithelial cells, is the most thorough[45]. The most potent lipids they found were POVPC and PGPC (oxidized lipids), glucosylsphingosine (a sphingolipid), and lyso-platelet-activation-factor (Lyso-PAF, an ether lipid). These lipids achieved TEER reduction of ~60-90% with ~10-20% reduction in cell viability following a 60 min treatment. 1 mM of these lipids were required to achieve at least a 90% reduction in TEER. While these results are

impressive, 16:0 Lyso-PC required 10-fold lower concentrations for the same TEER reduction in the present study.

The cells employed by Chen-Quay et al. had an average baseline TEER of 500 Ω-cm^2 and expressed Claudin, Occludin, and Zonula Occludins tight junction proteins, suggesting that they were comparable to the MDCKs employed in the present study. The kinetics of Lyso-PC-mediated TEER reduction in the present study suggests that the bioactive lipids employed by Chen-Quay et al. may have greater effects at earlier time points. It can nonetheless be concluded from the present study that to the author's knowledge, 16:0 Lyso-PC has the greatest therapeutic potential of the known tight-junction modulating lipids *in vitro*.

5.4.3. The role of proteins in Lyso-PC-mediated TJ disruption

In this section, Lyso-PC-mediated TJ disruption is considered with regard to Lyso-PC-sensitive signalling pathways, and enzymes involved in Lyso-PC metabolism.

In endothelial cells, Lyso-PC exposure has been shown to activate inflammation-related signalling pathways within minutes (e.g. G protein-coupled receptors, RANTES-pathway, and MAPK/ERK-pathway)[46–48], and to up-regulate leukocyte adhesion molecules resulting in an immunological response within hours[46,49]. Lyso-PC in the CNS has also been associated with activation of microglial cells[44], though these effects are not expected to play a role in US-BBBD owing to the slow trans-bilayer diffusion of Lyso-PC confining it to endothelial cells.

Unbeknownst to the author prior to the experiments of the present study, endothelial layer permeabilization by 16:0 Lyso-PC has been demonstrated previously by Lum and colleagues in cells without TJs (e.g. low TEER ~ 3-4 Ω-cm^2, not representative of BBB permeabilization)[47,48]. 16:0 Lyso-PC was found to induce a cytoskeletal response (e.g.

formation of actin fibres) in endothelial cells, mediated by activation of the RhoA signalling pathway and interaction with a G protein-coupled receptor (GPR-4). Short-interfering-RNA-mediated reduction of GPR-4 expression was found to partially prevent the effects of Lyso-PCs on TEER, and actin fibre formation suggesting that GPR-4 plays a role in Lyso-PC-mediated TEER reduction, at least in endothelial cells without TJs. GPR-4 expression has also been demonstrated in endothelial cells in human brain sections[48] suggesting that Lyso-PC-mediated activation of this pathway is relevant for US-BBBD.

While the cells studied by Lum and colleagues did not exhibit the permeability properties of the BBB or of TJ-expressing cells, it is worth noting the remarkable similarity between their results and the present study with regard to TEER reduction onset and recovery kinetics. Lum and colleagues demonstrated that 10 µM 16:0 Lyso-PC induced a max TEER reduction of ~12% at ~15 min exposure followed by full recovery in ~1 h. In the present study, MDCKs with 906 ± 270 Ω-cm^2 exposed to the same concentration of 16:0 Lyso-PC exposure achieved a 41 ± 8% max decrease in TEER in 1-15 min with full recovery in 1-2 h, and was associated with no significant changes in cell viability compared to controls. While it is problematic to compare results in TJ-expressing cells to those without, the fact that MDCKs with ~300-fold higher TEER than those employed by Lum and colleagues exhibited a greater decrease in TEER may point to additional contributing mechanisms in the present study.

In considering Lyso-PC-mediated TEER reduction recovery kinetics, it is important to consider the metabolism of Lyso-PC in living cells. The enzymatic conversion of Lyso-PCs to PCs and vice versa is described by Land's cycle. By this remodelling pathway, PCs are hydrolysed at the sn-2 position by the phospholipase A2 (PLA_2) enzyme, yielding one Lyso-PC and one fatty acid or cholesterol ester. Enzymatic re-acylation of

Lyso-PC into PC is achieved by lysophospholipid acyltransferase and acyl-coenzyme-A[50]. Lyso-PC can also be enzymatically converted into biologically-active lysophosphatidic acid (LPA). As these processes are expected to occur during the experiments in the present study[51], the conversion of Lyso-PC to PC or LPA, the latter of which has been shown to increase TEER in endothelial cells[52], may explain the full recovery of MDCK TEER in 1-3 h across all experiments.

5.4.4. The role of lipid order in Lyso-PC-mediated TJ disruption

In Chapter 4, the amount of Lyso-PC transferred to cells was estimated using the Lyso-PC partition coefficient from Chi and Wu[53] and the corresponding reduction in cell membrane cholesterol estimated by comparison with the study by Golan et al[54]. The number of Lyso-PCs estimated to partition into cell membranes in the present study (~$2.9*10^5$ Lyso-PCs/cell) is remarkably similar to that at which max cholesterol depletion was found to occur by Golan et al. (~$2.5*10^5$ Lyso-PCs/cell) as estimated by using the red blood cell surface area and 16:0 Lyso-PC partition coefficient from Chi and Wu. It is thus expected that the transfer of Lyso-PCs and depletion of cholesterol described by Golan et al. also applies to the present study.

In the previous chapter, it was argued that under these conditions, Lyso-PC exposure increases the spontaneous curvature of the exterior bilayer leaflet in cells which could be compensated for by an increase in membrane surface tension or cell volume (e.g. by budding) such that the probability of water defects forming in the bilayer is increased. Indeed, exposure of MDCKs to Lyso-PCs significantly increased hydration and decreased lipid order as indicated by a significant reduction in C-Laurdan GP obtained by spectral imaging ($\Delta GP = -0.039 \pm 0.027$).

The reduction in cell membrane cholesterol and lipid order following Lyso-PC exposure is expected to contribute to TJ disruption. Early histological studies demonstrated that the cell membrane is rich in cholesterol in the vicinity of TJs[31]. Detergent-insoluble, cholesterol-rich lipid rafts have since been shown to contain large fractions of TJ proteins occludin, ZO-1, and claudins[29,30]. Treatment of a TJ model (Caco-2s) with methyl-β-cyclodextrin (MβCD), which acutely depletes cell membranes of cholesterol, resulted in ~40% cholesterol depletion commensurate with TEER reduction and enhanced permeability to FITC-dextrans[32]. Subsequent recovery of TEER was achieved by reintroducing cholesterol to cell membranes with MβCD-cholesterol. In a follow-up study, MβCD treatment was shown to dissociate tight junctional proteins from detergent-insoluble rafts[30]. In addition, reduction of cholesterol content by MβCD in MDCKs reduced TEER and reversibly altered TJ morphology as observed by transmission electron microscopy[33]. Cholesterol depletion by treatment with lovastatin, which inhibits an enzyme required for cholesterol synthesis, also resulted in significant TEER reduction, concomitant with occludin redistribution from tight junctions to the intracellular space[29].

There is mounting evidence supporting the notion that cholesterol-rich domains link tight junctional proteins in the intracellular cleft, such as occludin and claudin, with zonula occludins scaffolding proteins that anchor TJ strands to the cytoskeleton. Depolymerization of the actin cytoskeleton induced by latrunculin A, which binds actin monomers, for instance, has been shown to induce both TEER reduction, and relocation of occludin to intracellular vesicles via caveolae-mediated endocytosis in MDCKs[56]. Knockdown of caveolin-1, involved in caveolae-mediated endocytosis, has been shown to both inhibit TJ disruption by latrunculin A in a cholesterol-dependent manner[56], and

to deplete tight junctional proteins[57]. This suggests a complex role for lipid rafts, rich in caveolin-1, in regulating TJs and paracellular permeability.

Lyso-PCs are also known to reversibly inhibit hemi-fusion at cell-to-cell contacts, within seconds[58]. It follows that if the protein-lipid hybrid TJ hypothesis is correct, Lyso-PC exposure may temporarily inhibit hemi-fusion between neighbouring cells required for TJ formation and function. The flip-flop of Lyso-PCs would enhance this effect, inducing severe spontaneous curvature mismatch between Lyso-PC and inverted cylindrical micelles in TJs. The trans-bilayer diffusion or "flip-flop" of Lyso-PC is exceptionally slow in model membranes lacking in cholesterol and proteins ($t_{\frac{1}{2}}$ > 24 h[59]), but may be higher in cells (measured at ~1.9%/h in red blood cell membranes[60,61]), partially as a result of enzymes that induce lipid flip-flop (e.g. flippases)[55]. When cholesterol is depleted as in the present study, flip-flop rates can reach as high as 7-8%/h[61]. The delayed reduction in TEER observed after 90 min exposure to 1-10 µM 16:0 Lyso-PCs in MDCKs may include effects of flip-flop of the transferred Lyso-PCs, whereas more rapid reductions in TEER are not expected to have any contribution from Lyso-PC flip-flop, but may still result from changes in membrane curvature.

In the previous section, enzymes that convert Lyso-PC to PC or LPA were posited to explain the recovery of MDCK TEER during Lyso-PC exposure. The transport of cholesterol from extracellular or intracellular pools, pre-existing or from *de novo* synthesis, to the cell membrane may also contribute to TEER recovery[62,63]. TEER recovery following cholesterol reduction in MDCKs or Caco-2s by MβCD treatment, which affects only membrane cholesterol, however, has been shown to require many hours[32,33]. This is consistent with the fact that there is far less intracellular cholesterol available for transfer than membrane cholesterol, and suggests that cholesterol repletion alone cannot explain the TEER recovery in the present study[33].

5.4.5. Summary of Lyso-PC-mediated TJ disruption mechanisms

Lyso-PCs reversibly disrupt TJs through a complex combination of mechanisms. Lyso-PC transfer to cell membranes and depletion of cell membrane cholesterol results in regions of increased membrane curvature, membrane hydration, and lipid disordering. These effects may disrupt cholesterol-rich lipid rafts between TJ proteins and the cytoskeleton, and/or lipid structures within the intracellular cleft, resulting in temporary disruption of TJs. Either directly or by their effects on lipid order and cholesterol, Lyso-PCs appear to activate inflammation signalling cascades, which may contribute to the observed effects. Effects on the cytoskeleton by any combination of these mechanisms may also play a role. Enzymatic transformation of Lyso-PCs into more innocuous species (e.g. PC or LPA) and cholesterol repletion may contribute to recovery during Lyso-PC treatment. Additional collaboration between membrane biophysicists, biochemists, and biologists is necessary to further elucidate the mechanisms of Lyso-PC-mediated TJ disruption and BBB permeabilization.

5.5. Concluding remarks

In this chapter, tight junctions were introduced as a critical obstacle to the delivery of drugs to the brain. It was hypothesized that exposure of tight-junction-bearing cells to membrane disordering lipids would temporarily increase trans-cellular permeability. To this end, the following was accomplished:

1) Seven lipids and two lipid classes were screened for their tight junction (TJ) modulating capacities and Lyso-PCs were identified as candidates of interest
2) Lyso-PCs were shown for the first time to disrupt TJs *in vitro* and are, to the author's knowledge, the most potent TJ disrupting lipids known.

3) Lyso-PC-induced TEER reduction of ~40-90% occurred within seconds to minutes, followed by complete recovery in 1-3 h across all experiments.

4) Lyso-PC-induced TJ disruption corresponded with an over 1200-fold increase in monolayer permeability to 4.4 kDa TRITC-dextran.

5) Lyso-PC was found to hydrate and disorder MDCK cell membrane lipids which may contribute to the underlying mechanism of TJ disruption.

6) Lyso-PC was found to reversibly disrupt TJs at concentrations exhibiting negligible cytotoxicity.

7) A thorough review of the potential mechanisms underpinning Lyso-PC-mediated TJ disruption and BBB permeabilization was presented.

Having identified Lyso-PCs as capable of reversibly disrupting TJs, an ultrasound-mediated blood-brain barrier disruption (US-BBBD) *in vitro* setup is presented in Appendices II-III for the investigation of Lyso-MBs for US-BBBD.

5.6. References

1. Carpentier, A. *et al.* Clinical trial of blood-brain barrier disruption by pulsed ultrasound. **8,** (2016).
2. Abbott, N. J., Patabendige, A. a K., Dolman, D. E. M., Yusof, S. R. & Begley, D. J. Structure and function of the blood-brain barrier. *Neurobiol. Dis.* **37,** 13–25 (2010).
3. Bradbury, M. W. B. The blood-brain barrier. 453–472 (2014).
4. Engelhardt, B. Development of the blood-brain barrier. *Cell Tissue Res.* **314,** 119–129 (2003).
5. Pardridge, W. M. The blood-brain barrier: bottleneck in brain drug development. *NeuroRx* **2,** 3–14 (2005).
6. Reese, T. S. & Karnovsky, M. J. Fine structural localizatin of blood-brain barrier to exogenous peroxidase. *J Cell Biol* **34,** 207–217 (1967).
7. Brightman, M. W. & Reese, T. S. Junctions between intimately apposed cell membranes in the vertebrate brain. *J. Cell Biol.* **40,** 648–677 (1969).
8. Pardridge, W. M. Drug transport across the blood–brain barrier. *J. Cereb. Blood Flow Metab.* **32,** 1959–1972 (2012).

9. Martìn-Padura, I. *et al.* Junctional adhesion molecule, a novel member of the immunoglobulin superfamily that distributes at intercellular junctions and modulates monocyte transmigration. *J. Cell Biol.* **142,** 117–27 (1998).

10. Lampugnani, M. G. *et al.* A novel endothelial-specific membrane protein is a marker of cell-cell contacts. *J. Cell Biol.* **118,** 1511–22 (1992).

11. Dejana, E. Endothelial cell-cell junctions: happy together. *Nat. Rev. Mol. Cell Biol.* **5,** 261–270 (2004).

12. Tsukita, S. & Furuse, M. Occludin and claudins in tight-junction strands: leading or supporting players? *Trends Cell Biol.* **9,** 268–273 (1999).

13. Furuse, M. *et al.* Occludin: a novel integral membrane protein localizing at tight junctions. *J. Cell Biol.* **123,** 1777–88 (1993).

14. Furuse, M., Fujita, K., Hiragi, T., Fujomoto, K. & Tsukita, S. Claudin-1 and -2: novel integral membrane proteins localizing at tight junctions with no sequence homology to occludin. *J. Cell Biol.* **141,** 1539–1550 (1998).

15. Itoh, M. *et al.* Direct Binding of Three Tight Junction-Associated Maguks, Zo-1, Zo-2, and Zo-3, with the Cooh Termini of Claudins. *J. Cell Biol.* **147,** (1999).

16. Saitou, M. *et al.* Occludin-deficient Embryonic Stem Cells Can Differentiate into Polarized Epithelial Cells Bearing Tight Junctions. *J. Cell Biol.* **141,** 397–408 (1998).

17. Nitta, T. *et al.* Size-selective loosening of the blood-brain barrier in claudin-5–deficient mice. *J. Cell Biol.* **56538,** 21–9525 (2003).

18. Tang, V. W. *et al.* Proteomic and bioinformatic analysis of epithelial tight junction reveals an unexpected cluster of synaptic molecules. *Biol. Direct* **1,** 37 (2006).

19. Kachar, B. & Reese, T. S. Evidence for the lipidic nature of tight junction strands. *Nature* **296,** 464–466 (1982).

20. van Meer, G., Gumbiner, B. & Simons, K. The tight junction does not allow lipid molecules to diffuse from one epithelial cell to the next. *Nature* **322,** 639–641 (1986).

21. Grebenkfimper, K. & Galla, H.-J. Translational diffusion measurements of a fluorescent phospholipid between MDCK-I cells support the lipid model of the tight junctions. *Chem. Phys. Lipids* **71,** 133–143 (1994).

22. Dragsten, P. R., Blumenthal, R. & Handler, J. S. Membrane asymmetry in epithelia: is the tight junction a barrier to diffusion in the plasma membrane? *Nature* **294,** 718–722 (1981).

23. Hein, M. *et al.* Implications of a non-lamellar lipid phase for the tight junction stability PartII: Reversible modulation of transepithelial resistance in high and low resistance MDCK-cells by basic amino acids, Ca 2+, protamine and protons. *Chem. Phys. Lipids* **63,** 223–233 (1992).

24. Hein, M., Post, A. & Galla, H. J. Implications of a non-lamellar lipid phase for the tight junction stability. Part I: Influence of basic amino acids, pH and protamine on the bilayer-hexagonal II phase behaviour of PS-containing PE membranes. *Chem. Phys. Lipids* **63,** 213–21 (1992).

25. Lee, D. B. N., Jamgotchian, N., Allen, S. G., Abeles, M. B. & Ward, H. J. A lipid-protein hybrid model for tight junction. doi:doi:10.1152/ajprenal.00097.2008

26. Van Oss, C. J. Energetics of cell-cell and cell-biopolymer interactions. *Cell Biophys.* **14,** 1–16 (1989).

27. Chernomordik, L., Zimmerberg, J. & Kozlov, M. Membranes of the world unite! *MINI-REVIEW J. Cell Biol.* **175,** 201–207 (2006).

28. Kan, F. W. Cytochemical evidence for the presence of phospholipids in epithelial tight junction strands. *J. Histochem. Cytochem.* **41,** 649–656 (1993).

29. Nusrat, A. *et al.* Tight junctions are membrane microdomains. *J. Cell Sci.* **113,** (2000).

30. Lambert, D., O'Neill, C. A. & Padfield, P. J. Methyl-beta-cyclodextrin increases permeability of Caco-2 cell monolayers by displacing specific claudins from cholesterol rich domains associated with tight junctions. *Cell. Physiol. Biochem.* **20,** 495–506 (2007).

31. Feltkamp, C. A. & Van Der Waerden, A. W. M. Junction Formation Between Cultured Normal Rat Hepatocytes An Ultrastructural Study On The Presence Of Cholesterol And The Structure Of Developing Tight- Junction Strands. *J. Cell Sci* **63,** 271–286 (1983).

32. Lambert, D., O'Neill, C. A. & Padfield, P. J. Depletion of Caco-2 cell cholesterol disrupts barrier function by altering the detergent solubility and distribution of specific tight-junction proteins. *Biochem. J.* **387,** 553–60 (2005).

33. Francis, S. A. *et al.* Rapid reduction of MDCK cell cholesterol by methyl-cyclodextrin alters steady state transepithelial electrical resistance. *Eur. J. af Cell Biol.* **78,** 473–484 (1999).

34. Wilhelm, I., Fazakas, C. & Krizbai, I. a. In vitro models of the blood-brain barrier. *Acta Neurobiol. Exp. (Wars).* **71,** 113–128 (2011).

35. Elick, H. E. S. & Rove, J. R. U. G. MDCK (Madin − Darby Canine Kidney) Cells : A Tool for Membrane Permeability Screening. **88,** (1999).

36. Deli, M. a., Ábrahám, C. S., Kataoka, Y. & Niwa, M. Permeability studies on in vitro blood-brain barrier models: Physiology, pathology, and pharmacology. *Cell. Mol. Neurobiol.* **25,** 59–127 (2005).

37. Reichel, A., Begley, D. J. & Abbott, N. J. An overview of in vitro techniques for blood-brain barrier studies. *Methods Mol. Med.* **89,** 307–324 (2003).

38. Yusof, S. R., Avdeef, A. & Abbott, N. J. In vitro porcine blood–brain barrier model for permeability studies: pCEL-X software pKaFLUX method for aqueous boundary layer correction and detailed data analysis. *Eur. J. Pharm. Sci.* **65,** 98–111 (2014).

39. Chesné, C. *et al.* Drug transfer across the blood-brain barrier: comparison of in vitro and in vivo models. *Adv. Exp. Med. Biol.* **331,** 113–115 (1993).

40. Cecchelli, R. *et al.* Modelling of the blood–brain barrier in drug discovery and development. *Nat. Rev. Drug Discov.* **6,** 650–661 (2007).

41. Gaillard, P. J. & De Boer, A. G. Relationship between permeability status of the

blood-brain barrier and in vitro permeability coefficient of a drug. *Eur. J. Pharm. Sci.* **12,** 95–102 (2000).

42. Lindmark, T., Kimura, Y. & Artursson, P. Absorption Enhancement through Intracellular Regulation of Tight Junction Permeability by Medium Chain Fatty Acids in Caco-2 Cells 1. at <http://www.jpet.org>

43. Röpke, M., Unmack, M. A., Willumsen, N. J. & Frederiksen, O. Comparative Aspects of Actions of a Short-Chain Phospholipid on Epithelial Na 2 Channels and Tight Junction Conductance. *Biochem. Physiol* **118,** 211–214 (1997).

44. Ousman, S. S. & David, S. Lysophosphatidylcholine induces rapid recruitment and activation of macrophages in the adult mouse spinal cord. *Glia* **30,** 92–104 (2000).

45. Chen-quay, S., Eiting, K. T., W-a, A. L., Lamharzi, N. & Quay, S. C. Identification of Tight Junction Modulating Lipids. (2008). doi:10.1002/jps.21462

46. Murugesan, G. *et al.* Lysophosphatidylcholine regulates human microvascular endothelial cell expression of chemokines. *J. Mol. Cell. Cardiol.* **35,** 1375–84 (2003).

47. Huang, F. *et al.* Lysophosphatidylcholine increases endothelial permeability: role of PKC and RhoA cross talk. *Am J Physiol Lung Cell Mol Physiol* **289,** 176–185 (2005).

48. Qiao, J. *et al.* Lysophosphatidylcholine impairs endothelial barrier function through the G protein-coupled receptor GPR4. at <https://www.physiology.org/doi/pdf/10.1152/ajplung.00508.2005>

49. Kume, N., Cybulsky, M. 1 & Gimbrone, M. A. Lysophosphatidylcholine, a Component of Atherogenic Lipoproteins, Induces Mononuclear Leukocyte Adhesion Molecules in Cultured Human and Rabbit Arterial Endothelial Cells. **90,** 1138–1144 (1992).

50. LANDS, W. E. Metabolism of glycerolipids. 2. The enzymatic acylation of lysolecithin. *J. Biol. Chem.* **235,** 2233–7 (1960).

51. Hishikawa, D. *et al.* Discovery of a lysophospholipid acyltransferase family essential for membrane asymmetry and diversity. at <http://www.pnas.org/content/pnas/105/8/2830.full.pdf>

52. Minnear, F. L., Patil, S., Bell, D., Gainor, J. P. & Morton, C. A. Platelet lipid(s) bound to albumin increases endothelial electrical resistance: mimicked by LPA. at <https://www.physiology.org/doi/pdf/10.1152/ajplung.2001.281.6.L1337>

53. Chi, L. M. & Wu, W. G. Effective bilayer expansion and erythrocyte shape change induced by monopalmitoyl phosphatidylcholine. Quantitative light microscopy and nuclear magnetic resonance spectroscopy measurements. *Biophys. J.* **57,** 1225–1232 (1990).

54. Golan, D. E., Furlong, S. T., Brown, C. S. & Caulfield1 '#, J. P. Monopalmitoylphosphatidylcholine Incorporation into Human Erythrocyte Ghost Membranes Causes Protein and Lipid Immobilization and Cholesterol Depletion^. *Biochemistry* **27,** 2661–2667 (1988).

55. Devaux, P. F., Herrmann, A., Ohlwein, N. & Kozlov, M. M. How lipid flippases

can modulate membrane structure. *Biochim. Biophys. Acta - Biomembr.* **1778,** 1591–1600 (2008).

56. Shen, L. & Turner, J. R. Actin Depolymerization Disrupts Tight Junctions via Caveolae-mediated Endocytosis □ V. *Mol. Biol. Cell* **16,** 3919–3936 (2005).

57. Song, L., Ge, S. & Pachter, J. S. Caveolin-1 regulates expression of junction-associated proteins in brain microvascular endothelial cells. *Blood* **109,** 1515–23 (2007).

58. Chernomordik, L., Chanturiya, A., Green, J. & Zimmerberg, J. The Hemifusion Intermediate and its Conversion to Complete Fusion: Regulation by Membrane Composition. *Biophys. J.* **69,** 922–929 (1995).

59. Bhamidipatf, S. P. & Hamilton, J. A. Interactions of Lyso 1-Palmitoylphosphatidylcholine with Phospholipids: A 13C and 31P NMR Study+. *Biochemistry* **34,** 5666–5677 (1995).

60. Mohandas, N., Wyatt, J., Mel, S. F., Rossi, M. E. & Shohet, S. B. Lipid Translocation across the Human Erythrocyte Membrane. **257,** 6537–6543 (1982).

61. Bergmann, W. L., Dressler, V., Haest, C. W. M. & Deuticke, B. Reorientation rates and asymmetry of distribution of lysophospholipids between the inner and outer leaflet of the erythrocyte membrane. *Biochim. Biophys. Acta - Biomembr.* **772,** 328–336 (1984).

62. Phillips, M. C., McLean, L. R., Stoudt, G. W. & Rothblat, G. H. Mechanism of cholesterol efflux from cells. *Atherosclerosis* **36,** 409–422 (1980).

63. Phillips, M. C., Johnson, W. J. & Rothblat, G. H. Mechanisms and consequences of cellular cholesterol exchange and transfer. *Biochim. Biophys. Acta* **906,** 223–276 (1987).

64. Heye, A. K. *et al.* Assessment of blood–brain barrier disruption using dynamic contrast-enhanced MRI. A systematic review. *YNICL* **6,** (2014).

VI.

Concluding remarks

6.1. Primary research contributions

In this thesis, lipid transfer from microbubbles to cells was investigated as a potential mechanism, synergistic with cavitation phenomena, for cell membrane and cell-cell junction permeabilization in ultrasound-mediated drug delivery.

In Chapter 1, cavitation phenomena and the mechanisms associated with ultrasound and microbubble-mediated drug delivery were described. The structures, behaviours, and functions of lipids as they occur in phospholipid-shelled microbubbles and cell membranes were also introduced. Further evidence from the literature was provided showing that drug delivery by ultrasound and microbubble exposure coincides with localized lipid delivery. This thesis puts forth the concept that the delivery of foreign lipids to target regions in the body has the potential to modulate cellular functions, including membrane and junctional permeability, which may be leveraged to improve ultrasound-mediated drug delivery outcomes.

In Chapter 2, it was shown that lipids can transfer from microbubbles to cell membranes, influencing cell membrane lipid order and hydration. Critically, this effect was found to be highly dependent on the microbubble formulation (e.g. carrier lipid chain length, emulsifier species, and molar ratio of lipid to emulsifier). It was argued that lipid transfer from microbubbles that decreased cell membrane lipid order would lower the energy barrier to pore formation in cell membranes. As pore formation is a principle pathway for increased drug uptake in sonoporation, the permeabilization of cells by ultrasound and microbubble exposure, it was hypothesized that a decrease in cell membrane lipid order would increase sonoporation efficiency. Interestingly, however, no such increase was observed for the laboratory and clinical microbubble formulations investigated.

In Chapter 3, saturated phosphatidylcholines (PCs), the primary component in phospholipid-shelled microbubbles, were investigated as cell membrane modulators for enhancing sonoporation. The solubility of PCs in aqueous solution increases as the chain length is reduced, resulting in higher lipid transfer rates. Additionally, the transfer of shorter PCs to cell membranes introduces a chain length mismatch. It was thus hypothesized that lowering the PC hydrocarbon chain length enhances the disordering effect of PC exposure on cell membrane lipids. Indeed, it was found that cells exposed to PCs exhibited cell membrane disordering that was inversely proportional to the PC hydrocarbon chain length. The shortest PC investigated, 10:0 PC, for example, was found to rapidly (~90 s) alter the lipid order of cancer cell plasma membranes and intracellular lipids, resulting in concentration-dependent cell membrane permeabilization and cytotoxicity.

A medium hydrocarbon chain length lipid, 12:0 PC, which was found to disorder cell membrane lipids to a greater extent than previously tested microbubble formulations without permeabilizing cells on its own, was further investigated for its impact on sonoporation. Surprisingly, exposure to 12:0 PC immediately prior to sonoporation did not increase the number of cells permeabilized. With this result, it was concluded that enhancing sonoporation by a lipid-transfer mechanism would not be achieved by optimization of saturated PC exposure. Increasing the PC chain length from 18 to 22 in PC-PEG40S microbubbles, however, resulted in microbubbles that produced more sustained acoustic emissions and a 3-fold increase in the percentage of cells sonoporated.

Having investigated common laboratory and clinical microbubble formulations, in addition to systematically varying the chain length of PCs used to make microbubbles, a further investigation into the role of PC shape in ultrasound-mediated drug delivery was

conducted in Chapter 4. It was hypothesized that lipids more conical in shape, in this case saturated lysophosphatidylcholine (Lyso-PC), would be better suited to promoting pore formation and pore stability in cell membranes. Indeed, this concept has been used to design thermosensitive liposomes that use Lyso-PCs to stabilize liposomal pores upon exposure to mild hyperthermia, achieving impressive triggered release characteristics. Lyso-PCs, PCs with one hydrocarbon chain removed by hydrolysis, are more soluble in aqueous solution than PCs of equivalent chain length giving them higher lipid transfer rates. The reduction of the hydrophobic region of Lyso-PCs compared to PCs also gives them negligible transverse diffusion or membrane "flip-flop" rates, meaning that they are confined to the extracellular membrane leaflet, imparting significant curvature stresses in the cell membrane, commensurate with increased membrane hydration and decreased lipid order. Consistent with the arguments of Chapter 2, Lyso-PCs at sufficient concentrations, like 10:0 PC, were found to induce pore formation in cell membranes in the absence of ultrasound and microbubbles exposure.

In Chapter 4, microbubbles containing 16:0 Lyso-PC (Lyso-MBs) were developed to assess the effects of Lyso-PC on sonoporation. It was found that exposing cells to 16 µM Lyso-PC in Lyso-MBs resulted in ~6-fold increase in the number of permeabilized cells compared to microbubbles made with the same quantity of a non-hydrolysed PC with an equal hydrocarbon chain length (16:0 PC). This difference could not be attributed to microbubble size distributions, concentrations, or acoustic emissions, and thus appears to demonstrate that sonoporation can indeed be enhanced by designing microbubbles to exploit lipid transfer mechanisms. Where in Chapter 2, cell membrane poration was caused by the mechanical effects of cavitation, and in Chapter 3 lipids were found capable of porating cells in the absence of ultrasound, in Chapter 4

sonoporation was achieved with Lyso-MBs which may involve both cavitation-mediated and lipid-mediated mechanisms. Additional experiments are required to clarify this mechanism but it is emphasized that in order for pore formation to occur, the membrane hydration must increase and the lipid order must correspondingly decrease. Whether this occurs by the mechanical stresses associated with cavitation, or by the transfer of lipids to and from the cell membrane, or by some synergistic mechanism, has yet to be determined.

In Chapter 5, the concept of enhancing ultrasound-mediated drug delivery by lipid transfer mechanisms was extended from sonoporation to blood-brain barrier opening. Saturated PCs and Lyso-PCs were screened for their effects on tight junctions. Lyso-PCs were shown for the first time to reversibly disrupt tight junctions and to increase permeability of a tight-junction-bearing cell model *in vitro*, at concentrations exhibiting negligible cytotoxicity. In addition, Lyso-PC exposure was found to hydrate and disorder membrane lipids in tight-junction-expressing cells which may contribute to the underlying mechanisms of tight junction disruption.

One limitation of this work was the narrow range of ultrasound parameters employed and comparable levels of acoustic emissions throughout. This leaves two open questions that bear highlighting: 1) Ultrasound and cavitation did not appear to change the effect of microbubbles on cell membrane lipid order in Chapter 2. Could ultrasound parameters not investigated, or length scales and time scales not probed reveal a significant role for ultrasound in modifying cell membrane lipid order? Since cavitation can permeabilize cells, there should be local and transient changes in membrane hydration that could likely be measured but may be difficult to capture. Furthermore, the role of ultrasound pressure, frequency, duty cycle, PRF, and exposure duration have yet to be characterized in this regard. 2) In Chapter 4 it was found that many

microbubble remained after sonoporation. Since ultrasound appears necessary to trigger the release of Lyso-PC from Lyso-MBs, it follows that this process could be quite dependent on ultrasound parameters, yet this has not been characterized yet. Direct characterization of Lyso-PC shedding from Lyso-MBs and the resultant permeabilization of cells as a function of the aforementioned ultrasound parameters would contribute to a better understanding of the observed phenomena. Another limitation comes from the in vitro models employed. In addition to cancerous and non-cancerous epithelial cells, it would strengthen the arguments in the thesis to demonstrate these effects in more cell types, e.g. in endothelial cells. To this end, repetition of the experiments in Chapter 5 with the in vitro BBB model detailed in Appendix II is ongoing. A final limitation that bears mentioning, concerns the types of lipids investigated. While PEGylated fatty acids, PCs and Lyso-PCs formed a logical initial investigation, it would certainly be interesting to continue investigation with other lipids, such as the alkyl ether lipids proposed in Chapter 4, or phospholipids with different headgroups, for instance.

Overall, the contributions of this thesis may be summarised as follows:

1) Lipid transfer from the shells of microbubbles to the plasma membranes of cells was found to impact cell membrane physicochemical properties including lipid order and membrane hydration.
2) Under the ultrasound exposure conditions tested and using numerous conventional microbubble formulations, microbubble-mediated cell membrane modulation by lipid transfer was found not to play a significant role in sonoporation.

3) Cavitation was found to enhance the delivery of microbubble shell material to cell membranes in a manner that corresponded with microbubble-mediated cell membrane modulation.
4) The disordering of cell membranes by PCs, which can be incorporated into MB shells, was found to be inversely correlated with hydrocarbon chain length. The shortest non-water-soluble PC (10:0 PC) induced rapid membrane permeabilization, consistent with the proposed pore formation model.
5) Lyso-PCs were found to disorder cell membrane lipids in three cell lines, and were found to reversibly disrupt tight junctions, increasing permeability at sub-cytotoxic concentrations in MDCK cells. Permeabilization by Lyso-PCs, which are conical, is also consistent with the proposed pore formation model.
6) Lyso-PCs were incorporated into microbubbles resulting in a novel cavitation agent, Lyso-MBs, which appeared to promote pore formation in cell membranes via a lipid transfer mechanism. Lyso-MBs were hypothesized to be compatible with alkyl ether lipids, a class of antineoplastic agents comprising synthetic lysolipids.
7) Lyso-MBs increased the number of cells sonoporated by ~4-fold and are an interesting candidate for reversible ultrasound-mediated blood-brain barrier disruption.

6.2. Future work

6.2.1. Elucidation of lipid order modulation mechanisms

Throughout this thesis, spectral imaging with C-Laurdan, a mechanism-agnostic method with high spatial and temporal resolution, provided a means of quantifying cell membrane lipid order in response to ultrasound and microbubble exposure. Further characterization of the lipid exchange between microbubbles and cell membranes by

HPLC with mass spectrometry (MS) and/or evaporative light scattering detection (ELSD) could be employed to determine the mechanisms of the observed phenomena. Specifically, the transfer of lipids and emulsifiers from microbubbles to cell membranes could be quantified, and the transfer of lipid species (e.g. cholesterol) from cells to microbubbles could be confirmed and the lipids identified and quantified.

6.2.2. Influence of blood constituents on lipid exchange and cavitation dynamics

Much effort has been expended designing and characterizing microbubbles that exhibit low polydispersity and ideal shell mechanical properties or stability in water or salt solutions at room temperature, with the understanding that such parameters are influential in ultrasound-mediated drug delivery. Correspondingly, correlations between microbubble size distribution and shell characteristics and drug delivery outcomes *in vivo* have been demonstrated[1,2]. Notwithstanding, as microbubbles are transferred from a water or a salt solution *in vitro* to blood *in vivo*, the chemical composition, pH, and temperature of the medium change among other factors, which is expected to alter the behaviour of the lipid and gas molecules comprising microbubbles (see Chapter 1). Indeed, microbubble size distributions and concentrations were observed to shift substantially upon transfer to a medium at 37°C (see Chapter 2). The question remains, however, of whether microbubble characterizations in the absence of blood constituents, at room temperature, in water, and often under static conditions, are truly representative of the *in vivo* condition, and if optimizing for such characterizations is misleading microbubble design.

It is well known that particles, when injected into the bloodstream can gain a coating, commonly referred to as the "protein corona", consisting of proteins, lipids, and sugars[3]. The adsorption of such biomolecules to the surface of drug-carrying vehicles can markedly affect their circulation times and shell properties. The protein corona of

phospholipid-shelled microbubbles (or other cavitation agents) after flowing in blood, however, has not been characterized in detail to the author's knowledge. Additionally, the effects of different protein coronas, which vary with animal model and disease, on microbubble cavitation dynamics has not been studied. The systematic characterization of microbubble cavitation dynamics, size distributions, stability, and lipid transfer kinetics as a function of potential protein coronas, blood constituents, and other physiological parameters, may contribute to our understanding of microbubble behaviour in circulation, and to the development of microbubble formulations with superior *in vivo* behaviour.

Additionally, lipid transfer is undoubtedly influenced by the presence of blood constituents both adsorbed to the microbubble shells and in solution. Lipoproteins and blood cells are known to alter transfer kinetics and, as highlighted by the results in Appendix I, can be critical for lipid transfer mechanisms. For the successful translation of a lipid-transfer-dependent drug delivery strategy, the influence of blood constituents on transfer rates would have to be well-characterized.

6.2.3. Sonoporation with Lyso-MBs *in vivo*

Before progressing to sonoporation studies with pore-promoting microbubbles (e.g. Lyso-MBs) *in vivo*, further development of the microbubble formulation, clarification of mechanisms, and characterization of lipid transfer and sonoporation in whole blood is warranted. One potential application in this regard is sonoporation of the lymphatics for the treatment of metastatic cancer in the sentinel lymph node, which has been achieved previously but requires improvements in sonoporation efficiency for clinical translation[4].

6.2.4. The role of cavitation microstreaming in sonoporation

To characterize the µLAR device employed in Chapter 2, an algorithm for the quantification of cavitation microstreaming flows by the analysis of streak velocimetry images was developed[5]. Subsequent analysis of cavitation microstreaming flows in various ultrasound setups revealed that it is not clear that cavitation microstreaming contributes significantly sonoporation. Further experiments are thus required to assess the role of cavitation microstreaming in sonoporation, which is often cited as a principle mechanism without adequate experimental evidence (see discussion in Chapter 2). This investigation is readily achievable with the software developed in this thesis in combination with the µLAR device.

6.2.5. Ultrasound-mediated blood-brain barrier disruption with Lyso-MBs

In Chapter 4, it was shown that phospholipid-shelled microbubbles can be formed with Lyso-PCs (Lyso-MBs). In Chapter 5 it was demonstrated that Lyso-PCs can reversibly disrupt tight junctions, permeabilizing the blood-brain barrier, at non-toxic and relatively low concentrations (~10-100 µM). These findings, taken together, suggest that lipid transfer from Lyso-MBs could provide a synergistic mechanism with cavitation for ultrasound-mediated blood-brain barrier disruption (US-BBBD). Investigation of this hypothesis should progress with comparison of the performance of Lyso-MBs with non-Lyso-MBs *in vitro* with regard to,

1) The kinetics and magnitude of US-BBBD and recovery
2) The relationships between US-BBBD and recovery and ultrasound and MB parameters
3) The acoustic emissions associated with US-BBBD and recovery

Whilst high quality US-BBBD mechanistic studies have been performed *in vivo*[6–11], several fundamental questions remain, and such experiments offer limited control over

experimental factors at a significant cost to life. Unfortunately, no standardized method for assessing US-BBBD and recovery *in vitro* has been established. A setup for investigating US-BBBD *in vitro* is thus needed in general, for mechanistic studies and for screening novel US-BBBD strategies prior to *in vivo* experimentation, and more specifically for assessing Lyso-MBs for US-BBBD. To this end, an *in vitro* US-BBBD setup is in development for the proposed experiments (see Appendix III).

If Lyso-MBs were found to improve US-BBBD *in vitro*, further investigation *in vivo* would ideally employ DCE-MRI to assess changes in BBB permeability with sufficient spatial and temporal resolution, µPET for confirmation of lipid delivery, and some form of acoustic emissions monitoring, e.g. PAM.

6.3. Perspective

Over the course of performing the experiments detailed in this thesis, ultrasound and cavitation agents have broken through previously insurmountable barriers to drug delivery. Ultrasound-mediated blood-brain barrier disruption has been achieved clinically both invasively[12] and non-invasively[13] and additional clinical trials investigating its use for the treatment of brain cancer[14], amyotrophic lateral sclerosis[15], Alzheimer's disease[16] are underway. Metastatic liver tumours have been treated by ultrasound-mediated triggered release of cancer therapeutics from thermosensitive liposomes in a further clinical trial in Oxford[17], and a clinical trial applying this technique to solid tumours in children is currently underway[18]. A clinical trial employing ultrasound to induce an immune response for the enhancement of immuno-oncology drugs in women diagnosed with stage IV metastatic breast cancer is also ongoing[19]. The vast number of successful animal trials for cancer and other indications in recent years, in combination with the aforementioned human clinical trials point to a

bright future for the non-invasive and targeted delivery of drugs by ultrasound and cavitation agents.

This thesis endeavoured to investigate the potential of lipids to enhance ultrasound-mediated drug delivery, identifying Lyso-PC as a candidate for promoting sonoporation and blood-brain barrier disruption that can be incorporated successfully into phospholipid-shelled microbubbles. Two of the above human clinical trials already rely on Lyso-PCs to enhance triggered release from thermosensitive liposomes by a pore stabilization mechanisms. The precedence for ultrasound in combination with Lyso-PCs in human clinical trials has thus been established. Indeed, lipids, such as Lyso-PCs may offer a safe and effective way to enhance ultrasound-mediated drug delivery with minimal regulatory hurdles. Furthermore, Lyso-PCs are readily metabolized by cells and appear to pose no threat to healthy tissue when administered below cytotoxic concentrations.

The outlook of this thesis is that the experiments within, however early in their development, are nonetheless promising in their findings. Indeed, it is the author's view that this thesis may serve as a first step in a greater effort towards leveraging lipid delivery for the enhancement of ultrasound-mediated drug delivery. With ~43000 lipid structures identified to date, there is undoubtedly so much more to discover.

6.4. References

1. Choi, J. J. *et al.* Microbubble-Size Dependence of Focused Ultrasound-Induced Blood–Brain Barrier Opening in Mice In Vivo. *IEEE Trans. Biomed. Eng.* **57,** 145–154 (2010).
2. Wu, S.-Y., Chen, C. C., Tung, Y.-S., Olumolade, O. O. & Konofagou, E. E. Effects of the microbubble shell physicochemical properties on ultrasound-mediated drug delivery to the brain. *J. Control. Release* **212,** 30–40 (2015).
3. Palchetti, S. *et al.* The protein corona of circulating PEGylated liposomes. *Biochim. Biophys. Acta - Biomembr.* **1858,** 189–196 (2016).
4. Datta, S. *et al.* Correlation of cavitation with ultrasound enhancement of

thrombolysis. *Ultrasound Med. Biol.* **32,** 1257–1267 (2006).

5. Pereno, V. *et al.* Layered acoustofluidic resonators for the simultaneous optical and acoustic characterisation of cavitation dynamics, microstreaming, and biological effects. *Biomicrofluidics* **12,** 34109 (2018).
6. Nhan, T. *et al.* Drug delivery to the brain by focused ultrasound induced blood-brain barrier disruption: Quantitative evaluation of enhanced permeability of cerebral vasculature using two-photon microscopy. *J. Control. Release* **172,** 274–280 (2013).
7. Sun, T. *et al.* Acoustic cavitation-based monitoring of the reversibility and permeability of ultrasound-induced blood-brain barrier opening. *Phys. Med. Biol.* **60,** 9079–9094 (2015).
8. Samiotaki, G. *et al.* Pressure and microbubble size dependence study of focused ultrasound-induced blood-brain barrier opening reversibility in vivo. *AIP Conf. Proc.* **1481,** 300–306 (2012).
9. Marty, B. *et al.* Dynamic study of blood-brain barrier closure after its disruption using ultrasound: a quantitative analysis. *J. Cereb. Blood Flow Metab.* **32,** 1948–58 (2012).
10. Raymond, S. B., Skoch, J., Hynynen, K. & Bacskai, B. J. Multiphoton imaging of ultrasound / Optison mediated cerebrovascular effects in vivo. 393–403 (2007). doi:10.1038/sj.jcbfm.9600336
11. Park, J., Zhang, Y., Vykhodtseva, N., Jolesz, F. A. & McDannold, N. J. The kinetics of blood brain barrier permeability and targeted doxorubicin delivery into brain induced by focused ultrasound. *J. Control. Release* **162,** 134–142 (2012).
12. Carpentier, A. *et al.* Clinical trial of blood-brain barrier disruption by pulsed ultrasound. **8,** (2016).
13. Lipsman, N. *et al.* ACTR-42. Initial Experience Of Blood-Brain Barrier Opening For Chemotherapeutic-Drug Delivery To Brain Tumours By Mr-Guided Focused Ultrasound. *Neuro. Oncol.* **19,** vi9-vi9 (2017).
14. ExAblate Blood Brain Barrier Disruption (BBBD) for Planned Surgery in Glioblastoma - ClinicalTrials.gov. at <https://clinicaltrials.gov/ct2/show/NCT03322813>
15. Blood-Brain Barrier Opening Using MR-Guided Focused Ultrasound in Patients With Amyotrophic Lateral Sclerosis - ClinicalTrials.gov. at <https://clinicaltrials.gov/ct2/show/NCT03321487>
16. Blood Brain Barrier Opening in Alzheimer' Disease - ClinicalTrials.gov. at <https://clinicaltrials.gov/ct2/results?pg=1&load=cart&id=NCT03119961>
17. Lyon, P. C. *et al.* Clinical trial protocol for TARDOX: a phase I study to investigate the feasibility of targeted release of lyso-thermosensitive liposomal doxorubicin (ThermoDox®) using focused ultrasound in patients with liver tumours. *J. Ther. Ultrasound* **5,** (2017).
18. A Phase I Study of Lyso-thermosensitive Liposomal Doxorubicin and MR-HIFU for Pediatric Refractory Solid Tumors - ClinicalTrials.gov. at <https://clinicaltrials.gov/ct2/show/NCT02536183>

19. Focused Ultrasound and Pembrolizumab in Metastatic Breast Cancer - ClinicalTrials.gov. at <https://clinicaltrials.gov/ct2/show/NCT03237572>

Appendix I

Saturated lysophosphatidylcholine in thermosensitive liposomes for triggered release by ultrasound-mediated mild hyperthermia

A1.1. Abstract

In this appendix, the effect of lysophosphatidylcholines (Lyso-PCs) in thermosensitive liposomal formulations (Lyso-TSLs) previously employed in animal and human trials for enhanced drug delivery with ultrasound-mediated mild hyperthermia[1–3] on cells is investigated. In Lyso-TSL formulations, Lyso-PCs are used to promote and stabilize pores that enable rapid drug release upon exposure to mild hyperthermia[4]. Lyso-PCs are also known to have similar pore promoting and stabilizing effects on cell membranes[5], although this has not been demonstrated previously as a mechanism for drug delivery with Lyso-TSLs to the author's knowledge. It was hypothesized that under mild hyperthermia, Lyso-PCs desorb from Lyso-TSLs, transfer to cell membranes, and disorder cell lipids, providing a synergistic mechanism with mild hyperthermia for enhanced drug delivery. For this preliminary study, mild hyperthermia was achieved by increasing the temperature of incubation rather than by ultrasound exposure. It was found that incubation with Lyso-TSLs did not alter cell membrane lipid order or permeability which is attributed to the dependence of Lyso-PC transfer on the vesicle-to-cell ratio. The potential for Lyso-PC transfer from Lyso-TSLs *in vivo* is described.

A1.2. Introduction

A1.2.1. Incorporating Lyso-PCs into TSLs improves their delivery characteristics

Thermosensitive liposomes (TSLs) are an attractive platform for localized drug delivery by triggered release. TSLs are designed, ideally, to provide stable encapsulation of drugs at body temperature and rapid release (e.g. >60% in <3s) under mild hyperthermia as well as sufficiently long clearance times for successful drug delivery[6]. TSLs should also be small enough to circulate in capillaries and to potentially benefit from the enhanced permeability and retention (EPR) effect[6].

16:0 PC was implemented as the sole constituent of the first TSL and is the most used phospholipid in all of thermal drug delivery[7]. 16:0 PC, a naturally-occurring long-chain phospholipid found in abundance in cell membranes[8], has a melting temperature slightly above body temperature (T_m=41.5-41.9 °C)[4,9]. While 16:0 PC TSLs are more permeable at phase transition, they suffer from slow and incomplete release of drugs upon heating, and a lack of protection from blood constituents and the immune system[4,8,10].

Incorporation of 18:0 PE-PEG2000 into 16:0 PC TSLs solves the latter issue by providing steric protection. PEG-conjugated lipids, such as 18:0 PE-PEG2000, prolong the circulation time of liposomes by protecting them from adsorption of proteins, shielding the surface charge, and reducing adhesion to cells[8]. Thus, while 18:0 PE-PEG does not significantly impact drug loading or release properties of TSLs[11], it provides clear benefits drug delivery.

Mills and Needham discovered that incorporating Lyso-PCs, PCs with one acyl chain removed by hydrolysis, into 16:0 PC and 18:0 PE-PEG2000 TSLs, TSLs with near ideal characteristics were achieved (Lyso-TSLs)[4]. Lyso-TSLs are in gel state at body temperature, exhibiting extremely low permeability. Upon exposure to mild hyperthermia (38-42°C), Lyso-TSLs release rapidly (within 3 min[11]). Incorporation of Lyso-PCs into TSLs has a negligible effect on drug loading and phase transition temperature[4,11]. Furthermore, Lyso-TSLs exhibit a half-life of ~1.3 h, which is long enough for successful drug delivery[11].

The increased liposomal permeability of Lyso-TSLs near phase transition can be explained by the formation and stabilization of high-permeability defects in the Lyso-TSL bilayer. These defects include pores (from fusion of inner and outer bilayer leaflets

joining intervesicular fluid with the aqueous bulk) and grain boundaries (regions of maximized compressibility and permeability between regions of different phase states)[4]. The conical shape of Lyso-PCs helps them occupy the highly curved surfaces at pores[6,7,11], resulting in a lower critical energy for pore formation, as described in Chapter 2. Owing to its more conical geometry and shorter chain length, 16:0 Lyso-PC is more effective than 18:0 Lyso-PC for enhancing pore formation and stabilization in Lyso-TSLs[4], although both formulations are a vast improvement over 16:0 PC TSLs.

A1.2.2. Drug delivery with Lyso-TSLs

Delivery of Dox is a common benchmark for novel drug-loaded nanoparticles or liposomes, owing in part to the fact that the first FDA-approved drug-loaded liposome, Doxil, was loaded with doxorubicin (Dox)[12]. The clinical utility of free Dox, a chemotherapeutic that inhibits DNA and RNA synthesis to non-specifically kill tumour cells[13], is hampered by its high levels of cardiotoxicity[14]. Improvements in delivery afforded by liposomal encapsulation and/or mild hyperthermia alone are not sufficient to overcome the off-target effects of Dox and guarantee successful treatment[12,15,16]. To this end, triggered release of Dox from Lyso-TSLs exposed to mild hyperthermia in a target region (e.g. by ultrasound exposure), is under investigation for improving treatment outcomes[13].

Release and delivery of Dox from Dox-loaded Lyso-TSLs *in vivo* was first demonstrated in combination with radio-frequency ablation as part of the HEAT trial. Ultrasound-mediated mild hyperthermia, however, has a better safety profile as it is non-invasive, non-ionizing, and targeted. Ultrasound-mediated release of Dox from Dox-Lyso-TSLs was first demonstrated in humans in a Phase I clinical trial (TARDOX) at the University of Oxford[1,17].

A number of animal trials have also investigated the use of ultrasound-mediated mild hyperthermia in combination with Lyso-TSLs. Manzoor et al., for instance, performed real-time confocal fluorescence microscopy in mice throughout treatment using surgically-implanted window chambers[2]. They found that heat-induced release of Dox from Dox-18:0-Lyso-TSLs not only increased accumulation of drug within tumours compared to free Dox controls, but also enhanced extravasation, achieving upwards of 80 µm drug penetration from the tumour vasculature.

One concern with Dox-18:0-Lyso-TSLs is that up to 50% of the encapsulated Dox can be released 60 min post-intravenous administration in the absence of mild hyperthermia[3]. By using a larger drug, leakage of the drug from Lyso-TSLs can be reduced. Kheirolomoom et al. demonstrated, for instance, that copper-Dox crystals could be effectively loaded into 16:0-Lyso-TSLs, were more stable and circulated for longer than Dox-18:0-Lyso-TSLs, and provided a substantial therapeutic benefit in animal trials[3]. Combination of Lyso-TSLs with microbubbles and ultrasound has also been attempted but was not much more effective than Lyso-TSLs with heating alone[18].

A1.3. Methods

A1.3.1. Lyso-PC preparation

Lyso-PCs were prepared by the methods described in Chapter 4.

A1.3.2. Lyso-TSL nomenclature

In this chapter, Lyso-PC-containing thermosensitive liposome (Lyso-TSL) formulations, incorporating either 18:0 Lyso-PC or 16:0 Lyso-PC, are referred to as 16:0-Lyso-TSLs and 18:0-Lyso-TSLs respectively. 18:0-Lyso-TSLs loaded with doxorubicin (Dox) are referred to as Dox-18:0-Lyso-TSLs. Dox-18:0-Lyso-TSLs were acquired from Celsion (ThermoDox). The descriptive name, Dox-18:0-Lyso-TSLs, was

employed to highlight that Dox-free ThermoDox is the same as 18:0-Lyso-TSLs. The chemical names, molecular weights, transition temperatures, and critical micelle concentrations, where applicable, for each Lyso-TSL constituent are presented in Table 1. Lyso-TSL formulations are summarized in Table 2.

A1.3.3. Lyso-TSL preparation

The "in-house" Lyso-TSL formulations were 16:0 PC, 18:0 PE-PEG (2000), and either 16:0 Lyso-PC or 18:0 Lyso-PC (for 16:0-Lyso-TSLs and 18:0-Lyso-TSLs respectively) in a 90:10:4 molar ratio. Lipid films containing the Lyso-TSL constituents were prepared by chloroform evaporation on a hot plate, resuspended, and dispersed by the same methods used for Lyso-PC preparation described in a previous section. Lyso-TSLs were then extruded five times through two polycarbonate membrane filters of pore size 0.1 μm at 50° C. For experiments, Lyso-TSLs were diluted to contain a final

Short name	16:0 PC (DPPC)	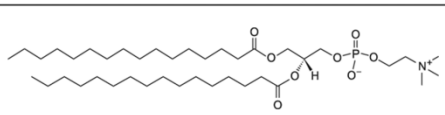
Chemical name	1,2-dipalmitoyl-sn-glycero-3-phosphocholine	
Molecular weight	734.039	
T_m (°C)	41	
CMC (nM)	0.46	
Short name	16:0 Lyso-PC (MPPC)	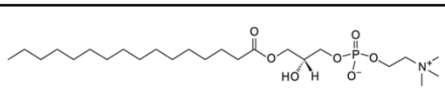
Chemical name	1-palmitoyl-2-hydroxy-sn-glycero-3-phosphocholine	
Molecular weight	495.630	
CMC (μM)	4.0 - 8.3	
Short name	18:0 Lyso-PC (MSPC)	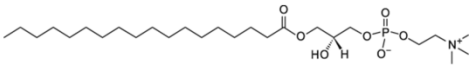
Chemical name	1-stearoyl-2-hydroxy-sn-glycero-3-phosphocholine	
Molecular weight	523.683	
CMC (μM)	0.4	
Short name	18:0 PE-PEG2000 (DSPE-PEG2000)	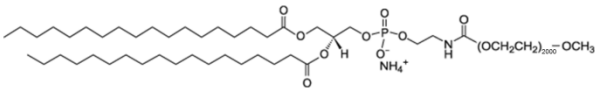
Chemical name	1,2-distearoyl-sn-glycero-3-phosphoethanolamine-N-[methoxy(polyethylene glycol)-2000] (ammonium salt)	
Molecular weight	2805.497	
T_m (°C)	12.8	
Short name	Dox	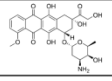
Chemical name	Doxorubicin, Adriamycin, Hydroxyduanorubicin	
Molecular weight	543.525	

Table 2: Lyso-TSL constituents.

Formulation	Lipids and emulsifiers	Molar Ratio	Preparation
16:0-Lyso-TSL	16:0 PC, 16:0 Lyso PC, 18:0 PE-PEG2000	86:10:4	Chloroform evaporation, sonication, extrusion
18:0-Lyso-TSL	16:0 PC, 18:0 Lyso PC, 18:0 PE-PEG2000	86:10:4	Chloroform evaporation, sonication, extrusion
Dox-18:0-Lyso-TSL (ThermoDox®)	16:0 PC, 18:0 Lyso PC, 18:0 PE-PEG2000	86:10:4	Dox-loaded by pH-gradient by Celsion.

Table 1: Lyso-TSL formulations.

Lyso-PC concentration of 125 µM.

A1.3.4. Lyso-TSL sizing by dynamic light scattering

The size distribution of Lyso-TSLs after extrusion was determined by dynamic light scattering (Zetasizer Nano-ZS, Malvern) (see Figure 1). The sizes of 18:0 Lyso-TSLs, 16:0 Lyso-TSLs, and Dox-18:0 Lyso-TSLs were 142 ± 53 nm, 149 ± 39 nm, and 129 ± 47 nm, respectively, in agreement with expected values.

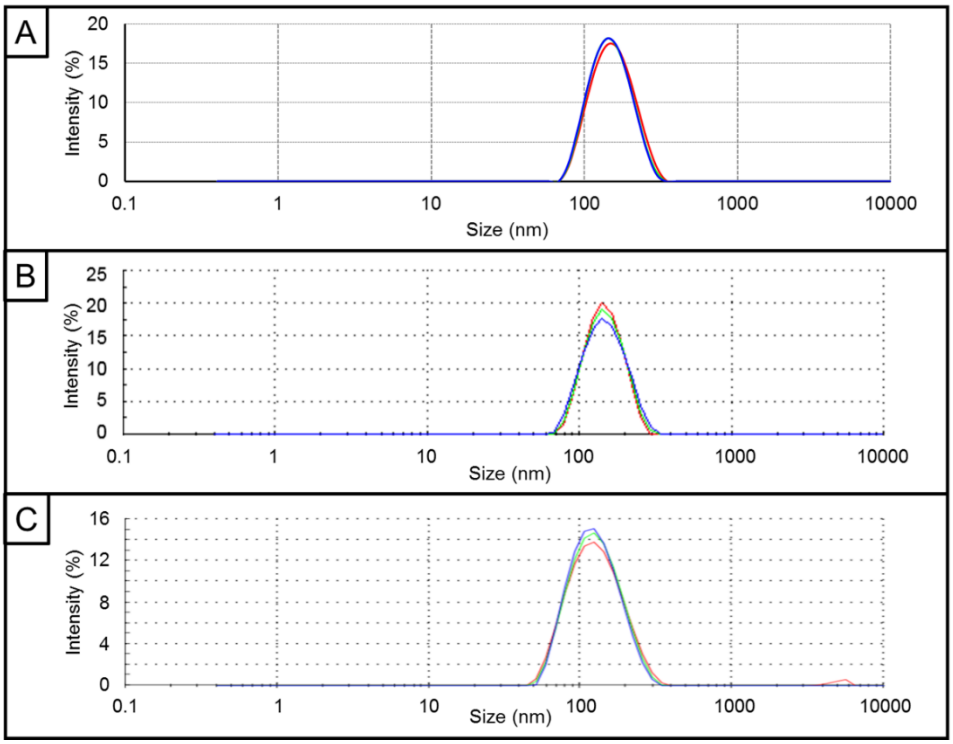

Figure 1: DLS size distribution by intensity for Lyso-TSLs. (A) 18:0 Lyso PC-TSLs were 142 ± 53 nm, (B) 16:0 Lyso PC-TSLs were 149 ± 39 nm, (C) Dox-18:0-Lyso-TSLs (ThermoDox®, Celsion) were 129 ± 47 nm. Three samples shown for each. (A) and (C) were kindly provided by Dr. Joshua Owen and Dr. Paul Lyon respectively.

A1.3.5. Cell culture

Immortalized human colorectal cells (DLD-1s) were chosen for these experiments owing to their strong response to Dox treatment with minimal dependence on cell growth-phase[19]. DLD-1s also came recommended by Dr. Paul Lyon who employed them in his previous work with the same liposome formulation. DLD-1s were grown in Dulbecco's Modified Eagle Medium (DMEM) with 10% fetal bovine serum and 1%

penicillin/streptomycin. Cells grown in T-75 flasks were passaged every three days at approximately 80% confluence. Cells were grown in a temperature- and CO2-controlled incubator at 37°C and 5% CO2. For experiments, approximately 5×10^4 cells were seeded in 8-well chamber slides (µSlide, 9.4 x 10.7 x 6.8 mm wells, Ibidi) in 250 µl growth medium ~24 h before experiments. Sub-confluent cells were chosen for these experiments to improve the reliability of image analysis based on the quantification of membrane lipid order. All cell culture materials were purchased from ThermoFisher UK.

A1.3.6. Spectral imaging

Cells were twice washed with phosphate buffered saline (PBS) and the medium was replaced with an optically transparent DMEM formulation (FluoroBrite, Thermo Fisher). Cells were labelled with 400 nM C-Laurdan in FluoroBrite for at least ~60 s prior to spectral imaging.

To verify that the presence of Dox did not affect the C-Laurdan generalized polarization (GP) measurements, a no cell control was conducted using C-Laurdan-labelled liposomes with and without Dox. No difference in GP was found. It was also found that Dox-spiked FluoroBrite did not produce significant fluorescence emissions in the wavelengths used to calculate GP. For detailed spectral imaging experimental methods see Chapter 2.

A1.3.7. Mild hyperthermia

Exposure of cells to mild hyperthermia was achieved using a portable incubator developed in-house. The temperature of the suspending medium in a cell-free sample was manually recorded using a digital thermocouple. The desired temperature was maintained by manual adjustment of the heating element output as needed. The cell-free

sample was kept with the cell-containing samples throughout the experiments. For experiments with mild hyperthermia, cells were gradually heated to 42°C over the course of 5-10 min and maintained at 42°C for 10 min which is expected to release virtually all the Dox from Dox-Lyso-TSLs with no impact on cell viability from mild hyperthermia[4]. A representative temperature profile can be seen in Figure 2. It was found that C-Laurdan fluorescence emission intensity was unreliably low at 42°C. Thus, following exposure to mild hyperthermia, cells were cooled back to 37°C before labelling with C-Laurdan for spectral imaging.

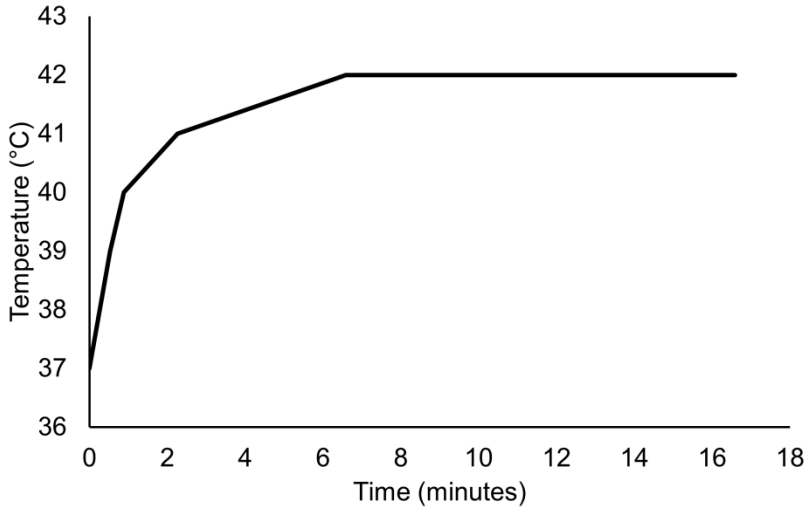

Figure 2: Representative temperature profile for exposure of cells to mild hyperthermia. Once the temperature reached 42°C, it was maintained for 10 min before returning cells to incubation at 37°C.

A1.3.8. Doxorubicin imaging

Doxorubicin fluorescence (Ex: 470 nm, Em: 585 nm) from cells exposed to Dox was imaged by confocal fluorescence microscopy. Because Dox is cell permeable, release of Dox from Dox-18:0-Lyso-TSLs was confirmed by imaging cells after exposure to Lyso-TSLs. To enable comparison of Dox fluorescence across samples, the confocal microscope acquisition parameters (e.g. hardware gain, pinhole diameter, laser power etc.) were fixed for all images acquired. A custom MATLAB image processing routine

was developed for quantifying the nuclear Dox fluorescence intensity, in which cells were segmented and thresholded, and the mean and standard deviation of the pixels belonging to the cell nucleus were recorded.

A1.3.9. Permeability to propidium iodide

Propidium iodide (15 µM) was used as a fluorescent marker for the permeabilization of DLD-1 cells exposed to Lyso-PCs and Lyso-TSLs by the methods described in Chapter 3 and as shown in Figure 3B.

A1.3.10. MTS assays

MTS assays were performed to determine the cytotoxicity of Lyso-PCs by the methods described in Chapter 3. For MTS assays cells were exposed to treatments for ~12 h (see Figure 3C).

A1.3.11. Exposure of cells to Lyso-PCs

Cells were treated with Lyso-PCs in the same concentration present in the Lyso-TSL formulations (125 µM) for 10 min at 37°C. Either spectral imaging with C-Laurdan or permeability assessment with propidium iodide was then performed as described above (see Figure 3A-B).

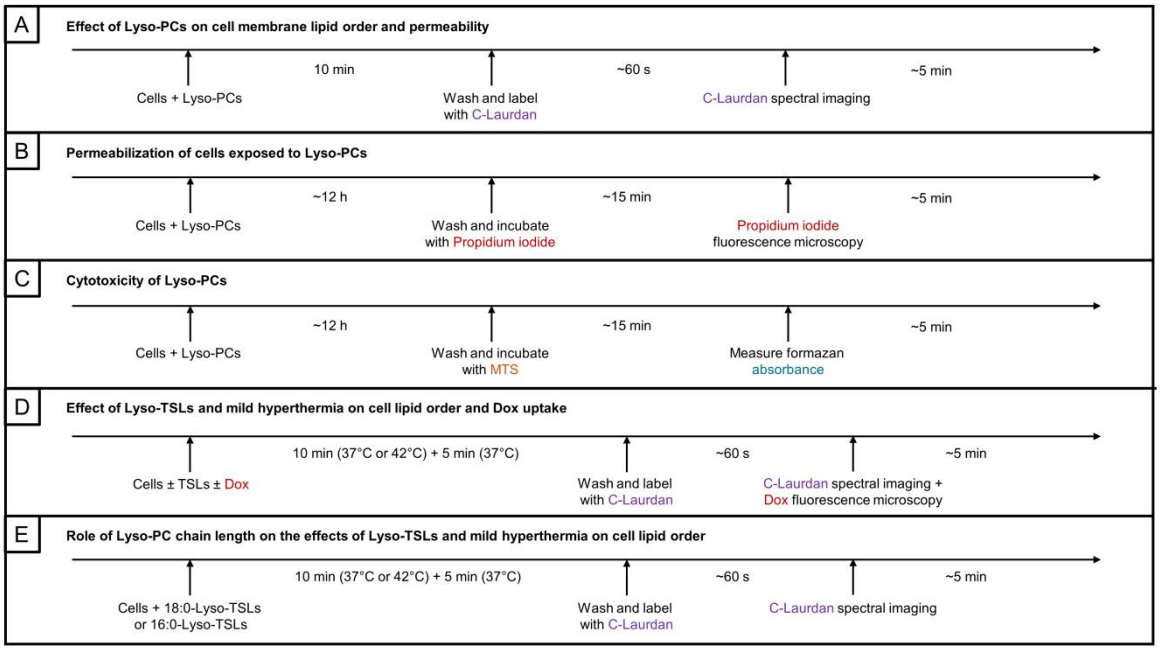

Figure 3: Experimental timelines for investigating the effects of Lyso-PCs and Lyso-TSLs on cell lipid order and viability.

A1.3.12. Effect of Lyso-TSLs, Dox, and mild hyperthermia on cell lipid order and Dox uptake

Cells were treated with Lyso-TSLs or free Dox for 10 min with or without exposure to mild hyperthermia. Spectral imaging with C-Laurdan was then conducted, followed by Dox fluorescence microscopy where applicable, as described above. The experimental timelines are depicted in Figure 3D-E).

A1.3. Results

A1.3.1. Lyso-PCs disorder cell membrane lipids and permeabilize cells

16:0 and 18:0 Lyso-PCs were both found to have a strong disordering effect on cell membrane lipids with $\Delta GP = -0.24 \pm 0.03$ and $\Delta GP = -0.20 \pm 0.03$ respectively (see Figure 4). 16:0 Lyso-PC induced a significantly greater change in GP than 18:0 Lyso-PC ($p < 0.01$). Cell membrane lipid disordering by Lyso-PCs was observed to coincide with total sample permeablization to propidium iodide (see Figure 5).

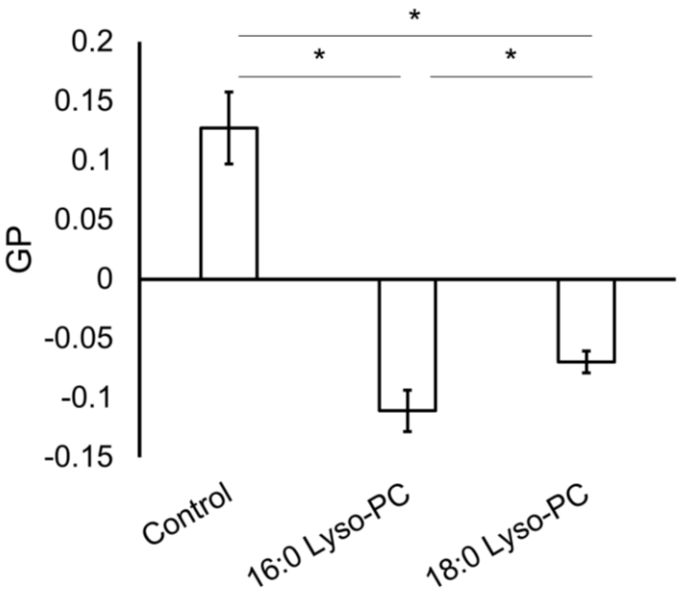

Figure 4: Effect of Lyso-PCs on DLD-1 cell membrane lipid order. Membrane GP decreased significantly ($p < 0.01$) following exposure to 16:0 and 18:0 Lyso-PCs (125 µM for 10 min, n=4). 16:0 Lyso-PC was more effective than 18:0 Lyso-PC at disordering cell membrane lipids ($p < 0.01$).

A1.3.2. Effect of Lyso-TSLs and mild hyperthermia on cell lipid order

To test the role of the Lyso-PC chain length, Lyso-TSLs were made with 16:0 Lyso-PC and their effect on cell membrane lipid order compared with that of 18:0-Lyso-TSLs. Exposure of cells to 16:0-Lyso-TSLs with or without exposure to mild hyperthermia did

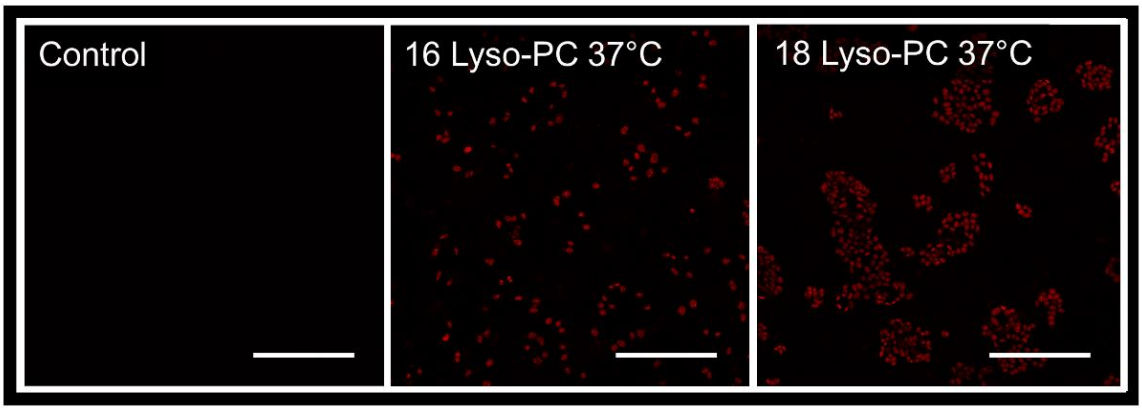

Figure 5: Cell permeabilization following exposure to 125 uM Lyso-PCs for 10 min at 37°C. Exposure to either 16:0 or 18:0 Lyso-PCs resulted in total sample permeabilization as indicated by propidium iodide fluorescence (red) in the representative images above. No permeabilization was observed in control samples. Scale bars: 212 µm.

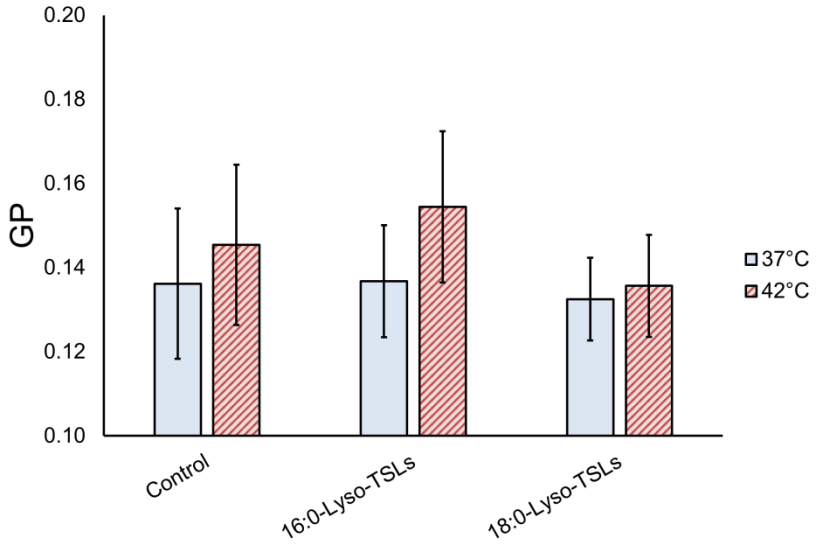

Figure 6: Effect of mild hyperthermia and Lyso-TSLs on DLD-1 cell membrane lipid order. Lyso-TSL formulations with two different chain length Lyso-PCs, 16:0 Lyso-PC and 18:0 Lyso-PC, referred to as 16:0-Lyso-TSLs and 18:0-Lyso-TSLs respectively, were investigated for their effects on cell membrane lipid order by quantifying the C-Laurdan spectral shift (GP) acquired by spectral imaging. All imaging was conducted at 37°C. n = 9 for all conditions except 16:0-Lyso-TSLs without hyperthermia which has n = 7 owing to poor labelling with C-Laurdan of two samples.

not induce a statistically significant change in cell membrane lipid order compared to controls (see Figure 6).

A1.3.3. Mild hyperthermia releases Dox from Dox-18:0-Lyso-TSLs and increases Dox uptake by cancer cells

Doxorubicin fluorescence in DLD-1 cells was measured following exposure to either Dox or Dox-18:0-Lyso-TSLs (ThermoDox), with and without exposure to mild hyperthermia respectively. It can be seen in Figure 7, that upon exposure to mild hyperthermia, Dox is released from Dox-18:0-Lyso-TSLs. It can also be seen that cells uptake more free Dox upon exposure to mild hyperthermia.

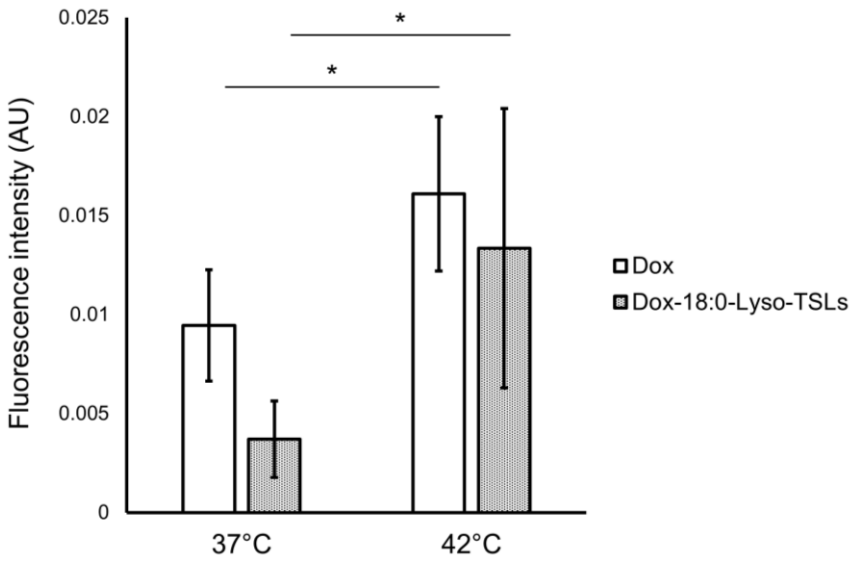

Figure 7: Release of Dox from Dox-18:0-Lyso-TSLs and subsequent delivery to DLD-1 cell nuclei is triggered by mild hyperthermia. Bar plot shows the fluorescence intensity of Dox in cell nuclei for n = 6 independent samples each. Stars indicate statistical significance ($p < 0.01$).

A1.3.4. The effect of Dox-18:0-Lyso-TSLs and mild hyperthermia on cell lipid order

The cell membrane GP of control cells exposed to a FluoroBrite sham with and without exposure to mild hyperthermia were GP = 0.136 ± 0.029 and GP = 0.135 ± 0.030

respectively. Exposure to free Dox, 18:0-Lyso-TSLs, or Dox-18:0-Lyso-TSLs, with or without exposure to mild hyperthermia respectively, had no statistically significant effect on cell membrane lipid order relative to controls (see Figure 7 and 8). One control, simultaneous exposure of cells to Dox-free Lyso-TSLs and free Dox, was not tested and so a statistical test for 3-way interaction effects could not be performed. Nonetheless, mild hyperthermia was found to be a significant factor by 3-way ANOVA ($p = 0.018$). Two-way interaction effects were thus studied by performing 2-way ANOVAs with mild hyperthermia and Dox exposure (e.g. from free Dox or Dox released from TSLs), or mild hyperthermia and Lyso-TSL exposure as factors. While the interaction effect between Dox exposure and mild hyperthermia was found to be

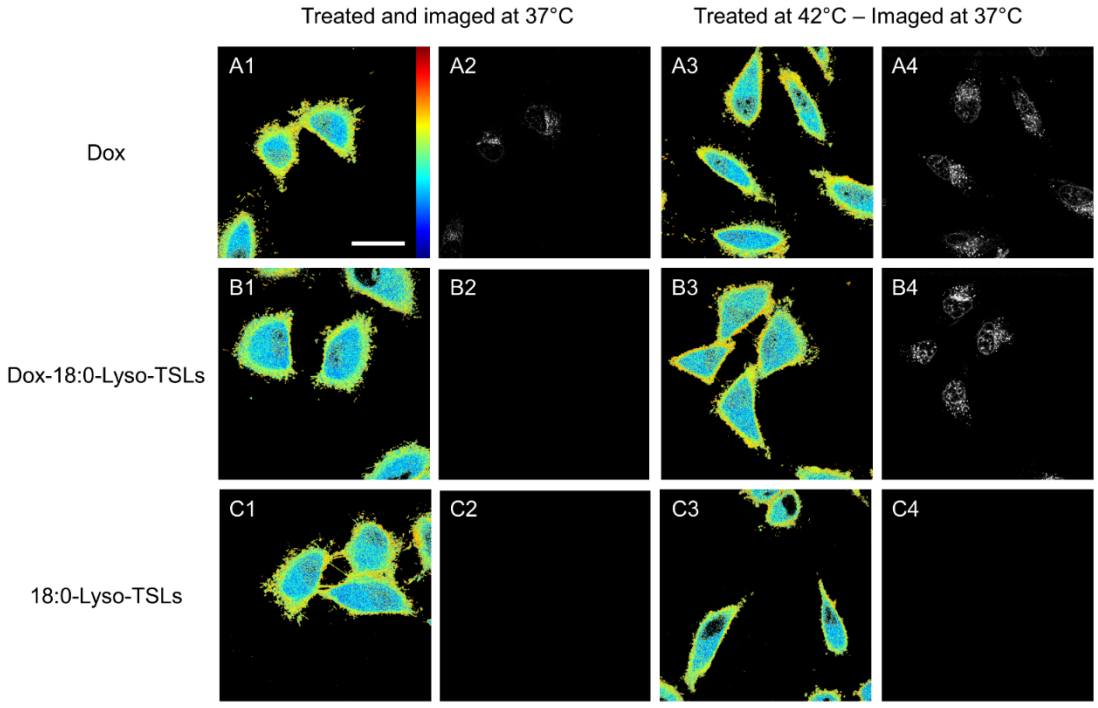

Figure 8: Representative images demonstrating the acquisition of both Dox fluorescence and C-Laurdan GP in DLD-1 cells. Rows A-C refer to samples treated with Dox, Dox-18:0-Lyso-TSLs, and 18:0-Lyso-TSLs respectively. Columns 1-2 refer to samples treated at 37°C. Columns 3-4 refer to samples treated at 42°C. All samples were imaged after treatment at 37°C. C-Laurdan GP maps (columns 1 and 3) and fluorescence Dox imaging (columns 2 and 4) are shown for the same cells for each condition. Scale bar in panel (A1) is 40 µm and applies for all images. The colour bar in panel (A1) applies for all GP maps and ranges from GP = -1 (blue) to GP = 1 (red).

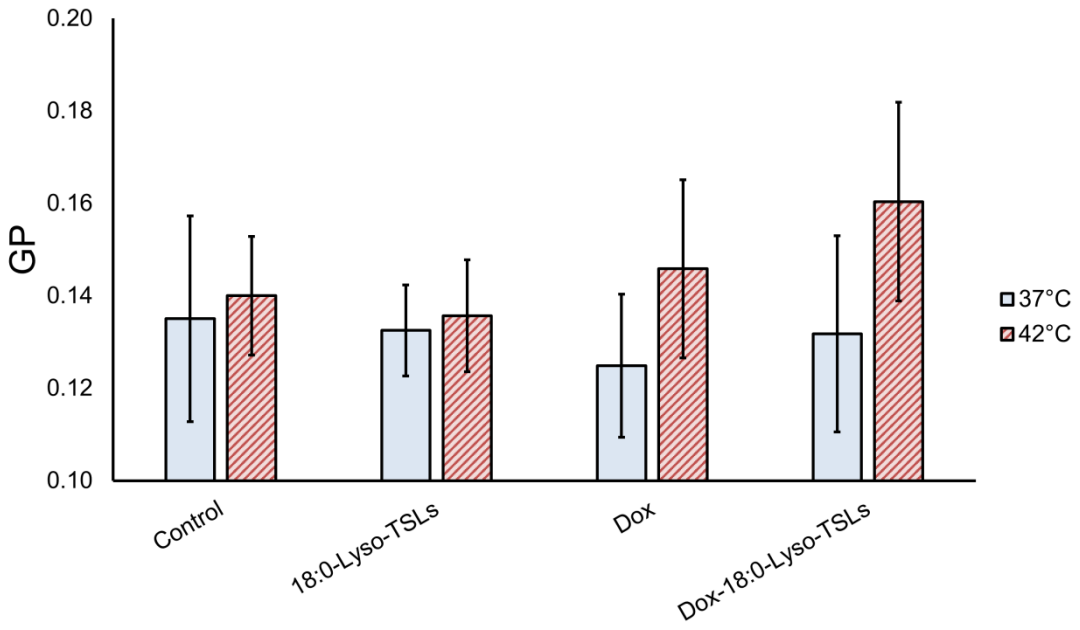

Figure 9: Effect of Dox, 18:0-Lyso-TSLs, and Dox-18:0-Lyso-TSLs on DLD-1 cell lipid order with and without exposure to mild hyperthermia. Lipid order was quantified by C-Laurdan spectral shift (GP). All imaging was conducted at 37°C. n = 9.

statistically significant ($p = 0.03$), the effect size was small compared with that induced by Lyso-PCs, for instance.

A1.4. Discussion

A1.4.1. The effects of Lyso-PCs on DLD-1 cancer cells

Exposure of DLD-1 cells to 125 µM of either 16:0 Lyso-PC or 18:0 Lyso-PC resulted in a substantial decrease in cell membrane lipid order ($\Delta GP = -0.24 \pm 0.03$ and $\Delta GP = -0.20 \pm 0.03$ respectively). 16:0 Lyso-PC induced a significantly greater change in GP than 18:0 Lyso-PC ($p < 0.01$). As expected, the shorter chain length Lyso-PC had a significantly greater effect on cell membrane lipid order[20]. This is in agreement with the results in Chapter 4 and 5 which demonstrated that Lyso-PCs can also disorder A-549 and MDCK cell membrane lipids. It follows that the same mechanistic arguments presented in Chapter 4 apply.

A1.4.2. On the effects of Dox and mild hyperthermia on cell lipid order

In agreement with previous studies[15,16], exposure to mild hyperthermia was found to significantly increases uptake of free Dox by cancer cells. Release and delivery of Dox from Dox-18:0-Lyso-TSLs (ThermoDox®, Celsion) exposed to mild hyperthermia, was also confirmed by fluorescence confocal microscopy. Delivery of Dox was expected to influence cell membrane GP owing to its intercalation in cell membranes which has been reported elsewhere to decrease both lipid order and lipid mobility[21,22]. In the present study, it was found that mild hyperthermia in combination with either free Dox or Dox-18:0-Lyso-TSLs (both at ~100 µg/ml Dox) was a statistically significant factor in increasing cell membrane GP ($\Delta GP = 0.011 \pm 0.029$ and $\Delta GP = 0.025 \pm 0.031$, respectively, compared to controls with and without hyperthermia, $\Delta GP = 0.000 \pm 0.031$ and $\Delta GP = 0.000 \pm 0.031$, respectively).

In contrast to the present study, Dox intercalation has been shown to immobilize lipid headgroups while disordering lipid tails[21,22]. It thus appears that thermally-induced defects (e.g. changes in protein conformation from mild hyperthermia treatment), may contribute to the observed effect of Dox intercalation in the present study. The effect size of Dox and mild hyperthermia on cell membranes, however, is small compared with that of Lyso-PCs, for example, and may not be sufficient to impact drug delivery. Nonetheless, Dox-mediated modulation of cell membrane lipid order and membrane protein conformation has been associated with sensitization of cells to hyperthermia, and thus should not be neglected[23].

A1.4.3. The cell-to-TSL ratio is a critical factor for Lyso-PC transfer to cells

Having observed the strong effects of Lyso-PCs on cell membrane lipid order and permeability, exposure of cells to mild hyperthermia in the presence of Lyso-TSLs with an equivalent concentration of Lyso-PC was expected to have similar effects. Exposure of cells to Lyso-TSLs and mild hyperthermia, however, was not found to affect the lipid order of cell membranes in the present study, even for Lyso-TSLs made with the shorter 16:0 Lyso-PCs.

The 18:0 PE-PEG2000 in Lyso-TSLs may reduce direct interaction of Lyso-TSLs with cell membranes. It is not, however, expected to inhibit the transfer of Lyso-PC by an aqueous diffusion mechanism. Accordingly, the lack of Lyso-PC transfer in the present study can be attributed to low desorption of Lyso-PCs from Lyso-TSLs which depends on the water solubility of Lyso-PCs, the thermal behaviour of Lyso-TSLs, and the cell-to-TSL ratio.

Lyso-PCs are expected to have much higher water solubility than two-tailed PCs of the same chain length. 16:0 Lyso PC, for instance, has the same number of hydrophobic hydrocarbons as short chain 8:0 PC, which is water soluble and hygroscopic. 16:0 PC, however, has very low water solubility and does not readily transfer between lipid vessels. Water solubility is thus an unlikely candidate for explaining the lack of Lyso-PC transfer in the present study.

Owing to the dependence of lipid transfer on the packing of surrounding lipid molecules, it is conceivable that the stability of the Lyso-TSL formulation makes Lyso-PC desorption unfavourable. While desorption should be enhanced upon exposure to mild hyperthermia, Lyso-PCs are also expected to form the boundaries of stable pores in Lyso-TSLs, which may reduce desorption. Indeed, in agreeance with the present

study, Mills et al. found that Lyso-PCs did not significantly desorb from Lyso-TSLs to form pure Lyso-PC lipid constructs, even under excessive dilution[4].

Critically, Mills et al. performed desorption experiments in the absence of acceptor particles. In contrast, Sandström and colleagues demonstrated that ^{14}C-16:0 Lyso-PC in the outer bilayer of 18:0-Lyso-TSLs, transferred completely to egg-PC multi-lamellar vesicles within 10 min with a ~100 vesicle-to-TSL ratio[24]. It follows that in addition to formulation, the cell-to-TSL ratio is a critical factor for Lyso-PC transfer. The Lyso-PCs must not only desorb from Lyso-TSLs, they must transfer to nearby cell membranes without being reabsorbed by competing Lyso-TSLs.

Owing to the use of adherent cells in the present study, the cell-to-TSL ratio was low (~O(-6)), which has been shown to favour cholesterol depletion[25], but could be unfavourable for lipid transfer owing to competition between cells and TSLs for free Lyso-PC. The cell-to-TSL ratio, however, is high *in vivo*, owing to the presence of blood cells and the vascular endothelium, and dilution in blood. Lipoproteins, which are plentiful in whole blood, can also act as acceptors and intermediaries for lipid transfer. While Lyso-PC transfer was not observed in the present study, Lyso-PC transfer *in vivo* is thus expected.

Indeed, Banno et al. quantified an impressive 70% Lyso-PC loss from Lyso-TSLs within 1 h post-injection in mice[11]. Interestingly, the loss of Lyso-PC was found to not detriment DOX release until at least 2 h in circulation, in agreement with results from Lyso-TSLs prepared with correspondingly less Lyso-PC[11,24]. While plasma constituents may affect Lyso-TSL properties, the importance of an excess of acceptors (e.g. cells) is highlighted by the loss of Lyso-PC from Lyso-TSLs in whole blood but not in plasma at 37°C[11]. Finally, while not highlighted in their publication, Kheirolomoom et al. found

that the red blood cell count in mice exposed to mild hyperthermia and copper-Dox-containing 16:0-Lyso-TSLs was reduced by roughly half compared to controls[3]. While the change in red blood cell count could be a symptom of Dox exposure, following eight TSL injections over 28 days, the transfer of 16:0 Lyso-PCs to red blood cells could also be a contributing factor.

While beyond the scope of this thesis, it would be interesting to perform the Lyso-TSL experiments of the present study using non-adherent cells, where the role of the cell-to-TSL ratio could be investigated without reducing the Lyso-PC concentration below its threshold for activity.

A1.5. Concluding remarks

The present study demonstrates the following:

(1) 16:0 and 18:0 Lyso-PCs (125 µM) were found to severely disorder DLD-1 cell membrane lipids resulting in membrane permeabilization and uptake of propidium iodide

(2) Release of Dox from Dox-18:0-Lyso-TSLs was triggered by mild hyperthermia

(3) Lyso-TSLs were not observed to alter the cell membrane lipid order of a DLD-1 monolayer

This study highlights the role of the cell-to-TSL ratio on Lyso-PC transfer *in vivo*.

A1.6. References

1. Lyon, P. C. *et al.* Clinical trial protocol for TARDOX: a phase I study to investigate the feasibility of targeted release of lyso-thermosensitive liposomal doxorubicin (ThermoDox®) using focused ultrasound in patients with liver tumours. *J. Ther. Ultrasound* **5,** (2017).

2. Manzoor, A. A. *et al.* Overcoming limitations in nanoparticle drug delivery: triggered, intravascular release to improve drug penetration into tumors. *Cancer Res* **72,** 5566–5575 (2012).

3. Kheirolomoom, A. *et al.* Complete regression of local cancer using temperature-sensitive liposomes combined with ultrasound-mediated hyperthermia. doi:10.1016/j.jconrel.2013.08.019

4. Mills, J. K. & Needham, D. Lysolipid incorporation in dipalmitoylphosphatidylcholine bilayer membranes enhances the ion permeability and drug release rates at the membrane phase transition. *Biochim. Biophys. Acta - Biomembr.* **1716,** 77–96 (2005).

5. Chi, L. M. & Wu, W. G. Effective bilayer expansion and erythrocyte shape change induced by monopalmitoyl phosphatidylcholine. Quantitative light microscopy and nuclear magnetic resonance spectroscopy measurements. *Biophys. J.* **57,** 1225–1232 (1990).

6. Hijnen, N., Langereis, S. & Grüll, H. Magnetic resonance guided high-intensity focused ultrasound for image-guided temperature-induced drug delivery. *Adv. Drug Deliv. Rev.* **72,** 65–81 (2014).

7. Boissenot, T., Bordat, A., Fattal, E. & Tsapis, N. Ultrasound-triggered drug delivery for cancer treatment using drug delivery systems: From theoretical considerations to practical applications. *J. Control. Release* **241,** 144–163 (2016).

8. Kohli, A. G., Kierstead, P. H., Venditto, V. J., Walsh, C. L. & Szoka, F. C. Designer lipids for drug delivery: From heads to tails. *J. Control. Release* **190,** 274–287 (2014).

9. Boissenot, T., Bordat, A., Fattal, E. & Tsapis, N. Ultrasound-triggered drug delivery for cancer treatment using drug delivery systems: From theoretical considerations to practical applications. *J. Control. Release* **241,** 144–163 (2016).

10. Carruthers, A. & Melchior, D. L. Studies of the Relationship between Bilayer Water Permeability and Bilayer Physical State1. *Biochemistry* **22,** 5797–5807 (1983).

11. Banno, B. *et al.* The functional roles of poly(ethylene glycol)-lipid and lysolipid in the drug retention and release from lysolipid-containing thermosensitive liposomes in vitro and in vivo. *J. Pharm. Sci.* **99,** 2295–2308 (2010).

12. Barenholz, Y. (Chezy). Doxil® — The first FDA-approved nano-drug: Lessons learned. *J. Control. Release* **160,** 117–134 (2012).

13. Li, M. *et al.* Thermo-Sensitive Liposome co-Loaded of Vincristine and Doxorubicin Based on Their Similar Physicochemical Properties had Synergism on Tumor Treatment. *Pharm. Res.* **33,** 1881–1898 (2016).

14. Shan, K., Lincoff, A. M. & Young, J. B. Anthracycline-Induced Cardiotoxicity. *Ann. Intern. Med.* **125,** 47 (1996).

15. Liu, Y. *et al.* Ultrasound-Induced hyperthermia increases cellular uptake and cytotoxicity of P-glycoprotein substrates in multi-drug resistant cells. *Pharm. Res.* **18,** 1255–61 (2001).

16. Needham, D., Anyarambhatla, G., Kong, G. & Dewhirst, M. W. A New Temperature-sensitive Liposome for Use with Mild Hyperthermia: Characterization and Testing in a Human Tumor Xenograft Model 1. *CANCER Res.* **60,** 1197–1201 (2000).

17. Lyon, P. C. *et al.* Safety and feasibility of ultrasound-triggered targeted drug delivery of doxorubicin from thermosensitive liposomes in liver tumours (TARDOX): a single-centre, open-label, phase 1 trial. *Lancet Oncol.* **19,** 1027–1039 (2018).

18. Yudina, A. *et al.* In vivo temperature controlled ultrasound-mediated intracellular delivery of cell-impermeable compounds. *J. Control. Release* **161,** 90–97 (2012).

19. Luk, C. K. & Tannock, I. F. Flow Cytometric Analysis of Doxorubicin Accumulation in Cells From Human and Rodent Cell Lines. *JNCI J. Natl. Cancer Inst.* **81,** 55–59 (1989).

20. Golan, D. E., Furlong, S. T., Brown, C. S. & Caulfield1 '#, J. P. Monopalmitoylphosphatidylcholine Incorporation into Human Erythrocyte Ghost Membranes Causes Protein and Lipid Immobilization and Cholesterol Depletion^. *Biochemistry* **27,** 2661–2667 (1988).

21. Murphree, S. A., Tritton, T. R., Smith, P. L. & Sartorelli, A. C. Adriamycin-induced changes in the surface membrane of sarcoma 180 ascites cells. *Biochim. Biophys. Acta - Biomembr.* **649,** 317–324 (1981).

22. Jedrzejczak, M., Koceva-Chyla, A., Gwozdzinski, K. & Józwiak, Z. CHANGES IN PLASMA MEMBRANE FLUIDITY OF IMMORTAL RODENT CELLS INDUCED BY ANTICANCER DRUGS DOXORUBICIN, ACLARUBICIN AND MITOXANTRONE. *Cell Biol. Int.* **23,** 497–506 (1999).

23. Leyko, W. & Bartosz, G. Membrane effects of ionizing radiation and hyperthermia. *INT. J. RADIAT. BIOI* **49,** 743–770 (1986).

24. Sandström, M. C., Ickenstein, L. M., Mayer, L. D. & Edwards, K. Effects of lipid segregation and lysolipid dissociation on drug release from thermosensitive liposomes. *J. Control. Release* **107,** 131–142 (2005).

25. Phillips, M. C., Johnson, W. J. & Rothblat, G. H. Mechanisms and consequences of cellular cholesterol exchange and transfer. *Biochim. Biophys. Acta* **906,** 223–276 (1987).

Appendix II

An *in vitro* blood-brain barrier model with characteristics suited to permeability studies

A2.1. Abstract

In order to assess Lyso-MBs in ultrasound-mediated blood-brain barrier disruption *in vitro* as proposed in Chapter 6, an appropriate blood-brain barrier (BBB) model is required. A primary porcine brain endothelial cell (PBEC) model established by Patabendige et al. was chosen to serve this purpose[1,2]. In order to confirm successful reproduction of the PBEC BBB model described by Patabendige et al.[2], expression of TJ proteins was assessed by immunostaining, TEER was assessed with and without medium supplementation with 250 µM pCPT-cAMP and 17.5 µM RO-20-1724 included to aid BBB differentiation, solute permeability was assessed by measuring the flux of fluorescent dextrans, and removal of contaminating cells was achieved by puromycin treatment. The resulting BBB model was found to meet the criteria established in the literature for BBB permeability studies *in vitro*.

A2.2. Methods

A2.2.1. PBEC isolation

Porcine brain microvessel endothelial cells (PBECs) were isolated from fresh pig brains from the slaughterhouse (MutchMeats, UK) as described by Patabendige et al[1,2,i]. One of the advantages of PBECs is that they reproduce many characteristics of the *in vivo* BBB without the need for co-culture with astrocytes[1,2]. PBECs express the TJ proteins of the *in vivo* BBB, and produce a monolayer with high TEER and low permeability to solutes. PBECs have also been shown to express efflux transporters characteristic of the BBB[1,2].

[i] Dr. Anjali Seth kindly assisted with the PBEC isolation.

A2.2.2. PBEC cell culture

To culture PBECs, T-25 flasks were coated with rat-tail collagen in water at 300 mg/ml for two hours followed by human fibronectin at 7.5 mg/ml for two hours at room temperature. An aliquot of PBECs was then thawed by gentle swirling in a 37°C water bath. The thawed cells were then pipetted into 40 ml PBEC medium (Dulbecco's medium-eagle medium, 10% fetal bovine serum, 1% penicillin/streptomycin, 1% glutamine, 125 µg/ml heparin) containing 4 µg/ml puromycin, and distributed into two coated flasks. Puromycin was used to purify the vessel fragments of contaminating pericytes and smooth muscle cells as described by Perrière et al and Patabendige et al[2,3]. After ~18 h, the medium was replaced to remove the diluted dimethyl-sulfoxide and any non-adherent vessel fragments. After three days, the medium was replaced with puromycin-free PBEC medium. Cells were passaged at approximately 80% confluence. Once confluent after passaging for experiments, cells were supplemented with 550 nM hydrocortisone, 250 µM pCPT-cAMP, and 17.5 µM RO-20-1724 in serum-free PBEC medium. These supplements were used to induce TJ formation in PBECs[2].

A2.2.3. Trans-endothelial electrical resistance (TEER) and permeability

TEER and apparent permeability measurements were conducted as described in Chapter 5. PBECs were grown in 12 mm transwells in 12-well plates and measured daily.

A2.2.4. Immunostaining

PBECs, once passaged, were grown in 8-well chamber slides (Ibidi) coated with rat-tail collagen and human fibronectin as described previously. At room temperature, cells were washed with PBS, fixed with 3% paraformaldehyde in PBS for 45 min, and permeabilized using 0.1% Triton-X 100 in filtered de-ionized water as described by Patabendige et al.[3]. Non-specific binding was blocked with normal goat serum at 1:100

in PBS for 60 min, followed by addition of primary antibodies, rabbit anti-occludin, rabbit anti-claudin-5, or anti-α-smooth-muscle-actin (anti-α-sma) at 1:100 dilutions in PBS, and incubation at 4°C overnight. The following day, cells were washed for 60 min with PBS and given secondary antibodies in 1:100 dilutions in PBS for two hours at room temperature (Alexa-Fluor 594 labelled goat anti-rabbit for claudin-5 and occludin staining, and a biotinylated secondary followed by 30 minutes FITC-avidin for the α-sma primary). Cells were incubated for three minutes with DAPI, 1:100 in PBS, at room temperature prior to imaging.

A2.3. Results

A2.3.1. PBEC morphology

Six porcine brain hemispheres yielded 15x 1 ml of aliquots of both PBECs caught on 150 μm and 60 μm nylon meshes. In agreement with Patabendige et al.[1], the TEER of PBECs caught on 60 μm nylon meshes was found to be higher than that of PBECs caught on 150 μm nylon meshes and were subsequently used for the remainder of experiments (data not shown).

Within three days of thawing, endothelial cells were observed to grow from vessel fragments, and were ready to be passaged within six days (see Figure 1). The cell morphology was qualitatively similar to that described by Patabendige et al., and occasionally more spindle-like, which is desirable for *in vitro* BBB models[1]. It was found that cells could be passaged twice without noticeable degradation of the endothelial phenotype; after this mutations were evident.

A2.3.2. PBEC TEER

To quantify the charge-selectivity of the barrier, the trans-endothelial electrical resistance (TEER) was measured.

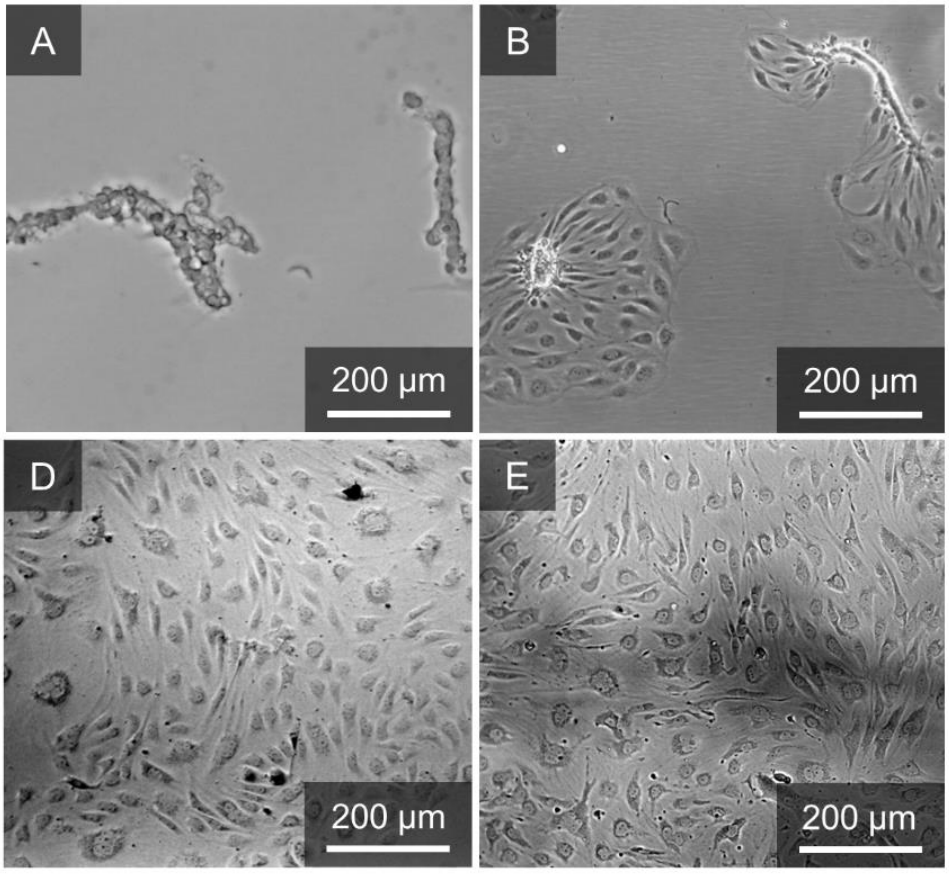

Figure 2: Bright-field microscopy of PBECs grown from porcine microvessel fragments. After thawing (A), isolated microvessels began adhering to the collagen and fibronectin- coated substrate. After three days (B), cells could be seen growing from microvessel explants. By the sixth day (C), cells formed a monolayer and were ready for passaging. After passaging (D), PBECs were observed to form a tightly-packed monolayer.

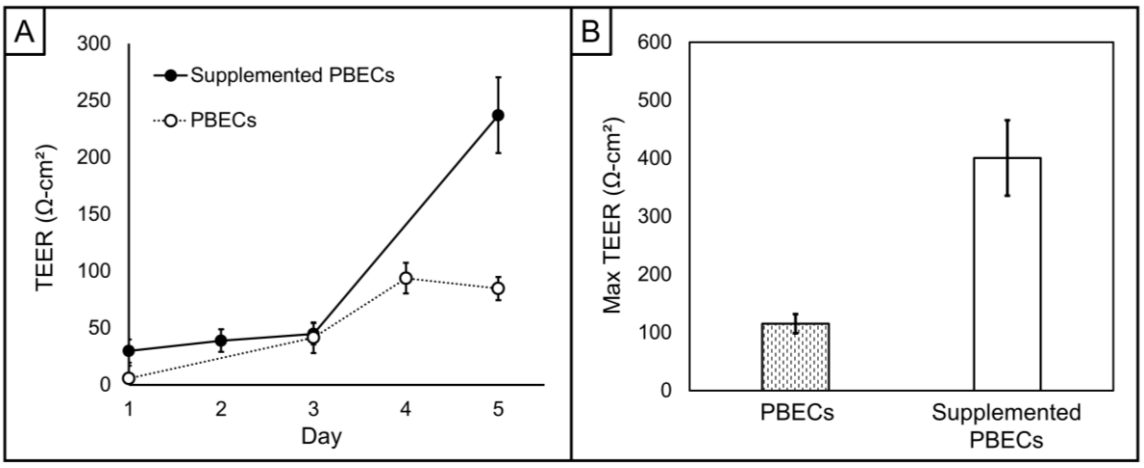

Figure 1: TEER of PBECs with and without supplementation. (A) TEER of confluent PBECs with and without medium supplementation was measured daily (n = 5). The max TEER achieved with and without supplementation (n = 19). Supplemented PBECs were found to meet the minimum criteria for BBB permeability studies.

It was found that sufficiently high TEER could be achieved at second passage by supplementing medium with RO-20-1724 and pCPT-cAMP, in addition to hydrocortisone, and by switching to serum-free medium at confluence. TEER of PBECs monolayers was found to peak within five days post-confluence (see Figure 2).

Patabendige et al. report a mean TEER of ~800 Ω-cm^2 at passage one with the same supplements[1], although the timing of medium supplementation in their manuscript is ambiguous. While the PBEC TEER of 400 ± 65 Ω-cm^2 in the present study is lower than that of Patabendige et al., it exceeds the minimum criteria of 150 Ω-cm^2 required for physiologically-relevant permeability studies[4], and is quite high with respect to most other BBB models[5].

A2.3.3. PBEC apparent permeability to TRITC-dextrans

The permeability of PBECs to 4.4 kDa TRITC-dextrans was determined for samples with TEER of 256 ± 43 Ω-cm2. The apparent permeability (P_{app}) of PBEC monolayers to 4.4 kDa TRITC-dextrans was 1.48 ± 0.45 E-6 cm/s (n = 3). In Figure 3, the

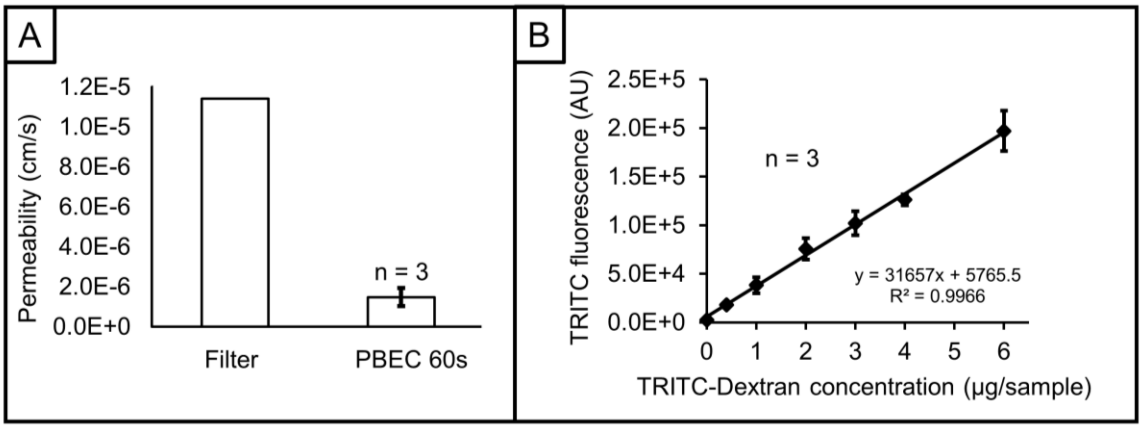

Figure 3: Apparent permeability of PBECs to 4.4 kDa TRITC-dextran. (A) Contribution of the transwell filter (control) and PBECs to the measured permeability (n = 3). The PBEC permeability is adjusted to account for the transwell filter. (B) Standard curve for TRITC fluorescence vs 4.4 kDa TRITC-dextran concentration (µg/sample). Linear regression was used to calculate the flux of TRITC-dextran through the transwell filters and the PBECs.

contribution to the total measured permeability calculated for the PBECs, and measured for the polycarbonate filter of 400 nm pore size alone are presented.

A2.3.4. Expression of TJ proteins at cell boundaries

Immunostaining results agree with the findings of Patabendige et al.[1], that PBECs do indeed express claudin-5 and occludin. In addition, expression of scaffolding protein ZO-1, and adherens junctional protein, VE-cadherin, were demonstrated by immunostaining (see Figure 4).

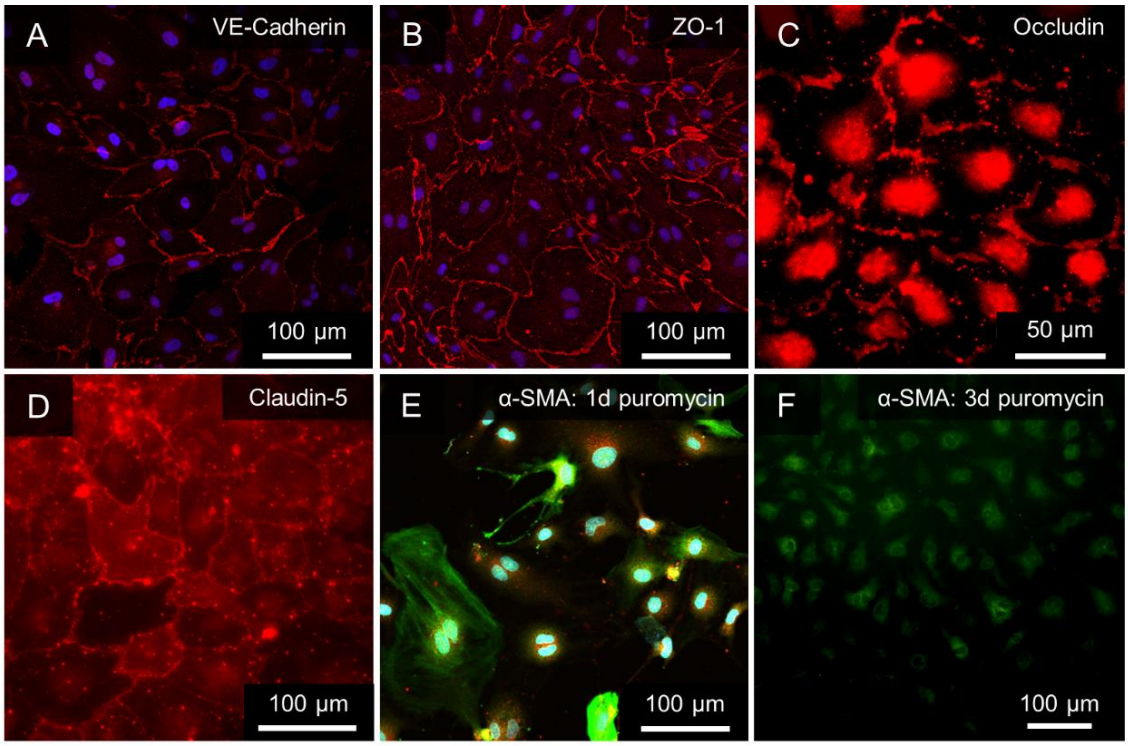

Figure 4: Immunostaining of PBECs. (A) VE-cadherin (red) and DAPI (blue), (B) ZO-1 (red) and DAPI (blue), (C) occludin (red), (D) claudin-5 (red), (E) α-SMA (green) and occludin (red), (F) α-SMA (green). (A)-(D) show expression of tight-junctional proteins. (E) shows poor occludin expression (red) in the presence of many pericytes and/or smooth muscle cells (green). (F) shows that with 3 days of puromycin treatment, the culture is purified of the vast majority of contaminating pericytes.

A2.3.5. Removal of contaminating cells

Immunostaining for smooth muscle actin (α-sma) demonstrated the presence of pericytes and/or smooth muscle cells growing beneath PBECs. In samples that contained more contaminating cells, the expression of TJ proteins was noticeably

weaker. It has been suggested that pericytes, attached to endothelial cells at their basement membranes at isolation, hinder tight junction formation by introducing defects in the endothelial monolayer[4]. Increasing the puromycin treatment duration from one day (Figure 4E) to three days (Figure 4F) per the protocol of Perriere et al[3], removed all signs of contaminating cells expressing α-sma.

A2.4. Discussion

There is currently no *in vitro* BBB model in the literature that accurately reproduces the many intricate complexities of the *in vivo* BBB. As such, *in vitro* BBB models are developed on an application-specific basis[4]. For permeability studies, the BBB model must have a physiologically realistic cell architecture, restricted paracellular permeability, expression of tight-junctional proteins, and expression of ABC-efflux transporters[6]. Unfortunately, immortalized cell lines do not meet these criteria[5]. Of the primary models, rodent models have low yield and poor permeability characteristics, bovine models either require co-culture or are poorly characterized, and human models are rare due to the difficulty in acquiring healthy and clean brain tissue for both ethical and logistical reasons[5–7]. To this end, the methods of Patabendige et al.[5,6], building on the methods of Franke et al.[8], were reproduced to establish a primary porcine BBB model (PBECs) for the investigation of the effects of lipids on the BBB.

In the present study, culture medium supplements were employed as an alternative to co-culture or culture under flow, which would add considerable complexity to experiments[2,5,7,9,10]. Purification of PBECs of contaminating pericytes and smooth muscle cells, which improves permeability characteristics[1,3,5], was achieved by puromycin exposure as demonstrated by immunostaining for smooth muscle actin. The resulting PBECs expressed TJ proteins claudin-5, ZO-1, and occludin, as well as adherens junctional protein, VE-cadherin, required for BBB differentiation.

The TEER of PBECs was found to reach 400 ± 65 Ω-cm^2 which exceeds the minimum criteria for BBB permeability studies of 150 Ω-cm^2 proposed by Abbott et al., above which diminishing returns in the flux of many compounds are expected[4]. Patabendige et al. reported that PBECs could achieve a TEER of ~800 Ω-cm^2 which is in agreement with the present study. It is hypothesized that the TEER of PBECs in the present study could be improved by an optimization of the enzyme digestion timings and methods employed for PBEC isolation, and/or the timings of the medium supplementation.

The apparent permeability of PBECs to 4.4 kDa TRITC-dextrans in the present study, $1.48*10^{-6}$ ± $0.45*10^{-6}$ cm/s, is in line with that observed in the *in vivo* rat brain to 4 kDa FITC-dextrans of $0.62*10^{-6}$ ± $0.10*10^{-6}$ cm/s as measured by multiphoton microscopy[11]. For reference, the apparent permeability of PBECs to [^{14}C] sucrose (which is ~13 times smaller than 4.4 kDa dextrans), used to characterize PBECs by Patabendige et al., was ~$6*10^{-6}$ cm/s[1,2].

A2.5. Concluding remarks

In summary, the PBECs of the present study reproduce many of the characteristics of the *in vivo* BBB and meet the criteria for *in vitro* BBB permeability studies. Furthermore, PBECs do not require co-culture with other cells from the neurovascular unit to differentiate, and can grow on acoustically-transparent filters making them well-suited to US-BBBD experiments.

A2.6. References

1. Patabendige, A., Skinner, R. a. & Abbott, N. J. Establishment of a simplified in vitro porcine blood-brain barrier model with high transendothelial electrical resistance. *Brain Res.* **1521,** 1–15 (2013).
2. Patabendige, A., Skinner, R. a., Morgan, L. & Joan Abbott, N. A detailed method for preparation of a functional and flexible blood-brain barrier model using porcine brain endothelial cells. *Brain Res.* **1521,** 16–30 (2013).
3. Perrière, N. *et al.* Puromycin-based purification of rat brain capillary endothelial cell cultures. Effect on the expression of blood-brain barrier-specific properties. *J. Neurochem.* **93,** 279–289 (2005).
4. Reichel, A., Begley, D. J. & Abbott, N. J. An overview of in vitro techniques for blood-brain barrier studies. *Methods Mol. Med.* **89,** 307–324 (2003).
5. Deli, M. a., Ábrahám, C. S., Kataoka, Y. & Niwa, M. Permeability studies on in vitro blood-brain barrier models: Physiology, pathology, and pharmacology. *Cell. Mol. Neurobiol.* **25,** 59–127 (2005).
6. Gumbleton, M. & Audus, K. L. Progress and limitations in the use of in vitro cell cultures to serve as a permeability screen for the blood-brain barrier. *J. Pharm. Sci.* **90,** 1681–1698 (2001).
7. Wilhelm, I., Fazakas, C. & Krizbai, I. a. In vitro models of the blood-brain barrier. *Acta Neurobiol. Exp. (Wars).* **71,** 113–128 (2011).
8. Franke, H., Galla, H. & Beuckmann, C. T. Primary cultures of brain microvessel endothelial cells : a valid and flexible model to study drug transport through the blood – brain barrier in vitro. *Transport* **5,** 248–256 (2000).
9. Lai, C. H. & Kuo, K. H. The critical component to establish in vitro BBB model: Pericyte. *Brain Res. Rev.* **50,** 258–265 (2005).
10. Cucullo, L. *et al.* Immortalized human brain endothelial cells and flow-based vascular modeling: a marriage of convenience for rational neurovascular studies. *J. Cereb. Blood Flow Metab.* **28,** 312–328 (2008).
11. Zeng, M. Quantification of Blood-Brain Barrier Solute Permeability and Brain Transport by Multiphoton Microscopy. **136,** 1–9 (2015).

Appendix III

An *in vitro* setup for ultrasound-mediated blood-brain barrier disruption

A3.1. Abstract

In this section, the setup for conducting US-BBBD experiments *in vitro* proposed for future work in Chapter 6 is presented[i]. Additionally, relevant selections from the literature are reviewed.

A3.2. Introduction

A3.2.1. Kinetics of US-BBBD *in vivo*

In the small subset of *in vivo* studies that investigate US-BBBD kinetics[1–6], a wide range of experimental parameters and techniques are employed. This may contribute to discrepancies in reported BBB recovery times which span orders of magnitude, from minutes[1], to hours[4,6], to days[2,3].

Ultrasound frequencies range from 0.69 to 1.5 MHz, pressures from 0.2 to 0.9 MPa, burst lengths from 67 to 10000 µs (100-6900 cycles), PRFs from 1 to 10 Hz, and durations from 60 to 120 s (see Table 1). The mechanisms responsible for US-BBBD likely differ across these exposure conditions. The Nhan et al.[1] and Sun et al.[2] studies, for instance, demonstrated a correlation between acoustic pressure and BBB permeability and opening volume. This is intuitive in the sense that at higher pressures, cavitation is more violent and acts to further open the BBB. Correspondingly, BBB permeability was also found to correlate with the acoustic emissions recorded during US-BBBD. In addition to BBB permeabilization, the kinetics of BBB disruption and recovery have been correlated with acoustic pressure. BBB recovery time has also been demonstrated to correlate with acoustic emissions[2,3].

[i]This work was presented at the ASA Boston 2017 and BBB Symposium 2017 conferences.

The studies of Sun et al. and Marty et al.[4] further demonstrated that BBB closing time was inversely correlated with MB diameter and payload molecule size. It follows that MB formulation plays an important role in US-BBBD, as demonstrated by Konafagou et al.[7]. The cavitation agents employed in the aforementioned US-BBBD kinetics studies include clinical MBs Definity®, Optison®, and SonoVue®, in addition to custom laboratory formulations. MB dosages varied by an order of magnitude in MBs per unit animal weight, and two orders of magnitude with regard to MB solution volume per unit animal weight. Animal models varied in species (e.g. mice or rats), weight (e.g. rat

Study	f (MHz)	P (MPa)	Burst length (ms)	PRF (Hz)	Duration (s)
Raymond et al., 2007	1.029	0.2	10	1	45-60
Nhan et al., 2013	1.2	0.2-0.8	10	1	120
Sun et al., 2015	1.5	0.3-0.9	0.0666	5	60
Samiotaki et al., 2012	1.5	0.3-0.6	0.0666	10	60
Marty et al., 2012	1.5	0.45	3	10	60
Park et al., 2012	0.690	0.6-0.8	10	1	60

Table 1: Ultrasound parameters employed in studies that investigate US-BBBD kinetics in vivo[1–6]. Parameters include the ultrasound frequency (f), peak negative pressure (P), burst length, pulse repetition frequency (PRF), and exposure duration.

Study	Microbubbles	Tracer size (Da)	Permeability assessment	Animal model	Anesthesia
Raymond et al., 2007	Optison 5-8 x 10^8 MB/ml 0.3 ml/kg	960 to 70000	2PFM	C57 wild-type mice 20.2-28.5 g	avertin (1.3% 2,2,2-tribromoethanol, 0.8% tert- pentylalcohol; 250 mg/kg)
Nhan et al., 2013	Definity 1.2 x 10^9 MB/ml 0.02 ml/kg	10000 and 70000	2PFM	Male Wistar rats 150-250 g	5% isoflurane initially, reduced to 2% for US-BBBD
Sun et al., 2015	18:0 PC, PEG40S 9:1 (C_4F_{10} gas) 8 x 10^8 MB/ml Dose not reported	591	DCE-MRI (9.4 T)	Male mice (C57BL/6) 24.21 ± 1.72 g	1.5-2% isoflurane gas mixed with oxygen
Samiotaki et al., 2012	18:0 PC, PEG40S 9:1 (C_4F_{10} gas) 8 x 10^8 MB/ml 1 ml/kg	574	DCE-MRI (9.4 T)	Male mice (C57BL/6) 20–25 g	1.25-2.50% isoflurane mixed with oxygen
Marty et al., 2012	SonoVue, 1.5 x 10^8 MB/ml 2-2.5 ml/kg (then 0.1 ml saline)	754 to 800000+	MRI (7 T) in multiple animals at different time points	Sprague Dawley male rats 80-100 g	1.5% isoflurane mixed with air and oxygen
Park et al., 2012	Definity 1.2 x 10^9 MB/ml 0.01 ml/kg	938	DCE-MRI (3 T)	Sprague–Dawley rats 250-300 g	80 mg/kg of ketamine and 10 mg/kg of xylazine

Table 2: Selected experimental parameters employed in studies that investigate US-BBBD kinetics in vivo[1–6]. MB formulations, concentrations, and dosages are presetned where available. The tracer size in Marty et al. were converted from 1-65 nm hydrodynamic radii to Da using available data from the manufacturers. Sex is included in the animal model where data was available. The anesthesia protocols are presented as reported. 2PFM is two-photon fluorescence microscopy. DCE-MRI is dynamic contrast-enhanced magnetic resonance imaging.

weight varies from 80 to 350g) and model (e.g. Sprague-Dawley or Wistar rats), further complicating comparison between studies (see Table 2).

Detection modalities also vary between *in vivo* US-BBBD kinetics studies. Sun et al.[2], Samiotaki et al.[3], and Park et al.[6], for example, elected to employ dynamic contrast-enhanced MRI (DCE-MRI) for daily BBB permeability assessment. DCE-MRI can be used to generate spatial BBB permeability maps, and to determine BBB opening volumes by measuring the transfer rate of MRI contrast agent from blood vessels to the extracellular space. Park et al. further demonstrated a correlation between DCE-MRI-derived permeability and the quantity of drug delivered following US-BBBD[6], suggesting that DCE-MRI may aid US-BBBD assessment in the clinic.

Another approach for determining BBB permeability was published by Marty et al.[4] using contrast-enhanced MRI techniques with an *in vitro* relaxivity calibration that enabled consistent measurement across experimental subjects. To obtain BBB closing times, the BBB permeability of 10 rats were determined at various time points after treatment.

Building on the work of Raymond et al.[5], Nhan et al.[1] assessed BBB permeability at the microscale by measuring the flux of fluorescent tracers through the BBB with two-photon microscopy via cranial windows in rats. This technique enables BBB permeability assessment with excellent temporal and spatial resolution. Nhan et al. demonstrated that BBB opening time and permeabilization are inversely correlated with vessel size[1]. Vessel size may impact the cavitation behaviour of MBs, as demonstrated by high-speed imaging of MB oscillations in *ex vivo* blood vessels and computational methods[8–10]. The circumferential stress in the vessel wall during ultrasound and MB exposure has also been suggested to be inversely proportional to vessel size[8]. MB

coalescence[9] and the presence of red blood cells[11] are also likely contributing factors to the relationship between vessel size and US-BBBD observed by Nhan et al.

In summary, valuable mechanistic insights have been made by *in vivo* US-BBBD methods, although the vast parameter space can make comparison of results across studies difficult, and many open questions remain.

A3.2.2. Acoustic emissions monitoring of US-BBBD *in vivo*

Under conditions in which the cavitation required for US-BBBD exceeds safe levels, damage to healthy tissue has been reported to range from a few extravasated erythrocytes or dark neurons, to more severe brain damage, or even mortality[12–15]. While US-BBBD under ideal conditions appears safe, treatment monitoring and control systems are needed to ensure successful translation to humans.

Controlling cavitation activity during ultrasound exposure has been achieved by employing a feedback control whereby the acoustic emissions produced by cavitation are recorded passively using an ultrasound transducer or passive cavitation detector (PCD), processed in real-time, and used to adjust the ultrasound exposure parameters, keeping the emissions within a certain energy range[16]. Advances in passive acoustic emissions monitoring, such as the developments of two and three dimensional mapping of cavitation events using transducer arrays (passive acoustic mapping, PAM)[17], improved real-time data processing algorithms[18,19], transcranial acoustic emissions monitoring[20] extended to three-dimensional transcranial PAM[21] and transcranial PAM with CT-based skull corrections[22], point to a bright future for non-invasive treatment monitoring and control in US-BBBD. Other important advances in ultrasound imaging such as ultrafast (e.g. frames per second > 1000) plane-wave imaging[23], mapping of the brain vasculature and single microbubbles with super-resolution ultrasound imaging[24],

and with super-resolution applied to ultrafast plane-wave imaging[25] further support this notion.

Furthermore, correlations between harmonic and/or broadband acoustic emissions and the response of the BBB and surrounding tissue have been demonstrated in the literature. Broadband acoustic emissions have been associated with biological damage *in vivo*[28,29]. In contrast, harmonic and ultraharmonic acoustic emissions have been associated with safe and effective US-BBBD in animal studies[15,28,30]. Harmonic acoustic emissions have been further correlated with the extent of BBB permeabilization and with BBB closing time[2,16]. In one study, the delivery of small molecules (3 and 7 kDa) by US-BBBD corresponded with harmonic acoustic emissions, whereas delivery of larger molecules (500 and 2000 kDa), akin to antibodies or gene vectors in size, necessitated conditions that produced broadband acoustic emissions[29]. Harmonic and broadband acoustic emissions can be recorded through the intact skull, however, the ability to measure certain harmonics, subharmonics, and ultraharmonics depends on the sensitivity of the cavitation detector used, its position relative to the skull, and filtering from the skull, among other factors[28].

A3.2.3. Selected *in vitro* US-BBBD background

Given the increasingly wide parameter space for US-BBBD, especially as novel cavitation agents are developed[12,31–34], the systematic investigation of US-BBBD mechanisms and novel delivery strategies appears well-suited to *in vitro* work. Few *in vitro* studies have been performed, however, despite the initiation of US-BBBD clinical trials in humans[34].

As described in Appendix II, *in vitro* BBB models, first established in the late 1970s, now approximate many of the characteristics of the *in vivo* BBB required for permeabilization studies[35]. The most common approach in ultrasound-mediated barrier

permeabilization research *in vitro*, however, is to employ a cell line that is either endothelial and/or is purported to express tight junctional proteins[36,37], neither of which are necessarily representative of the BBB. The expression of tight junctional proteins in endothelial cells, for instance, does not necessarily correspond to low permeability. Deli et al. provide two excellent examples in their review, (1) cells with high levels of occludin can have low TEER (e.g. high permeability) and (2) claudin-5 knockout in mice were shown to be only selectively permeabilized to some small molecules[35].

Helfield and colleagues demonstrated by time-lapse fluorescence microscopy, the restructuring of the cell-cell contacts of human umbilical vein endothelial cells (HUVECs) during ultrasound exposure[37]. The micron-scale gaps in their images, however, far exceed those expected of BBB tight junction disruption, and cannot be distinguished from endothelial cell contractions upon cavitation-mediated insult. Kooiman et al.[36], also studied HUVEC monolayer permeability upon exposure to ultrasound and MBs, in this case by measuring the trans-endothelial electrical resistance (TEER < 25 Ω-cm^2) to assess the ionic permeability at cell-cell junctions. These studies are not applicable to US-BBBD because HUVECs, of non-cerebral origin[38], form leaky monolayers as indicated by their TEER which is an order of magnitude too low to approximate the permeability characteristics of the BBB[39].

Lelu et al. published the only US-BBBD study that implemented a viable BBB model (the same as implemented in Appendix II, although conceived independently), but failed to achieve US-BBBD *in vitro* due to destruction of the endothelial monolayer upon transfer to their ultrasound setup[40]. This setup did not enable TEER measurements or any other biological assessment during ultrasound exposure but rather involved the transfer of a monolayer grown on a filter into an ultrasound-enabled water tank. As a result of their inability to establish a reliable control, Lelu et al. were unable to produce

any insights regarding US-BBBD. The US-BBBD *in vitro* setup proposed below aims to overcome these challenges.

A3.2.4. Criteria for US-BBBD *in vitro*

For the experiments described in Chapter 6, the US-BBBD *in vitro* setup should contain the following:

(1) A relevant BBB model (see Appendix II)

(2) BBB integrity monitoring

(3) Ultrasound exposure

(4) Acoustic emissions monitoring

(5) Assessment of biological response (e.g. by fluorescence microscopy).

A3.3. Methods

A3.3.1. Overview of the US-BBBD *in vitro* setup

A modified version of the BBB-on-a-chip developed by the BIOS Lab-on-a-Chip group at the University of Twente, was employed in the US-BBBD setup. The BBB-on-a-chip is an ultrasound-compatible *in vitro* device incorporating electrodes for TEER measurements that enables real-time BBB integrity monitoring. Professor Loes Segerink and Dr. Marinke van der Helm kindly provided photolithographic moulds and methodological information for reproducing their BBB-on-a-chip devices. TEER monitoring during US-BBBD was achieved using the voltage-controlled current source described by Aroom et al.[41]. To monitor TEER recovery after US-BBBD, a multiplexed TEER system was developed with Dr. Lester Barnsley with the capacity to monitor the TEER of up to 16 samples concurrently in a cell culture incubator. A water tank setup with a clinical ultrasound transducer and a passive cavitation detector (PCD) were employed for ultrasound exposure and acoustic emissions monitoring respectively.

Finally, fluorescence microscopy during ultrasound exposure for the investigation of the biological response during US-BBBD was achieved using an optical setup developed by Dr. Shamit Shrivastava. By simultaneously monitoring TEER, fluorescence, and acoustic emissions during ultrasound exposure of the *in vitro* BBB model described in Appendix II, the setup described herein meets the aforementioned criteria for US-BBBD *in vitro*.

A3.3.2. BBB-on-a-chip for US-BBBD *in vitro*

A3.3.2.1. Concept

Microfluidic BBB-on-a-chip devices were fabricated according to the protocol of van

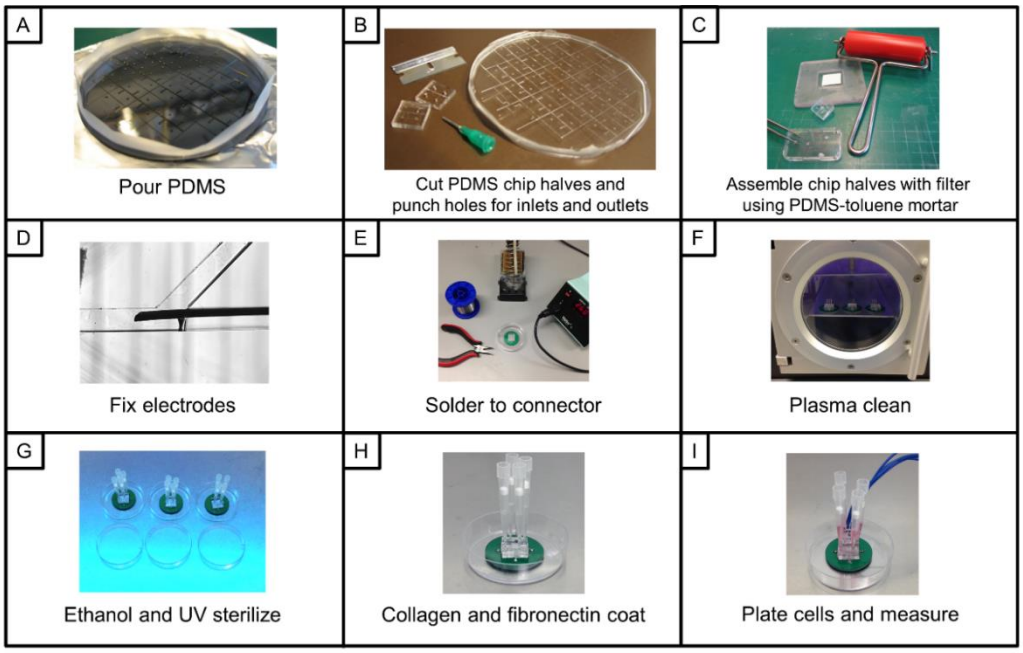

Figure 1: Photographic protocol for BBB-on-a-chip device fabrication. First PDMS is poured into a photolithographic SU-8 or a 3-D printed mold (A). After curing for at least 4 h, the PDMS is peeled from the mould, chip halves are cut out using a razor blade, and holes are punched for inlets and outlets (B). PDMS-toluene mortar is then applied to the chip halves using a paint roller and a custom rolling platform, filters are added to one half, and the BBB-on-a-chip devices are assembled and cured for another 4 h (C). Platinum wire is then inserted into the 4x electrode ports and fixed with UV-curable adhesive at a microscope (D). BBB-on-a-chip devices are then soldered to custom PCBs (E). Before use, BBB-on-a-chip devices are plasma cleaned to sterilize and enhance hydrophobicity of the flow channels (F). Devices are further sterilized by ethanol and UV exposure for 20 min (G), before extracellular matrix coating with collagen and fibronectin (H), at which point devices are ready for cell culture and TEER measurements (I). (B) and (C) are adapted from van der Helm et al.

der Helm et al. and Griep et al., with minor modifications outlined below[42,43] (see Figure 1). The BBB-on-a-chip model features embedded electrodes for TEER measurements, and two crossing flow channels separated by a semi-permeable filter upon which the cell monolayer is grown.

A3.3.2.2. BBB-on-a-chip device electrodes

In the protocol of van der Helm et al., electrical connections were made using alligator clips directly on the platinum wire. Because the weight of the alligator clips exceeded that of the BBB-on-a-chip devices, great care had to be taken not to damage the devices by pulling on the electrodes. In this study, BBB-on-a-chip devices were soldered to custom circular PCBs (PCB-Way) with a 16 mm radius and a 15 mm square window for ultrasound access (see Figure 1E). By soldering the BBB-on-a-chip device, electrical connections were made using a standard kk-connector (see Figure 1I). This removed the risk of damaging the device or losing electrical connection during manipulation.

A3.3.2.3. Preparing BBB-on-a-chip devices for cell culture

Prior to use, the completed BBB-on-a-chip devices were plasma cleaned to help sterilize the devices and to render the channels more hydrophilic which helps seeding of the BBB-on-a-chip devices without trapping air bubbles (see Figure 1F).

For seeding cells in BBB-on-a-chip devices, devices were sterilized by filling the flow channels with 70% ethanol in filtered distilled and de-ionized water (ddH_2O) and exposing to UV light in a sterile cross-flow hood for 30 min (see Figure 1G). The flow channels were subsequently washed with PBS before filling with rat-tail collagen at 300 mg/ml followed by human fibronectin at 7.5 mg/ml both in filtered ddH_2O for 2 h each at room temperature (see Figure 1H). Coating the filters in the BBB-on-a-chip devices

with collagen and fibronectin extracellular matrix proteins provided a substrate conducive to tight junction formation.

A3.3.2.4. Cell culture in BBB-on-a-chip devices

Madin-Darby canine kidney cells (MDCKs) were cultured as described in Chapter 5. Following a final wash with PBS, the BBB-on-a-chip devices were seeded with ~$5*10^6$ cells/ml (see Figure 1I). Cells were allowed to settle for ~12 h before washing and replenishing the medium with fresh cell culture media for growth.

A3.3.2.5. Recovery of BBB-on-a-chip device electrodes and PCBs

After experiments, platinum wires were recovered by removing them from BBB-on-a-chip PCBs with a soldering iron. The PCBs were then washed with isopropanol and the platinum wires submerged in dichloromethane (DCM) in a glass vial for a minimum of 60 min. Following treatment with DCM, the glue used to secure the platinum wire easily rubbed off and the wire could be utilized to make new devices. No difference in performance between BBB-on-a-chip devices made with fresh or recovered platinum electrodes was observed. This enabled the cost-effective scale-up of the protocols described by Griep at al. and van der Helm et al. in which the platinum was discarded after use.

A3.3.3. Ultrasound for US-BBBD *in vitro*

A3.3.3.1. Ultrasound field

A 0.5 MHz high-intensity focused ultrasound transducer was used for ultrasound exposure (H-107, Sonic Concepts, Bothell, WA). The ultrasound transducer was confocally-aligned with the BBB-on-a-chip filter and was positioned with a 60° angle between the plane of the cells and the axis of ultrasound propagation (see Figure 2).

A3.3.3.2. Ultrasound field measurement

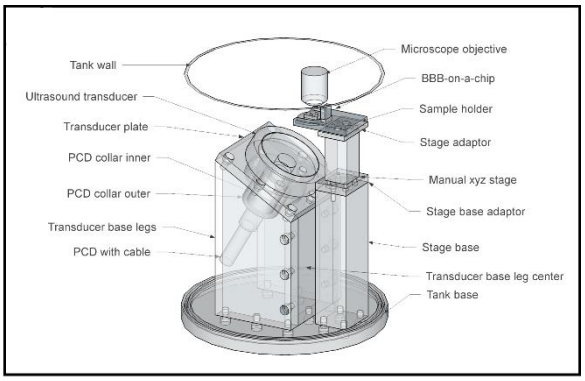

Figure 2: Drawing of the US-BBBD water tank setup with the BBB-on-a-chip device.

The ultrasound transducer was driven using the signal generator and RF amplifier described in Chapter 2. The output of the amplifier was passed through a matching network and a high-voltage probe was placed between the matching network and ultrasound transducer.

Ultrasound pressure fields were measured using a fibre-optic hydrophone measurement system (Precision Acoustics). To facilitate alignment of the BBB-on-a-chip target with the ultrasound focus, and to reduce the need for alignment between samples, an acoustic absorber (Aptflex F28, Precision Acoustics) with a circular window (32 mm diameter) was fastened flush to the outer edge of the transducer to reduce the aperture, increasing the beam width.

A3.3.3.3. Ultrasound pressure in the BBB-on-a-chip

The pressure inside a BBB-on-a-chip device at the ultrasound focus (without the acoustic absorber aperture) was taken by carefully inserting a fibre-optic hydrophone through one of the electrode ports of the BBB-on-a-chip device.

A3.3.3.4. Acoustic emissions monitoring for US-BBBD in vitro

Acoustic emissions were monitored using a PCD (V320 Panametrics, Olympus) confocally-aligned with the ultrasound transducer. The PCD signal was amplified using a signal pre-amplifier with 5X gain (Stanford Research Systems).

A3.3.4. TEER for US-BBBD *in vitro*

A3.3.4.1. TEER measurements

In Chapter 5, TEER measurements were performed by temporarily submerging

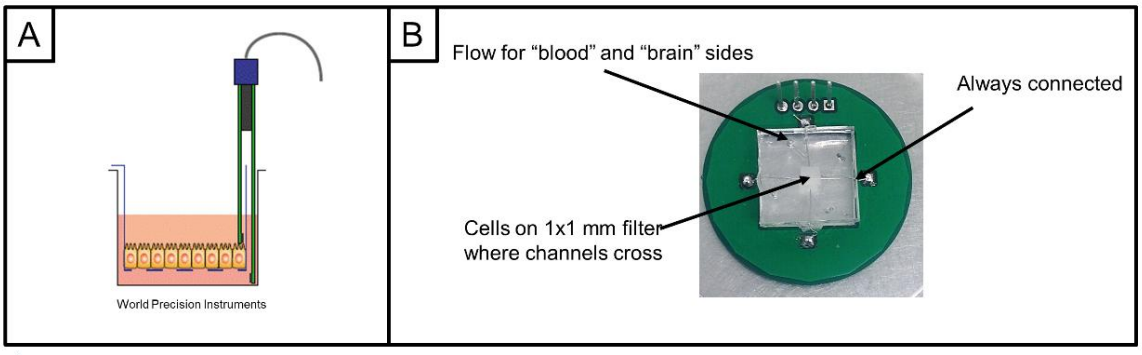

Figure 3: Methods for measuring TEER. Transwell TEER measurements with chopstick electrodes (A) are a standard method in the literature. The BBB-on-a-chip approach involves platinum wire electrodes in two flow channels separated by a membrane filter upon which cells are grown. With the BBB chamber (C), copper-plated tin pins from standard electrical connectors serve as two electrode pairs in fluid chambers separated by a membrane filter upon which cells are grown. In (A) electrodes are manually placed for every measurement and cells must be removed from the incubator. In (B) electrode placement is achieved at a microscope with UV-adhesive. Devices cannot be re-used so electrode placement varies from sample to sample and experiment to experiment. In (C) electrodes are manually inserted once and remain for the life-time of the device. Devices can be re-used and electrode placement is defined by 3D printed or milled holes such that placement is uniform across samples and experiments.

electrodes into the apical and basolateral chambers of a transwell culture dish. This method can be improved by incorporating electrodes into the cell culture device such that the electrode placement is fixed (see Figure 3).Four-probe TEER measurements (e.g. with separate forcing and a sensing pairs of electrodes) were performed for increased accuracy over two-probe measurements, e.g. by reducing the influence of resistances associated with the electrodes. By maintaining a constant current across the monolayer, the resistance across the monolayer was determined by measuring the voltage drop across the sensing pair of electrodes. To this end, a constant current was supplied to BBB-on-a-chip devices using the voltage-controlled current source (VCCS) designed by Aroom et al[41]. For TEER measurements, the input voltage to the VCCS was 0.1 V_{pp} at 500 Hz resulting in a constant current of 8 µA.

A digital oscilloscope (Handyscope, HS3) was used for both driving the VCCS and measuring the voltage drop across the top and bottom chambers in the BBB-on-a-chip device. The membrane area for the TEER calculation was taken as 0.0025 cm^2.

A3.3.4.2. Multiplexing TEER measurements

A cell culture incubator is the ideal environment for the *in vitro* BBB model. To this

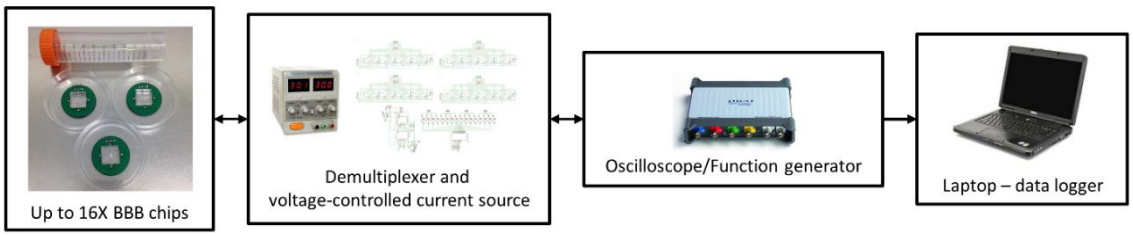

Figure 4: Multiplexing TEER measurements. A purpose-built LabView program running on a dedicated computer is used to programmatically control the function generator output, oscilloscope measurements, and Arduino. The Arduino is used to select 1 of 16 channels on the demultiplexer circuit which then opens the current-send and voltage-receive paths to the selected sample. The function generator output drives the VCCS which sends a constant current to the selected device. The oscilloscope then receives the voltage measured by the sensing electrode pair in the selected sample. This voltage trace is recorded and plotted with the purpose-built software.

end, a multiplexed TEER monitoring system was developed[ii] to maximize the time samples spend in the incubator, such that recovery monitoring of multiple samples after US-BBBD could be performed. TEER recovery after US-BBBD is expected to require minutes to hours such that a single-channel system would limit throughput. In-incubator screening for compounds or formulations that affect TEER can also be achieved with greater experimental control and higher throughput using this system. To this end, the multiplexed TEER monitoring system of the present study was designed to achieve automated monitoring of up to 16 BBB-on-a-chip devices (see Figure 4).

The multiplexer system consists of four parts: the demulitplexer/VCCS circuit, an Arduino UNO, a digital oscilloscope and function generator, and purpose-written LabVIEW software running on a laptop (see Figure 4). The LabVIEW software is used to send 4 bits to the digital I/O on the Arduino UNO, encoding for 1 of 16 channels. This signal is passed from the Arduino UNO to a non-inverting demultiplexer/decoder (Texas Instruments CD74HCT4515E), which routes the signal to two DPDT relays (e.g. for forcing and sensing electrode pairs) to perform the TEER measurement on the selected sample.

In addition to channel selection, the LabVIEW software was written to control the digital oscilloscope and function generator. The software allows for any subset of channels to be measured on a schedule, and can be modified during operation for experiments where multiple inter-measurement times may be required.

[ii] The circuit for the multiplexer and the LabVIEW software was designed by Dr. Lester Barnsley. I contributed to the PCB design, assembly, debugging, and software development.

A3.3.5. Fluorescence intensity measurement during US-BBBD *in vitro*

Fluorescence intensity was monitored using a custom-built microscope designed by Dr. Shamit Shrivastava. A high power light emitting diode (LED) followed by a bandpass filter was used for excitation. A dichroic mirror was used to send the filtered excitation source light through a microscope objective (4x, Nikon) and separated the emitted fluorescence for detection. The emitted fluorescence was then split by another dichroic mirror where it was collected by a Hamamatsu photomultiplier tube (PMT, H10493-003) or a fluorescence camera both fitted with a bandpass filter. All optics hardware was from Thorlabs.

A3.3.6. Temperature control for US-BBBD *in vitro*

The US-BBBD water tank was maintained at 37°C using a circulating heated water bath (VWR) (see Figure 5).

A3.3.7. Simultaneous measurement of TEER, acoustic emissions, and fluorescence

To achieve simultaneous measurement of TEER, acoustic emissions, and fluorescence intensity, two oscilloscopes with built-in signal generators were employed. The first, (Picoscope, PicoTech) was used to record the high-voltage probe set between the matching network and the transducer, the fluorescence intensity from the PMT(s), and the acoustic emissions signal with the PCD. The second (HS3, Handyscope) was used to record the TEER and to generate the 500 Hz, 0.1 V_{pp} signal used to drive the VCCS for TEER measurements.

The LED for fluorescence excitation, the signal generator for the ultrasound transducer, and the Picoscope measurements were triggered using square wave pulses from the

signal generator on the Picoscope. This trigger was also recorded on the HS3 oscilloscope, such that the TEER signal could be aligned with the ultrasound signal in post-processing.

The function generator used for the ultrasound transducer was triggered in burst mode with a delay set to the time required for the LED intensity to reach a steady state. Due to the orders of magnitude difference in frequencies for TEER and PCD measurements (e.g. 500 Hz vs 5 MHz) recording the TEER separately allowed for ideal sampling frequencies to be employed for each measurement. Furthermore, using the function generator output on the Picoscope oscilloscope to trigger the LED greatly reduced the effects of photo-bleaching.

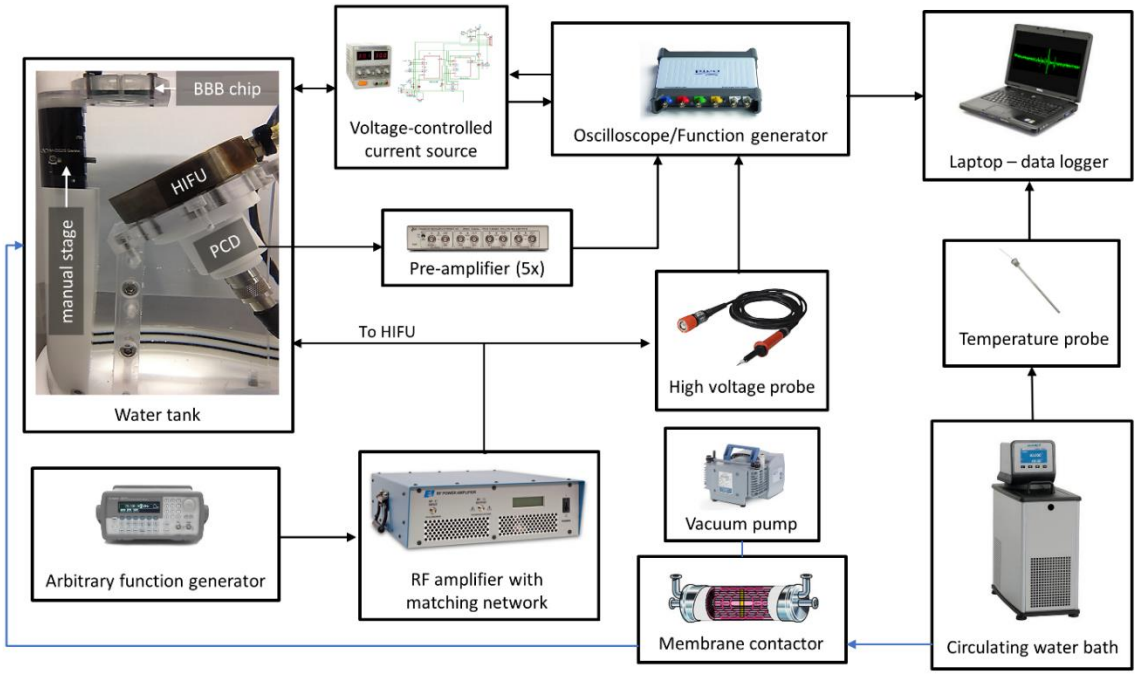

Figure 5: US-BBBD setup.

A3.4. Results

A3.4.1. VCCS calibration

The VCCS designed by Aroom et al. was reproduced to supply a constant current for TEER measurements in the BBB-on-a-chip device.

The output current of the VCCS was constant for frequencies ranging from 100 Hz to 100 kHz, and for input voltages ranging from 0.25 to 1 V_{pp}, in agreement with the theoretical value as determined by Aroom et al. (see Figure 6A-B). Electrical resistance

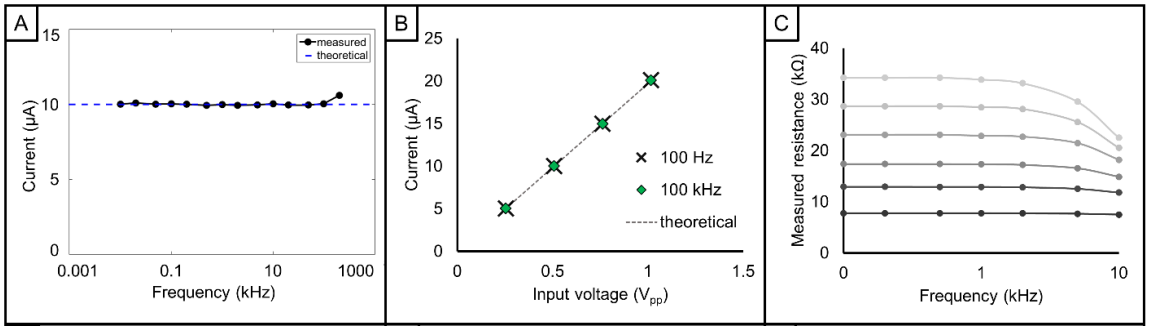

Figure 6: VCCS characterization. The current was found to behave as expected with regard to the input voltage and frequency (A) and (B). In (C) each line corresponds to a resistor with measurement of the nominal value achieved at 10 Hz.

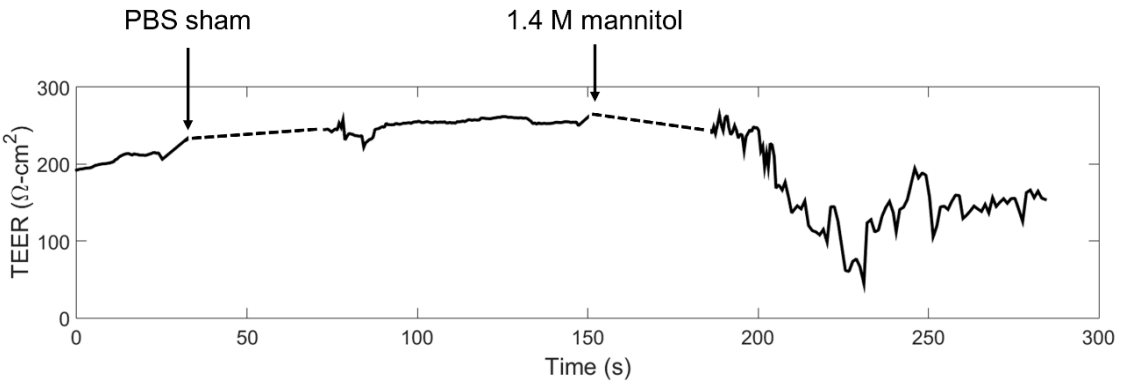

Figure 7: MDCK monolayer disruption in a BBB-on-a-chip device. Following the introduction of a PBS sham to the apical chamber of a BBB-on-a-chip device, no change in monolayer TEER is evident. Shortly after introduction of hyperosmolar mannitol (1.4 M) in PBS disruption of the monolayer was observed as indicated by the rapid decrease in TEER at ~200 s. The dotted lines show where a PBS bridge across electrodes was introduced following pipetting into the device. This resulted in the acquiring of unusable data over these periods. This is not a feature of the BBB-on-a-chip device and can be avoided by connecting pipette tips or flow lines to the BBB-on-a-chip outlets in future experiments.

measurement with the VCCS (7.5 to 35 kΩ) was more accurate at low frequencies (<1 kHz), tending to underestimate resistances at higher values and frequencies (see Figure 6C). When operated at 500 Hz and 0.1 V_{pp}, the VCCS can measure TEER in the range of 2.5 to 500 Ω-cm^2 in the BBB-on-a-chip device which should be sufficient for US-BBBD experiments.

A3.4.2. TEER measurements in a BBB-on-a-chip device

While few BBB-on-a-chip models with confluent monolayers were successfully produced, a control experiment performed with one such sample suggests that the response to treatment of a tight junction model can be temporally-resolved using the BBB-on-a-chip device and VCCS discussed in the present study. Specifically, a BBB-on-a-chip device with confluent MDCKs was first exposed to PBS and then to hyperosmolar mannitol in PBS (1.4 M) during TEER measurements performed with the VCCS (see Figure 7). Hyperosmotic barrier disruption was chosen as a control treatment for decreasing TEER because it has been reported to disrupt the BBB *in vivo*[44] and *in vitro*[45]. Hyperosmotic BBB disruption is associated with vasodilation, osmotic shrinkage of endothelial cells, and the calcium-mediated contraction of the endothelial cytoskeleton[46]. It was found that exposure to PBS had a negligible effect on TEER whereas exposure to hyperosmolar mannitol resulted in monolayer disruption within ~60 s. Additional experiments, may elucidate disruption mechanisms and allow the determination of kinetic constants associated with disruption and recovery.

A3.4.3. Challenges producing reliable BBB-on-a-chip models

After many attempts with varying extracellular matrix coatings, cell seeding densities, culture medium replacement times, and filter materials, it was found that reliably culturing MDCK cells in BBB-on-a-chip devices presented an unexpected challenge.

Clearly, cell growth in BBB-on-a-chips can be achieved, as demonstrated by the BIOS Lab on a Chip group[42,43], and the few successful samples observed here.

The BIOS Lab on a Chip group employed hCMEC/D3 cells which formed leaky monolayers with 22 ± 1.3 Ω-cm^2 TEER when grown in BBB-on-a-chip devices[42]. This model is not representative of the permeability of the BBB or, in general, a tight-junction-forming tissue barrier. In the present study, MDCKs were employed which achieve two orders of magnitude higher TEER, representative of a monolayer with tight junctions and a significant permeability barrier.

It was conceivable that MDCKs, which require nutrient-rich medium, were more sensitive to the conditions in the BBB-on-a-chip devices, such as poor access to fresh medium. To test this factor, BBB-on-a-chip devices were plated with MDCKs and supplied with fresh medium every 2 h for 12 h once cells were visibly adhered. Still, none of the samples achieved confluent monolayers.

MDCKs were then grown on the same used in BBB-on-a-chip devices filters (10 µm thick with 400 nm track-etched pores) in well plates with an excess of fresh medium. These samples were systematically subjected to a number of factors that could hypothetically influence cell growth. It was found, for instance, that MDCKs could form confluent monolayers on filters regardless of whether they were plasma cleaned prior to use (data not shown). Likewise, MDCKs were found capable of forming confluent monolayers on polycarbonate (PC) or polyethylene terephthalate (PET) filters coated with either collagen for 3h, fibronectin for 3h, or collagen for 2h then fibronectin for 2h as described by Patabendige et al[47].

The PDMS-toluene mortar used to make BBB-on-a-chip devices may contribute to the difficulty in cell culture experienced. Toluene is highly cytotoxic. When MDCKs were grown on filters in the presence of toluene, the formation of a confluent monolayer was

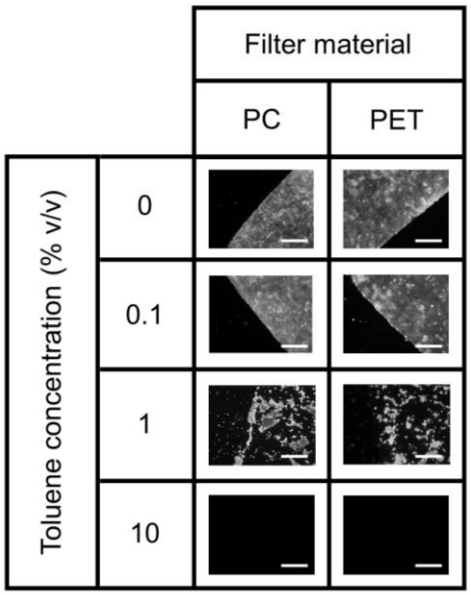

Figure 8: Growth of cells on polycarbonate (PC) and polyethylene terephthalate (PET) in the presence of toluene. Toxicity was evident at 1 % toluene.

prevented with a volume concentration threshold between 0.1 and 1 % (see Figure 8). The BBB-on-a-chip device has a total volume of ~7 µl such that volumes of toluene greater than 70 nl would be expected to prohibit monolayer formation. This miniscule amount may explain why MDCKs did occasionally form confluent monolayers but not in a reliable manner sufficient for US-BBBD experiments.

One difference between the present study and those of the BIOS Lab on a Chip group is the way in which the PDMS-toluene mortar was applied to the chips. They used a spin-coater to apply a very thin layer of PDMS-toluene mortar to a glass slide from which they coated the ink roller used to apply mortar to the chip halves. In the absence of a spin-coater in the present study, PDMS-toluene mortar was applied to a rolling platform

by pipetting and then transferred to the ink roller by rolling. It is thus conceivable that the method used in the present study resulted in more toluene per device.

Exposure of BBB-on-a-chip devices to conditions that vaporize toluene (40°C and under vacuum with pressure < 1 Pa) prior to cell culture was performed for 30 min, yet no improvement in cell culture was realized. It is conceivable that the toluene was unable to leave the PDMS-toluene mortar effectively in this experiment and then leeched into the culture medium over time. This may be improved by baking the BBB-on-a-chip devices above the boiling temperature of toluene (110°C).

A3.4.4. Ultrasound pressure measurements

Scans of the ultrasound field with the device holder used for the BBB-on-a-chip experiments demonstrated that the sample holder did not interfere with the ultrasound field (see Figure 9B). Using an acoustic absorber with a circular cutaway to reduce the aperture of the ultrasound transducer increased the width of the ultrasound focus in the plane of the BBB-on-a-chip channel by 50% with ~50% reduction in pressure. This simplified alignment of the device with the ultrasound focus and reduced the need to re-align between samples. The direct measurement of the pressure in the BBB-on-a-chip device as a function of the driving voltage is shown in Figure 9A.

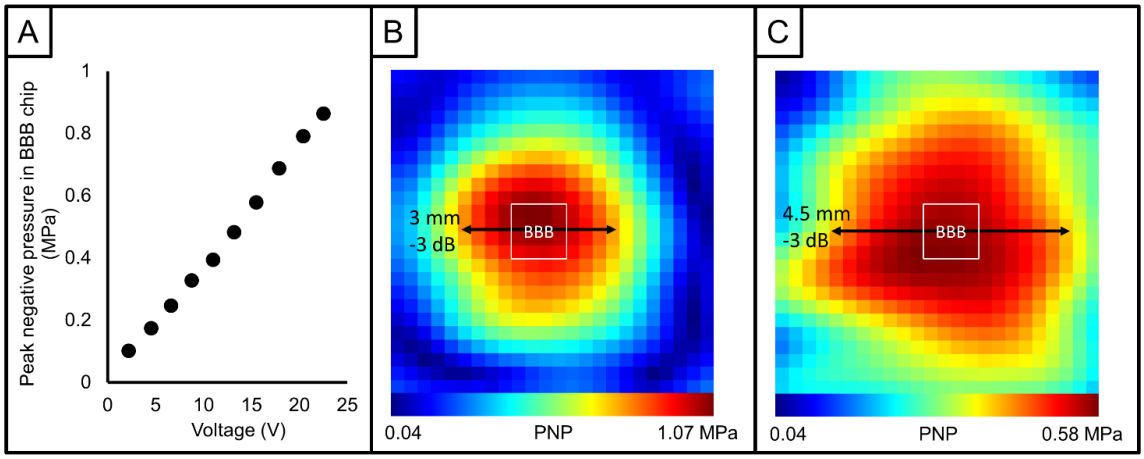

Figure 9: Ultrasound field measurement. The ultrasound pressure in a BBB-on-a-chip device in shown in (A). The ultrasound pressure field was scanned with the device holder at the plane of the BBB-on-a-chip device channel without a device present (B). The field was widened by employing an aperture-reducing acoustic window (C).

A3.4.5. Fluorescence microscopy in a BBB-on-a-chip during ultrasound exposure

Fluorescence microscopy during ultrasound and microbubble exposure in a BBB-on-a-chip device was demonstrated with the *in vitro* US-BBBD setup by recording cavitation microstreaming in the device with fluorescent tracer beads. Cavitation microstreaming was chosen because it demonstrates both cavitation activity and successful fluorescence

microscopy. Briefly, the apical chamber of the BBB-on-a-chip device was filled with 22:0 PC-PEG40S MB containing 1 µl/ml 2 µm fluorescent flow tracer beads (Sigma) and then transferred to the water tank setup and exposed to ultrasound (500 kHz at 0.6 MPa PNP, continuous wave) during fluorescence microscopy video acquisition.

Cavitation microstreaming was observed throughout the apical chamber of the BBB-on-a-chip device and was not observed in the basolateral chamber owing to the filter preventing fluorescent beads from crossing (see Figure 10). Microstreaming under these exposure conditions was observed on the order of 100-1000 µm/s following analysis of 100 frames by streak velocimetry using the methods employed in Chapter 2 and published elsewhere[48].

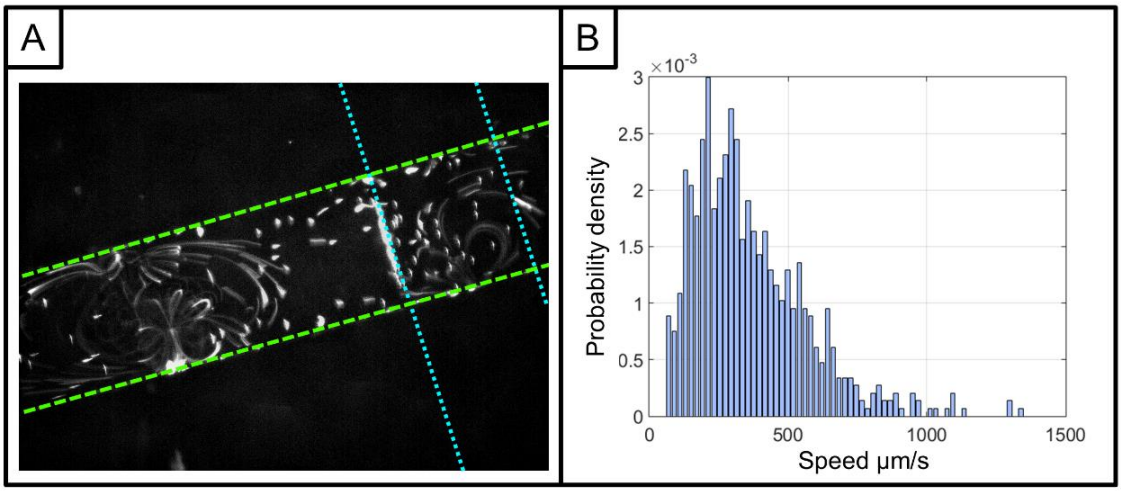

Figure 10: Cavitation microstreaming in a BBB-on-a-chip device during ultrasound and microbubble exposure in the in vitro US-BBBD setup. The representative fluorescence microscopy image in (A) shows microstreaming confined to the apical chamber (green dashed lines) and excluded from the basolateral chamber (blue dotted lines) by the membrane filter. The cross section of the channels is 0.5 x 0.5 mm. From an analysis of 100 frames captured during microstreaming using streak velocimetry, the speed distribution in (B) was produced illustrating fluid flows on the order of 100-1000 µm/s detected from cavitation microstreaming.

A3.4.6. Simultaneous acquisition of acoustic emissions and TEER

To demonstrate the US-BBBD *in vitro* setup, TEER and acoustic emissions were recorded during ultrasound exposure (500 kHz at 0.6 MPa PNP with 100 µs bursts at a 2.5% duty cycle) of a cell-free BBB-on-a-chip device loaded with 22:0 PC-PEG40S MB and maintained at ~37.5°C (see Figure 11E). It was found that ultrasound and 22:0 PC-PEG40S MB exposure did not affect the measured electrical resistance across the filter (see Figure 11A-B). Harmonic, ultraharmonic, and broadband acoustic emissions were observed throughout the exposure period (see Figure 11C-D). It follows that

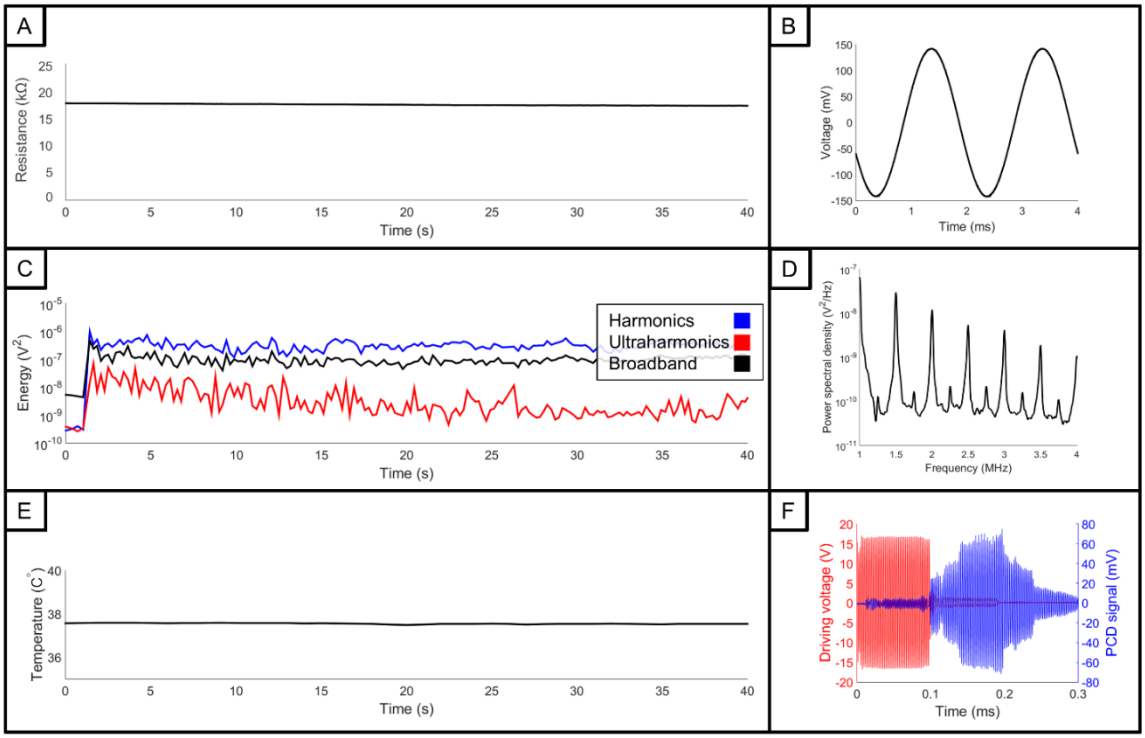

Figure 11: Simultaneous measurement of acoustic emissions and electrical resistance with the US-BBBD in vitro setup. The electrical resistance across the filter in a BBB-on-a-chip device without cells was measured during exposure to ultrasound and microbubbles injected into the apical chamber. The electrical resistance across the filter was unaffected by ultrasound and microbubble exposure as shown in (A). A representative voltage trace from the electrical resistance measurement is shown in (B). Harmonic, ultraharmonic, and broadband acoustic emissions from 22:0 PC-PEG40S MB were observed over the exposure period as shown in (C) with a representative power spectral density spectrum in (D). Temperature was maintained at ~37.5°C throughout the exposure as recorded by an RTD temperature sensor submerged in the water tank. The time-of-flight from the transducer to the BBB-on-a-chip and back to the PCD was ~ 0.1 ms (F). The ultrasound exposure for this experiment was 500 kHz at 0.6 MPa PNP with 100 µs bursts at a 2.5% duty cycle.

simultaneous acquisition of acoustic emissions and TEER during US-BBBD is feasible with this setup.

A3.5. Discussion

Several contributions to the BBB-on-a-chip device developed by Griep et al. and van der Helm et al. were made in preparation for US-BBBD experiments *in vitro*. The reusability of platinum electrodes used in BBB-on-a-chip devices was achieved by soaking platinum wires in DCM to remove cured UV-adhesive residues followed by cleaning with acetone and ethanol, resulting in a significant reduction in the cost of the devices. Electrical connections for BBB-on-a-chip devices were also improved by the use of inexpensive custom PCB connectors that allow for the use of standard electrical connectors in BBB-on-a-chip TEER measurements. This reduced the likelihood of accidentally dislodging electrodes from BBB-on-a-chip devices. Furthermore, plasma cleaning was introduced to the preparation process which was expected to improve device sterility and aid the wetting of the channels. Finally, the ultrasound pressure in BBB-on-a-chip devices was calibrated for US-BBBD experiments. Despite these developments, achieving confluent cell monolayers in BBB-on-a-chips was unreliable. This may be a result of cytotoxic toluene residues remaining from the PDMS-toluene mortar used to fabricate BBB-on-a-chip devices.

In addition, the multiplexed TEER measurement system presented in the present study has the potential to enable scale-up of *in vitro* BBB experiments employing TEER measurements with embedded electrodes. The ability to measure multiple samples on a measurement schedule in a cell culture incubator could facilitate the screening of compounds for their kinetic effects on BBB permeability and TEER, in addition to enabling the monitoring of monolayer formation and the kinetics of BBB recovery

following US-BBBD across multiple samples. With further optimization of the cell culture conditions for the BBB-on-a-chip model, the work presented herein has the potential to enable high-quality US-BBBD *in vitro* research.

A3.6. Conclusion

In this section, the design, fabrication, and characterization of an *in vitro* US-BBBD setup was presented. To this end the following was achieved:

1) The ultrasound-, microscopy-, and TEER-compatible BBB-on-a-chip was adapted from van der Helm et al.[42], and characterized for its potential in US-BBBD experiments *in vitro*.
2) A multiplexed TEER measurement system was developed to facilitate the monitoring of TEER in 16+ samples on a measurement schedule in a cell culture incubator.
3) An *in vitro* US-BBBD water tank setup was demonstrated for simultaneous acquisition of acoustic emissions, TEER, and fluorescence microscopy during ultrasound and cavitation-agent exposure of the BBB-on-a-chip.

A3.7. References

1. Nhan, T. *et al.* Drug delivery to the brain by focused ultrasound induced blood-brain barrier disruption: Quantitative evaluation of enhanced permeability of cerebral vasculature using two-photon microscopy. *J. Control. Release* **172,** 274–280 (2013).

2. Sun, T. *et al.* Acoustic cavitation-based monitoring of the reversibility and permeability of ultrasound-induced blood-brain barrier opening. *Phys. Med. Biol.* **60,** 9079–9094 (2015).

3. Samiotaki, G. *et al.* Pressure and microbubble size dependence study of focused ultrasound-induced blood-brain barrier opening reversibility in vivo. *AIP Conf. Proc.* **1481,** 300–306 (2012).

4. Marty, B. *et al.* Dynamic study of blood-brain barrier closure after its disruption using ultrasound: a quantitative analysis. *J. Cereb. Blood Flow Metab.* **32,** 1948–58 (2012).

5. Raymond, S. B., Skoch, J., Hynynen, K. & Bacskai, B. J. Multiphoton imaging of ultrasound / Optison mediated cerebrovascular effects in vivo. 393–403 (2007). doi:10.1038/sj.jcbfm.9600336

6. Park, J., Zhang, Y., Vykhodtseva, N., Jolesz, F. A. & McDannold, N. J. The kinetics of blood brain barrier permeability and targeted doxorubicin delivery into brain induced by focused ultrasound. *J. Control. Release* **162,** 134–142 (2012).

7. Wu, S.-Y., Chen, C. C., Tung, Y.-S., Olumolade, O. O. & Konofagou, E. E. Effects of the microbubble shell physicochemical properties on ultrasound-mediated drug delivery to the brain. *J. Control. Release* **212,** 30–40 (2015).

8. Qin, S. & Ferrara, K. W. Acoustic response of compliable microvessels containing ultrasound contrast agents. *Phys. Med. Biol.* **51,** 5065–5088 (2006).

9. Caskey, C. F., Stieger, S. M., Qin, S., Dayton, P. a & Ferrara, K. W. Direct observations of ultrasound microbubble contrast agent interaction with the microvessel wall. *J. Acoust. Soc. Am.* **122,** 1191–1200 (2007).

10. Sassaroli, E. & Hynynen, K. Resonance frequency of microbubbles in small blood vessels: a numerical study. *Phys. Med. Biol.* **50,** 5293–5305 (2005).

11. Wiedemair, W., Tuković, Ž., Jasak, H., Poulikakos, D. & Kurtcuoglu, V. On ultrasound-induced microbubble oscillation in a capillary blood vessel and its implications for the blood–brain barrier. *Phys. Med. Biol.* **57,** 1019–1045 (2012).

12. Kamimura, H. a S. *et al.* Chirp- and random-based coded ultrasonic excitation for localized blood-brain barrier opening. *Phys. Med. Biol.* **60,** 7695–7712 (2015).

13. Hynynen, K., McDannold, N., Martin, H., Jolesz, F. a. & Vykhodtseva, N. The threshold for brain damage in rabbits induced by bursts of ultrasound in the presence of an ultrasound contrast agent (Optison??). *Ultrasound Med. Biol.* **29,** 473–481 (2003).

14. McDannold, N., Vykhodtseva, N. & Hynynen, K. Effects of Acoustic Parameters

and Ultrasound Contrast Agent Dose on Focused-Ultrasound Induced Blood-Brain Barrier Disruption. *Ultrasound Med. Biol.* **34,** 930–937 (2008).

15. McDannold, N., Vykhodtseva, N. & Hynynen, K. Targeted disruption of the blood-brain barrier with focused ultrasound: association with cavitation activity. *Phys. Med. Biol.* **51,** 793–807 (2006).

16. O'Reilly, M. a. & Hynynen, K. Blood-Brain Barrier: Real-time Feedback-controlled Focused Ultrasound Disruption by Using an Acoustic Emissions-based Controller. *Radiology* **263,** 96–106 (2012).

17. Collin, J., Coviello, C., Lyka, E., Leslie, T. & Coussios, C. C. Real-time three-dimensional passive cavitation detection for clinical high intensity focussed ultrasound systems. *Cit. Proc. Mtgs. Acoust* **19,** (2013).

18. Lyka, E., Coviello, C., Kozick, R. & Coussios, C.-C. Sum-of-harmonics method for improved narrowband and broadband signal quantification during passive monitoring of ultrasound therapies. *J. Acoust. Soc. Am.* **140,** (2016).

19. Coviello, C. M., Faragher, S. R. & Coussios, C. Robust Capon beamforming for passive cavitation mapping during high-intensity focused ultrasound therapy. *J. Acoust. Soc. Am.* **128,** 2280–2280 (2010).

20. Tung, Y.-S., Marquet, F., Teichert, T., Ferrera, V. & Konofagou, E. E. Feasibility of noninvasive cavitation-guided blood-brain barrier opening using focused ultrasound and microbubbles in nonhuman primates. *Cit. Appl. Phys. Lett* **98,** (2011).

21. O'Reilly, M. A., Jones, R. M. & Hynynen, K. Three-dimensional transcranial ultrasound imaging of microbubble clouds using a sparse hemispherical array. *IEEE Trans. Biomed. Eng.* **61,** 1285–94 (2014).

22. Jones, R. M., O'Reilly, M. A. & Hynynen, K. Transcranial passive acoustic mapping with hemispherical sparse arrays using CT-based skull-specific aberration corrections: a simulation study. *Phys. Med. Biol.* **58,** 4981–5005 (2013).

23. Couture, O., Fink, M. & Tanter, M. Ultrasound contrast plane wave imaging. *IEEE Trans. Ultrason. Ferroelectr. Freq. Control* **59,** (2012).

24. O'Reilly, M. A. & Hynynen, K. A super-resolution ultrasound method for brain vascular mapping. *Med. Phys.* **40,** 110701 (2013).

25. Errico, C. *et al.* Ultrafast ultrasound localization microscopy for deep super-resolution vascular imaging. *Nature* **527,** 499–502 (2015).

26. Hu, Y., Wan, J. M. F. & Yu, A. C. H. Membrane Perforation and Recovery Dynamics in Microbubble-Mediated Sonoporation. *Ultrasound Med. Biol.* **39,** 2393–2405 (2013).

27. Fan, Z., Liu, H., Mayer, M. & Deng, C. C. X. Spatiotemporally controlled single cell sonoporation. *Proc. Natl. Acad. Sci. U. S. A.* **109,** 16486–16491 (2012).

28. Tung, Y.-S. *et al.* In vivo transcranial cavitation threshold detection during ultrasound-induced blood–brain barrier opening in mice. doi:10.1088/0031-9155/55/20/007

29. Chen, H. & Konofagou, E. E. The size of blood-brain barrier opening induced by focused ultrasound is dictated by the acoustic pressure. *J. Cereb. blood flow Metab.* **34,** 1197–204 (2014).

30. McDannold, N., Arvanitis, C. D., Vykhodtseva, N. & Livingstone, M. S. Temporary disruption of the blood-brain barrier by use of ultrasound and microbubbles: Safety and efficacy evaluation in rhesus macaques. *Cancer Res.* **72,** 3652–3663 (2012).

31. Chen, Y.-C. *et al.* Targeting Microbubbles-carrying TGFβ1 Inhibitor Combined with Ultrasound Sonication Induce BBB/BTB Disruption to Enhance Nanomedicine Treatment for Brain Tumors. *J. Control. Release* **211,** 53–62 (2015).

32. Åslund, A. K. O. *et al.* Efficient Enhancement of Blood – Brain Barrier Permeability Using Acoustic Cluster Therapy (ACT). **7,** 23–30 (2017).

33. Chen, C. C. *et al.* Targeted drug delivery with focus ultrasound-induced blood-brain barrier opening Using acoustically-activated nanodroplets. *IEEE Int. Ultrason. Symp. IUS* **172,** 615–618 (2013).

34. Carpentier, A. *et al.* Clinical trial of blood-brain barrier disruption by pulsed ultrasound. **8,** (2016).

35. Deli, M. a., Ábrahám, C. S., Kataoka, Y. & Niwa, M. Permeability studies on in vitro blood-brain barrier models: Physiology, pathology, and pharmacology. *Cell. Mol. Neurobiol.* **25,** 59–127 (2005).

36. Kooiman, K., Van Der Steen, A. F. W. & De Jong, N. Role of intracellular calcium and reactive oxygen species in microbubble-mediated alterations of endothelial layer permeability. *IEEE Trans. Ultrason. Ferroelectr. Freq. Control* **60,** 1811–1815 (2013).

37. Helfield, B., Chen, X., Watkins, S. C. & Villanueva, F. S. Biophysical insight into mechanisms of sonoporation. *Proc. Natl. Acad. Sci. U. S. A.* **113,** 9983–8 (2016).

38. Wilhelm, I., Fazakas, C. & Krizbai, I. a. In vitro models of the blood-brain barrier. *Acta Neurobiol. Exp. (Wars).* **71,** 113–128 (2011).

39. Reichel, A., Begley, D. J. & Abbott, N. J. An overview of in vitro techniques for blood-brain barrier studies. *Methods Mol. Med.* **89,** 307–324 (2003).

40. Lelu, S. *et al.* Primary porcine brain endothelial cells as in vitro model to study effects of ultrasound on blood-brain barrier function. *IEEE Trans. Ultrason. Ferroelectr. Freq. Control* 1–1 (2016). doi:10.1109/TUFFC.2016.2597004

41. Aroom, K. R. *et al.* Bioimpedance Analysis: A Guide to Simple Design and Implementation. *J. Surg. Res.* **153,** 23–30 (2009).

42. Van Der Helm, M. W. *et al.* Direct quantification of transendothelial electrical resistance in organs- on-chips. (2016). doi:10.1016/j.bios.2016.06.014

43. Griep, L. M. *et al.* BBB on CHIP: Microfluidic platform to mechanically and biochemically modulate blood-brain barrier function. *Biomed. Microdevices* **15,** 145–150 (2013).

44. Pardridge, W. M. The blood-brain barrier: bottleneck in brain drug development. *NeuroRx* **2,** 3–14 (2005).

45. Cucullo, L., Marchi, N., Hossain, M. & Janigro, D. A dynamic in vitro BBB model for the study of immune cell trafficking into the central nervous system. *J. Cereb. Blood Flow Metab.* **31,** 767–777 (2011).

46. Rapoport, S. I. Osmotic opening of the blood-brain barrier: Principles, mechanism, and therapeutic applications. *Cell. Mol. Neurobiol.* **20,** 217–230 (2000).

47. Patabendige, A., Skinner, R. a., Morgan, L. & Joan Abbott, N. A detailed method for preparation of a functional and flexible blood-brain barrier model using porcine brain endothelial cells. *Brain Res.* **1521,** 16–30 (2013).

48. Pereno, V. *et al.* Layered acoustofluidic resonators for the simultaneous optical and acoustic characterisation of cavitation dynamics, microstreaming, and biological effects. *Biomicrofluidics* **12,** 34109 (2018).